Strained HgTe/CdTe topological insulators, toward spintronic applications

Candice Thomas

Communauté
UNIVERSITÉ Grenoble Alpes

THÈSE

Pour obtenir le grade de

DOCTEUR DE la Communauté UNIVERSITÉ GRENOBLE ALPES

Spécialité : **Nanophysique**

Arrêté ministériel : 7 Août 2006

Présentée par

Candice THOMAS

Thèse dirigée par **Tristan Meunier**
et codirigée par **Philippe Ballet**

préparée au sein **CEA-LETI et Institut Néel**
et de **l'École doctorale de Physique de Grenoble**

Strained HgTe/CdTe topological insulators, toward spintronic applications

Thèse soutenue publiquement le **15 Décembre 2016**,
devant le jury composé de :

E. Tournié
Professeur, Université de Montpellier - CNRS , Rapporteur

D. Weiss
Professeur, Institut für Experimentelle und Angewandte Physik, Universität Regensburg, Rapporteur

J. Cayssol
Professeur, Université de Bordeaux, LOMA - CNRS, Examinateur

H. Mariette
Directeur de recherche émérite, Institut Néel - CNRS, Président

L. Vila
Ingénieur de recherche, CEA-INAC, Invité

T. Meunier
Chargé de recherche, Institut Néel - CNRS, Directeur de thèse

P. Ballet
Ingénieur de recherche, CEA-LETI, Co-Directeur de thèse

Acknowledgements

Parce que je n'aurais jamais réussi à réaliser cette thèse toute seule, je souhaiterais remercier l'ensemble des personnes qui ont permis à ce travail d'éclore à la fois par leur contribution scientifique mais également par leur bonne humeur et leur gentillesse. Tout ceci m'a permis d'être dans les meilleures dispositions.

Je voudrais tout d'abord remercier Tristan Meunier et Philippe Ballet mes deux directeurs de thèse pour m'avoir fait confiance et m'avoir permis de travailler sur ce projet. Tous les deux vous m'avez donné envie de continuer dans ce métier de chercheur, merci pour ça et j'espère qu'on sera amené à retravailler ensemble par le futur.

Tristan, merci d'avoir été là au quotidien quand je mesurais au bâtiment M. Merci pour ton aide et pour m'avoir poussé à aller au fond des choses. Je me souviendrais toujours du soir où on a vu apparaître les premiers vrais plateaux avec Olivier, Clément et toi. Après avoir passé de nombreux échantillons sans succès, s'être convaincu qu'on avait des débuts de signatures d'effet Hall en fait ce n'était rien, et là, enfin, on avait quelque chose qui marchait. Tout l'engouement qu'il y avait eu ce soir-là te caractérise bien et c'est ce qui m'a beaucoup plu en travaillant avec toi.

Philippe... que dire (à part que j'attends toujours mon enveloppe...). Merci pour tout. Merci pour tout cet "amusement" au quotidien. Le temps passe vite quand on travaille en s'amusant et pfiou elle est passée tellement vite cette thèse. Merci d'avoir été là tous les jours à me soutenir (et même au hand), merci pour tout ce que tu m'as appris, ... je pourrais en écrire des pages et des pages.

Je souhaiterais ensuite remercier l'ensemble des membres du jury: Eric Tournié, Dieter Weiss, Jérome Cayssol, Laurent Vila et Henri Mariette pour avoir accepté d'évaluer mon travail. Merci beaucoup et j'espère qu'on pourra rester en contact pour discuter entre autre des isolants topologiques HgTe mais aussi de mon nouveau projet de postdoctorat.

Je tiens à remercier désormais l'ensemble des personnes avec qui j'ai pu interagir durant cette thèse. Tout d'abord l'équipe du LMS/D6. "Je t'explique" (copyright Dominique Giotta) que j'ai passé trois supers années au D6. Merci à Véronique Rouchon pour m'avoir aidé au quotidien en gérant parfaitement la partie administrative et en remportant le combat contre la CPAM. Merci à Philippe Duvaut, Sébastien Renet et Axel Chorier pour m'avoir supporté dans votre bureau et pour votre soutien. Merci à Dominique Giotta pour m'avoir raconté 36 fois les mêmes histoires et pour les tours de Modus. Merci à Xavier Baudry pour tous ces spectacles (et promis on s'en fout pas de tout), je t'attends à Purdue ou à Stockholm. Merci à Erik Gout, Clément Lobre et Aymeric Tuaz pour les matchs de badminton. Merci à Sonia Busseuil et Delphine Brellier pour avoir organisé les soirées bar. Merci à David Collonge pour avoir été chercher l'eau à chaque repas, à Gilbert Gaude pour le soleil de Noyarey, à Pascale Giacomini pour son peps, à Jérémy Merlin pour ses tenues improbables de cycliste, à Rémy Obrecht pour ses bières, à Antoine Pagot pour avoir illuminer mes journées, à Bernard Polge pour ses connaissances sur les voyages, à Jean-Louis Santailler pour les analyses handball... En bref, merci à tous ceux que j'ai cité mais également aux autres (la liste est trop importante) pour ces bons moments passés avec vous.

Merci aux chefs Anne Roule, Alain Million et Bernard André de croire en ce projet un peu atypique au Leti et de le défendre. Merci également au LPFE de Jacques Baylet et particulièrement à Guillaume Bourgeois pour m'avoir accueilli et formé en salle blanche.

Ensuite, je voudrais remercier l'ensemble de l'équipe du bâtiment M. Merci à Olivier Crauste et Clément Bouvier pour m'avoir initié aux isolants topologiques et permis de débuter cette thèse dans des conditions optimales. Merci à Vivien Thiney-Reboulet, alias mon jumeau de thèse, pour avoir partagé cette expérience avec moi, merci pour tout. Merci à Mathias Solana pour ces grandes soirées musicales que je n'oublierai pas, non jamais... Merci à Pierre-André Mortemousque (PAPAPAPAM..) pour toute ton aide au quotidien sur petit Kiwi et ta disponibilité. Merci également à Christopher Bäuerle, Benoit Bertrand, Baptiste Jadot, Hanno Flentje, Gregoire Roussely, Shintaro Takada ...

Il me faut également remercier tout particulièrement l'équipe Nanofab. Merci à Sebastien Dufresnes pour toutes ces lithos, ces records d'alignement et tout le reste. Merci à Thierry Crozes, Bruno Fernandez, Gwenaëlle Julie et Jean-François Motte. Ça a été un plaisir de travailler avec vous.

Je voudrais remercier ensuite l'ensemble des personnes de l'INAC/LETI/ENS Lyon/Institut Néel avec qui j'ai pu collaborer dans le cadre de ce projet. Tout d'abord, merci à Xavier Biquard et Denis Jalabert pour toutes ces manips à l'ESRF et au MEIS et votre bonne humeur communicative. Merci à Benedikt Haas, Pierre-Henri Jouneau et Nicolas Mollard pour l'ensemble des analyses TEM, pour votre réactivité, votre travail de pointe et pour l'ensemble des discussions très enrichissantes que j'ai pu avoir avec vous. Merci à Paul Nöel, Yu Fu et Laurent Vila pour avoir donné une autre dimension à ce projet en y introduisant du spin avec les mesures de spin-pumping. Merci pour tous vos conseils et pour toutes nos discussions. Merci également à Marc Veillerot et Jean-Paul Barnes pour les analyses SIMS. Merci à David Carpentier et Laurent Lévy pour les discussions sur l'effet Hall quantique dans les 3D TI et sur les mesures d'ARPES.

Enfin pour finir, j'aimerai remercier ma famille et mes amis pour leur soutien sans faille tout au long de cette thèse que ce soit dans les bons moments mais aussi et surtout dans les moments de doute.

J'oublie certainement encore des gens et je m'en excuse. En tout cas, ces trois années ont été superbes et c'est grâce à vous tous donc encore MERCI et j'espère à bientôt.

Abstract

Topological Insulators (TI) are a new class of materials that recently attracts a large interest both theoretically and experimentally thanks to the unique electronic and spin properties that arise on their interfaces. Indeed, with graphene-like transport properties carried by massless Dirac fermions and a topological protection preventing from backscattering phenomena, TI surfaces are full of promise for the design of future quantum electronics.

However, so far, only few material systems fulfill the requirements to make strong TIs. With an inverted band structure, the semi-metal HgTe is one of them assuming the opening of a bandgap by tensile strain.

This PhD thesis aims at experimentally demonstrating the topological nature of strained HgTe as well as its eligibility for applications, especially for spintronics.

To do so, strong efforts have been dedicated to the improvement of the growth process by molecular beam epitaxy. Chemical composition, strain, defect density and sharpness of the HgTe interfaces have been identified as the major parameters of study and improvement to ensure HgTe inverted band structure, bulk gap opening and to emphasize the resulting topological surface state electronic properties. Verification of the topological nature of this system has then been performed using low temperature magneto-transport measurements of Hall bars designed with various HgTe thicknesses. It is worth noting that the high desorption rate of Hg has made the nanofabrication process more complex and required the development of a low temperature process adapted to this constraint. While the thicker samples have evidenced very complex transport signatures that need to be further investigated and understood, the thickness reduction has led to the suppression of any additional contributions, such as bulk or even side surfaces, and the first demonstration of quantum Hall effect with vanishing resistance. Consequently, we have managed to demonstrate direct evidences of Dirac fermions and their transport mechanism by temperature dependent analysis of the quantum Hall effect. The next step has been to use the topological properties and especially the locking predicted between momentum and spin to test the HgTe potential for spintronics. Spin pumping experiments have demonstrated the power of these topological structures for spin injection and detection. Moreover, the implementation of HgTe into simple p-n junction has also been investigated to realize a first spin-based logic element.

Abstract-Français

Les isolants topologiques constituent une nouvelle classe de matériaux suscitant un intérêt grandissant grâce à l'association de propriétés électroniques et de spin uniques à leurs interfaces. En effet, avec un transport régit par des particules à énergie de dispersion linéaire couramment appelées fermions de Dirac ainsi qu'une protection topologique empêchant tout phénomène de rétrodiffusion, les surfaces des isolants topologiques apparaissent comme une plateforme prometteuse pour l'électronique de demain.

Cependant, à ce jour, seulement quelques systèmes possèdent les caractéristiques requises pour former un isolant topologique. Avec une structure de bande inversée, le semi-métal HgTe est l'un d'entre eux à condition de croître sous tension ce qui permet l'ouverture d'un gap de volume.

L'objectif de cette thèse a été de démontrer expérimentalement le potentiel de l'isolant topologique HgTe pour des applications notamment dans le domaine de la l'électronique de spin ou spintronique. Pour ce faire, d'importants efforts ont été mis en œuvre pour améliorer le procédé de croissance par épitaxie par jets moléculaires. La composition chimique, la contrainte ainsi que la qualité des interfaces de la couche de HgTe ont été identifiées comme des axes majeurs de travail et d'optimisation afin d'obtenir une structure de bande inversée, l'ouverture d'un gap de volume, ainsi que pour protéger les propriétés électroniques des états de surface topologiques. Fort de ces caractéristiques, notre matériau possède à priori toutes les qualités nécessaires pour permettre de sonder les propriétés topologiques. Accéder à ces propriétés particulières est possible par des mesures d'effet Hall quantique sur des structures de type barres de Hall. La fabrication de ces dispositifs a néanmoins requis une attention particulière à cause de la forte volatilité du mercure et a nécessité le développement d'un procédé de nanofabrication à basses températures. Des mesures d'effet Hall quantique à très basses températures ont ensuite été réalisées dans un cryostat à dilution. Tout d'abord des couches épaisses de HgTe ont été mesurées et ont démontré des mécanismes de transport très complexes mêlant les états de surface topologiques à d'autres contributions attribuées au volume et aux états de surface latéraux. La réduction de l'épaisseur des couches de HgTe a permis de limiter l'impact de ces contributions en les rendant négligeables pour les couches les plus fines. Dans ces conditions, ces structures ont affiché pour la première fois les propriétés attendues de l'effet Hall quantique avec notamment une annulation de résistance. L'analyse en température de l'effet Hall quantique a permis de démontrer la nature des porteurs circulant sur les états de surface topologiques et de les identifier à des fermions de Dirac. Avec la mise en évidence de la nature topologique de notre système, l'étape suivante a été d'utiliser les propriétés topologiques et plus particulièrement le blocage entre le moment et le spin d'un électron pour tester le potentiel du système 3D HgTe/CdTe pour la spintronique. Premièrement, des mesures de spin pumping ont été réalisées et ont mis en exergue la puissance de ces structures pour l'injection et la détection de spin. Deuxièmement, ces structures ont été implémentées sous la forme de jonction p-n dans l'idée de réaliser un premier dispositif de spintronique.

Contents

Introduction

The past few years have been the theatre of an impressive boom and development of electronic devices such as smart phones, computers, and so on. If these devices are nowadays everywhere and more and more efficient, this is principally due to the huge progress made on their electronic chips mainly composed of small elementary devices called transistors. Developed from a semiconductor material, the transistor has been the first electronic component to be able to both amplify and switch on/off an electronic signal, thus fully controlling the flow of electrical information. These components were uncovered in 1947 by J. Bardeen, W. Schockley and W. Brattain at Bell laboratories. Revolutionizing the world of electronics, this invention has been considered as one of the most important of the 20^{th} century and led its inventors to the Nobel prize in 1956. A few years later in 1965, Gordon Moore, one of the co-funders of Intel, predicted that the number of transistors on a chip will double every two years without increasing its price just thanks to technological progress. But to increase transistor density, one needs to reduce their size. Important progress in the resolution of lithography process and etching methods enabled to confirm this prediction and to obtain nowadays transistors with channel length of tens of nanometers. With such nanometer-size, billions of transistors can now be implemented on a chip leading to devices with greatly enhanced functionalities.

However at such a small scale, these transistors suffer from high leakage currents decreasing drastically their efficiency in comparison to their energy consumption. Finding novel technologies with lower energy consumption to replace the existing charge-based electronic building-blocks is currently a hot topic in both academic and industrial research.

Spin electronics, also called spintronics, appears as a solution, currently attracting a huge interest by proposing to no longer transfer information by the charge but by the angular momentum of the electrons. Nowadays, spintronic devices constitute a serious alternative for the implementation of logic elements and memories. Among them, Magnetic Random Access Memory (MRAM) is distinctly the most promising device as it provides non-volatile memory scalable to high density and high speed with an infinite write/erase cycle [TSC+99]. MRAM are made of basic elements such as magnetic tunnel junctions which are formed by two ferromagnetic layers separated by a thin insulating layer. The first ferromagnetic layer is a permanent magnet acting as a reference for reading and writing, while the second one has a free magnetization allowing to store information. By sending important currents, one manage to induce a magnetic field orientating the magnetization of this latter magnetic layer. If the two magnetizations are parallel, a low resistance state is obtained which corresponds to the binary information 1. In the opposite case, a high resistance state corresponds to 0.

However, for an extending application of these devices, strong efforts are required to investigate and develop technologies allowing an orientation of the magnetization with minimal current and power. In this thought, the development of Spin-Transfer Torque (STT) based MRAM leads to a first reduction of current [CAD+10]. Indeed, the STT mechanism uses spin-polarized electrons to transfer their spin between the magnetic layers thus creating a torque on the magnetization of the free layer, forcing its orientation.

The past few years have seen considerable progress in these technologies thanks to the identification of spin-orbit coupling as a mechanism generating spin currents at the interface between heavy elements and ferromagnetic layers using the spin Hall effect for bulk materials [ATI+11] [MGG+11] or even the Edelstein effect

for 2D electron gas [Ede90] [RSRL$^+$14]. Indeed, these two effects enable a pure transverse spin current to be generated from a charge current, thus leading to an efficiency increase of the magnetization switching in the free magnetic layer. Nowadays, the efforts are so focused on the determination of the best materials to optimize the charge to spin conversion. In this quest, the use of new type of materials have been suggested [FVMK16]. These materials are widely known as topological insulators and are characterized by a large spin-orbit coupling resulting in a perfect locking between the spin and the momentum of the electrons. Some recent experiments have already demonstrated the huge potential of these topological insulators by recording better conversion efficiency than the best spin Hall materials known to date such as Pt, W or Ta [MLR$^+$14] [RSOF$^+$16].

More than just standard spintronics, other long-term solutions exist for the replacement of conventional transistors with lower energy consumption. Indeed, with the size reduction, the properties of these devices are now implying quantum mechanics. While these appearing quantum phenomena may be viewed as a huge conceptual difficulty and could constitute a limit to the size reduction, they are above all a major and incredible opportunity to further improve the information processing. This technological shift constitutes a real innovation and opens the way toward the exciting world of quantum computing [Ste98]. Conventional computers made of transistors are coding information using binary digits, also referred as bits, which take the value 0 or 1. Quantum computation considerably differs with the use of quantum bits allowing this time a superposition of states: $a|0\rangle + b|1\rangle$ and so an increased capacity of information storage and sharing. However, for these operations to success, the quantum bits need to be in a sufficiently isolated environment to ensure long coherence time, but they also need to be accessible for their stored information to be manipulated. Finding the good compromise is not an easy task and justifies the variety and the number of different physical systems currently investigated to build the best quantum bits. Superconducting circuits with Josephson junction [PSB$^+$11], nuclear spins controlled with nuclear magnetic resonance technique [WGC97], linear optics with photon counting [KMN$^+$07] are only a small selection of the studied approaches. In the recent years, an other strategy has emerged with the discovery of topological insulators naturally protected from disorder and scattering, thus full of promise in the quest of limiting information transfer errors.

The future of electronics appears to be guaranteed with the development of spintronic devices and the implementation of quantum computing. It is worth noting that spintronics can also be used for quantum computation with especially the use of spin-polarized currents to build spin-based logic element. In all these developments, topological insulators seem to have a major role to play.

But what is a topological insulator? First introduced in 2005 by Kane and Mele [KM05], topological insulators are a new class of materials revolutionizing the existing material classification, consisting of insulators, semi-conductors and metals, by combining an insulating surface and metallic boundaries. They introduced the first two dimensional (2D) topological insulator system also referred as Quantum Spin Hall Effect (QSHE). This new state of matter was first predicted to arise on graphene populated with particles having linear energy dispersion, commonly referred as Dirac fermions. With spin-orbit coupling, electrons propagating in graphene were supposed to experience an effective magnetic field in the direction of their isospin, thus allowing to generate two counter-propagating edge channels. The propagation of these channels illustrates the spin-momentum locking property expected in these systems preventing them from backscattering in the absence of a spin-flip mechanism such as the presence of magnetic impurities or the application of a magnetic field. With this property, these 2D topological insulators are very promising for applications. However, graphene spin-orbit coupling turned out not to be large enough for the realization of this new state of matter.

It has therefore been necessary to look for large spin-orbit materials with electronic properties similar to graphene. In these thoughts, Bernevig, Hughes and Zhang identified, in 2006, HgTe/CdTe quantum well as an excellent candidate to experience QSHE [BHZ06]. The experimental evidence of this effect in these latter structures did not wait too long as only one year later, Molenkamp's group demonstrated its realization [KWB+07].

In parallel, several theoretical works predicted the expansion of topological properties to three dimensions (3D) [FKM07] [MB07] [Roy09], thus resulting in structures combining an insulating bulk and conducting surfaces with a massless and chiral Dirac band structure.

The rise of these new states of matter has generated a growing enthusiasm in the condensed matter community. A lot of theoretical predictions about the topological nature of one material or another resulted in an impressive list of potential topological materials [And13]. However, the experimental confirmation of whether a material is a topological insulator or not has been most of the time a remaining issue. In the case of 3D topological insulator, the easiest and the most convincing way is to observe the Dirac cone by performing Angle Resolved PhotoEmission Spectroscopy (ARPES). Moreover, using spin-resolved ARPES, one can identify the spin-momentum locking property specific to topological insulators [HXQ+09]. This technique has clearly demonstrated the topological nature of some Bi-based compounds [XQH+09] and of HgTe [COB+13]. However, ARPES is not adapted for all materials and presents some limitations such as an energy resolution limited to a few meV only.

An other way to investigate the topological band structure and access topological properties is the use of magneto-transport measurements. By applying large magnetic fields, the quantum Hall effect regime enables the Hall resistance to become quantized and the longitudinal resistance to experience oscillations. The determination of the quantization values and the evolution of resistance oscillations with magnetic field, gate voltage or even temperature constitute a combined probe of the carrier nature. With this procedure, 3D HgTe systems have demonstrated some signatures of quantum Hall effect but with no vanishing resistance oscillation minima [BLN+11], thus making difficult to extract information from the resistance oscillations and so to draw a clear conclusion about their topological nature. Concerning the Bi-based compounds, the first generation of material has evidenced important issues due to a large bulk conduction. However, nowadays, quaternary alloys such as BiSbTeSe are grown and enable to position the Dirac point inside the bulk gap thus limiting the bulk contribution allowing to obtain first evidences of quantum Hall effect.

In a nutshell, it appears that the number of 3D topological systems ready for applications is limited to date.

The major objective of this PhD thesis has been to experimentally demonstrate the eligibility of HgTe 3D topological insulator system for applications and especially for spintronics. In Chapter 1, the HgTe band structure is introduced as well as the expected quantum Hall signatures for this topological system. In Chapter 2, the efforts dedicated to the improvement of the growth process are reported relying on a set of various material characterizations. Chemical composition, strain, defect density and sharpness of the HgTe interfaces have been identified as the major parameters of study and improvement to ensure HgTe inverted band structure, bulk gap opening and to emphasize the resulting topological surface state electronic properties. In Chapter 3, the nanofabrication process and the magneto-transport measurement setup are described. While the realization of Hall bars technically appears to be simple, the high desorption rate of Hg makes the nanofabrication process more complex and requires the development of a low temperature process adapted to this constraint. Next, in Chapter 4, low temperature magneto-transport measurements are presented for both thick and thin 3D HgTe structures. While the thicker sample evidences very complex transport signatures, the thickness reduction leads to the suppression of additional contributions and the demonstration of quantum Hall effect with vanishing resistance.

Consequently, we demonstrate direct evidences of Dirac fermions by temperature dependent analysis of the quantum Hall effect. In Chapter 5, the first experiments aiming at testing the HgTe potential for spintronics are presented. Spin-pumping experiments demonstrate the power of these topological structures for spin injection and detection. The implementation of HgTe into simple $p-n$ junction is also investigated to realize a first spin-based logic element.

Chapter 1

HgTe/CdTe: 3D topological insulator

First predicted in 2007 [FKM07] [MB07] [Roy09] as a new class of matter, three-dimensional (3D) topological insulators combine an insulating bulk and conducting surfaces with a massless and chiral Dirac band structure for which the spin and the momentum are locked. The existence of a bulk gap associated with an inverted band structure at the center of the Brillouin zone are the two necessary conditions to obtain such 3D topological insulator structures. Inversion of band structure requires the use of large spin-orbit and so of heavy materials as the spin-orbit coupling scales in Z^4 with Z the atomic number.

With these considerations, many materials appear as potential candidates for experiencing this new state of matter. However, to date, only Bi-based compounds such as Bi_2Se_3 and Bi_2Te_3, and HgTe have demonstrated experimental evidences of their topological nature. The first demonstrations have been made using Angle Resolved PhotoEmission Spectroscopy (ARPES) measurements, which allow to probe and highlight the band structure by extracting surface electrons and analysing their excitations, and have been performed on Bi_2Se_3 crystals. Results of these measurements are presented in Fig.1.1[XQH+09]. Conduction and valence bands appear to be separated by a $\approx$ 300 meV bulk gap in which two linear surface states appear. These surface states are characterized by a Dirac cone-like energy dispersion, thus demonstrating the topological nature of this system. An other probe of the surface state existence and of the band structure relies on magneto-transport measurements. Indeed, in the quantum Hall regime, topological insulators and especially the surface states are expected to have unique signatures differentiating them from classical two dimensional electron gas. For these Bi-based compounds, the achievement of these measurements has difficulties as these materials are characterized by a high bulk conductivity and low carrier mobility in transport experiments caused by intrinsic doping of the crystals.

In this thesis, we focus on another material eligible to be a 3D topological insulator: HgTe. With an inverted band structure, the semi-metal HgTe has been identified as a strong topological insulator assuming the opening of a bandgap. Quantum confinement in two-dimensional case (2D) or application of a tensile strain in 3D case enable to generate a bandgap of a few tens of meV. The strained HgTe system is characterized with negligible bulk conduction and a high carrier mobility, thus allowing to easily access and effectively probe topological properties. However, this material is not widely available as it is mainly used for defense-related InfraRed applications and its growth is only mastered by a few groups in the world. Due to these reasons, the experimental demonstration of its topological nature has taken more time but first evidences have started to emerge in 2011 using magneto-transport measurements [BLN+11] and in 2013 using ARPES [COB+13].

This Chapter is divided in two parts. The first one introduces CdTe and HgTe band structures using standard $k.p$ and Kane models. HgTe band inversion as well as the opening of a band gap using tensile strain are discussed

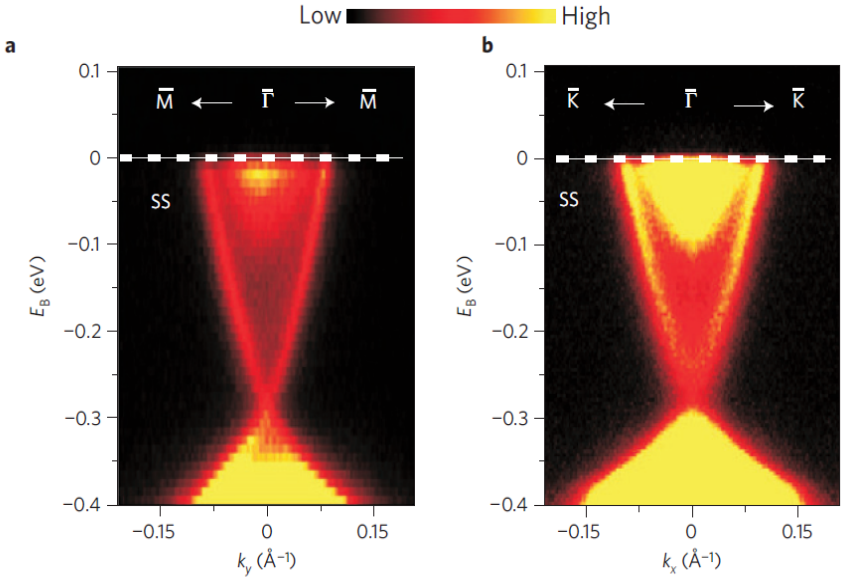

Figure 1.1 – *ARPES measurements of Bi_2Se_3 evidencing surface states with linear energy dispersion, forming a unique Dirac cone in the bulk gap. Taken from [XQH+09].*

and demonstrated. Due to the band inversion, metallic surface states arise at the interface between HgTe and CdTe. Estimation of the wavefunction extension of these surface states is presented relying on the Kane model. Finally, ARPES measurements of the HgTe band structure and of the metallic surface states are presented. In a second part, this Chapter describes the Quantum Hall Effect (QHE) signatures of 3D topological insulators and compare them to parabolic electrons or even to graphene. Energy spectrum as well as the expected Hall quantization are addressed in each case allowing to understand the peculiarities of the topological systems. This whole analysis gives the keys and the theoretical background to identify Dirac fermions and topological insulator transport signatures.

1.1 Band structure: $k.p$ and Kane models

An electronic band structure represents the set of energy levels of an electron as function of its momentum in the periodic arrangement of the crystal structure. In general, electric properties of a material can be deduced from its band structure, e.g. metallic or insulating, direct or indirect bandgap. Moreover, the value of the bandgap and the curvature of the conduction and valence bands play a key role in the carrier transport properties. For example, the band curvature is an indication of the effective mass of the carriers. The determination of a crystal band structure is thus essential to predict the particular electronic properties of a material. This was especially the case for topological insulators for which the combination of an inverted band structure and a bulk gap have led to the prediction of this new state of matter carrying massless chiral particles.

The objective of this section is to introduce and discuss the band structure of both CdTe and HgTe. These II-VI compounds crystallize in a zinc blende structure as represented in Fig. 1.2, with Cd or Hg atoms (in blue) organized in a face-centered cubic unit cell and Te atoms (red) in an other face-centered cubic unit cell shifted from $(\frac{1}{4}, \frac{1}{4}, \frac{1}{4})$. The lattice parameters of these two compounds are reported in Table 1.1. With these crystal symmetries, the band structure of both CdTe and HgTe is centered at the center of the Brillouin zone at the Γ point and its energy bands are a combination of s and p-states, the s-states corresponding to Hg or Cd and the p-states to Te.

Furthermore, these materials are characterized by narrow gaps (see Table 1.1) and a large spin-orbit coupling ($\Delta_{SO} \approx 1$ eV), thus resulting in a mixing of the different bands. For these interactions to be considered, the Kane model [Kan57] relying on the $k.p$ theory is used and is described in this section.

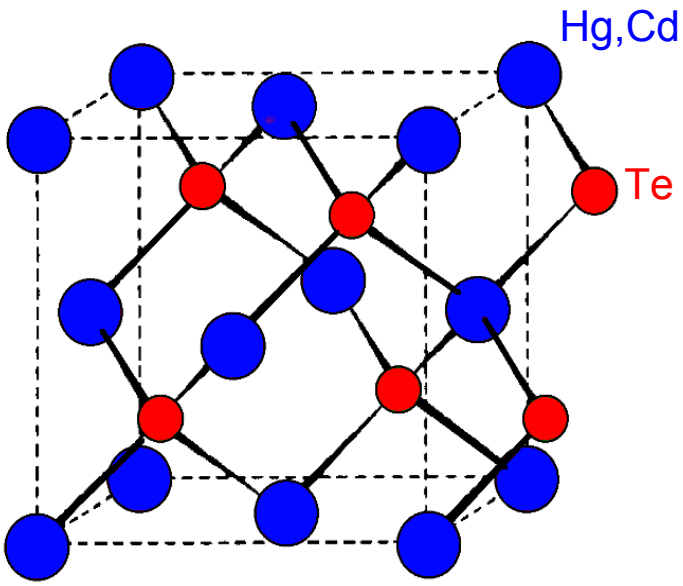

Figure 1.2 – *Schematic representation of the HgTe and CdTe zinc blende structure. Te atoms are depicted in red, while Hg or Cd are in blue.*

	HgTe	CdTe
a (Å)	6.4615	6.4815
E_g (eV)	-0.3	1.6
Δ_{SO} (eV)	1.08 [CS10]	1.08 [CS10]

Table 1.1 – *Lattice parameter a, energy gap E_g at 4 K and spin-orbit coupling Δ_{SO} of both HgTe and CdTe compounds.*

1.1.1 $k.p$ theory without spin-orbit coupling

First of all, it is important to note that the band structure presented in this section is calculated without considering the magnetic field. In the following of this section, we will note $\vec{p} = -i\hbar\vec{\nabla}$ the electronic momentum and $\hbar k$ the crystal momentum.

The determination of a crystal band structure needs to take into account the potential of the atomic structure through the use of Bloch waves:

$$\Phi_{n\vec{k}}(\vec{r}) = u_{n\vec{k}}(\vec{r}) \exp\left(i\vec{k}.\vec{r}\right) \tag{1.1}$$

with $\vec{k}$ the wave vector and $u_{n\vec{k}}(\vec{r})$ characterizing the periodicity of the crystal network. Energy levels of the bands are then directly obtained by solving the Schrödinger equation:

$$H\Phi_{n\vec{k}}(\vec{r}) = E_n(\vec{k})\Phi_{n\vec{k}}(\vec{r}) \tag{1.2}$$

Note that, for each k value, there are several solutions labelled by n, which correspond to the different energy bands. In this section, we are first considering the simplest case without any relativistic corrections. In these conditions, the unperturbed Hamiltonian H_I reads:

$$H_I = \frac{p^2}{2m_0} + V(\vec{r}) \tag{1.3}$$

where $V(\vec{r})$ is the periodic crystal potential.

Since:

$$\begin{aligned}(-i\hbar\vec{\nabla})\Phi_{n\vec{k}}(\vec{r}) &= \hbar k \exp\left(i\vec{k}.\vec{r}\right) u_{n\vec{k}}(r) + \exp\left(i\vec{k}.\vec{r}\right)(-i\hbar\vec{\nabla})u_{n\vec{k}}(\vec{r}) \\ (-i\hbar\vec{\nabla})^2\Phi_{n\vec{k}}(\vec{r}) &= \hbar^2k^2 \exp\left(i\vec{k}.\vec{r}\right) u_{n\vec{k}}(\vec{r}) + 2\hbar k \exp\left(i\vec{k}.\vec{r}\right)(-i\hbar\vec{\nabla})u_{n\vec{k}}(\vec{r}) + \exp\left(i\vec{k}.\vec{r}\right)(-i\hbar\vec{\nabla})^2 u_{n\vec{k}}(\vec{r})\end{aligned} \tag{1.4}$$

The derivation of the equation 1.2 with the Hamiltonian 1.3 yields to:

$$H_{kp}u_{n,\vec{k}}(\vec{r}) = (\frac{p^2}{2m_0} + V(\vec{r}) + \frac{\hbar}{m_0}\vec{k}.\vec{p})u_{n,\vec{k}}(r) = \epsilon_{n,\vec{k}}u_{n,\vec{k}}(\vec{r}) \tag{1.5}$$

with $\epsilon_{n,\vec{k}} = (E_{n,\vec{k}} - \frac{\hbar^2k^2}{2m_0})$. The third term corresponds to the $k.p$ interaction which accounts for the relations and coupling between all the bands. In the framework of the $k.p$ approximation, the $k.p$ term is treated as a perturbation.

Moreover, in the following, we assume that $\vec{k} = k\vec{z}$ and so $\vec{p} = -i\hbar\vec{z}\frac{\delta}{\delta z}$ to simplify the development and limit the coupling effects to this unique direction. In these conditions, the following basis of representation is considered: $|s\rangle$, $|x\rangle$, $|y\rangle$ and $|z\rangle$ where x, y and z correspond to the three p-orbitals. Such a basis is characterized by four bands and so four eigenvalues : one s-type also called Γ_1 and three p-type valence bands referred as Γ_{15}. Before solving equation 1.5, we define P as:

$$\langle s|\,\vec{p}\,|u_i\rangle = P \tag{1.6}$$

with $u_i = x, y$ or z. Energies at $k = 0$ of both s-type and p-type bands are defined as: $\langle s|\,H_{kp}\,|s\rangle = E_g$; $\langle z|\,H_{kp}\,|z\rangle = 0$; $\langle y|\,H_{kp}\,|y\rangle = 0$; $\langle x|\,H_{kp}\,|x\rangle = 0$.

As the solutions of $(\frac{p^2}{2m} + V(\vec{r}))u_{n,\vec{k}}(\vec{r}) = E_{n,\vec{k}}u_{n,\vec{k}}(\vec{r})$ are known, the perturbation method enables to

determine:

$$E_{n,\vec{k}} = E_{n,0} + \frac{\hbar^2 k^2}{2m_0} + \frac{\hbar^2}{m_0^2} \sum_{m \neq n} \frac{|\langle u_{n,0}| \vec{k}.\vec{p} |u_{m,0}\rangle|^2}{E_{n,0} - E_{m,0}} \tag{1.7}$$

Therefore, the band energy spectrum is defined as:

$$\begin{cases} E_s(\vec{k}) = E_g + \frac{\hbar^2 k^2}{2m_0}(1 + \frac{2P^2}{m_0 E_g}) \\ E_z(\vec{k}) = \frac{\hbar^2 k^2}{2m_0}(1 - \frac{2P^2}{m_0 E_g}) \\ E_{x,y}(\vec{k}) = -\frac{\hbar^2 k^2}{2m_0} \end{cases} \tag{1.8}$$

Note that the negative sign of $E_{x,y}$ does not originate from the coupling to the s and z bands but from the coupling to higher bands which are not considered in this model.

Each energy band is characterized by its effective mass of carrier m^*. The definition of m^* is given here for the conduction band:

$$E_s = E_g + \frac{\hbar^2 k^2}{2m_s^*} \tag{1.9}$$

thus resulting in:

$$m_s^* = \frac{m_0}{(1 + \frac{2P^2}{m_0 E_g})} \tag{1.10}$$

Similarly, we determine:

$$\begin{cases} m_{x,y}^* = -m_0 \\ m_z^* = \frac{m_0}{(1 - \frac{2P^2}{m_0 E_g})} \end{cases} \tag{1.11}$$

To get an estimation of the effective mass values and of the curvature of the bands for such narrow gap systems, one needs first to determine P value illustrating the strength of the coupling between the bands. As $\langle s| p |u_i\rangle = P$, P constitutes a momentum element on the whole Brillouin zone and can be extracted as $\hbar\frac{2\pi}{a}$, with a the lattice parameter of the crystal. Therefore, assuming $E_g = 1.6$ eV and $a = 6.4815$Å, $\frac{2P^2}{m_0} = 14$ eV. From this latter value, one finds $m_s^* = 0.10$ m$_0$ and $m_z^* = -0.12$ m$_0$ for CdTe bulk crystal.

From this, we can conclude that x and y states are forming the heavy hole (HH) band while the z state constitutes the light hole (LH) one. It is worth noting that the conduction and the light hole valence bands have similar curvature as the absolute values of their effective masses are almost the same. The resulting band structure is schematically represented in Fig. 1.3(a).

1.1.2 Kane model with spin-orbit coupling

By considering the effect of the Spin-Orbit (SO) relativistic correction, the Hamiltonian 1.3 transforms into:

$$H = H_I + H_{SO} = \frac{p^2}{2m_0} + V(\vec{r}) + \frac{\hbar}{4m_0^2 c^2}[\sigma \otimes \nabla V].\vec{p} \tag{1.12}$$

with σ the Pauli matrices.

The derivation of the equation 1.2 with the Hamiltonian 1.12 yields to:

$$(\frac{p^2}{2m_0} + V(\vec{r}) + \frac{\hbar}{m_0}\vec{k}.\vec{p} + \frac{\hbar}{4m_0^2 c^2}[\sigma \otimes \nabla V].(\vec{p} + \hbar\vec{k}))u_{n,\vec{k}}(\vec{r}) = (E(\vec{k}) - \frac{\hbar^2 k^2}{2m_0})u_{n,\vec{k}}(\vec{r}) \tag{1.13}$$

The fourth term corresponds to the SO term. This term can be approximated to $\frac{\hbar}{4m_0^2c^2}[\sigma \otimes \nabla V].\vec{p}$ in a first order approach as p is much larger than $\hbar k$ in such zinc-blende structures.

With the introduction of the spin degree of freedom, the basis of representation used previously is no more accurate and needs to be changed. The following basis is considered :

$|s,\downarrow\rangle, |iz,\downarrow\rangle, \frac{i}{\sqrt{2}}(|x,\uparrow\rangle - i|y,\uparrow\rangle), -\frac{i}{\sqrt{2}}(|x,\uparrow\rangle + i|y,\uparrow\rangle), |s,\uparrow\rangle, |iz,\uparrow\rangle, -\frac{i}{\sqrt{2}}(|x,\downarrow\rangle + i|y,\downarrow\rangle), \frac{i}{\sqrt{2}}(|x,\downarrow\rangle - i|y,\downarrow\rangle)$.

The resulting 8*8 Kane Hamiltonian is expressed as:

$$H_{Kane_{SO}} = \begin{pmatrix} H & 0 \\ 0 & H \end{pmatrix} \tag{1.14}$$

with:

$$H = \begin{pmatrix} E_s & P\frac{\hbar k}{m_0} & 0 & 0 \\ -P\frac{\hbar k}{m_0} & E_p & \sqrt{2}\frac{\Delta_{SO}}{3} & 0 \\ 0 & \sqrt{2}\frac{\Delta_{SO}}{3} & E_p - \frac{\Delta_{SO}}{3} & 0 \\ 0 & 0 & 0 & E_p + \frac{\Delta_{SO}}{3} \end{pmatrix} \tag{1.15}$$

by assuming that $\vec{k} = k\vec{z}$ and $\Delta_{SO} = \frac{3\hbar}{4m_0^2c^2}\langle x|\frac{\delta V}{\delta x}p_y - \frac{\delta V}{\delta y}p_x|iy\rangle$.

Therefore, solving Hamiltonian 1.15 leads to the parabolic bands below:

$$\begin{cases} E_s = E_g + \frac{\hbar^2k^2}{2m_0}(1 + \frac{2P^2}{3m_0}(\frac{2}{E_g} + \frac{1}{E_g+\Delta_{SO}})) \\ E_{HH} = -\frac{\hbar^2k^2}{2m_0} \\ E_{LH} = \frac{\hbar^2k^2}{2m_0}(1 - \frac{4P^2}{3m_0E_g}) \\ E_{so} = -\Delta_{SO} + \frac{\hbar^2k^2}{2m_0}(1 - \frac{2P^2}{3m_0(E_g+\Delta_{SO}))}) \end{cases} \tag{1.16}$$

with the corresponding effective masses:

$$\begin{cases} m_s^* = \frac{m_0}{1+\frac{2P^2}{3m_0}(\frac{2}{E_g} + \frac{1}{E_g+\Delta_{SO}})} \\ m_{HH}^* = -m_0 \\ m_{LH}^* = \frac{m_0}{1-\frac{4P^2}{3m_0E_g}} \\ m_{so}^* = \frac{m_0}{1-\frac{2P^2}{3m_0(E_g+\Delta_{SO}))}} \end{cases} \tag{1.17}$$

Note that similarly to the case without SO, the negative sign of the heavy hole band originates from the coupling to higher bands that our model does not account for.

By considering the energy gap ($E_g = 1.6$ eV) and spin-orbit coupling ($\Delta_{SO} = 1.08$ eV) values of CdTe, one finds: $m_s^* = 0.11$ m_0 and $m_{LH}^* = -0.20$ m_0.

The resulting band structure is represented schematically in Fig. 1.3(b). The effect of SO coupling essentially affects the p-type bands and demonstrates the lifting of the Γ_{15} p-type bands into the four-fold degenerated Γ_8 bands (total kinetic momentum J=$\frac{3}{2}$) and the two-fold degenerated Γ_7 band (J= $\frac{1}{2}$). Γ_8 bands correspond to the light (LH) and heavy holes (HH) bands while the Γ_7 represents the split-off (so) band. Γ_8 and Γ_7 are separated by the SO induced gap Δ_{SO} as deduced from 1.16 and represented in Fig. 1.3.

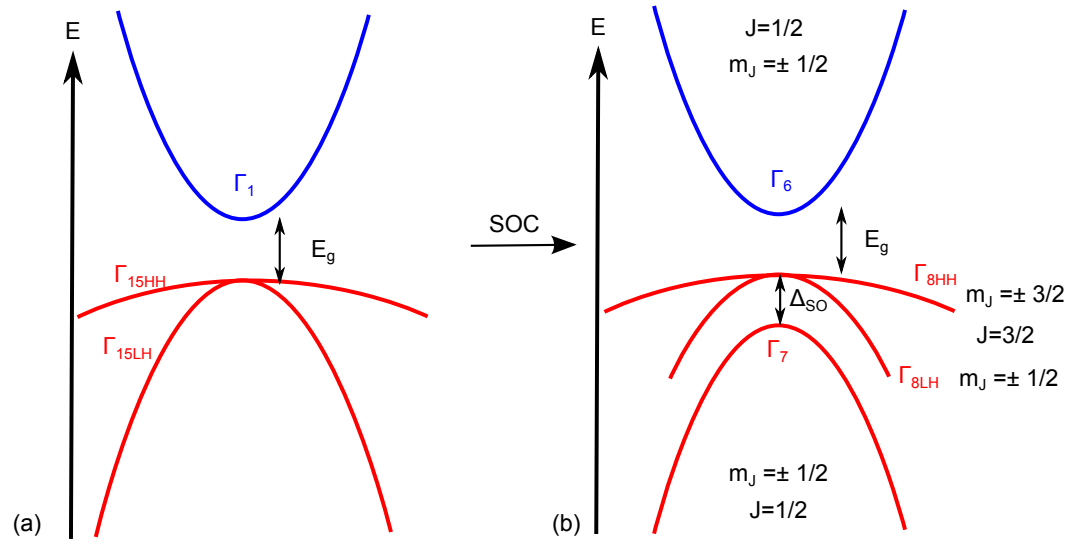

Figure 1.3 – *Schematic representation of the CdTe band structure extracted from Kane model without (a) and with (b) Spin-Orbit Coupling (SOC).*

We have just demonstrated the organisation of the bands with spin-orbit coupling in the case $\vec{k} = k\vec{z}$. Nevertheless, it is important to have an idea of the Kane Hamiltonian in the more general case where k is not fixed in one direction. Indeed, this Hamiltonian will be useful just after to account for the effect of strain on the band structure. Kane Hamiltonian of reference [NPJJ+05] is reported just below in the relevant basis:

$\left|\Gamma_6,+\frac{1}{2}\right\rangle = |s,\uparrow\rangle ; \left|\Gamma_6,-\frac{1}{2}\right\rangle = |s,\downarrow\rangle ; \left|\Gamma_8,+\frac{3}{2}\right\rangle = \frac{1}{\sqrt{2}}(|x,\uparrow\rangle + i\,|y,\uparrow\rangle); \left|\Gamma_8,+\frac{1}{2}\right\rangle = \frac{1}{\sqrt{6}}(|x,\downarrow\rangle + i\,|y,\downarrow\rangle - 2\,|z,\uparrow\rangle); \left|\Gamma_8,-\frac{1}{2}\right\rangle = \frac{1}{\sqrt{6}}(|x,\uparrow\rangle - i\,|y,\uparrow\rangle + 2\,|z,\downarrow\rangle); \left|\Gamma_8,-\frac{3}{2}\right\rangle = -\frac{1}{\sqrt{2}}(|x,\downarrow\rangle - i\,|y,\downarrow\rangle); \left|\Gamma_7,\frac{1}{2}\right\rangle = \frac{1}{\sqrt{3}}(|x,\downarrow\rangle + i\,|y,\downarrow\rangle + |z,\uparrow\rangle); \left|\Gamma_7,-\frac{1}{2}\right\rangle = \frac{1}{\sqrt{3}}(|x,\uparrow\rangle - i\,|y,\uparrow\rangle - |z,\downarrow\rangle).$

$$H_{Kane_{SO}} = \begin{pmatrix} T & 0 & -\frac{1}{\sqrt{2}}Pk_+ & \sqrt{\frac{2}{3}}Pk_z & \frac{1}{\sqrt{6}}Pk_- & 0 & -\frac{1}{\sqrt{3}}Pk_z & -\frac{1}{\sqrt{3}}Pk_- \\ 0 & T & 0 & -\frac{1}{\sqrt{6}}Pk_+ & \sqrt{\frac{2}{3}}Pk_z & \frac{1}{\sqrt{2}}Pk_- & -\frac{1}{\sqrt{3}}Pk_+ & \frac{1}{\sqrt{3}}Pk_z \\ -\frac{1}{\sqrt{2}}k_-P & 0 & U+V & -S_{1-} & R & 0 & \frac{1}{\sqrt{2}}S_{1-} & -\sqrt{2}R \\ \sqrt{\frac{2}{3}}k_zP & -\frac{1}{\sqrt{6}}k_-P & -S_{1-}^t & U-V & C & R & \sqrt{2}V & -\sqrt{\frac{3}{2}}S_{2-} \\ \frac{1}{\sqrt{6}}k_+P & \sqrt{\frac{2}{3}}Pk_z & R^t & C^t & U-V & S_{1+}^t & -\sqrt{\frac{3}{2}}S_{2+} & -\sqrt{2}V \\ 0 & \frac{1}{\sqrt{2}}k_+P & 0 & R^t & S_{1+} & U+V & \sqrt{2}R^t & \frac{1}{\sqrt{2}}S_{1+} \\ -\frac{1}{\sqrt{3}}k_zP & -\frac{1}{\sqrt{3}}k_-P & \frac{1}{\sqrt{2}}S_{1-}^t & \sqrt{2}V & -\sqrt{\frac{3}{2}}S_{2+}^t & \sqrt{2}R & U-\Delta & C \\ -\frac{1}{\sqrt{3}}k_+P & \frac{1}{\sqrt{3}}k_zP & -\sqrt{2}R^t & -\sqrt{\frac{3}{2}}S_{2-}^t & -\sqrt{2}V & \frac{1}{\sqrt{2}}S_{1+}^t & C^t & U-\Delta \end{pmatrix} \quad (1.18)$$

with:

$$\begin{aligned}
k_{/\!/}^2 &= k_x^2 + k_y^2 \\
k_\pm &= k_x \pm i k_y \\
T &= E_c + \tfrac{\hbar^2}{2m_0}[(2F+1)k_{/\!/}^2 + k_z(2F+1)k_z) \\
U &= E_v - \tfrac{\hbar^2}{2m_0}(\gamma_1 k_{/\!/}^2 + k_z\gamma_1 k_z) \\
V &= -\tfrac{\hbar^2}{2m_0}(\gamma_2 k_{/\!/}^2 - 2k_z\gamma_2 k_z) \\
R &= -\tfrac{\hbar^2}{2m_0}(\sqrt{3}\mu k_+^2 - \sqrt{3}\gamma k_-^2) \\
S_{1\pm} &= -\tfrac{\hbar^2}{2m_0}\sqrt{3}k_\pm((\gamma_3, k_z) + [\omega, k_z]) \\
S_{2\pm} &= -\tfrac{\hbar^2}{2m_0}\sqrt{3}k_\pm((\gamma_3, k_z) - \tfrac{1}{3}[\omega, k_z]) \\
C &= \tfrac{\hbar^2}{m_0}k_-[\omega, k_z]
\end{aligned} \tag{1.19}$$

with Luttinger parameters $\gamma_1, \gamma_2, \gamma_3, \omega$ and F characterizing the coupling between the bands, $\mu = \frac{\gamma_3 - \gamma_2}{2}$ and $\gamma = \frac{\gamma_3 + \gamma_2}{2}$.

Contrary to the case $\vec{k} = k\vec{z}$, this Hamiltonian takes into account all the coupling between the bands but especially introduces the coupling between opposite spins through the terms in $k_\pm$.

1.1.3 HgTe inversion of band structure

1.1.3.1 Effect of mass-velocity correction

The Kane model permits the derivation of the band structure of a large spin-orbit and conventional insulator like CdTe (conventional meaning with a normal band ordering Γ_6-Γ_8-Γ_7). However, in the case of HgTe, the band structure considerably differs due to the impact of another relativistic correction not yet mentioned: the mass-velocity correction $H_{mv} = -\frac{p^4}{8m^3c^2}$ [ZCS12] [CTDL77].

The effect of this relativistic correction on the band structure using Kane model is not detailed here but is expected to shift the bands toward lower energies as represented in Fig. 1.4 for both CdTe and HgTe [CS07] [FM13].

This relativistic effect is not equivalent for s and p type electrons as demonstrated in [CTDL77]. Indeed, the mean values of the mass-velocity correction for s and p electrons are reported to be $-\frac{13}{128}\alpha^4 m_0 c^2$ and $-\frac{7}{384}\alpha^4 m_0 c^2$, respectively, with $\alpha = \frac{e^2}{\hbar c}$. Therefore, the impact of mass-velocity correction is at least five times larger for the s electrons compared to the p ones. With a highest atomic mass and therefore more numerous electrons ($Z_{Hg} = 80$), the mass-velocity correction is also expected to be much higher for HgTe than for CdTe ($Z_{Cd} = 48$). The impact of this correction on the band structure is illustrated in Fig. 1.4. In the case of HgTe, the mass-velocity correction is enough important to bring the Γ_1 band very close from the Γ_{15} band. On the contrary, for CdTe, the effect is less important and the Γ_1 is still distant from the Γ_{15} band.

Added to that the effect of spin-orbit coupling H_{SO}, and the band structure becomes inverted for HgTe. Indeed, with a spin-orbit interaction estimated to be about 1.08 eV [CS10], the Γ_8 band is lifted above the Γ_6 thus resulting in the inverted band structure illustrated in Fig. 1.4. In the case of CdTe, the spin-orbit interaction is similar as it is related to the Te states but the energy separation between Γ_1 and Γ_{15} bands is more important and prevents the inversion of the band ordering.

To summarize, it is the addition of the mass-velocity correction and the spin-orbit coupling which is at the origin of the HgTe inversion of band structure.

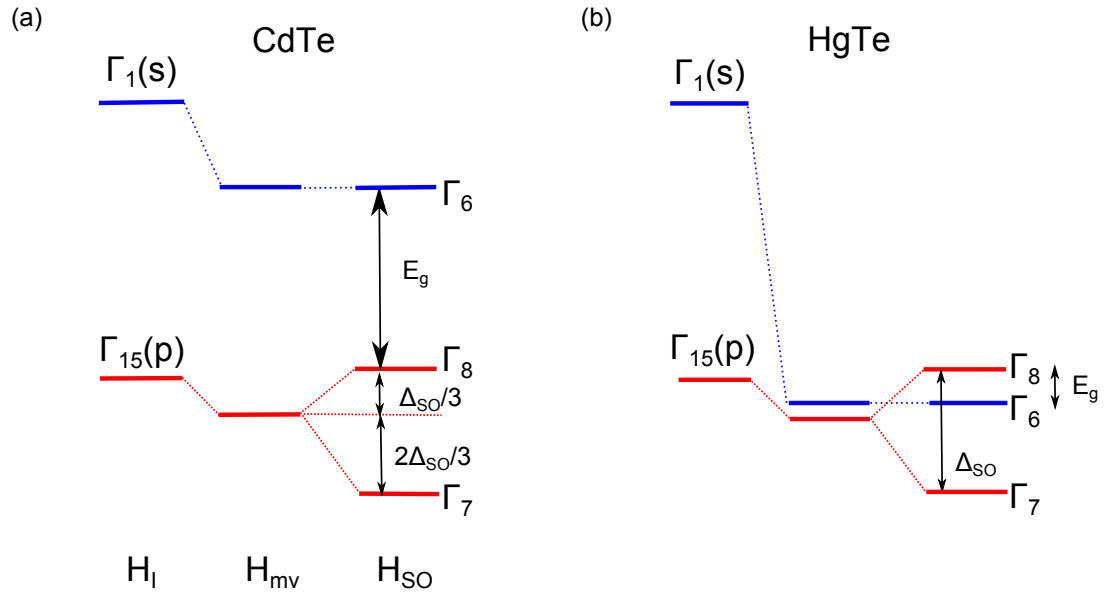

Figure 1.4 – *Schematic representation of the energy bands of (a) CdTe and (b) HgTe. This scheme illustrates the evolution of energy bands resulting from the unperturbed Hamiltonian (H_I) with the effect of relativistic corrections: the mass velocity correction (H_{mv}) and the spin-orbit coupling (H_{SO}). Adapted from [CS07].*

1.1.3.2 Introduction to HgCdTe

The inversion of the band structure between CdTe and HgTe raises the question of the continuity of the s-type and p-type bands at the interface between these two materials. Made of the $Hg_{1-x}Cd_xTe$ ternary alloy, these interfaces are characterized by a lattice parameter following the Vegard's law and resulting in a linear combination of CdTe and HgTe lattice parameters [SC01]:

$$a_{Hg_{1-x}Cd_xTe} = a_{CdTe}x + a_{HgTe}(1-x) \tag{1.20}$$

As the lattice parameter is a function of the Cd composition x, the crystal periodicity follows the same trend. This dependence directly impacts the band structure and especially the energy gap E_g through [HSC82]:

$$E_g = -0.302 + 1.93x - 0.81x^2 + 0.832x^3 + 5.35\,10^{-4}(1-2x)T \tag{1.21}$$

with E_g in eV and T in K.

Figure 1.5(b) displays the evolution of E_g as a function of x for $T = 4$ K evidencing a continuous transition from a positive 1.6 eV gap in CdTe to a negative -0.3 eV gap in HgTe. This property is especially used for InfraRed applications as it enables to probe several range of wavelengths. The change of sign of the gap occurs for $x_c = 17\%$, thus it is of main importance to keep the Cd concentration below this percentage to obtain a topological insulator. Note that this limit remains reliable for $T \leq 4$ K as the last term of the relation 1.21 becomes negligible.

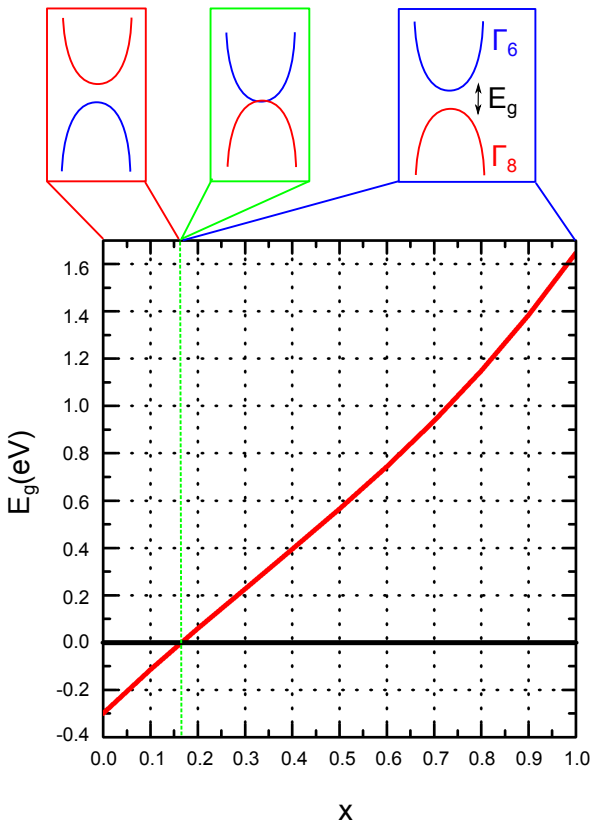

Figure 1.5 – *Energy gap E_g of $Hg_{1-x}Cd_xTe$ as a function of Cd composition x for $T = 4$ K. Top schemes schematically represent the band ordering. E_g becomes negative when crossing the black line corresponding to 0 gap for $x \leq 0.17\%$.*

1.1.4 Surface states extension

HgTe and CdTe band structures have just been explained and are represented in Fig. 1.6. While CdTe has a positive gap E_g, HgTe differs with $E_g \leq 0$. Therefore, at the interface between these two materials, the gap is forced to close to ensure band continuity between s and p states, thus creating metallic surface states. The aim of the following is to give a first description of the surface states and especially to estimate their extension in the HgTe layer.

This information is of main importance as it determines the required sharpness of the interfaces to prevent from surface scattering. Moreover, this is also relevant to determine the coupling between the top and bottom surface states. It is worth noting that the formalism presented thereafter does not take into account the chemical nature of the barriers surrounding the HgTe layer but only the HgTe band structure properties.

As somehow represented in Fig. 1.6, the topological surface states are generated from the Γ_6 s-type and the Γ_{8LH} p-type bands. By using the Kane Hamiltonian previously introduced in eq. 1.18, one manage to obtain a simplified Hamiltonian describing the topological surface states. Note that here we only consider the surface states perpendicular to the z axis and we neglect the diagonal term of coupling between the opposite spins in $\frac{1}{\sqrt{6}}Pk_{\pm}$. The surface state wavefunction is thus defined as:

$$\Phi(z) = C\exp(ik_z z) \tag{1.22}$$

with C an eigenstate. Note that here we only focus on the determination of the inverse extension λ. This parameter is obtained from the imaginary part of k_z thus justifying the substitution $k_z \rightarrow i\lambda$ thereafter.

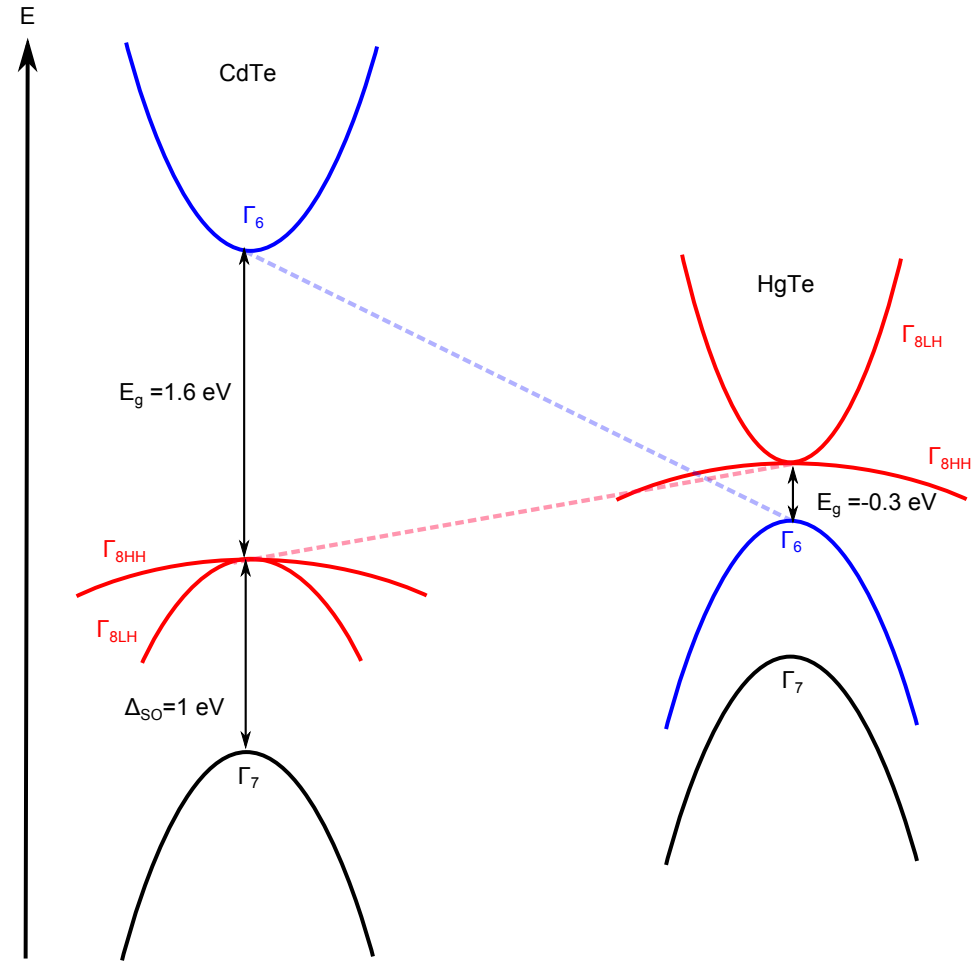

Figure 1.6 – *Schematic representation of the energy band structures of both CdTe and HgTe. Gapless surface states arise at the interface between CdTe normal band structure and HgTe inverted one due to band continuity. In 3D topological insulator, electronic transport occurs through these metallic surface states.*

Under these conditions, we are considering the following Hamiltonian:

$$H = \begin{pmatrix} h & 0 \\ 0 & h \end{pmatrix} \tag{1.23}$$

with:

$$h = \begin{pmatrix} T & \sqrt{\frac{2}{3}}Pk_z \\ \sqrt{\frac{2}{3}}Pk_z & U - V \end{pmatrix} \tag{1.24}$$

The energy gap is defined as $E_c = \frac{E_g}{2}$ and $E_v = -\frac{E_g}{2}$. Thus, T transforms into $\frac{E_g}{2} - \frac{\hbar^2}{2m_0}(2F+1)\lambda^2$ and $U - V = -\frac{E_g}{2} - \frac{\hbar^2}{2m_0}(2\gamma_2 + \gamma_1)\lambda^2$.

Solving the equation:

$$det(h - E\mathbb{I}) = 0 \tag{1.25}$$

directly leads to the determination of λ. Note that here for the sake of simplicity, we fixed $E = 0$. With these conditions, solving $det(h) = 0$ yields to the equation below:

$$a\lambda^4 + b\lambda^2 + c = 0 \tag{1.26}$$

with:

$$\begin{aligned} a &= -\frac{\hbar^4}{4m_0^2}(2F+1)(2\gamma_1+\gamma_2) \\ b &= -\frac{\hbar^2}{2m_0}(2\gamma_2+\gamma_1+2F+1)\frac{E_g}{2}+\frac{2}{3}P^2 \\ c &= -\frac{E_g^2}{4} \end{aligned} \tag{1.27}$$

This biquadratic equation gives two solutions λ_α, with $\alpha = 1, 2$:

$$\lambda_\alpha = \sqrt{\frac{-K+(-1)^\alpha\sqrt{R}}{2(D_1^2-B_1^2)}} \tag{1.28}$$

with:

$$\begin{aligned} A_1 &= \sqrt{\frac{2}{3}}P \\ B_1 &= \frac{\hbar^2}{4m_0}(2\gamma_2+\gamma_1+1) \\ D_1 &= \frac{\hbar^2}{4m_0}(2\gamma_2+\gamma_1-1) \\ K &= A_1^2-2B_1E_g \\ R &= K^2+4(D_1^2-B_1^2)E_g^2 \end{aligned} \tag{1.29}$$

λ_1 and λ_2 solutions can easily be calculated from the HgTe band structure presented in Table 1.2. As $R = b^2 - 4ac > 0$ for HgTe, the two solutions λ_1 and λ_2 are real. Extension values are estimated to be equal to $\frac{1}{\lambda_1} = 4.7$ nm and $\frac{1}{\lambda_2} = 0.12$ nm respectively. Therefore, the growth process will have to be adapted to limit the interface width (see Chapter 2), it means the interdiffusion and the roughness, below $\max(\frac{1}{\lambda_1}, \frac{1}{\lambda_2}) = 4.7$ nm not to damage the electronic properties of the conducting surfaces.

	E_g	$E_P = \frac{2m_0P^2}{\hbar^2}$	F	γ_1	γ_2
HgTe	-0.3 eV	18.8 eV	0	4.1	0.5

Table 1.2 – *Band structure parameters of HgTe for $T = 0$ K. Extracted from [NPJJ+05].*

With these two solutions, the wavefunction reads:

$$\Phi(z) = C_1\exp(-\lambda_1 z) + C_2\exp(-\lambda_2 z) \tag{1.30}$$

where C_1 and C_2 are constants.

In the case of a thick film, we assume the surface states are independent so we consider only a single surface with the open boundary conditions below [SLS10]:

$$\Phi(z=0) = 0 \text{ and } \Phi(z\to\infty) = 0 \tag{1.31}$$

meaning that we assume the surface states only exist in the HgTe layer with a finite distribution. With these conditions, $C_1 = -C_2$ and $\Phi(z) \sim \exp(-\lambda_1 z) - \exp(-\lambda_2 z)$.

Fig. 1.7 presents the resulting surface states normalized wavefunction $\Phi(z)$ for several HgTe thickness L. In the case of a symmetric HgCdTe/HgTe/HgCdTe structure, the red and the blue curves correspond to the bottom and the top surface wavefunctions Φ_b and Φ_t, respectively. Values of L have been chosen to represent the samples measured in Chapter 4. It is important to realize that this study and associated calculations are based on several approximations and just aim to provide a simple picture of the surface states, in order to get a feeling about their potential coupling.

As it can be seen in Fig. 1.7 (a), in the case of 100 nm-thick film, $\Phi_t + \Phi_b$ is vanishing in the HgTe layer thus demonstrating the independence of the two opposite surface states. For $L = 50$ nm (see Fig.1.7(b)), the two surface state wavefunctions are almost overlapping, suggesting an initiation of the hybridization for thinner layers. With the thickness reduction down to 25 (see Fig.1.7(c)) and 15 nm (see Fig.1.7(d)), the two surface state wavefunctions are unambiguously overlapping, evidencing the hybridization of the topological interfaces for such thin films. As a first approximation, we have used the same boundary conditions regardless the L value. However, in order to be more accurate, it would be necessary to adapt the boundary conditions, in the case of thin films, to consider the coupling of the surface states with $\Phi(z = 0) = 0$ and $\Phi(z = L) = 0$.

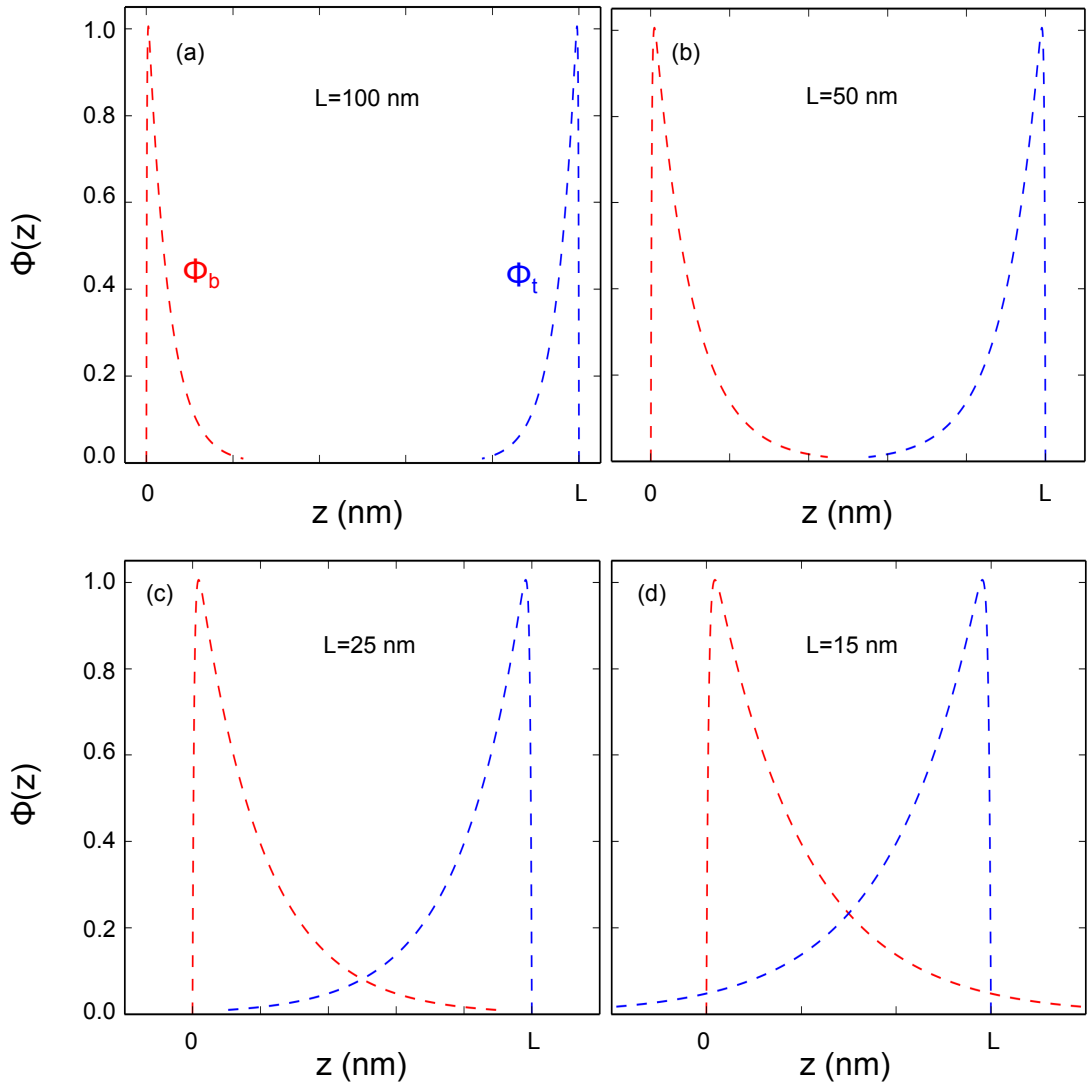

Figure 1.7 – *Surface state wavefunction Φ inside HgTe layer. Φ_t (Φ_b) corresponds to the top (bottom) surface state wavefunction represented in blue (red respectively). Four HgTe thicknesses are considered to analyse the overlap and therefore the coupling of the surface states: (a) 100 nm-, (b) 50 nm-, (c) 25 nm- and (d) 15 nm-thick HgTe layer.*

1.1.5 Bulk gap opening

The inverted band structure of HgTe has been previously determined and reported in Fig. 1.6. The two Γ_8 bands Γ_{8LH} and Γ_{8HH} are degenerate at the Γ point demonstrating that HgTe is semi-metallic.

This point is crucial and is inconsistent with topological insulator basic requirement of having an insulating bulk. Nevertheless, topological insulator properties are predicted to arise in HgTe based structures assuming the opening of a bandgap. Quantum confinement for 2D structures or application of a tensile strain for 3D bulk are strategies to open this bandgap. In this PhD thesis, we have essentially focused on 3D topological insulator systems with HgTe thickness ranging from 15 to a hundred of nm, therefore the HgTe layer must be tensile strained. It means that it must be grown on a larger lattice parameter substrate. Figure 1.8 evidences the lattice parameters of most semiconductor materials highlighting that only CdTe or even InSb would be suitable. The choice of a II-VI (CdTe) substrate is logical taking into consideration the II-VI (HgTe) type of the film.

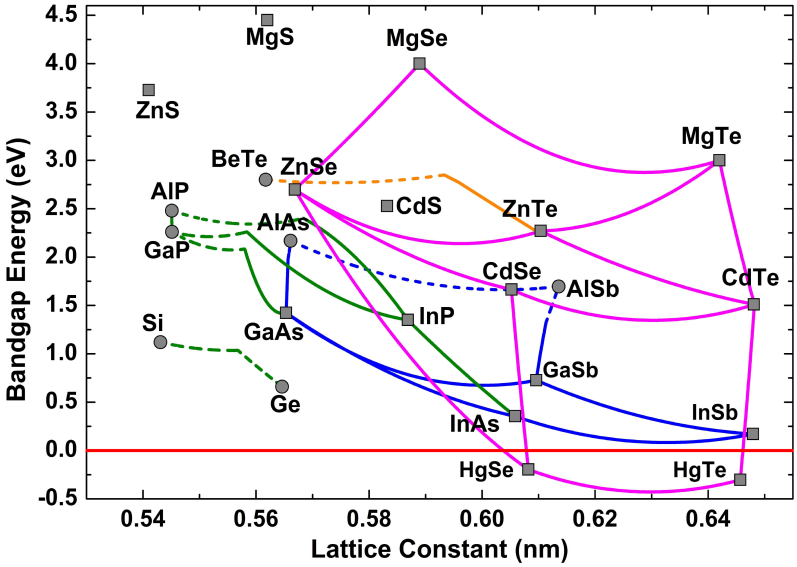

Figure 1.8 – *Bandgap as a function of lattice parameter for most semiconductors. The red line indicates the limit between normal and inverted band structure.*

When introducing strain into a crystal, the deformation of the crystalline network breaks cubic symmetry. This is resulting in shifts and modifications of the band structure energy levels [RE72]. Especially, a gap is opened between the Γ_{8LH} and the Γ_{8HH} bands. Such strain-induced band gap opening is described in details by the model of Bir and Pikus [BP74]. Before further considering the Bir-Pikus formalism, it is necessary to first define the tensile strain and the resulting critical thickness for plastic relaxation.

1.1.5.1 Definition of the tensile strain

Having a smaller lattice parameter, HgTe (a_f = 6.4615 Å) is tensile strained when grown on CdTe (a_s = 6.4815 Å) (see Fig. 1.9). This difference of lattice parameter induces a lattice mismatch f of about -0.31% as deduced from the expression below [BR96]:

$$f = \frac{a_f - a_s}{a_s} \tag{1.32}$$

To define the strain, we introduce a_{fs} the in-plane lattice parameter of strained HgTe. Note that, in the

following, all the parameters indexed with f, fs and s will refer to HgTe bulk, strained HgTe and CdTe unstrained substrate, respectively. The strain stretches the HgTe in-plane lattice parameter until it equals that of CdTe ($a_{fs} = a_s$). This in-plane deformation $\epsilon_{xx} = \epsilon_{yy} = \epsilon_{//}$ is expressed through the relation 1.33 and is equal to 0.31% for HgTe/CdTe.

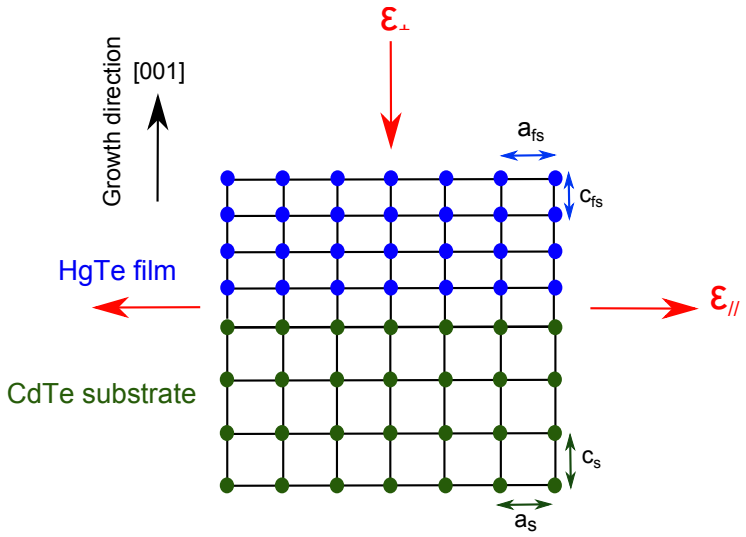

Figure 1.9 – *Schematic representation of the crystal deformation due to tensile strain in the case of HgTe grown on CdTe.*

$$\epsilon_{//} = \frac{a_{fs} - a_f}{a_f} \tag{1.33}$$

On the other hand, the out-of-plane lattice parameter of HgTe, c_f, is compressed giving rise to an out-of-plane deformation characterized by the quantity $\epsilon_{zz} = \epsilon_{\perp}$. To have an estimation of this deformation, it is useful to have a look on the stress tensor $\vec{\sigma}$:

$$\vec{\sigma} = \mathbf{C}.\vec{\epsilon} = \begin{pmatrix} C_{11} & C_{12} & C_{12} \\ C_{12} & C_{11} & C_{12} \\ C_{12} & C_{12} & C_{11} \end{pmatrix} . \begin{pmatrix} \epsilon_{//} \\ \epsilon_{//} \\ \epsilon_{\perp} \end{pmatrix} \tag{1.34}$$

where C_{12} and C_{11} are the stiffness constants equal to 36.6 GPa and 53.6 GPa for HgTe at 300 K respectively [CS75]. As there is no stress in the growth direction ($\sigma_z = 0$):

$$\sigma_z = C_{12}\epsilon_{//} + C_{12}\epsilon_{//} + C_{11}\epsilon_{\perp} = 0 \tag{1.35}$$

the out-of-plane strain deformation is thus defined as:

$$\epsilon_{\perp} = \frac{c_{fs} - c_f}{c_f} = -\frac{2C_{12}}{C_{11}}\epsilon_{//} \tag{1.36}$$

and is estimated to be about -0.41%.

To complete the definition of the tensile strain in our HgTe structures, the determination of the critical thickness of plastic deformation is of main importance and is presented below.

1.1.5.2 Critical thickness for plastic relaxation

Due to a structural stability problem of epitaxial films, a critical thickness h_c can be defined as the thickness above which it costs less energy to relieve the strain than to conserve it. The strain relief essentially appears through the formation of misfit dislocations above this critical thickness. Such dislocations spread over the whole layer until the free surface as illustrated in Fig. 1.10.

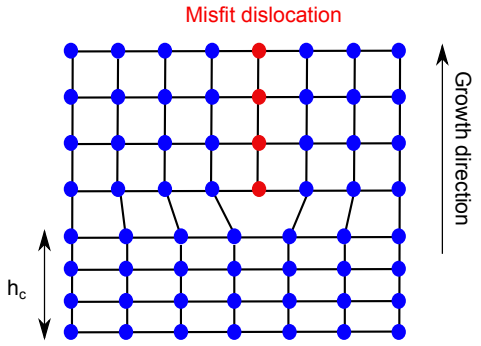

Figure 1.10 – *Schematic representation of the crystalline network of an epitaxial thin layer. Misfit dislocations appear above a critical thickness h_c of plastic relaxation and spread until the free surface.*

The determination of this critical thickness value is very important for material engineering. To estimate h_c, one has to find the equality conditions between the strain energy and the defect formation energy costs.

To do so, many models are available and give very different results. In this part, we selected the most famous one: the Matthews-Blakeslee model [MB74] [BB83]. The aim is just to give an estimation of the critical thickness value in our HgTe/CdTe (100) structures. This estimation will then be compared to experimental data using X-rays diffraction (see Chapter 2). In this model, the critical thickness is expressed as:

$$h_c = \frac{b(1-\nu cos\beta^2)}{8\pi(1+\nu)fsin\beta cos\gamma} ln(\frac{\alpha h_c}{b}) \tag{1.37}$$

where b is the Burger vector modulus, f the lattice mismatch, ν the Poisson coefficient, β the angle between the Burger vector and the dislocation, γ the angle between the interfacial and the slip plane of the dislocation and α is a factor depending on the core energy of the dislocations which is taken equal to four in our system [BB83]. In the HgTe(100) system, the dislocation angle is 60°, γ is equal to 54.74°and the Burger vector b is expressed as $\frac{a}{\sqrt{2}}$. In this case, Matthews equation 1.37 can be simplified and expressed as:

$$h_c = \frac{b(1-\nu/4)}{4\pi(1+\nu)f} ln(\frac{\alpha h_c}{b}) \tag{1.38}$$

Values of h_c as a function of f are presented in Fig. 1.11. With a lattice mismatch absolute value estimated to be 0.31%, the critical thickness for plastic relaxation in our structures is predicted to be 45 nm, according to this model. This value is quite small and we will see in Chapter 2 that it clearly underestimates the effective critical thickness for HgTe.

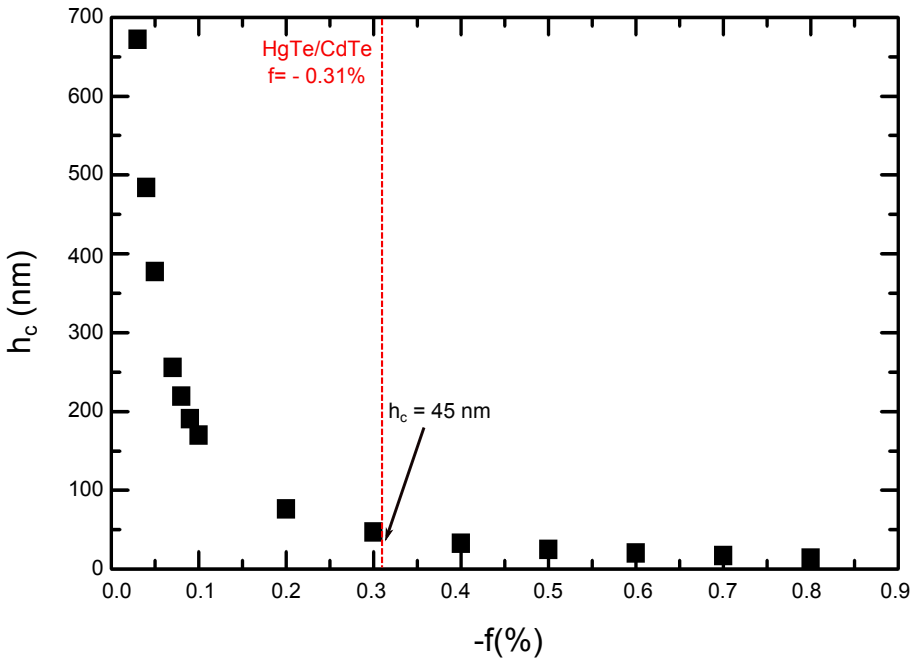

Figure 1.11 – *Critical thickness of plastic relaxation as a function of the lattice mismatch for HgTe (100).*

1.1.5.3 Determination of the bulk gap

Now that the tensile strain experienced by the HgTe layer and its critical thickness have been defined, we can consider the resulting Bir-Pikus Hamiltonian:

$$H_{BP} = \begin{pmatrix} T_{BP} & 0 & 0 & 0 & 0 & 0 & 0 & 0 \\ 0 & T_{BP} & 0 & 0 & 0 & 0 & 0 & 0 \\ 0 & 0 & U_{BP}+V_{BP} & 0 & 0 & 0 & 0 & 0 \\ 0 & 0 & 0 & U_{BP}-V_{BP} & 0 & 0 & \sqrt{2}V_{BP} & 0 \\ 0 & 0 & 0 & 0 & U_{BP}-V_{BP} & 0 & 0 & -\sqrt{2}V_{BP} \\ 0 & 0 & 0 & 0 & 0 & U_{BP}+V_{BP} & 0 & 0 \\ 0 & 0 & 0 & \sqrt{2}V_{BP} & 0 & 0 & U_{BP} & 0 \\ 0 & 0 & 0 & 0 & -\sqrt{2}V_{BP} & 0 & 0 & U_{BP} \end{pmatrix} \tag{1.39}$$

This Hamiltonian is obtained from the Kane Hamiltonian 1.18 by using the substitution $k_i k_j \rightarrow \epsilon_{ij}$. Note that this substitution is essentially applied on the T, U and V terms which are varying with: $k_z^2 \rightarrow \epsilon_{zz}$ and $k_{/\!/}^2 = k_x^2 + k_y^2 \rightarrow \epsilon_{xx} + \epsilon_{yy}$.

Moreover, Bir-Pikus Hamiltonian H_{BP} 1.39 terms are defined as:

$$\begin{aligned} T_{BP} &= C(1 - \tfrac{C_{12}}{C_{11}})\epsilon_{/\!/} \\ U_{BP} &= 2a(1 - \tfrac{C_{12}}{C_{11}})\epsilon_{/\!/} \\ V_{BP} &= b(1 + 2\tfrac{C_{12}}{C_{11}})\epsilon_{/\!/} \end{aligned} \tag{1.40}$$

with the deformation potentials:

$$\begin{aligned} C &= \frac{\hbar^2}{m_0}(2F+1) \\ a &= -\frac{\hbar^2}{2m_0}\gamma_1 \\ b &= -\frac{\hbar^2}{m_0}\gamma_2 \end{aligned} \tag{1.41}$$

The numerical value $b = -1.5$ eV for HgTe submitted to biaxial strain is used thereafter.

From H_{BP} presented in 1.39, one can deduce that Γ_{8LH} and Γ_{8HH} bands are separated in energy by $2V_{BP}$. The resulting bulk gap opening is thus expressed as:

$$E_s = 2|b(1+2\frac{C_{12}}{C_{11}})\epsilon_{/\!/}| \tag{1.42}$$

From equation 1.42 and the strain values, we deduce that a strain gap E_S of about 21.5 meV opens between the two Γ_8 bands.

The theory of Bir and Pikus has been confirmed for HgTe using ab-initio calculations [WYF14] presented in Fig. 1.12 which evidences the transition from semi-metallic state to insulator with the increase of lattice mismatch and so of the tensile strain. Note that in these calculations, $E_s = 25$ meV. This value is slightly larger than the one previously determined (21.5 meV). This can be due to a difference of definition of the lattice parameters and of the stiffness constants.

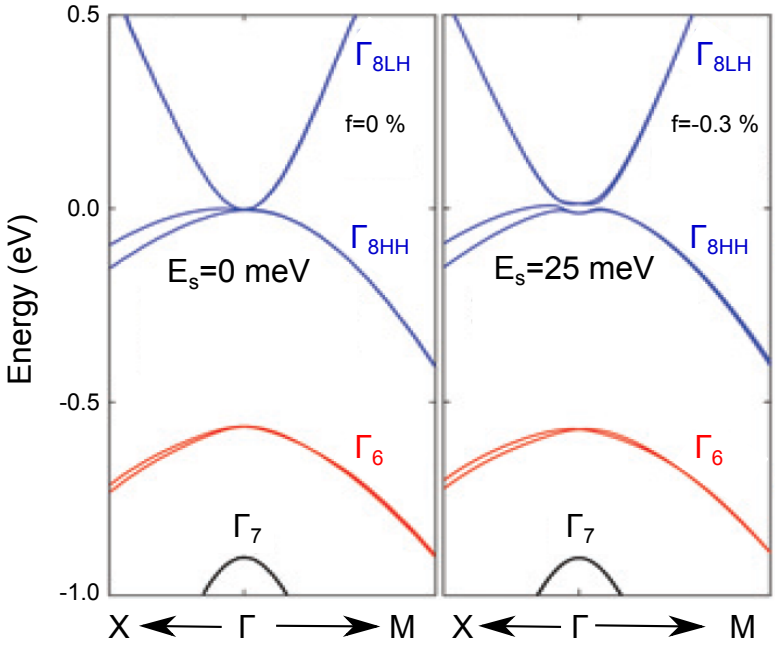

Figure 1.12 – *HgTe calculated band structure without strain (left) and when grown on CdTe (right) with lattice mismatch of* -0.3%. *Adapted from [WYF14].*

1.1.6 Experimental evidence of the band structure

The topological surface states of a 100 nm-thick HgTe layer grown on (100) CdTe have been measured using high-resolution Angle Resolved PhotoEmission Spectroscopy (ARPES) (CASSIOPEE line, synchrotron SOLEIL) as shown in Fig. 1.13. The reader is invited to refer to [COB+13] for further details about this study. The ARPES measurements performed on such strained HgTe topological insulator system report the linear energy dispersion of the surface states (highlighted by black lines in Fig. 1.13(a) and in yellow in Fig. 1.13(b)) consistent with the expected Dirac cone picture. Fermi velocity v_f of about $5.10^5 m.s^{-1}$ has been extracted from this linear dispersion. The cone is separated in two parts by the Dirac point: the top part hosting electrons and the bottom one carrying holes. One can notice that the Dirac point lies at the top of the heavy hole Γ_{8HH} bulk band. This is confirming that the hole-side of the Dirac cone is coupled to bulk states while the electron-side is not as it lies in the strain gap. This coupling to the Γ_{8HH} bulk band is of main importance and needs to be kept in mind for the understanding of the electronic transport mechanism presented in Chapter 4. Furthermore, no clear evidences of the Γ_{8LH} band are visible, thus suggesting a strain gap value larger than the expected 21.5 meV.

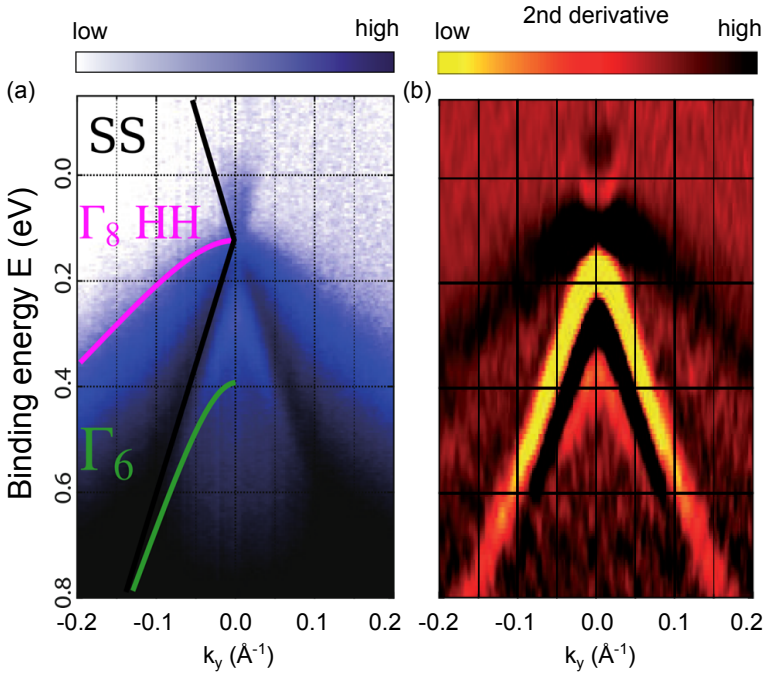

Figure 1.13 – *(a) ARPES intensity spectrum of the energy-momentum at the HgTe/vacuum interface. (b) Second derivative of the intensity. Adapted from [COB+13].*

1.2 Topological surface state properties

ARPES measurements have experimentally demonstrated the existence of topological surface states forming a Dirac cone. By hosting Dirac fermions, the surface states are described by a linear energy dispersion and are thus strongly different from standard 2D parabolic electron gas. In this PhD thesis, we propose to complete the ARPES demonstration of the HgTe band structure, especially of the surface states, by using magneto-conductance measurements. Therefore, the aim of this section is to introduce the reader to these measurements at both low (Hall effect) and high magnetic field (quantum Hall effect) and to define the expected signatures. Tools are reported to allow for the clear identification of Dirac fermions via quantum Hall transport spectroscopy. Moreover, additional keys are provided to differentiate 3D topological insulator transport mechanism from those observed in graphene, relying on the determination of the Landau Level (LL) energy spectrum and the Hall conductance.

1.2.1 Hall effect

Observed for the first time in 1879 by E.H. Hall, the Hall effect is driven by the Lorentz force which compelled the electrons to deviate from their initial way and to accumulate on one sample's side as represented in Fig. 1.14. This electron accumulation is directly accompanied by a hole accumulation on the opposite side of the sample. With such a charge difference, a voltage V_{xy}, also called Hall voltage, appears across the sample.

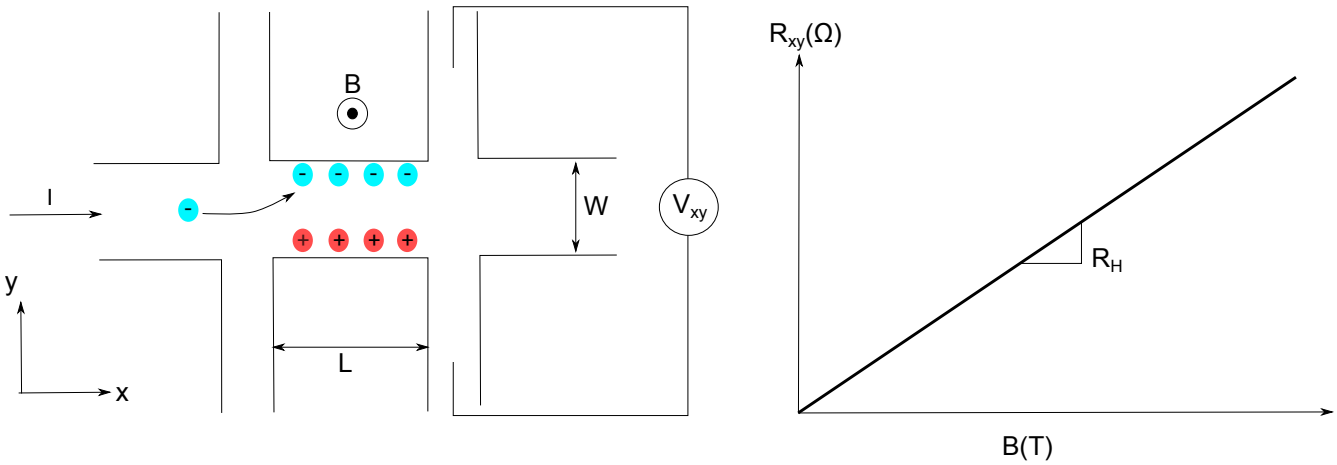

Figure 1.14 – *Principle of the Hall effect. A Hall bar of length L and width W is biased with a current I and submitted to a magnetic field B. Due to the Lorentz force, the electrons are deflected and accumulate on one side of the sample creating a difference of charge and so a voltage V_{xy}, also called Hall voltage. The associated Hall resistance R_{xy} linearly increases with the magnetic field with a slope R_H.*

In this Hall effect regime, the variation of the Hall resistance R_{xy} can be determined from the Drude model with one type of carrier. We are considering 2D systems for which the carriers are propagating on the sample surface with a mass m and a scattering time τ following the equation of motion below:

$$m\frac{d\vec{v}}{dt} = -e(\vec{E} + \vec{v} \otimes \vec{B}) - \frac{m\vec{v}}{\tau} \tag{1.43}$$

As the stationary state is defined by $\frac{d\vec{v}}{dt} = 0$, we obtain the following relation between the electric field and the velocity:

$$\begin{pmatrix} E_x \\ E_y \end{pmatrix} = \begin{pmatrix} -\frac{m}{e\tau} & -B \\ -B & -\frac{m}{e\tau} \end{pmatrix} \begin{pmatrix} v_x \\ v_y \end{pmatrix} \tag{1.44}$$

The current density being expressed as $\vec{j} = -en\vec{v}$ with n the carrier density, the longitudinal ρ_{xx} and Hall ρ_{xy} resistivities can be determined using equations 1.45 and 1.46, respectively.

$$\rho_{xx} = \frac{E_x}{j_x} = \frac{m}{e^2 n\tau} \tag{1.45}$$

$$\rho_{xy} = \frac{E_y}{j_x} = -\frac{B}{ne} \tag{1.46}$$

It is worth noting that in the case of 2D electron gas the Hall R_{xy} and the longitudinal R_{xx} resistances can be directly derived from these equations as they are defined as $R_{xy} = \rho_{xy}$ and $R_{xx} = \frac{L}{W}\rho_{xx}$, with L and W the length and width of the Hall bar respectively.

From equation 1.46, we demonstrate a linear dependence of R_{xy} with B in this Hall effect regime. Furthermore, the Hall resistance slope, called Hall constant thereafter, $R_H = \frac{1}{ne}$ constitutes a direct tool for the estimation of the carrier density. Carrier mobility can also be investigated, relying on both R_H and $R_{xx}(B = 0)$ gate voltage variations.

This development has been presented for a single carrier model. However, one needs to keep in mind that the expression of R_H depends on the number of carriers flowing in the sample. In the case of two carriers, the Hall voltage indeed depends on the density as well as the mobility of both type of carriers and its expression is adapted into [Mel66]:

$$R_H = \frac{p\mu_h^2 - n\mu_e^2}{e(n\mu_e + p\mu_h)^2} \tag{1.47}$$

with n the electron density, p the hole density, μ_e the electron mobility, and μ_h the hole mobility.

1.2.2 Quantum Hall Effect

When applying a larger magnetic field value, the HgTe surface states experience a new state of matter: the Quantum Hall Effect (QHE). With the increase of the Lorentz force, the electrons are forced to adopt a cyclotron trajectory thus creating insulating states in the surface and conduction channels on the edges as shown in Fig. 1.15.

Discovered by Von Klitzing [KDP80] in 1980, this state of matter transforms a continuous 2D density of states into discrete levels. It is the 2π periodicity of the electron wavefunction which imposes a quantization of the system energy forming the so-called Landau Levels (LLs). The appearance of these energy levels manifests through the quantization of the Hall resistance directly related to the number of available conduction channels. This number is called the filling factor ν thereafter. In parallel, the longitudinal resistance R_{xx} experiences quantum oscillations. Figure 1.15 evidences the quantized R_{xy} associated to the oscillations of R_{xx}. R_{xx} maximum evidences the N^{th} LLs while the minimum corresponds to the transition between the N^{th} and the $(N+1)^{th}$ LLs. Moreover the width of the oscillations illustrates the broadening of the LLs essentially induced by scattering disorder potential.

In the following of this PhD thesis, we will mainly talk about Hall and longitudinal conductivities. These

parameters are defined as follow:

$$\begin{cases} \sigma_{xy} = \frac{\rho_{xy}}{\rho_{xy}^2+\rho_{xx}^2} \\ \sigma_{xx} = \frac{\rho_{xx}}{\rho_{xy}^2+\rho_{xx}^2} \end{cases} \tag{1.48}$$

with $\rho_{xy} = R_{xy}$ and $\rho_{xx} = R_{xx}\frac{W}{L}$, for 2D electron gas.

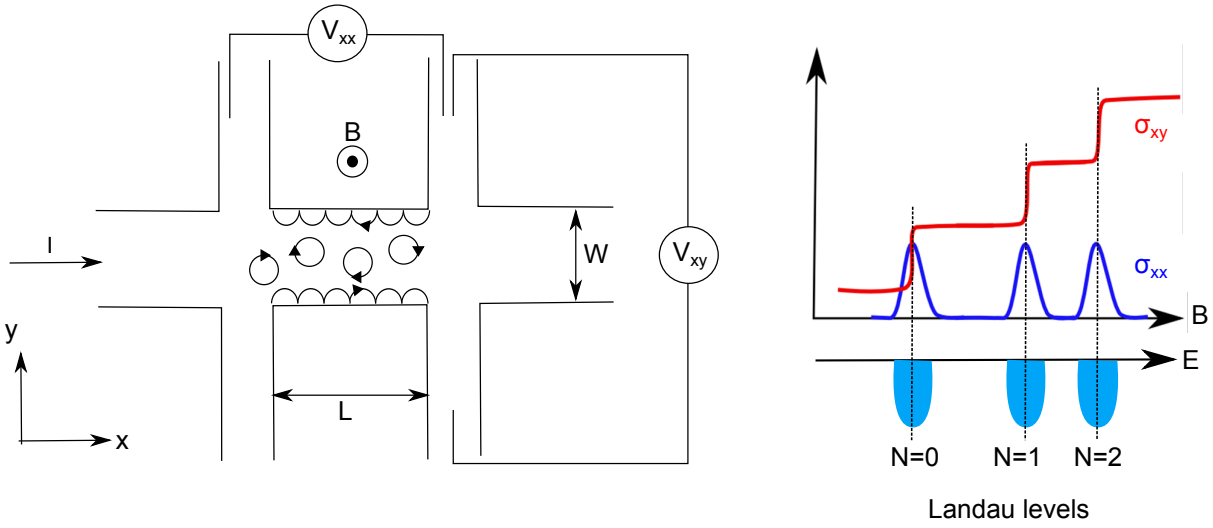

Figure 1.15 – *Quantum Hall Effect principle. When experiencing a high magnetic field B, electron trajectory becomes circular creating edge channels of conduction on the sample sides. These channels characterize the quantization of the energy levels accessible by the carriers, forming the so-called Landau levels (LL). Experimentally, these energy levels are measured and evidenced as quantized plateaus of the Hall conductivity σ_{xy} associated to vanishing minima of the longitudinal conductivity σ_{xx}.*

1.2.2.1 Parabolic electrons

In order to go one step further and to study the QHE transport signatures, we first focus on a 2D Electron Gas (2DEG) composed of parabolic electrons propagating in the (x,y) plane and submitted to a perpendicular magnetic field $\vec{B} = B\vec{z}$. The Hamiltonian of such system is expressed through:

$$H_{2DEG} = \frac{(\hbar k)^2}{2m^*} \tag{1.49}$$

It is worth noting that Zeeman coupling is neglected here implying that the effect of the magnetic field will only be orbital. The magnetic field is considered in this Hamiltonian through the Peierls substitution: $\vec{k} \rightarrow \vec{k} - e\vec{A}$ with the potential vector $\vec{A}$ determined by the Landau gauge (0, Bx, 0). In these conditions, k_y remains a good quantum number and we consider the following wavefunction $\Psi(x,y) = \exp(ik_y y)\Phi(x)$. Thus, the Hamiltonian transforms into:

$$H_{2DEG} = \frac{\hbar^2 k_x^2}{2m^*} + \frac{\hbar^2 k_y^2}{2m^*} + \frac{1}{2}m^* w_c^2 x^2 - w_c \hbar k_y x \tag{1.50}$$

with $w_c = \frac{eB}{m^*}$ the cyclotron frequency.

Ladder operators are introduced to facilitate the analysis and the determination of the eigenvalues. a and $a^\dagger$

are creation and annihilation operators, respectively. They are defined through the relations below:

$$\begin{cases} a = \frac{1}{\sqrt{2}}(q + ip) \\ a^\dagger = \frac{1}{\sqrt{2}}(q - ip) \end{cases} \tag{1.51}$$

where

$$q = \frac{X}{l_B} = \frac{x - k_y l_B^2}{l_B^2} \; ; \; p = -il_B\partial_X \tag{1.52}$$

and with $l_B^2 = \frac{\hbar}{eB}$.

The Hamiltonian 1.50 is thus transformed into:

$$H_{2DEG} = \hbar\omega_c(a^\dagger a + \frac{1}{2}) \tag{1.53}$$

As this Hamiltonian includes ladder operators, it is useful to remind the following relations:

$$\begin{cases} a^\dagger |N\rangle = \sqrt{N}\,|N-1\rangle \\ a\,|N-1\rangle = \sqrt{N}\,|N\rangle \end{cases} \tag{1.54}$$

Equations 1.50 and 1.53 mimic an Harmonic oscillator behavior with frequency w_c and cyclotron orbit centered in $x_0 = \frac{\hbar k_y}{w_c m^*}$. By considering the eigenvector $|N\rangle$, the energy spectrum follows:

$$E_N = \hbar w_c(N + \frac{1}{2}) \tag{1.55}$$

where N is the Landau level index. Figure 1.16 (a) displays the corresponding LLs energies with the addition of a confinement potential in the y direction. The resulting energy spectrum is expressed through:

$$E_N = \hbar w_c(N + \frac{1}{2}) + \frac{C}{B}k_y \tag{1.56}$$

where C is a constant. Far from the edges, the energy levels remain the same, however near the edges they experience a linear behavior.

We have just demonstrated the behavior of the LL energy spectrum in the case of a classical 2DEG made of parabolic electrons. Each electron is experiencing a cyclotron motion centered in x_0. LL degeneracy is thus defined by the number of cyclotron radius inside a sample of dimensions W and L. Two adjacent circle origins must be separated by the amount $\Delta x_0 = \frac{\hbar\Delta k_y}{eB} = \frac{\hbar}{eB}\frac{2\pi}{W} = \frac{h}{eBW}$. Therefore, LL degeneracy is given by $N_{LL} = \frac{L}{\Delta x_0} = LW\frac{eB}{h}$ and the LL degeneracy per unit area also called the LL index N is expressed as:

$$N = \frac{N_{LL}}{LW} = \frac{eB}{h} \tag{1.57}$$

From this, we can define the filling factor ν as the ratio between the carrier density n and the number of occupied Landau levels:

$$\nu = \frac{n}{N} = \frac{nh}{eB} \tag{1.58}$$

if ν is an integer, then the Fermi level E_F lies in the energy gap between two Landau levels. The reader should have noticed that ν determines a linear relation between n and B. This relation will be extensively used in Chapter 4 for the determination of the quantization of the Hall conductance which reads:

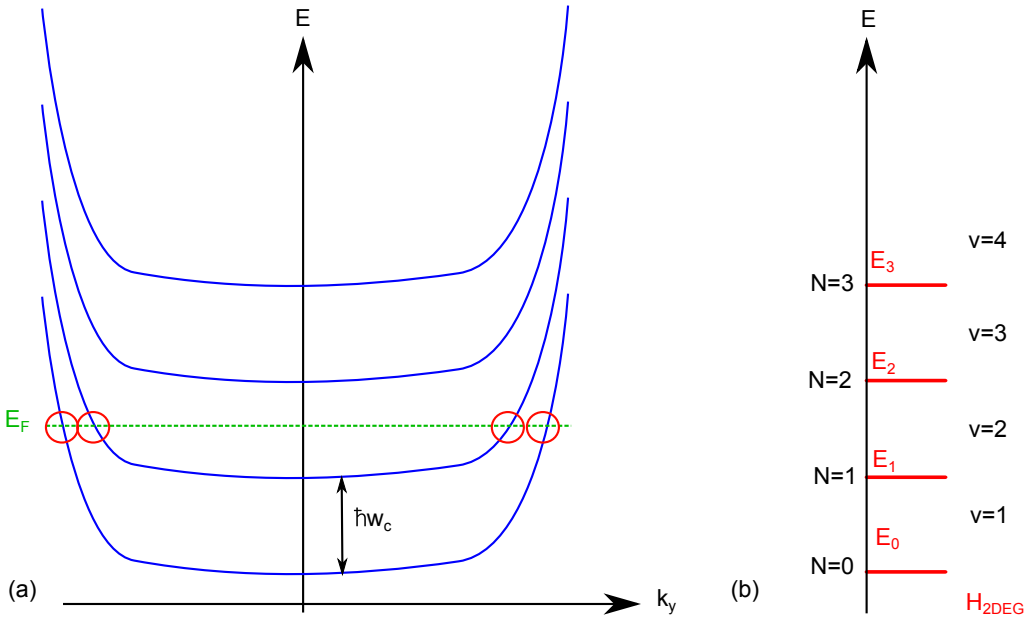

Figure 1.16 – *(a) Landau level energy separation of a trivial 2D Electron Gas (2DEG). The energy levels are separated by the same amount $\hbar w_c$. If E_F lies between two LLs, the surface is insulator while the edges are conductor. (b) The corresponding filling factors.*

$$\sigma_{xy} = \nu \frac{e^2}{h} \tag{1.59}$$

with $\frac{e^2}{h}$ the quantum of conductance.

Note that this expression of the Hall conductance is valid whatever the type of electrons. Only the authorized values of ν can differ from one type of electrons to the other. Moreover it also depends on the system degeneracy. In the case of 2D parabolic electrons, ν takes integer values as reported in Fig. 1.16(b) in the absence of any type of degeneracy.

1.2.2.2 Dirac electrons

The principle of the QHE and its associated quantization have just been discussed for a 2DEG with parabolic electrons (see Fig. 1.17(a)). Nevertheless, the experimental results that will be presented in this PhD thesis focus on 3D topological insulator systems for which the conducting surface states are acting as Dirac metallic 2DEG (see Fig. 1.17(b)).

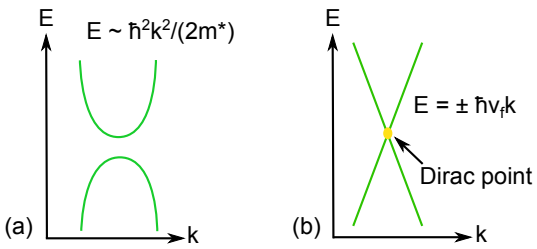

Figure 1.17 – *(a) Parabolic electron and (b) Dirac fermion energy dispersion.*

Dirac fermions are characterized by a linear energy dispersion law $E = \hbar v_f k$ where v_f is the Fermi velocity and by a spin-momentum locking property $(\vec{\sigma}.\vec{k})$, as represented in Fig. 1.18 (a). The aim of this section is thus

to introduce the Dirac fermion properties and their signatures when experiencing QHE. In the following we will consider the case of a single Dirac Cone (DC). The Hamiltonian of this system can be written as:

$$H_{DC} = v_f(\hat{z} \times \vec{\sigma}).(-i\hbar\vec{\nabla}) = \hbar v_f(k_y\sigma_x - k_x\sigma_y) \tag{1.60}$$

with $\vec{\sigma}$ the Pauli matrices.

By introducing magnetic field through Peierls substitution, the former Hamiltonian 1.60 transforms into:

$$H_{DC} = \hbar v_f((k_y - eBx)\sigma_x - k_x\sigma_y) \tag{1.61}$$

and with the use of ladder operators, it becomes:

$$H_{DC} = \eta\left(a\sigma_- + a^\dagger\sigma_+\right) \tag{1.62}$$

where we have introduced $2\sigma_\pm = \sigma_x \pm i\sigma_y$ and $\eta^2 = 2\frac{\hbar^2 v_f^2}{l_B^2} = 2\hbar v_f^2 eB$. Then H_{DC} reads:

$$H_{DC} = \eta\begin{pmatrix} 0 & a^\dagger \\ a & 0 \end{pmatrix} \tag{1.63}$$

By considering $|N-1\rangle$ and $|N\rangle$ as the basis of eigenvectors, the Hamiltonian transforms into:

$$H_{DC} = \eta\begin{pmatrix} 0 & \sqrt{N} \\ \sqrt{N} & 0 \end{pmatrix} \tag{1.64}$$

As the product of two anti-diagonal matrix is a diagonal one, it is convenient to take the square of the previous Hamiltonian:

$$H_{DC}^2 = \eta^2\begin{pmatrix} N & 0 \\ 0 & N \end{pmatrix} \tag{1.65}$$

This latter diagonal Hamiltonian directly provides the eigenvalues corresponding to the Dirac-like LL energy spectrum:

$$E_N^\pm = \pm\eta\sqrt{N} = \pm\sqrt{2e\hbar v_f^2 BN} \tag{1.66}$$

The resulting LL energy separation is no more a constant but a function of $\sqrt{N}$ as it can be deduced from the energy spectrum 1.66 and as illustrated in Fig. 1.18 (b). $\pm$ refers to electron- and hole-sides.

It is worth noting that, in the case of Dirac electrons, the zeroth LL has zero energy and is shared between electrons and holes as illustrated in Fig. 1.18. This is resulting in a half-integer shift of the Hall conductance as expressed in:

$$\sigma_{xy} = g(N + \frac{1}{2})\frac{e^2}{h} \tag{1.67}$$

where g stands for the number of degenerate Dirac fermions, obviously equal to 1 for a single Dirac cone.

However, it is of main importance to realize that the case of a single Dirac cone does not exist in reality as it corresponds to half channels of conduction. Degeneracy $g \geq 2$ is thus needed to obtain an integer number of conduction channels. This degeneracy can have several origins such as spin (isospin) or valley as it is the case for graphene for which $g = g(isospin) + g(valley) = 4$. Note that this Dirac cone model has essentially been developed in this section to introduce and build step-by-step the quantum Hall model of a 3D topological

insulator.

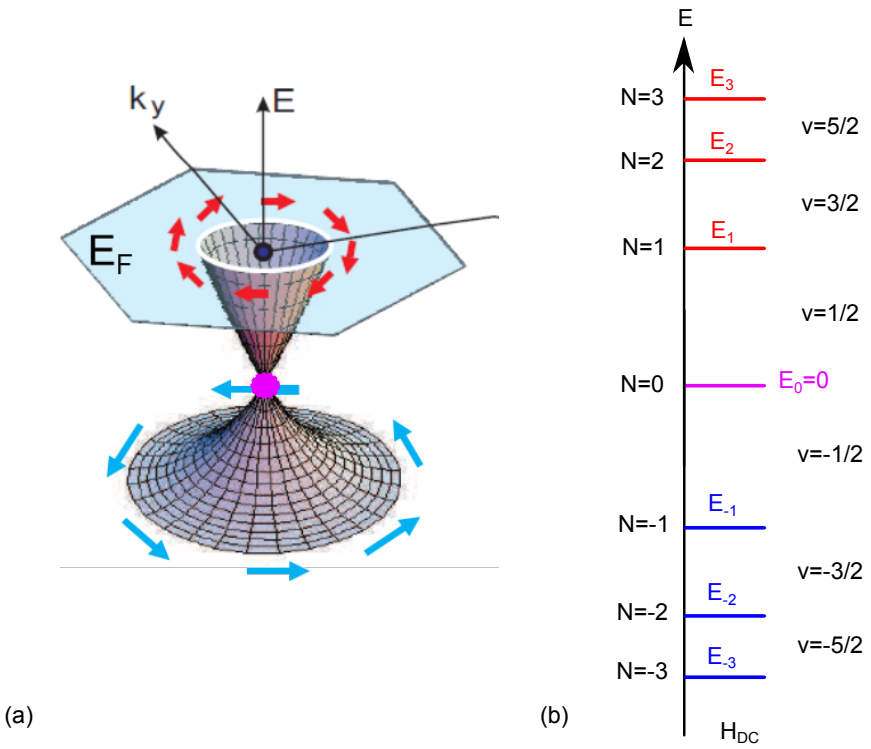

Figure 1.18 – *Single Dirac cone (a) linear energy dispersion with chiral spin polarization and (b) associated energy spectrum with the corresponding filling factors ν. The energy is zero at the Dirac point.*

1.2.2.3 Topological insulators

In the case of a single sheet of graphene, due to both isospin and valley degeneracies, the number of degenerate Dirac cones g is 4. This is resulting in the observation of a quantization in $\nu = 4N + 2$ [NGM+05]. However, 3D topological insulators differentiate themselves from graphene by two main points. The first one is that these materials are characterized by true spin, instead of isospin, which is locked with the momentum. The second difference is that each surface state hosts its own Dirac cone. More precisely, when applying $\vec{B} = B\vec{z}$, only top and bottom surfaces contribute to the electronic transport as illustrated in Fig. 1.19(a). As these two chiral Dirac cones are spatially separated, the strictly speaking degeneracy is one and the quantization only results from the addition of both top and bottom surface contributions acting in parallel. The objective of the following analysis is to develop and derive the QHE model for such a thick topological insulator having a thickness t much larger than the surface state extension $w = \frac{1}{\lambda}$. The resulting LL energy spectrum and the associated quantization will be discussed.

Furthermore, we also consider the case of a thin topological insulator for which $t \approx 2w$. In this case, the two Dirac cones hybridize thus lifting the spin degeneracy: $g = 2$. The evolution of the LL energy spectrum and of the quantization in this new regime will be addressed.

1.2.2.3.1 Thick topological insulator layer We first consider a thick layer of topological insulator material, with two parallel surfaces indexed by $\tau_z = +1$ for the Top (T) and $\tau_z = -1$ for the Bottom (B) surface. The effective Hamiltonian for the surface states is expressed as:

$$H_{thick} = v_f \, \tau_z \otimes (\hat{z} \times \vec{\sigma}).(-i\hbar\vec{\nabla}) + V\tau_z \otimes \mathbb{I} \tag{1.68}$$

The first term of this Hamiltonian describes the Dirac dispersion relation of the top and bottom surface states with opposite chirality (the spin winds in opposite ways around the Fermi surface) while the second term corresponds to the chemical potential difference V between the two surfaces which arises due to screening effects of the bottom surface by the metallic top surface and the bulk [SLS10] [ZLS15] (see Fig. 1.19(a)).

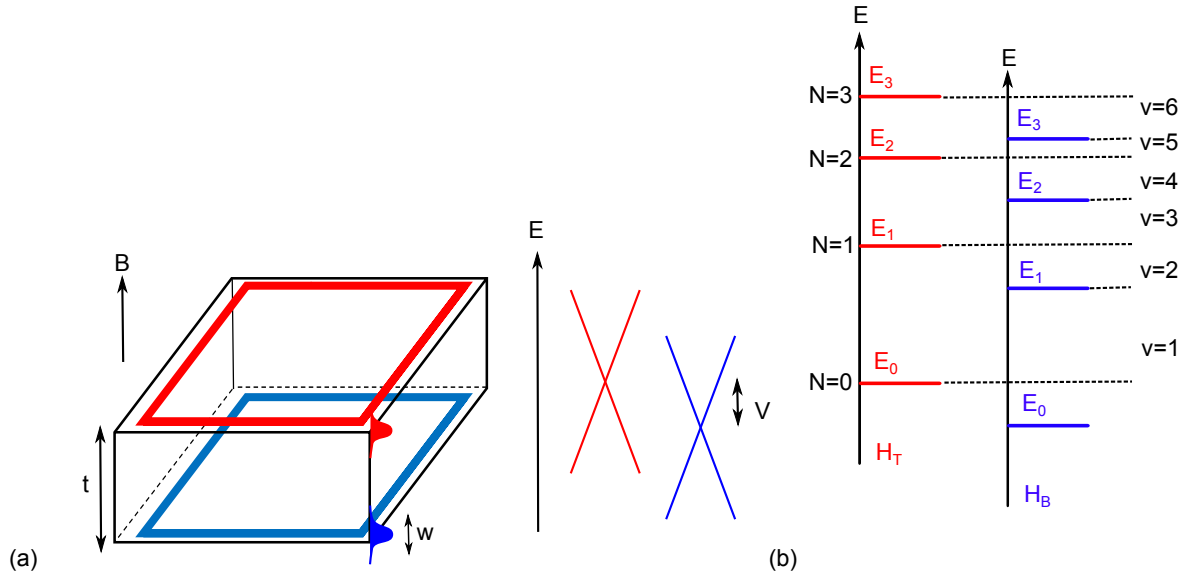

Figure 1.19 – *(a) 3D topological insulator structure with the top (red) and the bottom (blue) surface states. Due to the bulk offset, the two Dirac cones are shifted in energy. (b) The LL energy spectrum with the corresponding filling factors.*

Hamiltonian of this thick topological insulator system is derived using similar development than for the case of a single Dirac cone. However, now we are considering two surfaces so the basis transforms into: $|T,\uparrow,N\rangle, |T,\downarrow,N-1\rangle, |B,\uparrow,N\rangle, |B,\downarrow,N-1\rangle$.

In this basis, the reduced Hamiltonian reads for $N \geq 1$:

$$H_{thick} = -\eta\ \tau_z \otimes \left(a\sigma_- + a^\dagger\sigma_+\right) + V\tau_z \otimes \mathbb{I} = \begin{pmatrix} V & -\eta a^\dagger & 0 & 0 \\ -\eta a & V & 0 & 0 \\ 0 & 0 & -V & \eta a^\dagger \\ 0 & 0 & \eta a & -V \end{pmatrix} \tag{1.69}$$

By solving $\det(H_{thick}) = 0$, one finds the corresponding LL energy spectrum:

$$E^2_{N,\pm} = N\eta^2 + V^2 \pm 2\eta V\sqrt{N} = (\eta\sqrt{N} \pm V)^2 \tag{1.70}$$

This energy spectrum differs from the one of a single Dirac cone and so of a single sheet of graphene by the potential V. It is therefore useful to discuss the effect of this chemical potential asymmetry. The corresponding term in the Hamiltonian is $+V\tau_z \otimes \mathbb{I}$ and is only shifting the energies of the Landau levels of the top surface with respect to those of the bottom surface without modifying their nature and so without introducing degeneracy ($g = 1$).

With two independent surface states and so two independent Dirac cones, the transport properties of such thick topological insulator layers are obtained by summing up the distinct contributions of each interface resulting in the following Hall conductance expression:

$$\sigma_{xy} = (N_{top} + N_{bottom} + 1)\frac{e^2}{h} \tag{1.71}$$

where N_{top} (respectively N_{bottom}) is the LL index for the top (bottom) interface. The corresponding filling factors are determined in Fig. 1.19(b) and are integers. Similar transport behavior has already been claimed to be observed in HgTe [BLN+11] [KKO+14] [KBZ+16] and Bi-compounds [SOL+11] [XML+14] for t of the order of 70 nm and 20 nm, respectively.

To summarize, in the case of thick topological insulator structures, the Dirac cones of each surface are assumed to be independent and with an opposite chirality as demonstrated by the Hamiltonians of the top and bottom Dirac cones: $H_{top} = \hbar v_f(k_y\sigma_x - k_x\sigma_y)$ and $H_{bottom} = -\hbar v_f(k_y\sigma_x - k_x\sigma_y)$. This difference of chirality is also illustrated in Fig. 1.20 which highlights the fact that each Dirac cone owns a different spin specie. Therefore, if the two surfaces are independent, these spins cannot interact with each other and thus the spin degeneracy cannot be lifted. The coupling of the two surfaces is thus required for having a mixing between the two spin species allowing to observe spin splitting. One of the mechanism identified to lift this degeneracy is the hybridization of the two surface states by reducing the topological insulator thickness. This mechanism is the content of the following paragraph.

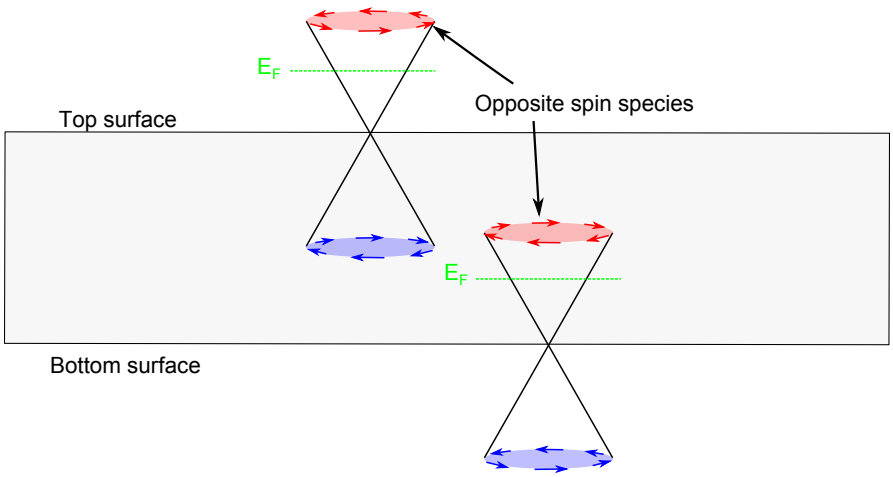

Figure 1.20 – *Single Dirac cones on the two surface states. Each surface is characterized by a different spin specie.*

1.2.2.3.2 Thin topological insulator layer We are now considering a thin layer of topological insulator material. By decreasing t closer and closer to w, the two topological surfaces start to couple giving rise to a non-negligible hybridization energy [LYS09] [LZY+10] [LSY+10]. The two topological surfaces are then gapped leading to two degenerate massive Dirac hyperbolas as represented in Fig. 1.21(a). The resulting gap Δ is varying in $\sim \frac{1}{t^2}$ as reported in references [SLS10] [LSY+10]. The effect of hybridization has been experimentally observed through ARPES measurements on Bi_2Se_3 compounds [ZHC+10] with the opening and increase of the surface state gap when decreasing the thickness.

For such thin topological insulator structure, the Hamiltonian is expressed as [LSY+10] [ZLS15]:

$$H_{thin} = v_f\ \tau_z \otimes (\hat{z} \times \vec{\sigma}).(-i\hbar\vec{\nabla}) + \left(\frac{\Delta}{2} + \frac{\hbar^2\nabla^2}{2M}\right)\tau_x \otimes \mathbb{I} + V\tau_z \otimes \mathbb{I} \tag{1.72}$$

In comparison with thick systems, the Hamiltonian is modified with the addition of the term $\Delta/2 - (\hbar k)^2/2M$. This mass term is obtained by the hybridization of the wavefunctions of both the top and bottom surface states. It is worth noting that Δ and $\frac{\hbar^2}{2M}$ terms depend on t and progressively vanish when increasing the topological insulator thickness.

The band structure corresponding to this model is symmetric with respect to $E = 0$, and reads:

$$E_{\pm}^2(\mathbf{k}) = \left(\frac{\Delta}{2} - \frac{\hbar^2k^2}{2M}\right)^2 + \left(V \pm \hbar v_f|k|\right)^2 \tag{1.73}$$

Using ladder operators, the Hamiltonian transforms into:

$$H_{thin} = -\eta\ \tau_z \otimes \left(a\sigma_- + a^\dagger\sigma_+\right) + \left(\frac{\Delta}{2} - \frac{\hbar\omega}{2}(2a^\dagger a + 1)\right)\tau_x \otimes \mathbb{I} + V\tau_z \otimes \mathbb{I} \tag{1.74}$$

where we have introduced $\hbar\omega = \frac{\hbar^2}{Ml_B^2} = \frac{\hbar eB}{M}$.

In the basis made of top and bottom surface states $|T,\uparrow,N\rangle, |T,\downarrow,N-1\rangle, |B,\uparrow,N\rangle, |B,\downarrow,N-1\rangle$, the 4*4

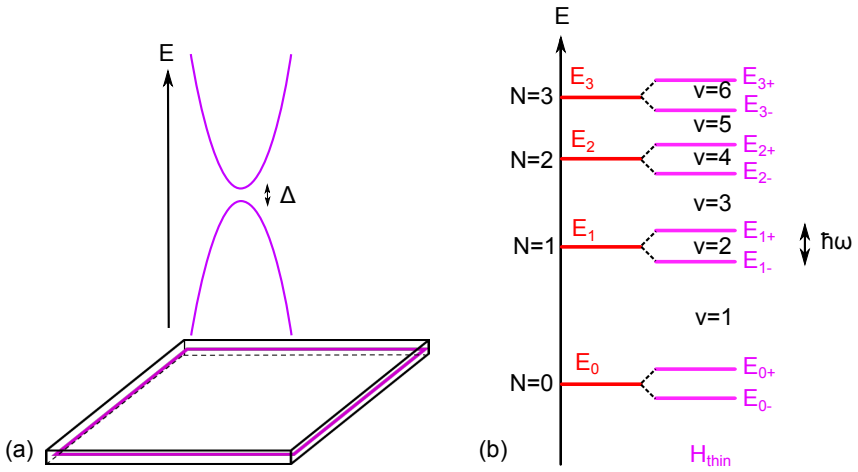

Figure 1.21 – *(a) 3D topological insulator structure with coupled surface states (magenta). The hybridization opens a gap Δ at the Dirac point and leads to two degenerate massive Dirac hyperbolas. (b) The resulting energy spectrum and the corresponding filling factors. Hybridization is at the origin of the splitting ħω.*

Hamiltonian reads:

$$H_{thin} = \begin{pmatrix} V & -\eta\sqrt{N} & \frac{\Delta}{2} - \frac{\hbar\omega}{2}(2N+1) & 0 \\ -\eta\sqrt{N} & V & 0 & \frac{\Delta}{2} - \frac{\hbar\omega}{2}(2N-1) \\ \frac{\Delta}{2} - \frac{\hbar\omega}{2}(2N+1) & 0 & -V & \eta\sqrt{N} \\ 0 & \frac{\Delta}{2} - \frac{\hbar\omega}{2}(2N-1) & \eta\sqrt{N} & -V \end{pmatrix} \tag{1.75}$$

which can be rewritten as:

$$H_{thin} = \tau_x \otimes \left[\left(\frac{\Delta}{2} - N\hbar\omega \right) \mathbb{I} + \frac{\hbar\omega}{2}\sigma_z \right] - \eta\sqrt{N}\, \tau_z \otimes \sigma_x + V\tau_z \otimes \mathbb{I} \tag{1.76}$$

Its energy spectrum is symmetric with respect to 0 and thus follows:

$$E^2_{N,\pm} = V^2 + N\eta^2 + \left(\frac{\hbar\omega}{2}\right)^2 + \left(\frac{\Delta}{2} - N\hbar\omega\right)^2 \pm \left(N\eta^2 \left(4V^2 + (\hbar\omega)^2\right) + (\hbar\omega)^2 \left(\frac{\Delta}{2} - N\hbar\omega\right)^2 \right)^{\frac{1}{2}} \quad \text{for } N \neq 0 \tag{1.77}$$

It is worth noting that similar energy spectrum has also been demonstrated in [ZLS15].

In the case of $N = 0$, the following basis is considered $|T,\uparrow,0\rangle$ and $|B,\uparrow,0\rangle$ and all the terms in $a\sigma_-$ and $a^\dagger\sigma_+$ cancel out, thus giving the effective Hamiltonian below:

$$H_0 = V\tau_z \otimes \mathbb{1} + \left(\frac{\hbar\omega - \Delta}{2}\right) \tau_x \otimes \mathbb{1} \tag{1.78}$$

with eigenvalues $\pm\sqrt{V^2 + (\hbar\omega - \Delta)^2/4}$.

We assume that there is no more screening effects and so that V vanishes in the case of thinnest HgTe layers where the two topological surface states are completely coupled. Indeed, the two Dirac cones experience exactly the same gate voltage potential. It is therefore important to establish the energy spectrum without this potential.

In this particular case ($V = 0$), we can rewrite equation 1.77 as:

$$\tilde{E}^2_{N,\pm} = N\eta^2 + \left(\frac{\hbar\omega}{2}\right)^2 + \left(\frac{\Delta}{2} - N\hbar\omega\right)^2 \pm \hbar\omega\left(N\eta^2 + \left(\frac{\Delta}{2} - N\hbar\omega\right)^2\right)^{\frac{1}{2}} = \left(\epsilon_N \pm \frac{\hbar\omega}{2}\right)^2 \quad (1.79a)$$

$$\tilde{E}^2_0 = \left(\frac{\hbar\omega - \Delta}{2}\right)^2 \quad (1.79b)$$

with

$$\epsilon_N = \left(N\eta^2 + \left(\frac{\Delta}{2} - N\hbar\omega\right)^2\right)^{\frac{1}{2}} \quad (1.80)$$

Here, we can immediately see that the degeneracy of the Landau levels ϵ_N is lifted by a splitting term $\pm\hbar\omega/2$. One can also notice that despite the fact that this splitting is not of magnetic origin, it is linear in magnetic field, and can thus be considered as an "effective Zeeman splitting" originating from the k^2 dependence of hybridization term between top and bottom surfaces [ZLS15]. The resulting LL energy spectrum for such thin 3D topological insulator is represented in Fig. 1.22. The gap opening Δ at the Dirac point is evidenced as well as the linear increase of splitting effect with B.

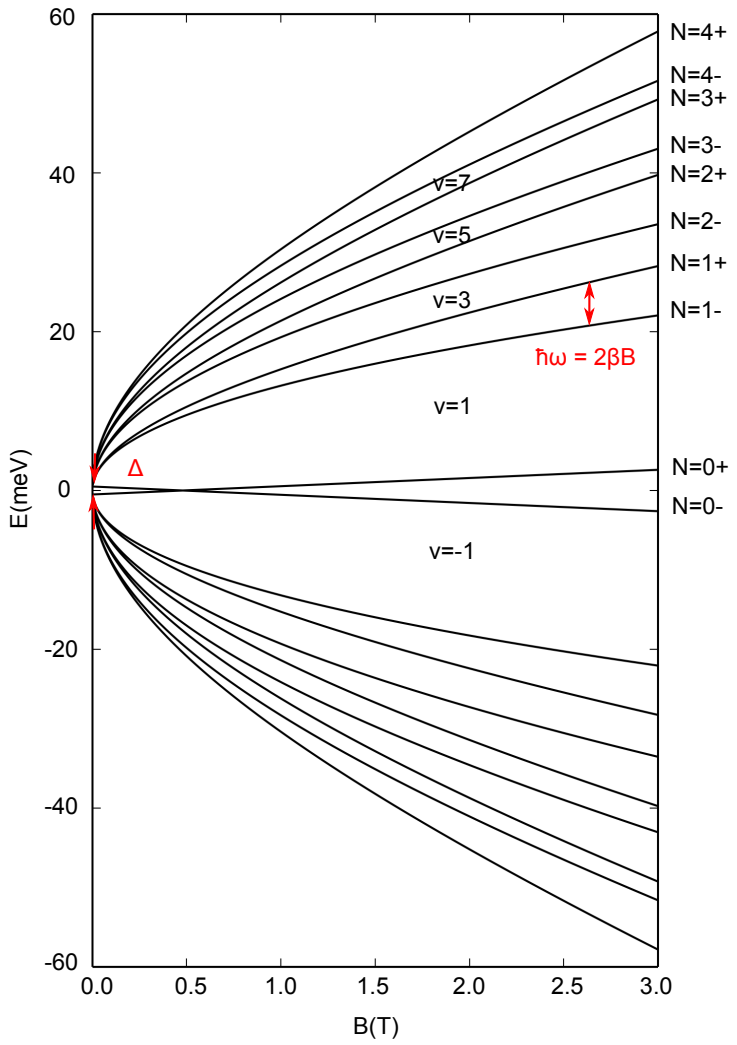

Figure 1.22 – *Energy spectrum as a function of B for LL index ranging from 0 to 4 in both electron- and hole-sides. LLs splitting as well as hybridization gap Δ are evidenced. Δ has been set to 2 meV, 2β to 2.07 meV/T and v_f to $\approx 4.10^5$ $m.s^{-1}$.*

This energy spectrum differs from the one of a thick topological insulator with two independent surface states by the addition of two terms of hybridization and splitting. The presence of these terms as well as their impact on the energy spectrum characterize Dirac fermion transport in our structures. It is therefore of main importance to further discuss the effects and mechanisms induced by these terms. To do so, we first have to introduce the eigenstates of the system. We consider the case $V = 0$ and in the limit $\Delta \to 0, \omega = 0$, thus the reduced Hamiltonian 1.76 reads:

$$H_N^{(0)} = -\eta\sqrt{N}\,\tau_z \otimes \sigma_x \tag{1.81}$$

The corresponding eigenstates are:

$$\psi^+_{N,+} = \frac{1}{\sqrt{2}}\left(|T,\uparrow,N\rangle - |T,\downarrow,N-1\rangle\right), \quad \psi^+_{N,-} = \frac{1}{\sqrt{2}}\left(|B,\uparrow,N\rangle + |B,\downarrow,N-1\rangle\right) \text{ for } \epsilon_N = \eta\sqrt{N} \tag{1.82a}$$

$$\psi^-_{N,+} = \frac{1}{\sqrt{2}}\left(|B,\uparrow,N\rangle - |B,\downarrow,N-1\rangle\right), \quad \psi^-_{N,-} = \frac{1}{\sqrt{2}}\left(|T,\uparrow,N\rangle + |T,\downarrow,N-1\rangle\right) \text{ for } \epsilon_N = -\eta\sqrt{N} \tag{1.82b}$$

These eigenstates are entirely localized in either the top or bottom surface, and carry no net magnetization as highlighted by the following relations:

$$\langle\psi^+_{N,\pm}|S_x|\psi^+_{N,\pm}\rangle = \langle\psi^+_{N,\pm}|S_y|\psi^+_{N,\pm}\rangle = \langle\psi^+_{N,\pm}|S_z|\psi^+_{N,\pm}\rangle = 0 \tag{1.83}$$

The idea is now to study their evolution when submitted to the hybridization and splitting operators.

Top / bottom surface hybridization is characterized by $\left(N\hbar\omega - \frac{\Delta}{2}\right)\tau_x \otimes \mathbb{I}$. This operator shifts the energies of the LLs and delocalizes the eigenstates on both top and bottom surfaces but without any splitting effect as demonstrated by:

$$\tau_x \otimes \mathbb{I}|\psi^\pm_{N,\pm}\rangle = |\psi^\mp_{N,\pm}\rangle \Rightarrow \langle\psi^+_{N,+}|\tau_x \otimes \mathbb{I}|\psi^+_{N,-}\rangle = 0 \tag{1.84}$$

The splitting is, for its part, characterized by $H_{Splitting} = \frac{\hbar\omega}{2}\,\tau_x \otimes \sigma_z$. This operator is a direct consequence of the coupling between the two surface states and arises from the k^2 term in 1.72. It satisfies:

$$H_{Splitting}|\psi^+_{N,+}\rangle = |\psi^+_{N,-}\rangle \tag{1.85}$$

and thus lifts the degeneracy between the eigenstates.

We have just demonstrated that hybridization and splitting are the two main effects and signatures of topological surface states in thin 3D topological insulator systems at the vicinity of the 2D transition. The question is now to understand how these effects manifest in the Hall conductance expression. Due to hybridization, the two Dirac cones are coupled and so $N_{top} = N_{bottom} = N$, thus resulting in the following Hall conductance:

$$\sigma_{xy} = 2(N + \frac{1}{2})\frac{e^2}{h} \tag{1.86}$$

Thus, the corresponding filling factors only take odd values [Lee09] [ZLS15]. However, due to the "effective Zeeman splitting", there is a lifting of the spin degeneracy and integer values of filling factors are expected [LSY+10] [ZLS15] as evidenced in Fig. 1.21(b).

1.2.2.4 Side surfaces

We have just demonstrated the energy spectrum and QHE signatures corresponding to top and bottom topological surface states. However, 3D HgTe topological insulators are characterized by six conducting surfaces. The idea is now to determine the effect of magnetic field on the remaining four facets parallel to the magnetic field.

We have previously demonstrated in this Chapter that a surface with a single Dirac cone is described by the Hamiltonian H_{DC}. For surfaces in the (y,z) plane, this Hamiltonian transforms into:

$$H_{DC} = v_f(\hat{x} \times \vec{\sigma}).(-i\hbar\vec{\nabla}) = \hbar v_f(k_z\sigma_y - k_y\sigma_z) \tag{1.87}$$

Magnetic field is considered using the substitution : $\vec{k} \rightarrow \vec{k} - e\vec{A}$ with $\vec{A} = (0, Bx, 0)$.

$$H_{DC} = \hbar v_f(k_z\sigma_y - (k_y - eBx)\sigma_z) \tag{1.88}$$

By solving $det(H_{DC} - E\mathbb{I}) = 0$, one finds the following formula for the energy dispersion of the side surfaces:

$$E = \hbar v_f\sqrt{(k_y - eBx)^2 + k_z^2} \tag{1.89}$$

We can conclude that the magnetic field has no effect except shifting the Dirac point from $(k_y = 0, k_z = 0)$ to $(-eBx, 0)$. Dirac cones on these side surfaces remain gapless and are forming metallic surfaces.

1.2.3 Berry's phase

We have just provided strong tools to identify the Dirac nature of the carriers propagating on the surface states. However, to use these tools, one need well-defined quantum Hall effect which, as far as we know, has never been reported for thick 3D topological insulators. Therefore, up to now, claiming the existence of Dirac fermions using magneto-transport measurements has been done with the sole determination of the Berry's phase [RTS+10] [QHX+10][YLZ+13].

The Berry's phase defines as the accumulated phase factor Φ during an adiabatic rotation along a closed path and is expressed as:

$$\beta = \frac{\Phi}{2\pi} \tag{1.90}$$

In topological insulator systems, this phase factor is dependent on the spin rotation along the circular Fermi surface. However, as previously mentioned, only $\frac{1}{2}$ spin particles are considered due to the chirality of the surface states thus forming a spin-vortex like pattern as illustrated in Fig. 1.23. With these characteristics, two complete rotations are required to acquire a phase of 2π [Has10] and β is thus expected to be half an integer for topogical systems.

It is worth noting that Berry's phase protects the surface states from backscattering from both disorder and impurities. Indeed due to spin-momentum locking property, an electron can not propagate from k to $-k$ or vice-versa since this will require a spin-flip mechanism and therefore magnetic impurities.

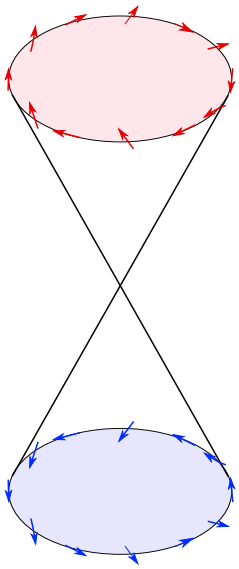

Figure 1.23 – *Spin rotation around the Fermi surface of a Dirac cone forming a vortex-like pattern.*

1.3 Conclusion

This Chapter has first introduced the CdTe band structure using the Kane model without and with spin-orbit coupling. Information about the band ordering and the effective mass have been provided allowing to define a four-band picture with Γ_6 conduction band, Γ_{8LH} and Γ_{8HH} valence bands and Γ_7 split-off band. However, in the case of HgTe, relativistic effects such as mass-velocity correction and spin-orbit coupling modify the band ordering with Γ_6 shifted below Γ_8. HgTe is thus defined by an inverted and semi-metallic band structure. The inversion of the band structure contributes to the formation of metallic surface states at the HgTe interfaces having an extension of about 4.7 nm. In parallel, the effect of tensile strain allows the opening of a 21.5 meV bandgap. These topological insulator characteristics are illustrated by ARPES measurements confirming the existence of surface states.

This Chapter has finally discussed the quantum Hall signatures expected for a 3D topological insulator. Contrary to trivial parabolic electrons, Dirac fermions demonstrate a LL energy separation varying with the LL index in $\sqrt{N}$. Note that this signature is used in Chapter 4 to experimentally reveal the presence of Dirac fermions in our HgTe structures. Even though 3D topological insulators are hosting Dirac fermions, they differ from graphene by the split of spin degeneracy between the two chiral surface states. Therefore, in the case of thick structures, the electronic transport properties and especially the quantization are obtained by summing up the individual contribution of each independent Dirac cone. Indeed, a coupling mechanism is required to lift the spin degeneracy. The hybridization of the wavefunctions of both top and bottom surface states when decreasing the topological insulator thickness has been identified as a mechanism lifting the degeneracy with the addition of a splitting term in the LL energy spectrum. Magneto-transport measurements exposed in Chapter 4 aim to experimentally verify and confirm these models.

Chapter 2

Growth and characterization of 3D HgTe/CdTe topological insulator structures

The growth of topological insulator materials is not an easy task as first the bulk needs to stay insulator not to impact the electronic transport arising on the surface states, and second the surfaces must be as flat as possible and free of defects to keep undamaged the intrinsic topological properties.

Widely used and grown for thermoelectric applications, Bi-based compounds, like Bi_2Se_3, Bi_2Te_3, ..., have been the first materials for which the topological nature was demonstrated. The growth of such compounds is mostly performed by chemical vapor deposition [CVL+12] or bulk Bridgman process [ERT+10]. However, these structures are characterized by large bulk conductivity and very low electronic mobility principally due to the lack of stoichiometry control. To improve the quality of these materials, new strategies are nowadays established and focus on the use of Molecular Beam Epitaxy (MBE) and the realisation of ternary $(BiSb)_2Te_3$ or quaternary $(Bi, Sb)_2$ $(Te, Se)_3$ alloys. Well-known for an atomic layer control of the deposition, MBE growth is expected to considerably enhance the quality of these 3D topological insulator structures. However, the growth parameters must be precisely determined as well as the substrate type and orientation [HKW13] to avoid structural defects. Results concerning these MBE structures begin to emerge in the literature such as the work of Yoshimi *et al.* [YTK+15] which reports evidences of two surface states from $(Bi_{1-x}Sb_x)_2Te_3$ grown on InP(111) substrates. The control of the composition ratio between Bi and Sb can be accurately monitored by MBE and is of main importance as it determines the Dirac point energy.

In this PhD thesis, we concentrate on the MBE growth of another 3D topological insulator: HgTe/CdTe. Due to very peculiar growth of such Hg-based materials (only mastered by a few laboratories in the world), this 3D system has required longer time to be experimentally demonstrated as topological. Our growth process mainly relies on 30 years of accumulated knowledge of CEA in the MBE growth of HgCdTe for InfraRed detection applications. Despite this strong background, the growth process has to be adapted to fulfil the topological insulator requirements. In this quest, two main issues have been addressed. The first one is related to the large Hg desorption rate and the second deals with the adaptation of the existing growth process of micrometer-thick HgCdTe layers to nanometer-thick HgTe layers having sharp interfaces and no bulk conduction. To address these issues, the control and characterization of crystal quality, tensile strain and so HgTe thickness, interface roughness and intermixing are of main importance.

The development and improvement of this process are the contents of this Chapter. In a first part, we will explain how to adapt the HgCdTe growth process originally developed for InfraRed detection application to HgTe topological insulators. In a second part, we will detail the topological insulator growth issues and describe

the critical points such as the chemical composition, the tensile strain and the quality of the interfaces. Detailed and complementary material characterizations will be presented to confirm these aspects and demonstrate that the growth process enables structures fulfilling all the topological insulator requirements to be successfully obtained. Finally, the last part will focus on the optimization of the growth temperature. Evolution with substrate temperature of parameters such as surface morphology, density of bulk defects as well as interdiffusion is reported and gives insights to improve material quality.

In this Chapter, numerous material characterization techniques are used. To facilitate the reading, principles of the most commonly used techniques are reported in Appendix A. Only Medium Energy Ion Scattering (MEIS) and specific Transmission Electronic Microscopy (TEM) techniques, which are not of common use, will be detailed in the main text.

2.1 Molecular Beam Epitaxy growth of HgTe/CdTe topological insulator structures

2.1.1 MBE principle

Molecular Beam Epitaxy (MBE) corresponds to an out-of-equilibrium growth process leading to the formation of a crystalline film on top of a single crystal substrate. Figure 2.1 schematically represents the MBE chamber characterized by a ultra high vacuum of about 10^{-10} mbar. By heating the effusion cells, flux of atomic species are obtained by thermal evaporation or sublimation. These fluxes Φ are indeed easily and precisely controlled by the temperature and the geometry of the sources [Mil82]:

$$\Phi \sim \frac{P_s}{\sqrt{2\pi MRT}} \frac{A}{\pi r^2} \tag{2.1}$$

where P_s is the saturated vapor pressure of the atoms at the cell temperature, M is the molar mass, R the perfect gas constant, A the cell area and r the distance between the substrate and the effusion cell.

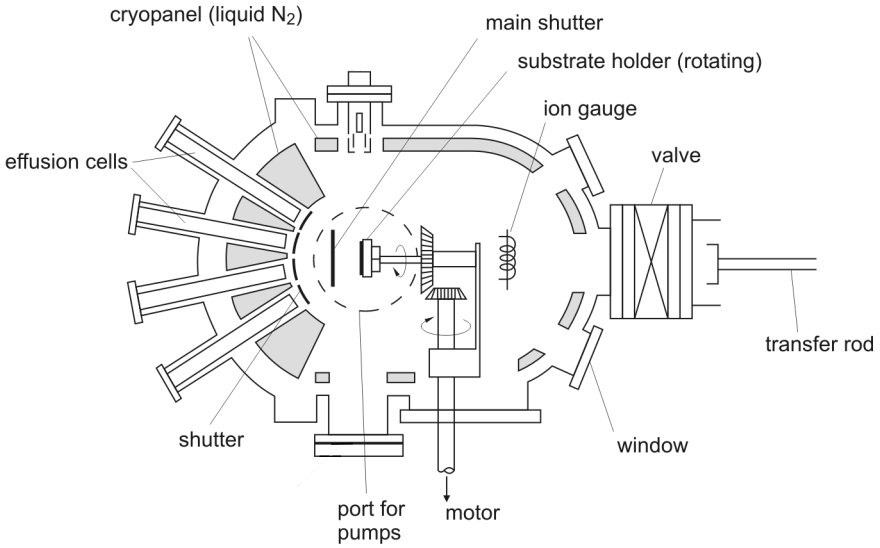

Figure 2.1 – *Schematic representation of the Molecular Beam Epitaxy chamber. Adapted from [IL09].*

These atomic or molecular fluxes are then reaching the substrate surface without interacting with each

other and the growth is initiated by the reaction of these fluxes with the crystalline substrate surface. Fig. 2.2 illustrates the different possible atom behaviors when reaching the substrate surface. These atoms, also called adatoms, are immediately adsorbed. They can then either diffuse and create clusters (nucleus) which are the basis for atomic layer growth, or be desorbed. Their behavior is actually governed by the energy competition between all these scenarios.

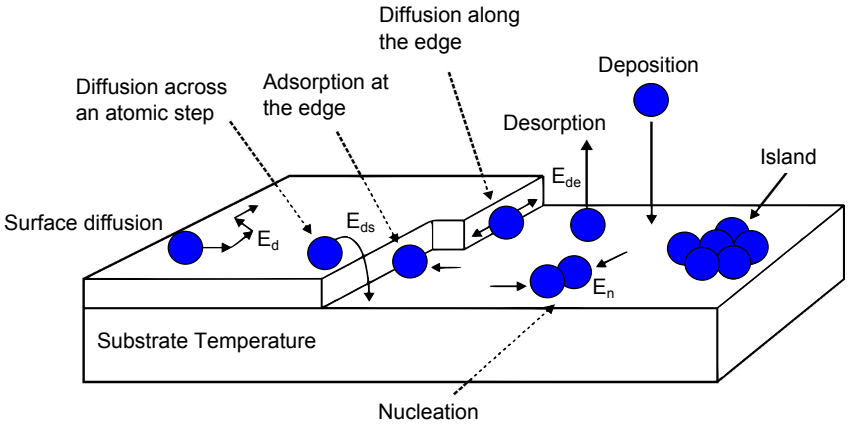

Figure 2.2 – *The different behaviors of the adatoms at the substrate surface. They can either diffuse to step edges, form nucleus, or be desorbed.*

In the field of thin film growth, the MBE technique is the most adapted. Its low growth rate (in the range of 1μm/h) associated with low growth temperatures (usually between 300°C and 600°C) are favorable for the controlled growth of heterostructures with sharp interfaces. Moreover, as the effusion cells can be closed by shutters which are individually driven, abrupt transitions from one material to another are possible, promoting interface sharpness.

In this study, MBE growth of HgTe/CdTe structures is studied. The sole presence of Hg makes the growth process more complicated due to its high desorption rate and especially requires the development of a very low temperature ($\leq$ 200 °C) growth process. The details of the developed growth process are explained thereafter.

2.1.2 MBE for InfraRed detection applications

The growth of HgCdTe materials is mastered at CEA-LETI thanks to the strong skills developed during the last thirty years for InfraRed detection applications [FMP82] [MOCGP88]. A lot of studies have been performed concerning substrate orientation, substrate preparation, growth temperature, the influence of the Hg flux in comparison with Cd and Te fluxes [MOCGP88], ... Obviously, this is a non-exhaustive list of the growth parameters that have been tested and optimized. Nowadays, reliable HgCdTe layers with thicknesses of several micrometers are grown on CdZnTe substrates [FZH+00] and provide the foundations of InfraRed detectors.

2.1.3 HgTe growth process

HgTe layers are grown in a Riber (Bezons, France) 32P chamber equipped with individual cells for Hg, Cd, Te, and CdTe. The substrates used are CdTe (100) (Nikko, Acrotec Japan), but some growth are also performed on CdZnTe(211)B, which is the conventional template for Infrared applications of HgCdTe alloys. (100) direction is here favored to simplify the material characterization especially concerning the strain estimation but also to facilitate the understanding of the electronic transport measurements. The choice of CdTe substrates is dictated by the tensile strain requirement for HgTe.

To grow nanometer scale thin films with sharp interfaces and high crystal quality, the growth rate is decreased down to 1.0 monolayer/s which is around three times less important than for HgCdTe layers used for InfraRed applications. Note that the growth rate is set by the Te flux. The Hg/Te ratio is taken in excess of 1000/1 to compensate for the low sticking coefficient of Hg in regards of that of Te and the growth temperature is considered in the range of 140 to 165°C . In this temperature range, wide terraces are generated and the growth mode is 2D, also called Franck van der Merwe mode, as illustrated in Fig. 2.3. The adatoms condensate on the crystalline substrate to form a first monolayer initiating a layer by layer growth. Moreover, with such low growth temperatures, the interdiffusion is expected not to deteriorate the interface sharpness.

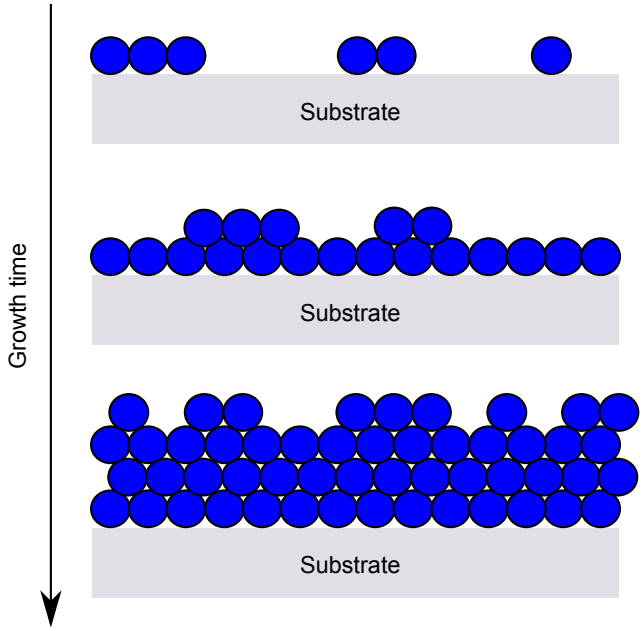

Figure 2.3 – *Franck van der Merwe layer by layer growth mode.*

Figure 2.4 displays the two different structures that have been grown: HgTe on top of CdTe and HgTe embedded between two $Hg_{0.3}Cd_{0.7}Te$ barriers on a CdTe substrate. The first structure has been dedicated to material characterization and optimization only, whereas the second one has been designed and extensively used for the electronic transport measurements. The addition of HgCdTe barriers enables HgTe top topological surface states to be effectively protected against Hg desorption and also to symmetrize the structure. Note that the growth of the whole stack but the buffer layer is done at the same temperature.

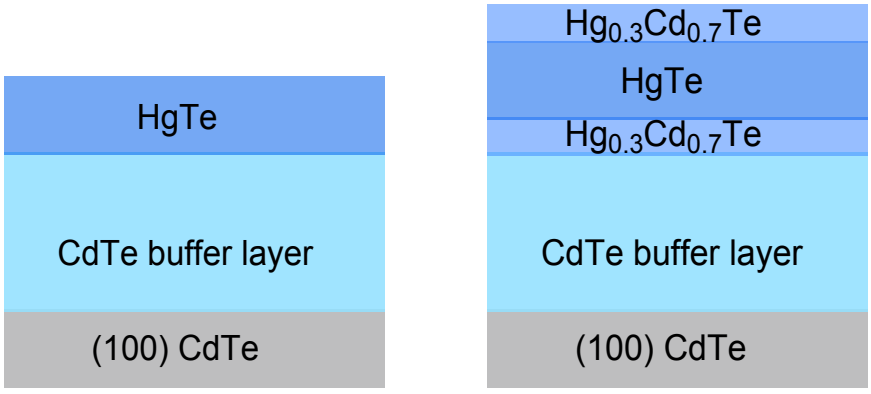

Figure 2.4 – *The two topological structures.*

Further explanations about the growth process and its improvements [BTB+14] constitute the contents of the following subsections. Each part of the stack is individually introduced and justified.

2.1.3.1 Preparation of CdTe substrates

After being polished, the substrates are chemically treated to remove the remaining oxide and the atomic layers damaged by the polishing process. Once in the growth chamber, the first step is to heat the substrate up to 350°C. The objective of this thermal rise is to thermally activate surface atomic mobility to obtain 2D terraces. Residual oxidation is also removed during this step.

2.1.3.2 Incorporation of a CdTe buffer layer

The incorporation of a buffer layer, between the substrate and the HgTe layer, is a solution to move the topological interface away from the substrate surface in order to compensate for the substrate defects and have a smooth surface ready for epitaxial growth of topological insulator layers. The buffer growth is considered using a CdTe effusion cell and its growth conditions need to be optimized to produce a very smooth surface. In this part, we will discuss how the growth of a buffer layer with the adapted growth conditions permits a significant improvement of the entire growth process.

Atomic Force Microscopy (AFM) (see A.3.1 for technical details) image is reported in Fig. 2.5 illustrating the presence of pyramidal-shape defects on the top surface of HgTe layers grown on CdTe substrates with a buffer layer of CdTe.

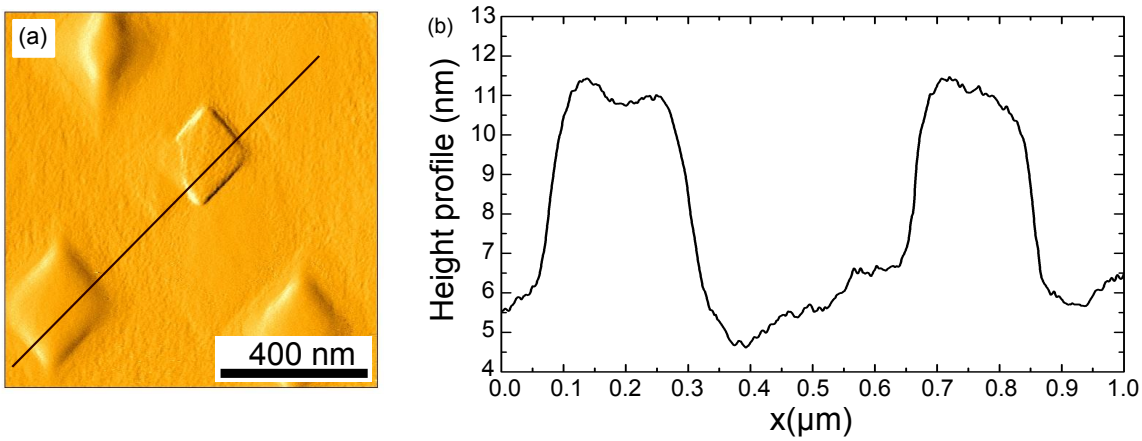

Figure 2.5 – *(a) 1µm x 1µm Atomic Force Microscopy (AFM) amplitude image of a HgTe layer grown on (100) CdTe substrate at 140°C. (b) Height profile of the defects.*

These pyramidal hillocks are about 5 nm high and spread over few hundreds of nanometers. Their distribution is quite homogeneous on the whole surface. Such hillocks are well-known to occur in II-VI compound growth and have been identified to be induced from inappropriate growth conditions [MOCGP88] [KS88] [HMY+89]. II-VI material growth is indeed known to be very sensitive to the flux ratio between the II and VI elements. The surface reconstruction and morphology are particularly impacted. In the particular case of CdTe, the surface reconstruction is c(2x2) when the growth is performed under Cd excess, while c(2x1) is reported for Te excess [BWTS86] [WBW+91]. Moreover, literature reports reflection high energy electron diffraction studies highlighting the difference of roughness between CdTe layers grown under either Cd or Te excess. Particularly, Lentz *et al.* [LPMM89] demonstrated high densities of pyramidal hillocks on the surface of CdTe layers grown

under Te excess whereas this phenomenon was negligible under Cd excess. Similar observations were also made concerning ZnTe where the highest quality material was obtained for Zn excess conditions [FAB+88]. From these studies, we conclude that the major way of improving our buffer layer is to apply the correct flux ratio between Cd and Te elements. The growth of a 200 nm-thick CdTe buffer layer is now performed under Cd excess. More practically speaking, the growth starts with the opening of the CdTe shutter and the Cd effusion cell runs the excess Cd flux.

Figure 2.6 (c)-(f) displays AFM images with the evolution of the surface morphology during the whole growth process from the ex-situ chemical treatment to the growth of the HgCdTe cap layer. These images clearly evidence the absence of pyramidal hillocks when the growth of CdTe buffer layer is performed in appropriate conditions. Moreover, the associated Root-Mean-Square (RMS) values are reported in Table 2.1. Note that after the polishing process, the substrate exhibits a roughness of about 0.9 nm. After an ex-situ chemical treatment and an in-situ thermal annealing, the RMS is considerably reduced down to 0.4 nm. This step is then directly followed by the buffer layer growth. Surface morphology of the buffer layer is reported in Fig. 2.6(c) and appears to be very flat with a roughness of only 0.2 nm. The growth of the HgTe layer slightly increases the RMS value up to the monolayer scale.

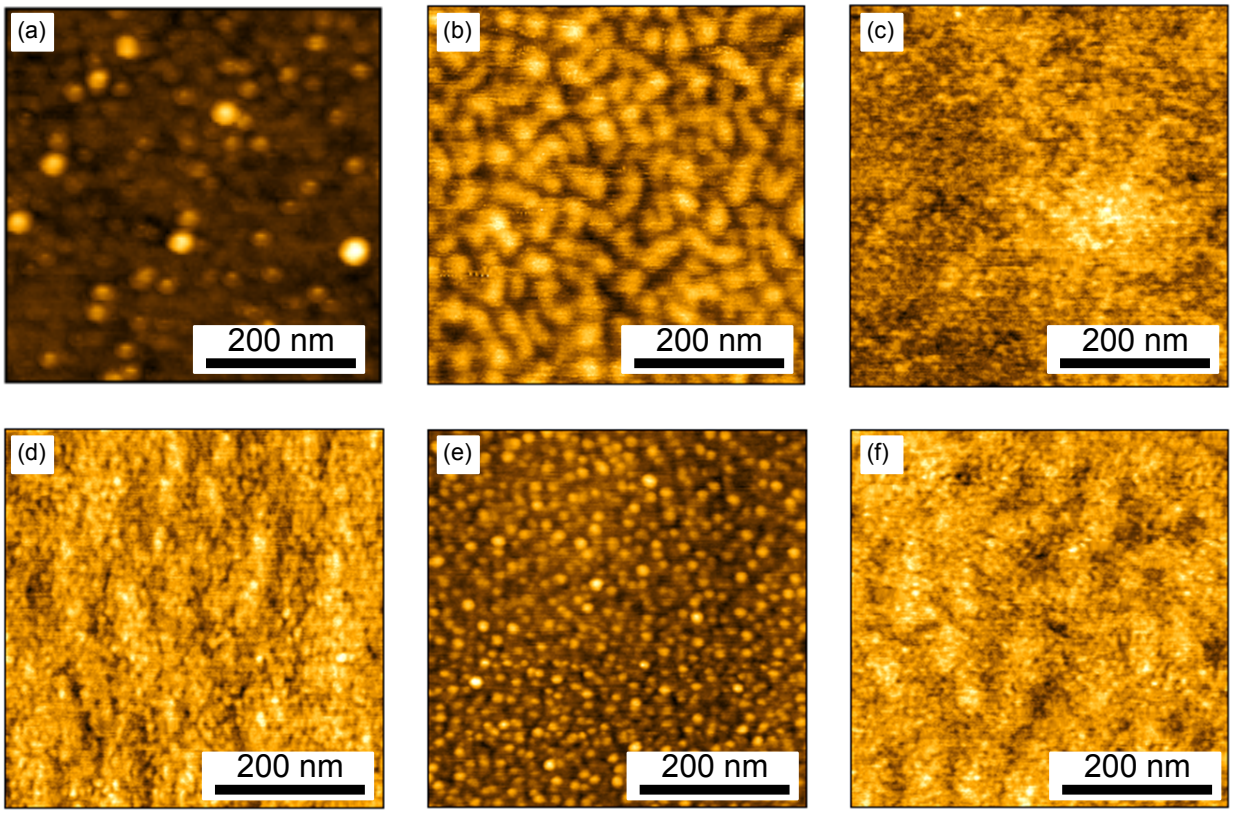

Figure 2.6 – *500 nm x 500 nm AFM images of (a) CdTe substrate before chemical treatment (Z-scale: 10.1 nm), (b) CdTe substrate after chemical treatment (Z-scale: 2.1 nm), (c) CdTe buffer layer (Z-scale: 1.2 nm), (d) HgCdTe barrier (Z-scale: 1.8 nm), (e) HgTe layer (Z-scale: 3.2 nm) grown at 165°C, (f) HgCdTe cap layer (Z-scale: 1.6 nm).*

The growth of a CdTe buffer layer in the appropriate growth conditions is thus an important step to get rid of most of the substrate surface defects and ensure the growth of the HgTe topological layer on a smoother surface.

Layer	CdTe substrate	CdTe substrate + wet etching	CdTe buffer (200 nm)	HgCdTe bottom barrier (30 nm)	HgTe (25 nm)	HgCdTe top barrier (30 nm)
Roughness (RMS) (nm)	0.9	0.4	0.2	0.2	0.4	0.2

Table 2.1 – *Roughness evolution along the substrate preparation and during the growth process.*

2.1.3.3 Addition of HgCdTe barriers

In order to improve HgTe top surface electronic properties, the growth of an additional barrier layer is considered as a protection against Hg desorption. $Hg_{0.3}Cd_{0.7}Te$ topologically trivial ternary alloy has been chosen as a capping layer because of its closer growth temperature to HgTe, compared to CdTe. Similar barrier layer is also grown underneath the HgTe layer to symmetrize the structure. With a thickness of 30 nm, $Hg_{0.3}Cd_{0.7}Te$ barriers are fully strained and are thick enough to effectively protect the HgTe top surface.

Note that the introduction of these barriers was a huge improvement of the growth process as it enabled the first observation of quantum Hall effect signatures in our structures when performing low temperature electronic transport measurements.

2.2 Topological insulator growth issues

The objective of this section is to discuss more specifically the growth process adjustments needed to fulfil the HgTe topological insulator requirements. The rise of surface metallic states at the HgTe interfaces associated with a bulk gap opening can only occur if:

1. the chemical composition is well controlled for the band structure to be inverted. Chemical composition and its monitoring are addressed in this section using the association of Scanning Transmission Electron Microscope (STEM) and Energy Dispersive X-rays spectroscopy (EDX).

2. HgTe is tensile strained to open a bulk gap. Demonstration and estimation of the tensile strain experienced by HgTe are provided through several material characterizations. Tensile strain as well as crystal quality and thickness of the HgTe layer are probed thanks to High Resolution X-Rays Diffraction (HRXRD). The experimental value of the critical thickness for plastic relaxation is also accessible using this technique and is directly compared to the value extracted from calculations using Matthews equation [MB74] (see Chapter 1 1.1.5.2). Another original technique, Medium Energy Ion Scattering (MEIS), is used to extract and confirm the strain value close to the HgTe/CdTe interface. Moreover, using Nanobeam Precession Electron Diffraction (NPED) TEM technique, a strain profile of the whole stack is accessible.

These two points are necessary conditions for HgTe to become a topological insulator. Nevertheless, in this Chapter, we will also focus on another important aspect which is the perfection of the interfaces. This last point is crucial to keep intact and even enhance the intrinsic electronic properties of the topological surface states. Roughness of the top HgTe surface in uncapped structures is especially discussed in regards of different end-of-growth in-situ surface treatments. High Resolution STEM (HRSTEM) has also been used to estimate both top and bottom interface widths of capped structures.

These three necessary conditions and the associated characterizations are now addressed and discussed individually with further details.

2.2.1 Inverted band structure: control of the chemical composition

In the case of $Hg_{1-x}Cd_xTe$ materials, the inverted band structure is directly related to the Cd composition x as previously reported in Chapter 1. When considering the growth of HgTe layer, a particular attention needs to be paid to the control of the chemical composition. Indeed, extra and non voluntary deposition of Cd due to shutter or cryopanel outgasing can significantly modify the energy gap value.

The chemical composition is studied using the association of STEM and EDX techniques. Precise chemical profiles are obtained and give access to a monitoring of Cd and Hg composition in the whole structure. For more details about STEM and EDX measurements, the reader can refer to A.3.2.2.

EDX analysis has been performed on a FEI Osiris microscope at 80 kV. Such low voltage was used to prevent from damaging the HgTe layers by charging effect from the electron beam. The sample preparation was performed using a gallium-ion thinning in a focused-ion-beam microscope resulting in about 50 nm-thick slices of material. Extraction of the chemical composition was done using a Cliff-Lorimer ratio method. Further details about this method can be found in [CL75].

Preserving the HgTe layer from Cd contamination was not an easy task as it can be seen in Fig. 2.7 where the results of STEM-EDX analysis on a 25 nm-thick HgTe layer are presented. In the chemical mapping of Fig. 2.7(a), Hg atoms are represented by the green color while Cd ones are in red. Good contrast allows to clearly distinguish HgTe, HgCdTe barriers and CdTe buffer layer. The extracted depth profiles of Hg, Cd and Te atoms are presented in Fig. 2.7(b). Such profiles allow the extraction of both thicknesses and compositions for each layer. A high Cd concentration is reported in the whole HgTe layer with x value ranging from 12% to 44% and is especially visible through the orange thin layer in the middle of HgTe. The black dashed line in Fig. 2.7 (b) illustrates the limit between normal and inverted band structure evidencing that with such high value of x this part of the "HgTe" layer is no more topological as it is characterized by a positive energy gap and thus a normal-ordering band structure. Nevertheless, it is complicated to estimate the thickness of the remaining topological layer due to the atomic composition resolution of this EDX measurement. The atomic composition of Te is indeed underestimated at $\approx$ 46.5 % in the whole structure instead of the expected 50 %, thus suggesting a resolution of $\approx$ 3.5 % at best.

Therefore, peculiar attention must be paid to the control of the cadmium flux during growth to avoid the HgTe layer to transform into a topologically trivial HgCdTe layer. More than just the usual shutter closing, an additional precaution is taken with a decrease of the Cd effusion cell power during the HgTe growth to prevent the shutter and the cryopanel from outgasing when heated by the cell. Moreover, the shutters are regularly replaced. Figure 2.8(a) displays a chemical mapping of a stack made of a 100 nm-thick HgTe layer surrounded by 30 nm-thick $Hg_{0.3}Cd_{0.7}Te$ barriers. The associated depth profiles of Hg, Cd and Te atoms are presented in Fig. 2.8(b). The thickness of the first barrier is estimated to 30 $\pm$ 1 nm with a Cd composition x of about 0.70 $\pm$ 0.02 (35 $\pm$ 1 %). These values very closely match the expected growth parameters. Moreover, the HgTe layer appears to be almost free of Cd within barely 2%. This value can be neglected in regards to the atomic composition resolution.

From these observations, we can conclude that, provided a proper use of the Cd source, chemical composition can be well-controlled and that HgTe layers can be considered as free of Cd. This is confirming the HgTe inverted

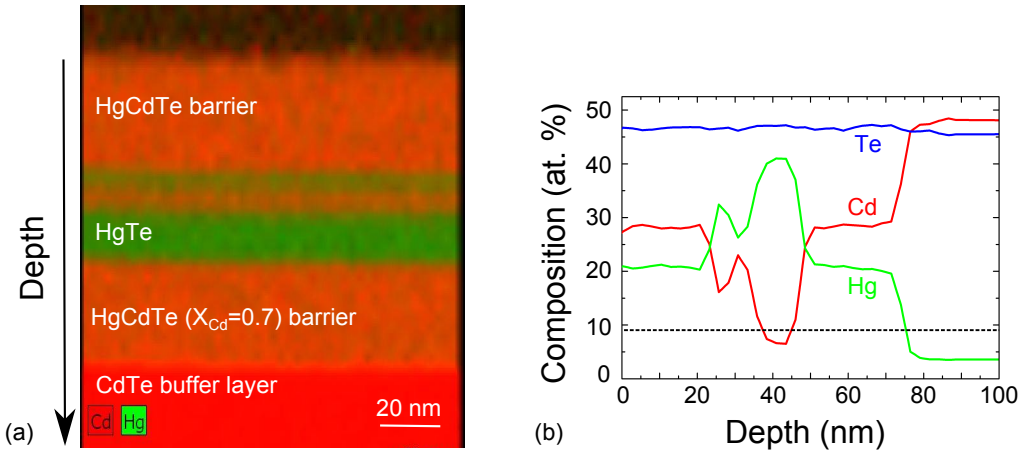

Figure 2.7 – *(a) Scanning Transmission Electron Microscopy - Energy Dispersive X-rays spectroscopy (STEM-EDX) mapping with Cd, Hg in red and green respectively. (b) Extracted quantitative depth profiles for Cd (red), Hg (green) and Te (blue). The horizontal black dashed line indicates the Cd composition for which the HgCdTe band structure transits from inverted to normal.*

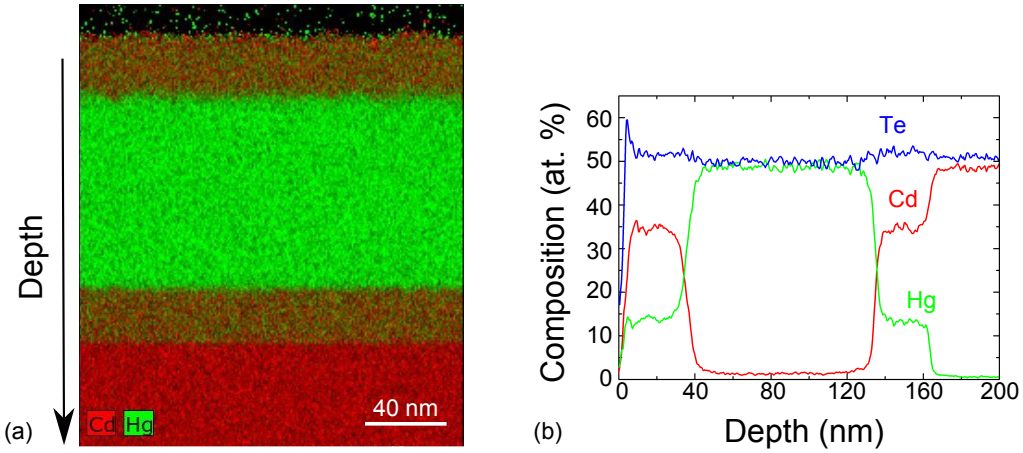

Figure 2.8 – *(a) STEM-EDX mapping with Cd and Hg in red and green, respectively. (b) Extracted quantitative depth profiles for Cd (red), Hg (green), and Te (blue).*

band structure which is the first requirement to obtain a topological insulator.

2.2.2 Bulk gap opening from tensile strain

As already noticed in Chapter 1, the HgTe band structure is initially semi-metallic. However, when tensile strained, HgTe opens a strain bulk gap whose value is directly proportional to the in-plane strain deformation $\epsilon_{//}$. Calculation of both in-plane ($\epsilon_{//} = 0.31\%$) and out-of-plane ($\epsilon_{\perp} = -0.41\%$) tensile strain deformations and the associated strain gap value ($E_s = 21.5$ meV) have been previously reported in Chapter 1 (see 1.1.5). In this section, we will experimentally complete this former strain analysis by performing several material characterizations. High resolution X-rays diffraction, medium energy ion scattering and transmission electron microscopy are used and complement each other to provide an accurate estimation of the tensile strain in our structures. One must realize that, for all these characterization techniques, the main difficulty lies in the measurement of such low strain values. Moreover, it is important to understand that high resolution X-rays diffraction enables the HgTe out-of-plane lattice parameter c_{fs} to be directly measured. The determination of $\epsilon_{\perp}$ is then possible knowing c_f. On the contrary, the measurement of c_{fs} is made relative to the CdTe substrate lattice parameter c_s for the two other techniques. It is therefore convenient to introduce the out-of-plane lattice mismatch directly representing the lattice parameter difference between the strained HgTe and the CdTe expressed as [BR96]:

$$\frac{\Delta c}{c} = \frac{c_{fs} - c_s}{c_s} = (1 + \frac{2C_{12}}{C_{11}})f \tag{2.2}$$

With $\frac{\Delta c}{c}$ measurement, c_{fs} and consequently $\epsilon_{\perp}$ can be directly determined. By considering the relation $\epsilon_{\perp} = -\frac{2C_{12}}{C_{11}}\epsilon_{//}$, the strain gap E_s can be expressed as $E_s = 2|b(1 + \frac{C_{11}}{2C_{12}})\epsilon_{\perp}|$ and be experimentally evaluated. The stiffness constants C_{12} and C_{11} are equal to 36.6 GPa and 53.6 GPa for HgTe at 300 K, respectively.

2.2.2.1 Using HRXRD

HRXRD is used to experimentally characterize the tensile strain experienced by HgTe by determining the out-of-plane deformation but also by estimating the critical thickness for plastic relaxation. The reader can refer to A.1.1 for details about setup and measurements.

2.2.2.1.1 Out-of-plane deformation (422) 2θ-ω scans are reported in Fig. 2.9 for a 100 nm-thick HgTe layer grown on (211)B $Cd_{1-x}Zn_xTe$ ($x = 4.1\%$) and pure (211)B CdTe substrates. In both cases, the HgTe layer is expected to experience tensile strain with mismatch of -0.07% and -0.31%, respectively. The two scans are dominated by the substrate peak. One can notice that Bragg angle associated to the substrate is shifted towards lower values when the zinc fraction decreases because of the corresponding increase in the substrate lattice parameter. As a consequence, the HgTe peak, which is much broader because of the much lower thickness of material, is found to be shifted towards larger angles when deposited on a substrate with larger lattice parameter. This shift of the HgTe peak toward larger angle is directly illustrating the out-of-plane deformation caused by the tensile strain which is maximum with the CdTe substrate ($c(HgTe/CdTe) < c(HgTe/CdZnTe)$).

To estimate this out-of-plane deformation $\epsilon_{\perp}$, we consider a 100 nm-thick HgTe layer grown on (100) CdTe substrate. The determination of the deformation is indeed straightforward in this crystallographic direction. The corresponding (400) HRXRD 2θ-ω scan is presented in the inset of Fig. 2.9. Using Bragg's law (eq. A.1) and the substrate and HgTe peak positions, one can estimate the out-of-plane lattice parameter c values which are reported in Table 2.2. The out-of-plane lattice mismatch $\frac{\Delta c}{c}$ and the out-of-plane deformation $\epsilon_{\perp} = \frac{c_{fs} - c_f}{c_f}$ can thus be determined. Finally, the strain gap value E_s is estimated to be about 23.9 meV. This result is consistent with the expected value (21.5 meV).

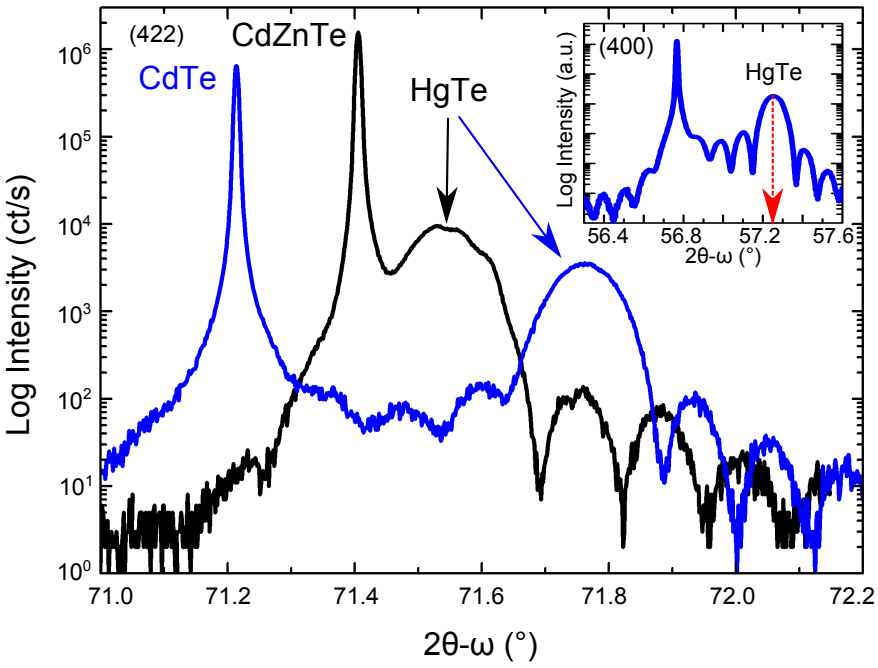

Figure 2.9 – *(422) High Resolution X-Rays Diffraction(HRXRD) 2θ-ω scan of 100 nm-thick HgTe grown on (211)B CdZnTe (black line) and (211)B CdTe (blue line). Inset: (400) HRXRD 2θ-ω scan of a 100 nm-thick HgTe grown on (100) CdTe.*

c_s(Å)	6.4818
c_{fs} (Å)	6.4315
$\frac{\Delta c}{c}$(%)	-0.77
$\epsilon_\perp$(%)	- 0.46
E_s (meV)	23.9

Table 2.2 – *Estimation of the out-of-plane deformation $\epsilon_\perp$ and of the strain energy gap E_s for a growth on (100) CdTe substrate using HRXRD.*

From this HRXRD strain study, we can conclude that:

- tensile strain has been demonstrated for a 100 nm-thick HgTe layer. This sole result rules out the critical thickness of 45 nm previously determined from Matthews-Blakeslee model (see Chapter 1 1.1.5.2).
- the choice of CdTe as a substrate allows to increase the tensile strain, compared to $Cd_{1-x}Zn_xTe$ (x=4.1%).
- HRXRD investigations of HgTe structure lead to the estimation of c_{fs}, and thus to the experimental determination of the out-of-plane strain deformation $\epsilon_\perp = -0.46\%$ and the associated strain gap $E_s = 23.9$ meV. These values are in full agreement with the calculations of Chapter 1 (see 1.1.5)($\epsilon_\perp = -0.41\%$ and $E_s = 21.5$ meV).

Additional HRXRD measurements on thicker samples are now presented and discussed to experimentally probe the limit for plastic relaxation.

2.2.2.1.2 Critical thickness for relaxation Five thin films based on HgTe layers grown at 140 °C on CdTe (100) substrates with increasing thickness are considered. Figure 2.10 shows the corresponding (400) 2θ-ω scans (thick lines) and associated simulations (thin red lines). CdTe and HgTe peaks are well-defined for HgTe

thickness larger than 13 nm and their positions directly provide their out-of-plane lattice parameters. The HgTe peak is broader than the CdTe one due to the large difference of thickness between the layer and the substrate. These two peaks are surrounded by Pendelössung fringes which act as a probe of the crystalline quality. Such fringes are resulting from interferences generated by the X-rays reflected on the layer top surface and the X-rays reflected on the layer/substrate interface. The HgTe thickness is obtained by fitting the Pendelössung fringes frequency using the X'pert Epitaxy software with a precision of the nanometer order. Note that a small and fixed amount of strain has been added to the fit model to reproduce the HgTe peak position and account for the slightly larger experimental value of $\epsilon_\perp$ reported just before.

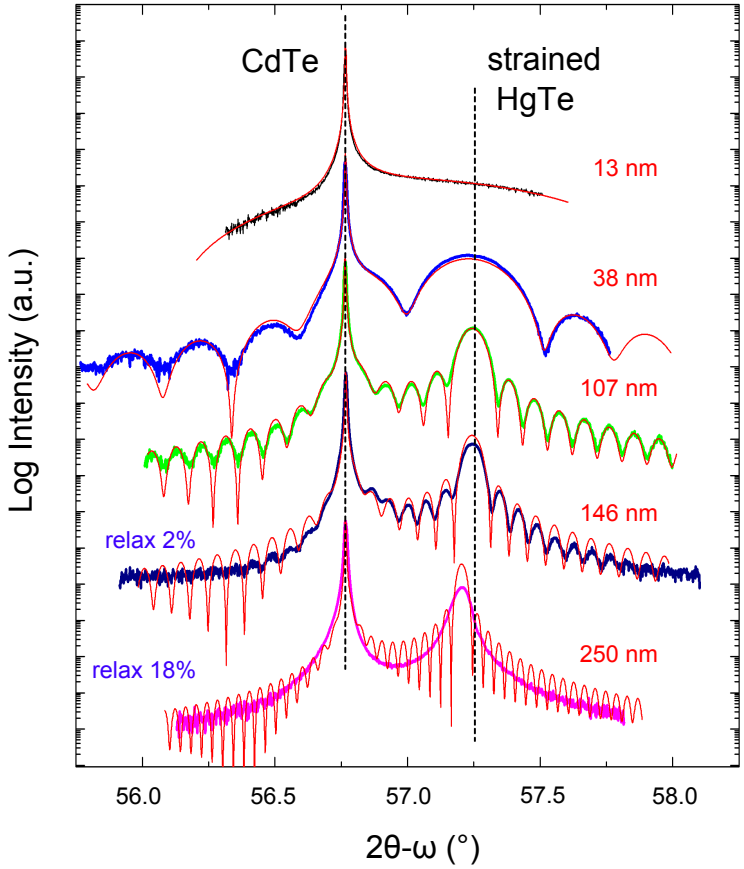

Figure 2.10 – *(400) HRXRD 2θ-ω scans (thick lines) and associated simulations (thin red lines) for five HgTe/CdTe(100) samples with various thicknesses. The adjusted thickness is given in each case on the right-hand side, while the amount of relaxation introduced in the model is given on the left-hand side, when needed. The vertical dashed lines are a guide to the eye for the expected peak position for the CdTe substrate and the fully strained HgTe layer.*

For samples with HgTe thickness typically lower than 25 nm, accurate determination of film thickness is not possible because of the large values of the Pendellösung fringe period, which is inversely proportional to the HgTe thickness. For samples with HgTe thickness in the range of 25 nm to about 130 nm, excellent agreement is found between simulation and experiment for a fully strained HgTe model.

One can notice that for 146 nm- and 250 nm- thick layers, the HgTe peak is shifted toward lower angles. This means its out-of plane lattice parameter is increasing. Moreover, the fringe amplitude is damped and is no more matching the fit model. Such intensity damping can be explained by the generation of extended defects, which is consistent with a beginning of relaxation and the appearance of misfit dislocations. The combination of these two effects indicates that the HgTe layer starts to relax. The amount of relaxation is estimated through fitting of the peak position and is given in the left-hand side of Fig. 2.10. From this study, we can conclude that HgTe

layers are fully strained up to about 140 nm. Furthermore, the relaxation process appears to be progressive with only 18% of relaxation for a sample 100 nm thicker than the critical thickness. Such a continuous relaxation can be explained by the soft elastic properties of HgTe and possible competing relaxation mechanisms.

Complementary measurements using Reciprocal Space Mapping (RSM) [LBG+97] are now presented to complete this analysis of strain and critical thickness for plastic relaxation.

2.2.2.1.3 Reciprocal Space Mapping Details about RSM principle and measurement conditions are given in Appendix A.1.2.

Figure 2.11 shows RSM for the (511) direction in the case of a 50 nm- (Fig. 2.11(a)) and a 146 nm-thick HgTe layer (Figure 2.11(b)). Q_x and Q_y are reciprocal-space coordinates, being directly proportional to the in-plane and out-of-plane lattice parameters, respectively. For the two samples investigated, the HgTe diffraction peak and corresponding Pendellösung fringes are located at the same Q_x value than the substrate. This implies that the in-plane lattice constant of HgTe perfectly matches that of the CdTe substrate. This provides direct proof that HgTe thin film is coherently strained on its substrate. For clear graphical interpretation of the RSM, the unstrained line is indicated by a thick red line in each figure. A fully relaxed HgTe layer would exhibit a diffraction spot along this line. It has to be noted that, for the 146 nm-thick HgTe layer, the diffraction spot appears to be greatly broadened compared to that of the 50 nm-thick sample. This significant broadening is mainly attributed to the substrate quality as CdTe peak is also much broader than for the previous sample. Nevertheless, the width of the HgTe peak appears larger than that of the CdTe substrate, thus suggesting the presence of extended defects. This width is also associated with a slight asymmetry of the peak for large values of Q_x, i.e., in the direction of the strain free line. These characteristics are most likely an indication that the HgTe layer approaches the onset for plastic relaxation, as already evidenced by the (400) $2\theta - \omega$ scan previously reported in Fig. 2.10.

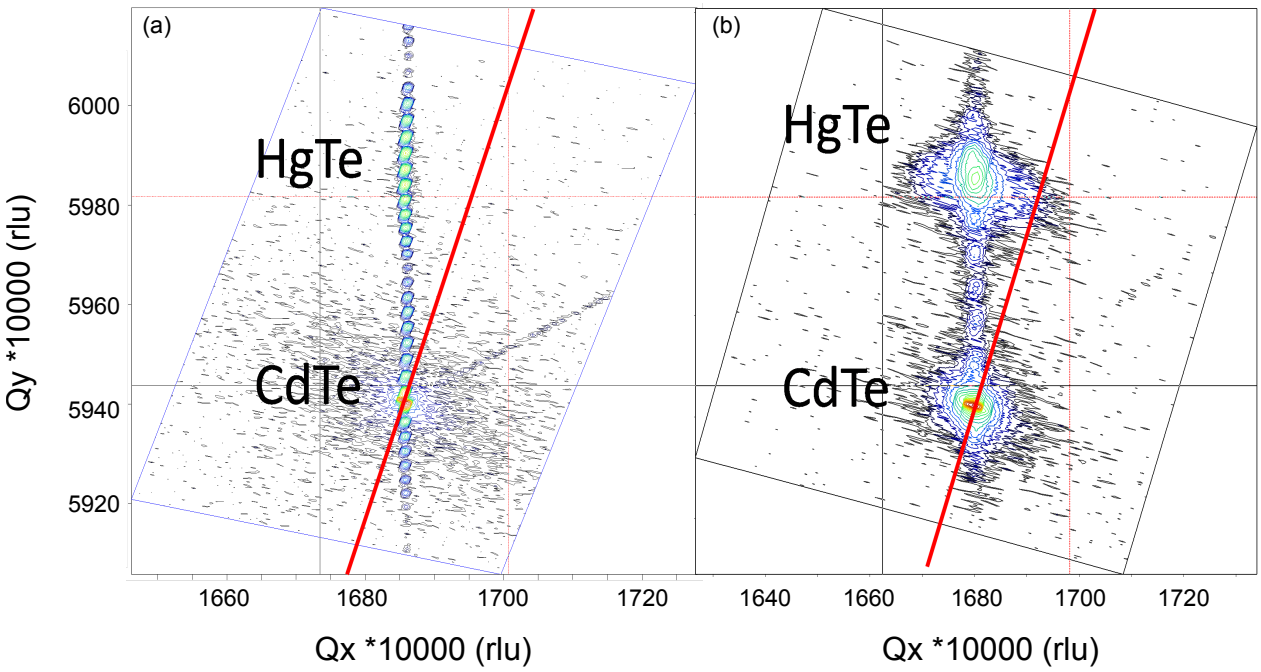

Figure 2.11 – *Reciprocal-space maps of the (511) reflection for two HgTe/CdTe(100) samples with HgTe thickness of 50 nm (a) and 146 nm (b). The CdTe and HgTe contributions are marked on the figures, and a straight red line is drawn to represent the unstrained material line.*

Combination of conventional HRXRD and RSM measurements has just demonstrated that the structures

are fully strained up to around 140 nm where some indications of plastic relaxation mechanism are reported.

Note that this estimated value of the critical thickness for plastic relaxation is more than three times larger than the one determined using the Matthews and Blakeslee model. Such kind of discrepancy have often been reported in the literature [MBVdV+87] [DJ87]. Several reasons are suitable to explain this shift. The first reason is probably the misfit dislocation generation mechanism. Matthews and Blakeslee model only considers the spreading of pre-existing dislocations within the substrates whereas other models include the contribution of dislocations generated by a half-loop mechanism on a free surface [PB85]. This last model has also been used for our structures and give overestimated values in the range of the μm. A second reason might be that these models do not take into account the difference between tensile and compressive strains. Experimental studies demonstrate the difference of relaxation mechanism for these two kinds of strain [BBP+13]. Many other parameters can also explain the shift between the experimental and the calculated values of the critical thickness such as other relaxation mechanisms or even the apparition of other families of dislocations.

HRXRD has just been used for the determination of tensile strain in our HgTe structures. However, this technique presents some limitations:

- thickness and accurate strain determination is difficult for layer thinner than 25 nm.
- strain estimation corresponds to an average over the whole layer thickness.
- only the crystalline phases are characterized.

These two first points prevent a complete and precise characterization of strain in our structures. Determination of the strain profile along a whole stack would be of great interest, especially to check the strain at or close to the interfaces and also to verify its homogeneity in each layer.

In this thought, MEIS has been performed and the results are presented in the next paragraph. This technique gives structural data on very thin layers ($\leq$ 10 nm for HgTe) and is able to probe both amorphous and crystalline phases. MEIS is thus used where HRXRD is no more reliable and should enable to extract strain profile of HgTe layer but also of the HgTe/CdTe interface. However, MEIS has also its own limitations: it is only applicable to very thin layers and has a strain resolution of about 0.1%. With such resolution, strain profile was difficult to obtain. An other type of characterization technique has thus been investigated. Based on TEM diffraction, NPED enables accurate strain profile to be obtained. With this technique, we concentrate on the characterization of capped structures to extract the strain profile of the whole stack and to check the strain symmetry of the barriers as well as the tensile strain homogeneity of HgTe layer.

2.2.2.2 Using Medium Energy Ion Scattering

MEIS is not a common characterization technique. Very similar to Rutherford Backscattering Spectrometry (RBS), this ion beam technique is particular due to its low accelerating voltage. With voltage in the MeV range, RBS enables the study of thick films, whereas with only hundreds of keV, MEIS is focusing on surface effect or very thin layers. In the case of heavy components such as HgTe and CdTe, the thickness of the films must indeed be kept below 10 nm to separate the Hg contribution from the Cd and Te ones to provide a precise analysis of the Hg profile from the top surface to the buried interface.

In this study, He^+ ions are used with an energy of about 200 keV. Being accelerated on the sample surface, the He^+ ions are then backscattered. The energy as well as the angle distribution of the scattered ions are then analysed and enable a chemical and structural analysis to be performed. Being directly related to the mass and to the depth of the target atom, the analysis of the energy of the scattered ions leads to the identification of the

chemical species.

To perform a structural analysis, one needs to consider the so-called blocking configuration To do so, both the incident θ_i and azimuthal θ_a angles (defined in Fig. 2.12(a)), which are determining the direction of propagation of the incident ions, need to be adjusted to send the ions on a given crystallographic direction. Furthermore, the range of scattering angles θ_s is also determined to align the detector with this axis. Figure 2.12(d) reports a mapping of the distribution intensity as a function of θ_a and θ_s. Horizontal lines are evidenced and illustrate the channelling effect (see Fig. 2.12(c)) which occurs when the incident ions are coming parallel to a crystallographic plane and are backscattered too deep in the sample to be able to travel back to the surface and be detected. This mapping also highlights dark circle arcs which lead to the identification of the crystalline directions using the stereographic projection of a (100) face-centered cubic crystal as explained in [Jal12]. With this method [-110] direction is evidenced (see Fig. 2.12(d)) and is considered for the following of this structural study.

The reader can already note that in the last part of this Chapter, MEIS chemical analysis will be used to address the issue of interdiffusion at the HgTe/CdTe interface. In this case, the ion beam will not be oriented along a crystallographic axis but randomly. The red rectangle in Fig. 2.12(d) is an example of good angle conditions to avoid any crystalline axis contribution.

Strain evolution through the whole structure can be extracted from the distribution intensity minima [JPGB+12]. Figure 2.12(b) illustrates the principle of this measurement with a the in-plane lattice parameter, c the out-of-plane lattice parameter and θ_{min} the angle corresponding to a minimum of intensity and so to a given crystallographic direction. Lattice parameters as well as strain value are directly extracted from equations 2.3 and 2.4. It is worth noting that, for strained HgTe layer, $a_{fs} = c_s$ thus eq. 2.4 enables the out-of-plane lattice mismatch $\frac{\Delta c}{c} = \frac{c_{fs}-c_s}{c_s}$ to be determined. The resolution of such analysis is about 0.1% for the strain value.

$$\theta_{min} = arctan(c/a) \tag{2.3}$$

$$\frac{c-a}{a} = tan(\theta_{min}) - 1 \tag{2.4}$$

The measurements have been performed on a 5 nm-thick HgTe layer grown on (100) CdTe with 140 keV He^+ ions. For this energy range, the thickness of HgTe layer must be limited to 7 nm in order to completely resolve the Hg contribution. Indeed, as the scattered ion energy depends on both atomic mass and depth, if the HgTe layer is too thick, the energy from the deepest Hg atoms will become similar to that of the surface Te atoms making it impossible to distinguish between the two elements.

The ion beam angles were adjusted to study the (100) crystalline plane. Figure 2.13(a) reports a mapping of the blocking dip in the [-110] direction with very clear intensity minimum. Hg and Te atoms corresponding to the HgTe layers are well split in energy due to their difference in atomic number. On the other hand, Cd and Te from the buffer layer are not easily distinguishable due to their very close masses. Two arrows indicate the absence of intensity minima for certain energies emphasising the presence of a thin amorphous layer composed of Hg and Te at the surface of the structure. Note that the θ_s values have been compensated to have $\theta_{min} = 45°$ in the CdTe reference ($c = a$) and facilitate the analysis.

Studying the dispersion of θ_{min} from 45 ° over the whole range of energy, using the blocking dip mapping of Fig. 2.13, should lead to the extraction of a strain profile along the whole structure and especially to the analysis of the strain at the interface between HgTe and CdTe. However in our case, with low expected strain value (order of magnitude of 0.4% while the resolution is about 0.1 %) associated with extra intensities appearing at

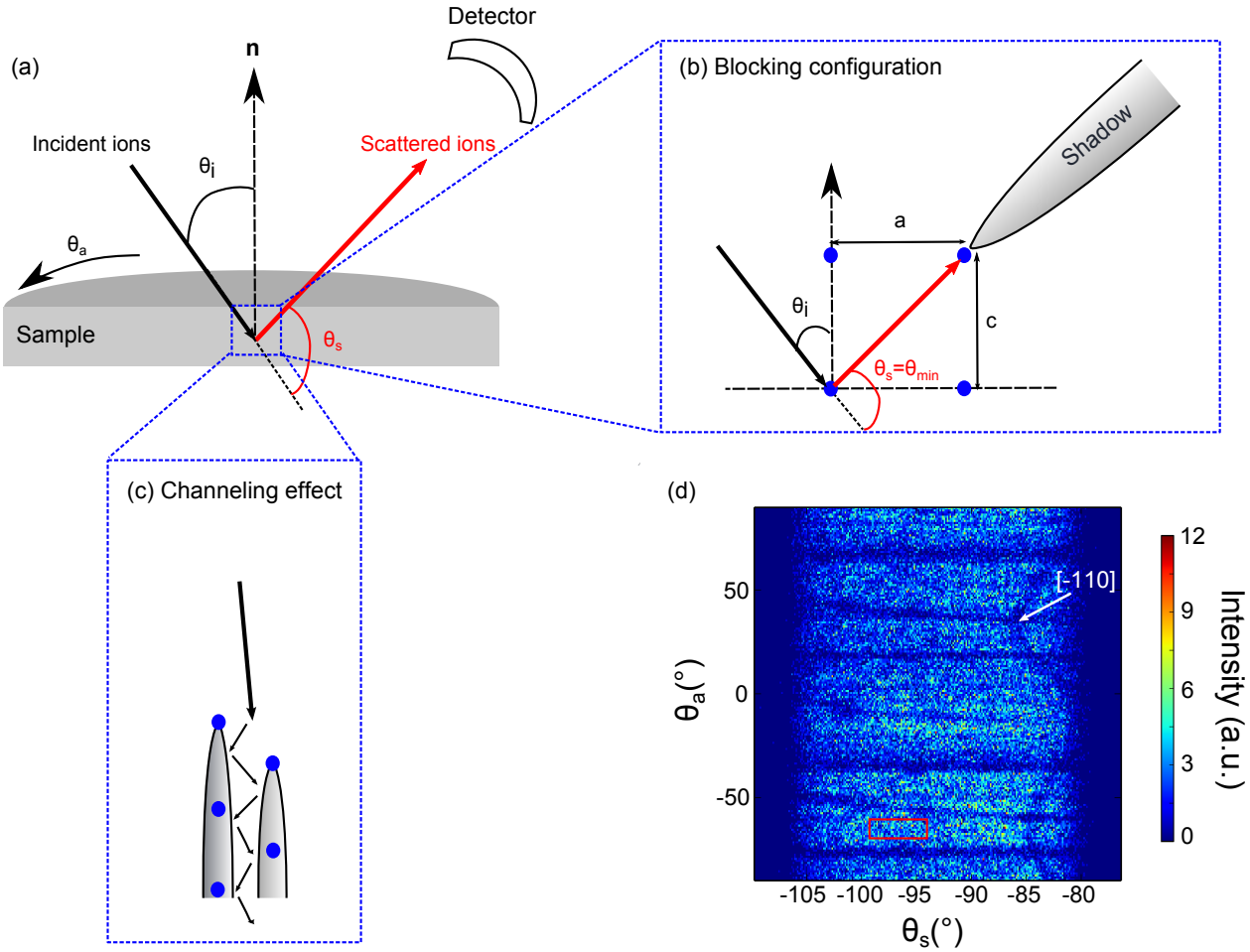

Figure 2.12 – *(a) MEIS experimental setup with θ_i the incident angle and θ_a the azimuthal angle determining the direction of propagation of the ion beam. θ_s is the angle of the scattered ions which are collected in the detector. (b) The blocking configuration appears when the incident ions are sent on a crystallographic direction (atoms represented in blue). For $\theta_s = \theta_{min}$, the scattered ions come in contact with the atoms of the crystallographic network resulting in a loss of intensity in the detector forming dark shadows. The determination of θ_{min} leads to the extraction of the $\frac{c}{a}$ ratio with a the in-plane and c the out-of plane lattice parameters. (c) Channelling effect appears when the incident ions come parallel to a crystallographic plane and are backscattered too deep in the sample. No intensity is detected. (d) Mapping of the He^+ scattered ion intensity as a function of both θ_a and θ_s. Horizontal lines illustrate the channelling effect. [-110] crystallographic direction is evidenced by a white arrow while the red area free of any crystallographic axis can be used for random chemical analysis.*

the dip borders (see Fig. 2.13(a)), the strain profile was not achievable.

Nevertheless, we manage to estimate the strain value by looking at the blocking dip minima position for both Hg and Cd atoms at 132.1 keV and 116.4 keV, respectively. The two associated intensity traces are plotted in Fig. 2.13(b) as a function of θ_s and result from the average over a 0.6 keV energy range. The energy positions corresponding to these traces have been reported on the mapping (see Fig. 2.13(a)) using black and red dashed lines for Hg and Cd, respectively. Regarding these energy ranges, we can estimate that the CdTe reference has been taken at least 20 nm away from the HgTe/CdTe interface and that in both HgTe and CdTe the strain value is averaged over a thickness of $\approx$ 1.5 nm.

Extraction of θ_{min} is performed using the association of two error functions:

$$f = Aerf(k(\theta_s - \theta_0)) + Berf(k_1(\theta_s - \theta_1)) + C \tag{2.5}$$

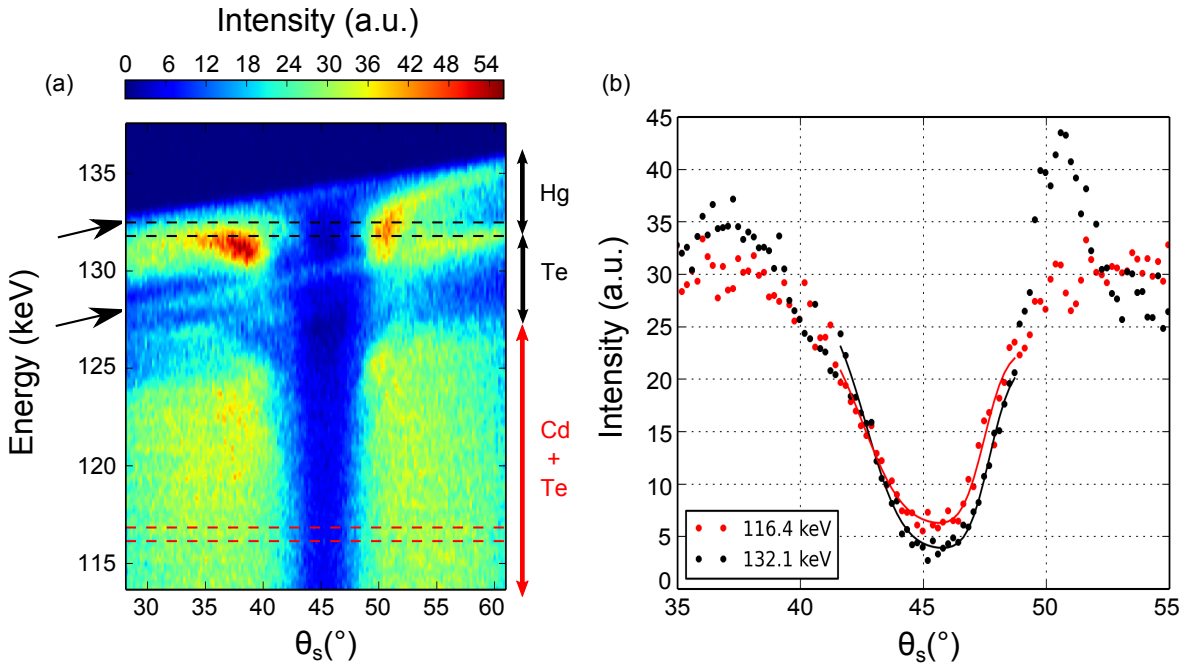

Figure 2.13 – *(a) Medium Energy Ion Scattering (MEIS) blocking dip mapping as a function of the energy collected in the detector and θ_s in the [-110] direction with He^+ ion energy at 140 keV. The two arrows indicate the presence of amorphous material principally composed of Hg and Te. The energies corresponding to Hg, Cd and Te (from HgTe layer and from CdTe) are highlighted on the right side of the figure. (b) Traces at two different energies: 116.4 keV (within CdTe), and 132.1 keV (within HgTe), summed over an energy range of 0.6 keV. The shift in the minima values of the intensity curves correspond to the strain effect. Experimental data are represented by the dots and fits are the solid lines.*

with A, B, C, k and k_1 constants mainly determining the background and the slope of the error functions, while θ_0 and θ_1 are the inflection point for each function. θ_{min} is then directly extracted from the mean value of θ_0 and θ_1.

Following this methodology, θ_{min} is estimated at 45.18 °for Hg atoms and the corresponding out-of-plane lattice mismatch is $\frac{\Delta c}{c} = -0.7\%$. This quantity leads to the determination of c_{fs} and $\epsilon_\perp = -0.4\%$ as reported in Table 2.3. This value and the associated gap ($E_s = 21$ meV) are consistent with HRXRD considering the resolution of this method.

θ_{min} (°)	45.18
$\frac{\Delta c}{c}$ (%)	-0.7
c_{fs} (Å)	6.4361
$\epsilon_\perp$ (%)	-0.4
E_s (meV)	21

Table 2.3 – *Estimation of the out-of-plane deformation $\epsilon_\perp$ and of the strain energy gap E_s for a growth on (100) CdTe substrate using MEIS.*

2.2.2.3 Using TEM and NPED

Promoted by the availability of aberration corrected microscopes, TEM is nowadays a powerful tool for the characterization of strain in semiconductor materials. Many techniques have been developed such as dark field electron holography, nanobeam diffraction or even geometrical phase analysis. The reader can refer to [CDB+16] for further details about these techniques and examples of measurements.

Experiments have been performed and analysed on the Nanocharacterization Platform CEA Grenoble using a FEI Titan Ultimate microscope and a non-standard technique of Nanobeam Precession Electron Diffraction (NPED).

The realization of NPED is done with TEM in diffraction mode (see Appendix A.3.2.1). The precession of the electron beam is obtained by scanning it with a constant angle around the optical axis as illustrates in Appendix (see Fig. A.8). With this precession motion, the resulting diffraction patterns are thus forming disks which are then compensated and turned into spots by the alignment tuning and the good adjustment of coils. With this technique, a more important number of diffraction spots is accessible and their uniformity is improved [RBM+13], thus leading to an enhancement of the diffraction precision. A typical diffraction pattern is presented in the inset of Fig. 2.14(c). The positions of the diffraction spots are first used to determine the crystallographic axis and their lattice spacing, each spot corresponding to a given crystallographic orientation. A reference pattern is first determined in the strain-free CdTe layer and then only relative measurements are performed. By scanning a large part of the sample, we can obtain diffraction patterns through the whole stack and compare them directly to the reference one. For a given crystallographic direction, the shift in position of its diffraction spot enables the variation of lattice parameter to be estimated and thus the corresponding strain value. Further details about strain value extraction can be found in [RBM+13].

In this study, (111) axis has been considered as it provides simultaneous information about in-plane and out-of-plane lattice parameters. The operating beam voltage has been adjusted to 200 kV and the beam resolution has been estimated to 2 nm from the diffraction spot diameters. NPED analysis is presented here for a 8 nm-thick HgTe layer embedded between two 30 nm-thick HgCdTe barriers. This stack is representative of the samples used for low temperature magneto-conductance measurements (see Chapter 4).

Two mappings are reported in Fig. 2.14(a) and (b) corresponding to in-plane ($\frac{\Delta a}{a} = \frac{a_{fs}-a_s}{a_s}$) and out-of-plane ($\frac{\Delta c}{c}$) lattice mismatches, respectively. The $\frac{\Delta a}{a}$ mapping evidences no variation of the in-plane lattice parameter along the whole stack with a negligible value of $\approx 0.04\%$. This demonstrates that no in-plane deformation is noticeable in our structures and so that all the Hg-based layers are coherently strained on the CdTe substrate.

Concerning the $\frac{\Delta c}{c}$ mapping, clear variations of the out-of-plane lattice parameter are observable between the layers. It is worth noting that the small fluctuations noticeable in each layer are due to local lattice parameter variations caused by sample preparation. Similar effect was observable on the $\frac{\Delta a}{a}$ mapping. It is important to realize that the resulting inhomogeneity of the contrast is not due to the sample quality but only to the fact that we are probing very low lattice parameter variations which are only one order of magnitude larger than those induced by sample preparation. To prevent these small fluctuations from impacting the results, the realization of map instead of a simple line scan has been preferred and developed in consequences.

The resulting out-of-plane lattice mismatch profile (see Fig. 2.14(c)) is obtained by summing $\frac{\Delta c}{c}$ over the whole mapping. As previously mentioned, the CdTe out-of-plane lattice mismatch is set to $\frac{\Delta c}{c} = 0\%$ by definition. However, one can distinguish a slight positive deformation recorded close to the interface between the CdTe and the bottom HgCdTe barrier, which would correspond to a compressive strain. Note that this peak of compressive strain is in mirror with another peak corresponding to tensile strain at the barrier interface, suggesting that these two contributions are compensating each other. Similar feature does not appear at the

HgTe/HgCdTe interfaces as the two layers are experiencing similar deformations. A few nanometers away from the CdTe interface, the bottom HgCdTe barrier is characterized by $\frac{\Delta c}{c} \approx -0.20\%$ equivalent to $\epsilon_{\perp} \approx -0.11\%$ (expected value: -0.14%) considering a Cd composition of 70 %. Similar deformation is noticeable for the top barrier. Strain in both barriers can therefore be considered as identical, thus confirming that the two topological insulator surface states are experiencing the same environment. Concerning the HgTe layer, the out-of-plane lattice mismatch $\frac{\Delta c}{c} \approx -0.50\%$ resulting in a tensile strain deformation $\epsilon_{\perp} \approx -0.20\%$. This value is very low compared with HRXRD and MEIS investigations. It is worth noting that, due to the beam resolution of 2 nm and to the low thickness of the HgTe (8 nm), the value of a steady deformation is only established on a ≈ 4 nm range. Additional measurements on thicker films would be of great interest to confirm this value and give insights on the strain homogeneity in the HgTe layer.

More than just strain value in the middle of each layer, what is also interesting here is to analyse the profile at the interface between HgCdTe topologically trivial layer and HgTe topologically non-trivial layer. The $\frac{\Delta c}{c}$ mapping unambiguously reveals a sharp top HgTe interface while the bottom one appears to be stretched out. This is confirmed by the profile evidencing a 3 nm-long top interface, illustrating a sharp interface in regards to the 2 nm beam resolution. The bottom interface width is in contrary estimated at 5 nm. Even though, this value does not allow a precise estimation of the interface width due to the beam resolution, it confirms the non-abruptness of this interface, compared to its top counterpart.

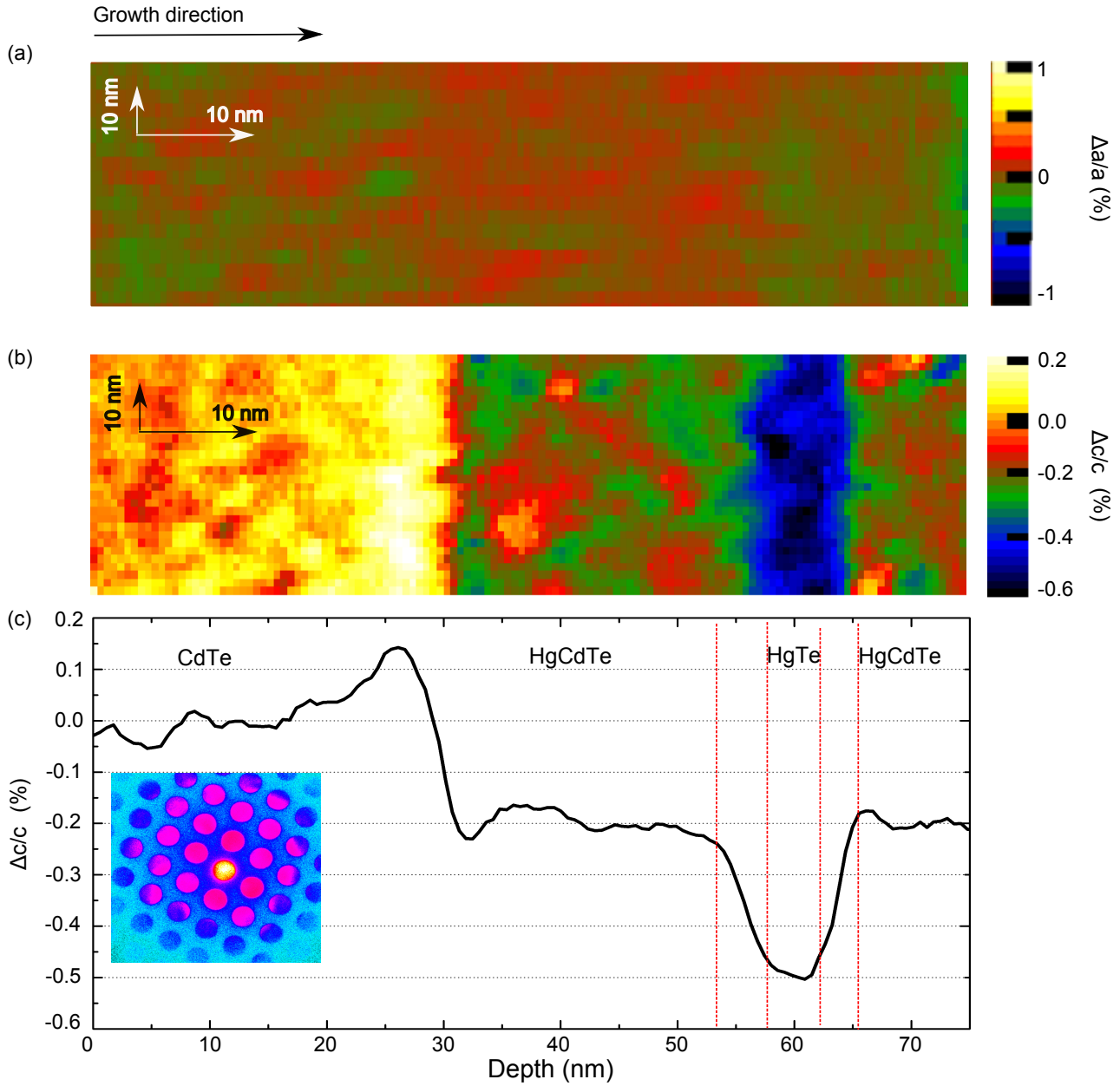

Figure 2.14 – *Nanobeam Precession Electron Diffraction (NPED) strain analysis of a 8 nm-thick HgTe capped structure. (a) In-plane lattice mismatch* $\frac{\Delta a}{a} = \frac{a_{fs}-a_s}{a_s}$ *mapping. (b) Out-of-plane lattice mismatch* $\frac{\Delta c}{c} = \frac{c_{fs}-c_s}{c_s}$ *mapping. (c)* $\frac{\Delta c}{c}$ *profile. Red dashed lines mark out the interfaces. Inset corresponds to a diffraction pattern obtained with the precession motion.*

The combination of HRXRD, MEIS and TEM measurements has demonstrated, at different scales, the tensile strain experienced by HgTe layers. The plastic relaxation mechanism has been determined from HRXRD measurements to appear at ≈140 nm and to be progressive. Analysis of the resulting out-of-plane deformation has thus been performed on thinner samples and the results obtained with these three characterization techniques are summarized in Table 2.4. With $\epsilon_\perp$ values between -0.20% to -0.46%, the corresponding strain gap has been estimated between 10.4 meV and 23.9 meV. These values confirm the opening of an insulating bulk, which is the second and last requirement for HgTe to become a topological insulator.

Note that the dispersion between the measured $\epsilon_\perp$ values can be explained by the measurement methods.

	HRXRD	MEIS	TEM (NPED)
$\frac{\Delta c}{c}(\%)$	-0.77	-0.7	-0.50
$\epsilon_{\perp}(\%)$	-0.46	-0.4	-0.20
E_s (meV)	23.9	21	10.4

Table 2.4 – *Estimation of the out-of-plane deformation $\epsilon_{\perp}$ and of the strain energy gap E_s as a function of the characterization technique for a HgTe layer grown on (100) CdTe substrate.*

Allowing only the strain determination on a 1.5 nm thick part of the HgTe layer, MEIS measurements are probably the less accurate. In comparison, HRXRD and NPED are giving access to strain value on the whole layer. Nevertheless, thinning the sample for TEM observation can result in a relief of lattice parameters on the free surfaces that is not taken into account in the analysis. Moreover, lattice parameter fluctuations due to sample preparation create uncertainty concerning the CdTe reference. Therefore, NPED is probably underestimating the out-of-plane lattice mismatch and so the strain value in our structures but has the major advantage of providing a deformation profile of the HgTe capped structures, representative from the samples used for low temperature magneto-conductance measurements. While a difference of abruptness of the interfaces has been pointed out, the two barriers experience the same deformation thus confirming the equivalence of the two topological surface states.

Before closing this discussion on the tensile strain, it is important to briefly address the effect of thermal expansion as the samples are subject to important temperature variations from the growth process to the low temperature measurements. From the thermal expansion coefficients of HgTe and CdTe [CWBS80] [SW75] [BGR93] and the temperature dependence of the stiffness constant C_{11} and C_{12} [CS75], we estimate a variation of the out-of-plane deformation of about 0.01% between 300 K and a few mK, thus confirming no significant impact of the temperature on the strain in our structures.

2.2.3 Interface: roughness and intermixing

To prevent from impacting carrier mobility and lifetime through surface scattering [MAHB91] and potential fluctuations, the interface widths of our HgTe topological layer need to be kept lower than the surface state wavefunction extension. Note that interface width includes both the effect of roughness and interdiffusion. Previous calculations, reported in Chapter 1, demonstrate a surface state wavefunction decay length of about 4.7 nm in the HgTe layer, thus imposing a limit concerning the roughness and intermixing of the interfaces.

Investigation of surface morphology and compositional intermixing are thus required to gain knowledge on the quality of the interfaces and to determine sources of optimization. We first focus on HgTe/CdTe simple structures and the reduction of top HgTe surface roughness thanks to end-of-growth in-situ surface treatment. In a second time, capped structures are considered and their interface widths are directly compared to the surface state extension.

Note that complementary characterization of the buried HgTe/CdTe interface of the simple structures has been performed but will be presented in the next section (see 2.3.3). This choice has been made to prevent from repeating the results. Estimation of this interface width has indeed been achieved for several growth temperatures and provides important insights for the optimization of this parameter.

2.2.3.1 HgTe/vaccum interface

With the initial growth process, the HgTe layers are characterized by trenches more than 10 nm deep resulting in a large roughness value of about 5.6 nm as shown in Fig. 2.15(a) and reported in Table 2.5. These trenches constitute strong evidences of Hg desorption during end-of-growth cooling down.

To prevent Hg desorption, the addition of an in-situ end-of-growth surface treatment is considered after the HgTe growth, that is, after closing the Te cell shutter. A first solution is to maintain the Hg flux during the cooling down to temperatures below 100°C for which no significant Hg desorption is expected. The resulting surface morphology is shown in Fig. 2.15(b). The deep trenches are no longer present, and the surface roughness is greatly improved with RMS values typically in the 0.5 nm to 1 nm range. However, this surface roughness, on the order of several monolayers, can be further improved by keeping the surface at elevated temperatures for a few minutes (see Fig. 2.15(c)). The surface morphology is still improved with RMS values down to the monolayer.

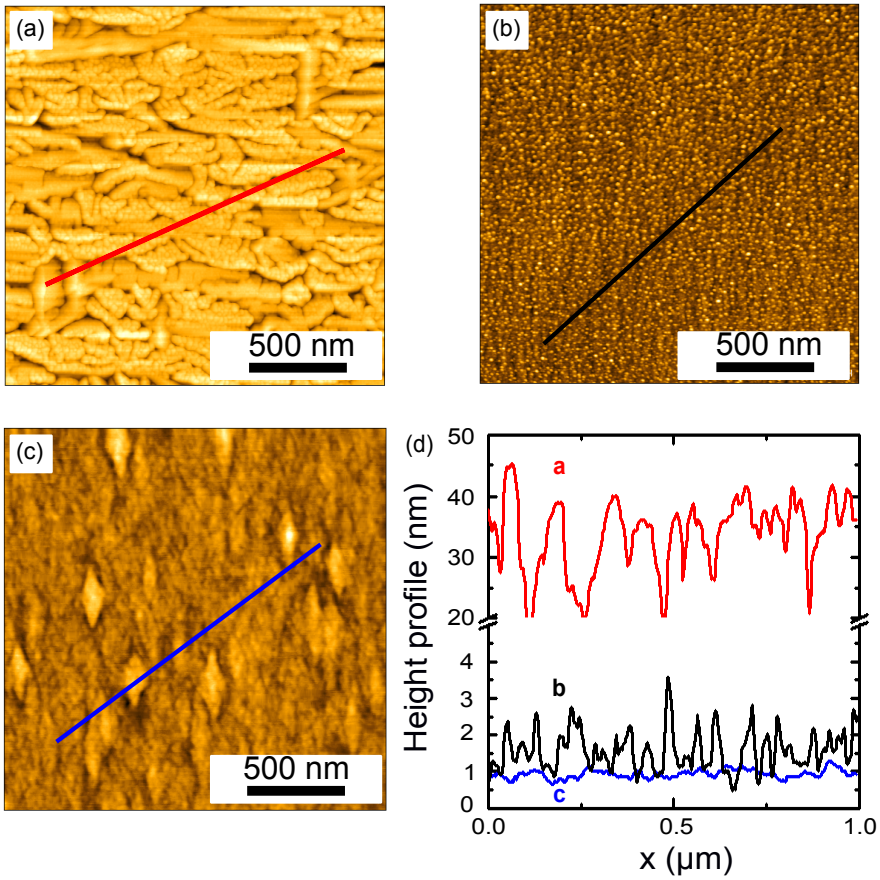

Figure 2.15 – *2 µm x 2 µm AFM images of the HgTe surface when cooled down without (a) and with Hg flux (b) and after a short annealing and cooldown with Hg flux (c). Z-scales are respectively 53.7 nm, 5.4 nm and 2.3 nm. Corresponding line profiles are given in (d).*

Treatment	Without Hg flux	With Hg flux	With Hg flux + annealing
Roughness (RMS) (nm)	5.6	0.6	0.2

Table 2.5 – *Roughness evolution using different end-of-growth in-situ surface treatments.*

The combination of both annealing step and preservation of Hg flux appears as the best solution regard-

ing the top surface roughness. However, this surface treatment takes few minutes during which the shutters outgasing can result in additional material deposits on the HgTe surface. Moreover, the annealing step can also affect the bottom interface by enhancing the intermixing effect. Therefore and in regards of the electronic transport measurement feedbacks, we decided to restrict the surface treatment to the sole cooling down under Hg flux. This solution is probably the best compromise to preserve two interfaces with low roughness (< 1 nm) and limit the intermixing. This end-of-growth surface treatment is now a part of the growth process but only in the case of simple HgTe/CdTe structures where the HgTe layer is not protected by the HgCdTe barrier.

2.2.3.2 HgTe/HgCdTe interfaces

We are now considering a capped HgTe structure and the associated HgTe/HgCdTe interfaces.

The determination of the interface width is usually done using standard techniques, such as X-Rays Reflectivity (XRR) (see Appendix A.1.3), which lead to a full characterization of the stack. However, the more numerous the layers, the more complicated the extraction of the characteristics for each layer. In the case of capped structures, the presence of the HgCdTe barriers makes this type of analysis even more complex. Therefore, in order to accurately characterize the HgTe/HgCdTe interfaces, we decide to use an atomic-scale structural investigation with HRSTEM in the High Angle Annular Dark Field (HAADF) mode. The interest of using this particular mode lies in the relation between the contrast and the atomic number Z which is in $Z^{1.7}$ [Pen89]. The presented measurements have been achieved using a FEI Titan Ultimate microscope with a beam voltage of 200 kV and a resolution of about 1 Å.

Fig. 2.16(a) displays a high magnification Z-contrast image of a stack made of a 8 nm-thick HgTe layer embedded between two 30 nm-thick $Hg_{0.3}Cd_{0.7}Te$ layers and grown at 160 °C. The atomic dumbbells are clearly distinguishable in each layer and represent the atomic columns over the whole thickness of the slab (usually between 50 and 100 nm).

The HgTe layer appears very bright due to its large atomic numbers: Z_{Hg} = 80 and Z_{Te} = 52. A zoom on this layer is presented in the red box and evidences two atomic columns. The brighter column on the right is attributed to Hg, whereas the left one corresponds to Te. The contrast becomes darker in the $Hg_{0.3}Cd_{0.7}Te$ barriers due to a reduction of the Hg fraction. A zoom is reported in the green box and highlights two atomic columns with similar brightness. While the left column has been attributed to Te, the right one corresponds to Hg and Cd atoms in the stoichiometric ratio 0.3/0.7 thus resulting in $Z = 0.3Z_{Hg} + 0.7Z_{Cd} = 57.6$ which is indeed very close from $Z_{Te} = 52$.

Concerning the interfaces, the contrast reveals a smooth and continuous transition from HgTe to HgCdTe, thus suggesting an intermixing of Hg and Cd atoms. To properly quantify this interdiffusion process, one needs to study the associated chemical profile presented in Fig. 2.16(b). Atomic dumbbells are reproduced through the intensity double peaks whose intensity ratio illustrates the difference of atomic number and so leads to the monitoring of the chemical composition over the whole stack.

Determination of the interface width relies on the evolution of the II and VI peaks intensity ratio $\frac{I_{II}}{I_{VI}}$ with I_{II} and I_{VI} the intensity of the II and VI elements, respectively. However, this analysis is made complex by the presence of a remaining Z-dependent intensity background which results from the broaden gaussian-like shape of the beam probe [DRDdJ12]. Therefore, even if the beam focus in between two atomic columns, it still interacts with nearby sample's atoms which are emitting a background signal. Removing the intensity background is thus needed to precisely determine the interface widths. However, one must realize that accurately subtracting this background is a very challenging exercise as it requires a precise and full characterization of the beam probe profile which has not yet been possible to date.

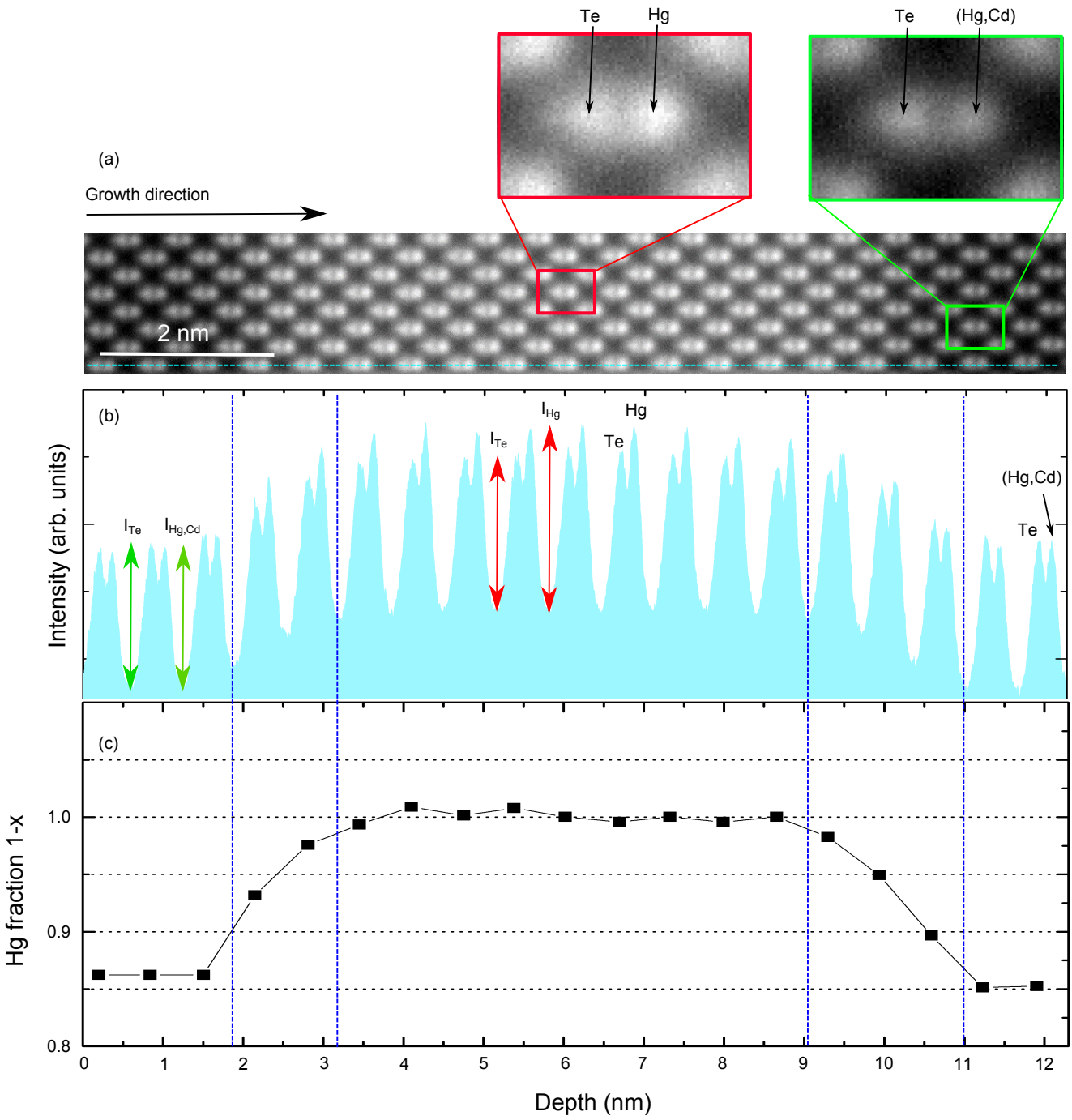

Figure 2.16 – *(a) High Resolution STEM (HRSTEM) High Angle Annular Dark Field (HAADF) image of HgCdTe/HgTe/HgCdTe structure. Red and green squares evidence HgTe and HgCdTe dumbbells respectively. (b) The corresponding intensity profile. Intensity double peaks correspond to the atomic dumbbells. (c) Evolution of the Hg fraction relying on the intensity ratio between II and VI elements. Interface widths are highlighted by blue dashed lines and are estimated to* ≈ 2 *nm.*

Nevertheless and despite the mentioned issues, we propose in this report to estimate the interface widths without subtracting the background signal but by adapting the definition of the peak intensity. The following analysis is therefore based on an approximation. The peak intensities are defined in Fig. 2.16(b) with the colored arrows between the peak maximum and the nearby minimum at the background signal level. Following this methodology, the Hg composition is obtained through the whole structure by normalizing it in the center of the HgTe layer and is reported in Fig. 2.16(c). Note that the Hg fraction in the $Hg_{1-x}Cd_xTe$ barriers

is overestimated, demonstrating the difficulty to extract a reliable chemical profile from these measurements. Nevertheless, even if this profile is not accurate in the absolute alloy fraction of HgCdTe, it still leads to the determination of the interface limits marked out by the blue dashed lines in Fig. 2.16(c). The top interface length is estimated to $\approx$ 2 nm, while the bottom one is considered between 1.5 and 2 nm.

To understand the slight difference between the top and bottom interfaces, it is important to realize that the measured values of interface widths are obtained by averaging over the whole slab thickness and so over several atomic layers. The roughness over the slab as well as the defects located at the interfaces can therefore significantly impact the measurement. Previous AFM measurements indeed demonstrate the higher roughness of HgTe, compared to HgCdTe (see 2.1). Moreover, it is worth noting that these results are not consistent with the NPED strain study which demonstrated a larger bottom interface extension, compared to the top one 2.2.2.3. The difference in the conclusion between these two measurements is so far not well understood.

Nevertheless, even if this HRSTEM study does not provide a very precise value of the interface width, it demonstrates that the HgTe interfaces are much narrower than the surface state wavefunction extension estimated to $\approx$ 4.7 nm.

This section has reported some efforts and improvements made on the growth of HgTe topological insulator layers. Various material characterization techniques have been used to provide a complete overview of the material quality. Particularly, we have demonstrated that a cautious control of the chemical composition leads to the growth of pure HgTe , thus allowing the band structure to be inverted. Moreover, the tensile strain experienced by the HgTe layer has been characterized with an out-of-plane strain deformation of about -0.4% corresponding to the opening of a $\approx$ 20 meV bulk gap. The quality of the interfaces has also been emphasized with an extension two times less important than the surface state wavefunction. With these characteristics, our HgTe structures, grown at T_g between 140 and 165 °C, are suitable for electronic transport measurements and already demonstrate clear signatures of a topological behavior as it will be reported in Chapter 4.

2.3 Further improvements: optimization of the growth temperature

The previous section has provided a complete picture of our material quality grown in the following temperature range: 140-165 °C. However, for such low growth temperatures, TEM characterization evidences the presence of dislocation loops. These defects are especially noticeable for the thicker films and for the lower growth temperatures. So far, the question of the impact of these defects on transport properties is still open. As transport properties of thick 3D topological insulators are suffering from bulk contribution (see measurements of Chapter 4), decreasing bulk defect density by optimizing the growth temperature could be a way to determine if this bulk contribution is intrinsic to the system or related to these defects.

HgTe layers have been successfully grown at temperatures up to 185 °C with apparently equivalent crystal quality as shown in the HRXRD spectra of Fig. 2.17. However, HRXRD is characterized by a lack of spatial resolution in the structure resulting in average estimates over sample area or depth. This prevents from probing slight or very localized variations in the crystalline network such as point defects or small dislocation loops. These defects can appear when the growth temperature is not adapted and are therefore good indicators to improve the growth process. STEM is used to probe nanometer-scale material variation and determine the corresponding bulk defect density. AFM analysis is then presented to study the evolution of the surface

morphology as a function of the growth temperature. Finally, we report the effect of the temperature on the interdiffusion using both X-Rays Reflectivity (XRR) and MEIS. With all these complementary characterizations, the objective is to determine the optimal value for the substrate temperature.

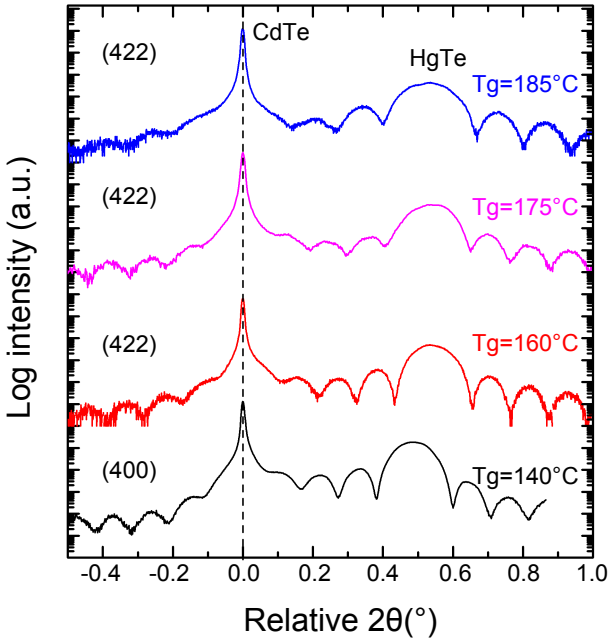

Figure 2.17 – *(422) (respectively (400)) HRXRD 2θ-ω scans of HgTe (thicknesses : 81 nm in blue , 100 nm in magenta, 100 nm in red and 94 nm in black) grown on (211)B ((100)) CdTe susbtrates for different growth temperatures ranging from 140°C to 185°C.*

2.3.1 Impact on bulk defect density

Scanning TEM is used and especially its Bright Field (BF) mode to characterize the bulk defects and their density as a function of the growth temperature.

Figure 2.18 presents STEM BF images of 100 nm-thick HgTe layers surrounded by two HgCdTe barriers and grown at 140, 165, 175 and 195 °C. One can directly notice that the HgTe layer of Fig. 2.18(a) is full of black spots which correspond to dislocations loops. It is worth noting that the number of dislocations seems to decrease with the rise of temperature. To accurately determine the associated bulk defect density, the determination of the slab thickness is required. As this data is not yet available to date, we manage even though to estimate the bulk defect density for each growth temperature by considering that the slab thickness varies between 50 and 100 nm for each samples. The resulting defect densities are reported in Fig. 2.19. The comparison between 140, 165 and 175 °C is difficult as the determined density ranges are comparable. However, for $T_g = 195$ °C, the reduction of the bulk defect density is noticeable.

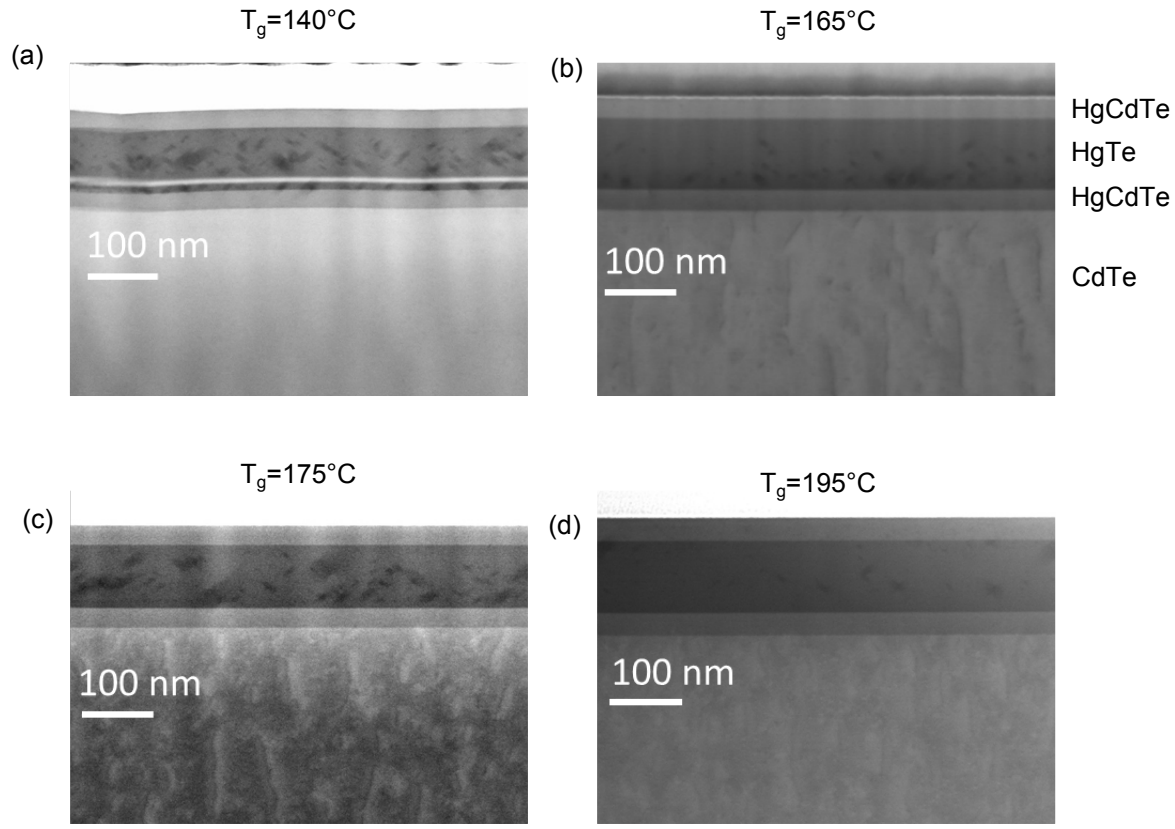

Figure 2.18 – *STEM Bright Field (BF) image of hundred nm-thick HgTe layers surrounded by two HgCdTe barriers and grown at (a) 140°C, (b) 165 °C , (c) 175 °C and (d) 195 °C.*

To further analyse these defects, Fig. 2.20 presents TEM and STEM BF and HAADF images focusing on one of these defects. These images have been obtained from a 10 nm-thick HgTe layer surrounded by two HgCdTe barriers and grown at 160°C. Both the TEM and the STEM BF images clearly highlight the resulting stacking fault and characterize its crystalline orientation which appears to be either [110] or [1-10]. One may have notice that the dislocation loop presented here spreads over the whole HgTe layer from one interface to the other. This is only happening because of the low thickness of this sample. Indeed, for thicker samples (see Fig. 2.18), the defects are not extended enough to spread from one interface to the other and are for the majority not even located near the interfaces, thus making their impact on the electronic transport properties difficult to

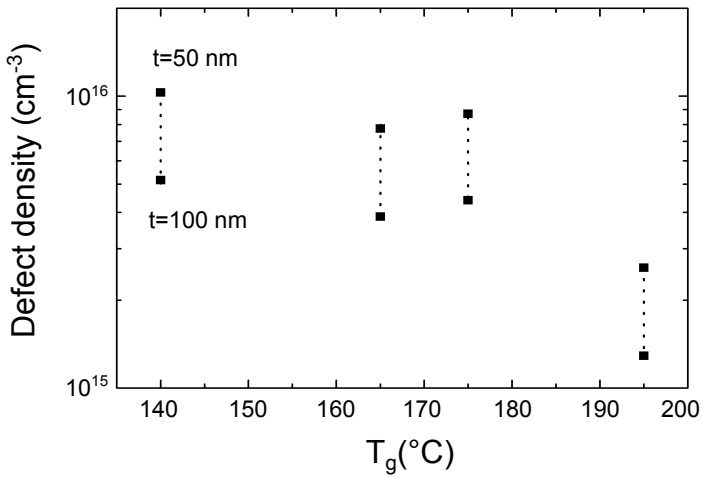

Figure 2.19 – *Bulk defect density as a function of the growth temperature. The upper points have been estimated considering a 50 nm-thick slab, while the lower ones consider a 100 nm-thick slab.*

estimate. Note that the dislocations are surrounded by some dark cloud witnessing the strain field around the defect. On the contrary, HAADF image, mainly sensitive to chemical composition, does not reproduce this pattern, thus confirming that these defects do not impact stoichiometry.

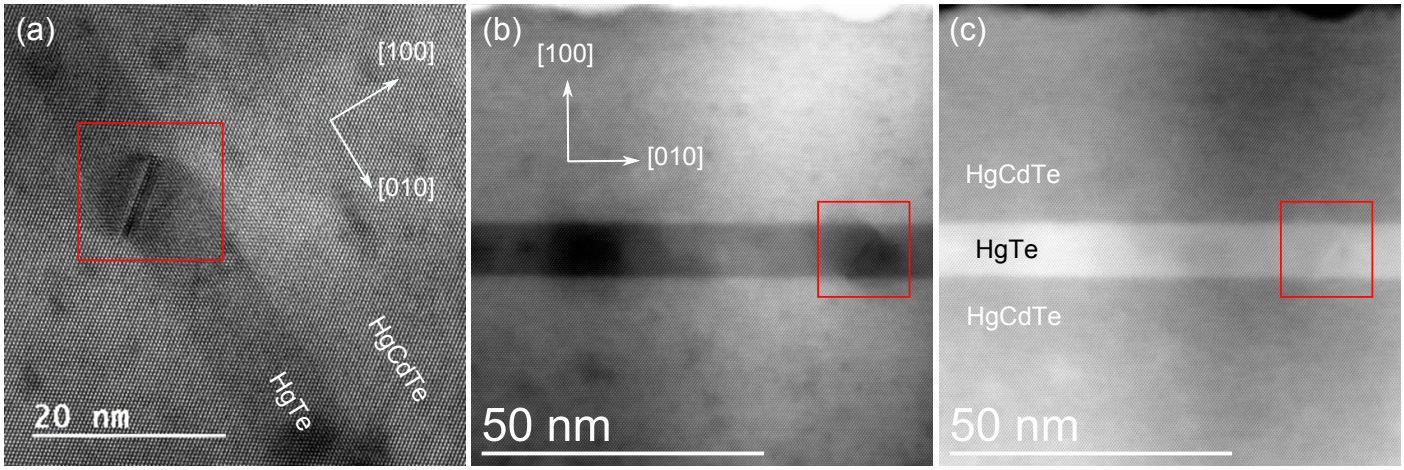

Figure 2.20 – *(a) TEM image, STEM (b) BF and (c) HAADF images of a 10 nm-thick HgTe layer surrounded by two HgCdTe barriers and grown at 160°C. A [110] ([1-10]) dislocation-loop is evidenced in the red square.*

The presence of such defects in our structures is raising some questions about their appearance mechanism. As they are mostly noticeable on the thick samples ($\approx$ 100 nm), the impact of the strain cannot be ruled out. However, the most reasonable explanation seems to lie in the growth temperature. With a low substrate temperature, the atom mobility on surface is limited and this phenomenon is even enhanced by the increased surface saturation by Hg. The adaptation of the Hg/Te ratio with temperature should enable to prevent from Hg accumulation but is difficult to monitor. Nevertheless, this should be envisaged for the future growth of HgTe structures.

2.3.2 Impact on surface morphology

AFM measurements have been performed on HgTe/CdTe (100) samples with a growth temperature T_g ranging from 140°C to 213°C. Figure 2.21 displays the AFM images and corresponding profiles of the HgTe top surface for each T_g highlighting a constant evolution of the surface morphology.

One can notice the appearance of steps which are hardly distinguishable for T_g = 175 °C and which become significant for $T_g \geq 195$°C. These steps define terraces whose width is increasing with T_g. While these terraces are full and properly defined for $T_g = 213$ °C, they are characterized by voids and clusters for $195 \geq T_g \geq 175$°C. The perfect and organized filling of these terraces characterizes the transition from the former 2D growth mode to the step flow mode which occurs between 195 and 213 °C.

Despite this change of growth mode, the RMS value is not impacted as can be seen in Fig. 2.21. However, at 213°C, step instabilities are distinguishable and are forming bunches (see red dashed lines) resulting in an apparent rougher surface and in height variations at the nanometer scale. This step-bunching phenomena can be induced from no more adapted growth kinetics in front of the high adatom mobility in this range of temperature and should be avoided to prevent from strong potential fluctuations at the HgTe interface.

From all these observations, we conclude that to preserve the surface morphology well below the surface state wavefunction extension, it is reasonable to limit the growth temperature range to 195 °C.

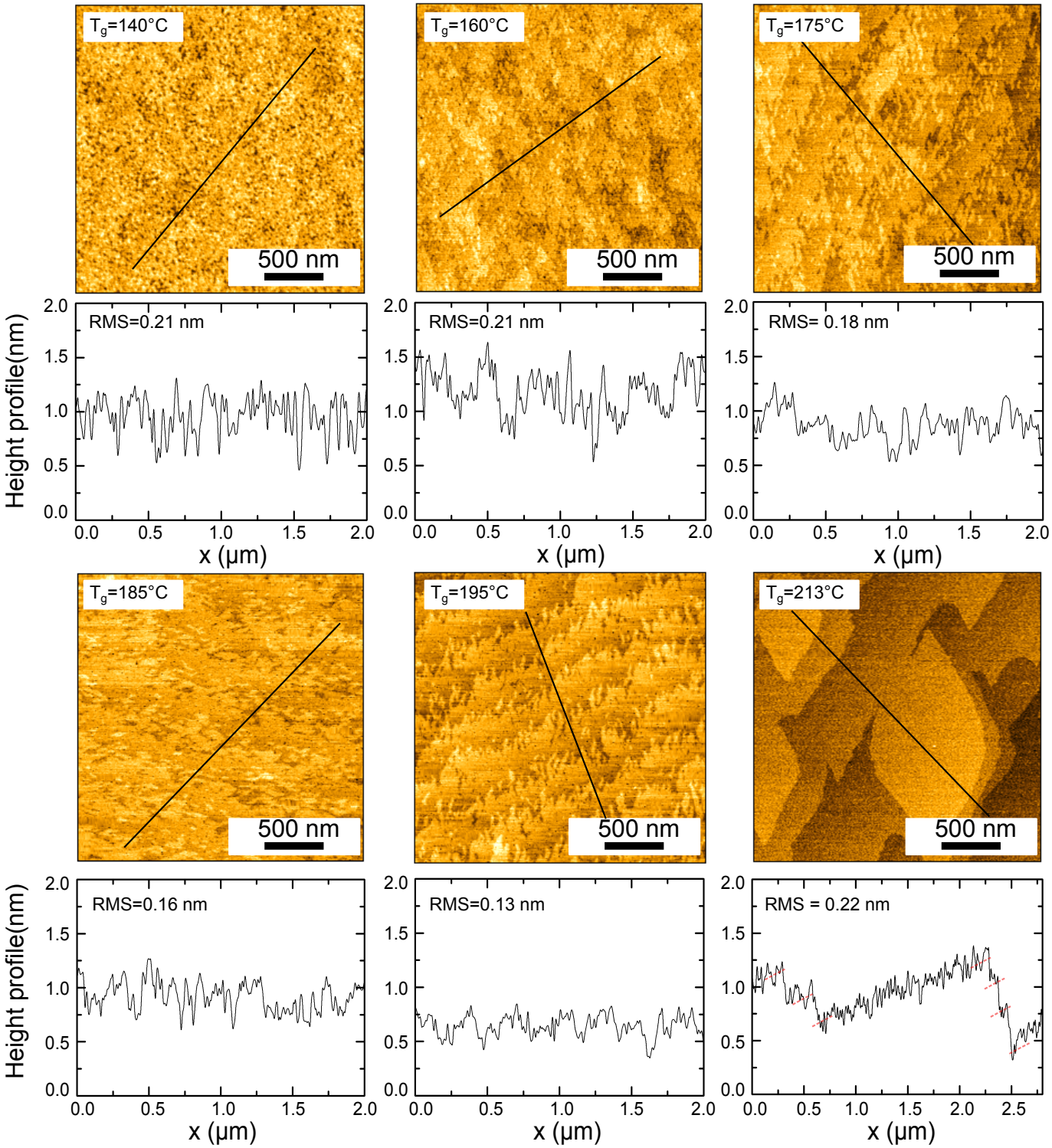

Figure 2.21 – *2.5 µm x 2.5 µm AFM images illustrating the growth mode evolution with temperature variation. Z-scales are in order: 1.7 nm, 2.1 nm, 1.5 nm, 1.7 nm, 1.3 nm and 2.2 nm. For $T_g \geq 175°C$, terraces are beginning to appear and they become completely filled for $T_g \geq 195$ °C. The corresponding height profiles (black lines) are plotted underneath the AFM images. In the last profile, the red dashed lines, representing monolayer steps, provide evidence for step-bunching.*

The combination of STEM and AFM, to study both bulk defect density and surface morphology, gives a first overview of the growth temperature dependence of the HgTe structures. Low growth temperatures provide flat

surfaces but with a high bulk defect density whereas for higher growth temperature ($\approx$ 195 °C), the bulk defect density is decreased while the roughness is still of the monolayer order. From these cross-analysis, one can conclude that increasing growth temperature from 140-165 °C to $\approx$ 195 °C is a solution to improve material quality. However, one important point has not yet been addressed and concerns the interdiffusion. It seems indeed reasonable to believe that a rise of growth temperature will considerably increase the intermixing thus resulting in graded interfaces. The following subsection is here to address this point and gives new arguments for the optimization of the growth temperature.

2.3.3 Interdiffusion

In this section, X-Rays Reflectivity (XRR) and Medium Energy Ion Scattering (MEIS) are used and complement each other to describe the interface evolution with growth temperature. This study has been performed on simple HgTe/CdTe structures and is therefore limited to the bottom topological interface. It is worth noting that Secondary Ion Mass Spectroscopy (SIMS) has also been used for the characterization of these interfaces but does not appear to be adapted here regarding its resolution (see the analysis presented in Appendix A.2).

2.3.3.1 Using X-Rays Reflectivity

XRR technique is explained in details in Appendix A.1.3. This low grazing angle characterization technique enables the determination of roughness and density contrast i.e. structural and compositional intermixing of the interfaces. However, to obtain an accurate description of the HgTe/CdTe interface, two criteria are required:

- the X-rays wavelength must be adapted to allow probing the buried HgTe/CdTe interface. Depending on the samples, this depth can vary between 5 and 100 nm. Due to the heavy mass of Hg, standard X-ray sources using either Cu or Co wavelengths have a limited penetration depth and are not able to probe the material characteristics at depth exceeding 80 nm.
- the flux intensity must be high enough to preserve signal to noise ratio at angles where information about interface roughness appears.

The use of synchrotron radiations is thus justified as it especially enables to adapt the working wavelength. The measurements presented thereafter have been performed using the Beamline BM 32 at the European Synchrotron Radiation Facility (Grenoble) with a beam wavelength near the Hg absorption threshold (1.0134 Å).

The results presented in this section concern 100 nm-thick HgTe layers with (211)B CdTe substrates and with different growth temperature T_g ranging from 160 to 185°C. Figure 2.22 represents the reflectivity spectra of a HgTe layer grown at $T_g = 185$°C as a function of the wavenumber $Q = \frac{4\pi sin(\theta)}{\lambda}$.

Data are fitted using the GenX software [BA07] and the model is described in the inset of Fig. 2.22. This model is composed of a CdTe layer acting for both the buffer layer and the substrate, a HgTe layer and finally an intermediate $Hg_{0.5}Cd_{0.5}Te$ layer characterizing the Hg/Cd intermixing at the interface. Determination of the HgCdTe thickness and roughness will characterize precisely the HgTe/CdTe interface. A thin oxide layer of 1.6 nm has been added to the model to fit the overall curvature of the spectra. Moreover, the XRR spectra of Fig. 2.22 unambiguously evidences two oscillation periods. The shorter one is related to the HgTe layer thickness whereas the larger one (highlighted by the green arrows) represents the HgCdTe layer one. Fitting parameters are reported in Table 2.6.

In this model, the roughness is considered as a layer with a thickness r. Therefore, the final thickness of the interface is defined by $t_f = t(HgCdTe) + \frac{r(HgCdTe)}{2} + \frac{r(CdTe)}{2}$ and by a roughness $r_f = \frac{r(HgCdTe)}{2}$. With this definition, the interface width is estimated to be about 4.5 nm with a roughness of about 0.7 nm.

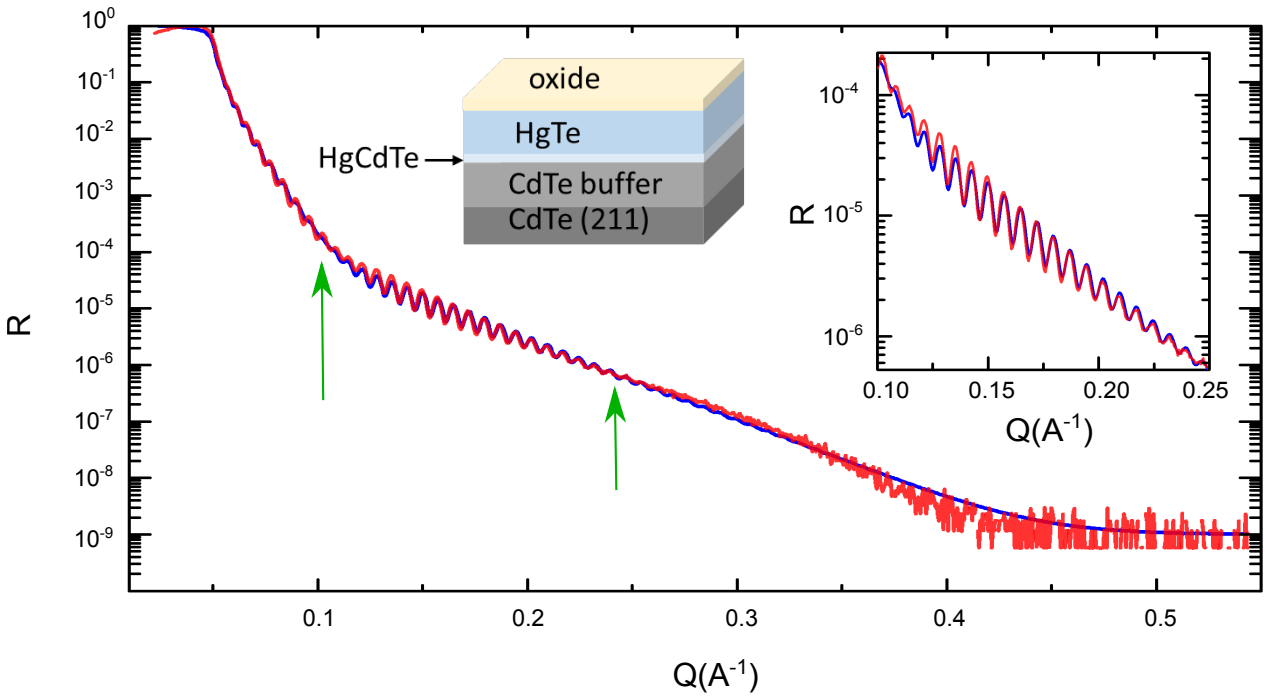

Figure 2.22 – *X-Rays Reflectivity (XRR) spectra of a 83 nm-thick HgTe layer with T_g = 185°C. The model structure used for the fit is represented in the inset as well as the spectral range of main importance for the fit. Green arrows illustrate the damping of the amplitude highlighting the period due to the interface of HgCdTe. The red dashed curve represents the experimental data and the blue curve is the fit using the GenX software [BA07].*

Layers	CdTe	HgCdTe	HgTe
Density d (g/cm^3)	5.9	7	8.1
Thickness t (nm)		**3.4**	**76.8**
Roughness r (nm)	**1.0**	**1.3**	**2.1**

Table 2.6 – *Fitting parameters in bold.*

Similar analysis have been performed on two additional HgTe layers with growth temperatures of 160 and 175°C. The interface width for each sample is given in Fig. 2.23. Error bars represent the roughness of the HgCdTe intermixed layer.

From these measurements, we deduce that the growth temperature needs to be kept below 175 °C to guarantee interface widths smaller than surface state extension. Complementary measurements using MEIS technique are now presented. Results are obtained on (100) structures with a wider range of growth temperatures. Note that the change of substrate orientation between (211) and (100) is not problematic for the comparison between XRR and MEIS results as diffusion in HgCdTe materials is insensitive at first order to substrate orientation [APW93].

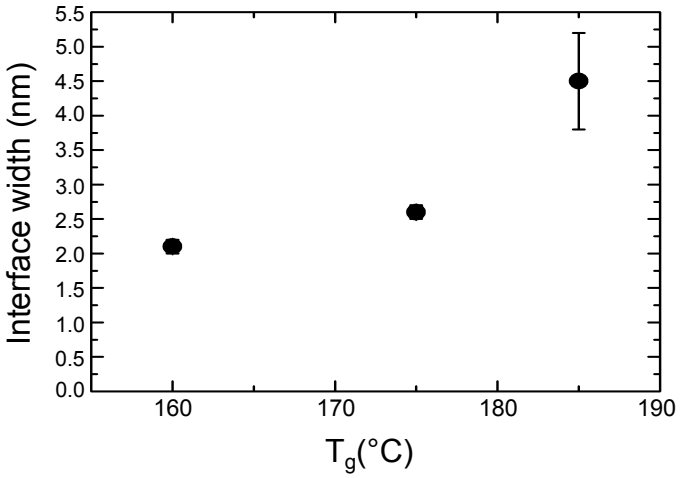

Figure 2.23 – *Interface width, determined using XRR, as a function of the growth temperature. Black points are the HgCdTe thickness values and error bars represent the corresponding roughness.*

2.3.3.2 Using Medium Energy Ion Scattering

MEIS has been previously used for structural analysis but this technique also leads to the chemical profile of our structures when randomly projecting the ion beam with respect to crystal symmetry. Similar to RBS, the energy of the backscattered ions on the surface atoms E_s is expressed through the relation:

$$\frac{E_s}{E_0} = \left(\frac{\sqrt{M^2 - m^2 \sin {\theta_s}^2} + m\cos\theta_s}{M+m}\right)^2 \tag{2.6}$$

with E_0 the energy of the incident He^+ particles, m their mass, M the mass of the target atom and θ_s the scattering angle. Moreover, when the ions are backscattered by atoms of the layer below the surface, it exists an additional energy loss resulting from the interaction of the ions with the matter when both entering the layer and when escaping to the detector. This additional energy loss can be calculated from the stopping power of He^+ in the target material [Zie77] and the couple (θ_i, θ_s) which defines the distance travelled inside the layer.

A typical mapping of the detected intensity as a function of energy of the backscattered ions and scattering angle is reported in Fig. 2.24 for a 7 nm-thick HgTe layer grown at 160 °C and with He^+ ion energy of 200 keV. Some blocking dips are still visible illustrating the difficulty to get rid of the crystalline axis contribution and to completely access a random configuration. Figure 2.24(b) displays a trace of intensity as a function of the energy for θ_s equal to 136.28°. The Hg peak is evidenced at the higher energies and is directly followed by the Te peak from the film. The shift in energy between these two peaks is due to the difference in mass M between these two elements as suggested by relation 2.6. A second Te peak is present and is due to Te from CdTe. The shift between the two Te peaks witnesses the depth effect on the detected intensity. The width of the Hg peak represents the depth at which Hg atoms can be probed. Therefore, the left slope of the Hg peak directly evidences the depth at which Hg is diffusing. With these considerations, fitting these traces thus provides material parameters such as the HgTe thickness and also the interdiffusion.

Similar measurements have been performed on six samples made of 7 nm-thick HgTe layers on (100) CdTe substrates. The growth temperature has been gradually increased from 140 to 213°C. The growth time of such thin samples being only a few seconds, we decide to let them at the growth temperature and under Hg pressure during 5 minutes before the cooling down in order to mimic the interdiffusion of a 100 nm-thick HgTe layer and be able to compare with XRR results.

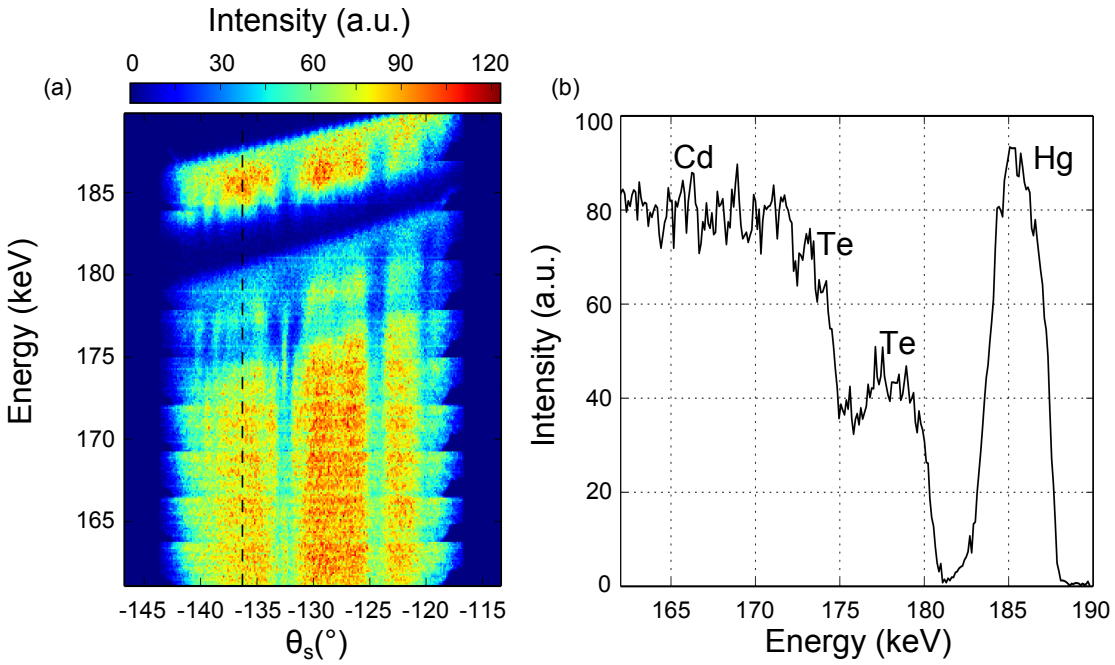

Figure 2.24 – *(a) Random MEIS mapping as a function of the energy and θ_s, with He^+ ion energy of 200 keV, of a HgTe layer grown at 160°C. (b) Intensity trace as a function of energy for $\theta_s = -136.28°$.*

Measurements presented in Fig. 2.24 have been repeated for each growth temperature. Intensity traces have been selected and fitted using an in-house software developed by D. Jalabert (CEA-INAC). This software is adapted to the MEIS energy range and takes into account experimental setup parameters such as the He^+ ion beam energy and the scattering angle. Material parameters such as composition, thickness and density of each layer are considered. For this study, the fit model is composed of a CdTe infinite layer, a $Hg_{0.2}Cd_{0.8}Te$ layer, a $Hg_{0.5}Cd_{0.5}Te$ layer, a $Hg_{0.8}Cd_{0.2}Te$ layer and finally a HgTe layer. The three HgCdTe layers aim to represent the composition gradient caused by interdiffusion.

Figure 2.25 presents intensity traces and associated fits for all probed growth temperatures. The fit parameters are in the inset of each plot. The interface width is calculated as the sum of all the HgCdTe thicknesses and the fit resolution has been determined to be about 0.4 nm. Note that all the data traces were not taken exactly at the same scattering angle due to extra intensities induced by the blocking dips. Blocking dips appear at the same angle for each sample but the extra intensities are not completely reproducible and sometimes difficult to avoid as can be seen in Fig. 2.25(e) or even in Fig. 2.25(f) where both the Hg and the Cd peaks present an extra intensity. Moreover, a 1 nm-thick oxide layer was added to the model to obtain more reliable fitting procedure concerning the right part of the Hg peak.

The evolution of the interface width as a function of the growth temperature is reported in Fig. 2.26, where the error bars correspond to the fit resolution.

Clear evolution of this width with the growth temperature is visible especially for $T_g \geq 195$°C with a transition from 2.5 nm at 195 °C up to 4.6 nm at 213 °C. On the contrary, for $T_g \leq 185$°C, the interface length is not significantly modified and is estimated to be of the order of 1.6 to 2.2 nm. From these observations, we conclude that the growth temperature range must be kept below 195 °C to limit interface width well below surface state extension.

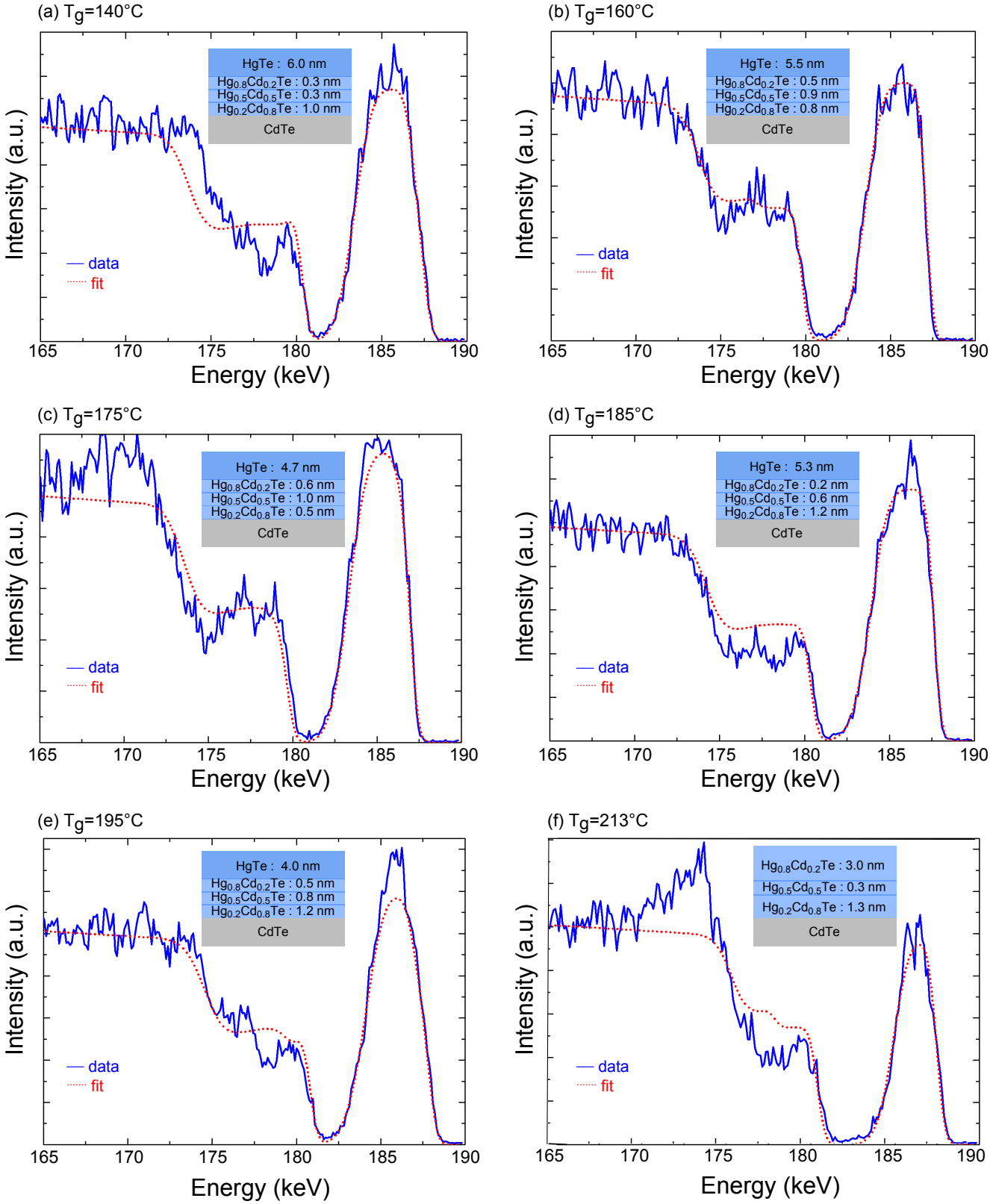

Figure 2.25 – *MEIS intensity traces with He^+ ion energy of 200 keV for (a) T_g=140°C and θ_s =-137.20°,(b) T_g=160°C and θ_s =-138.90°, (c) T_g=175°C and θ_s =-138.12°, (d) T_g=185°C and θ_s =-136.42°, (e) T_g=195°C and θ_s =-133.93°, (f) T_g=213°C and θ_s =-134.06°.*

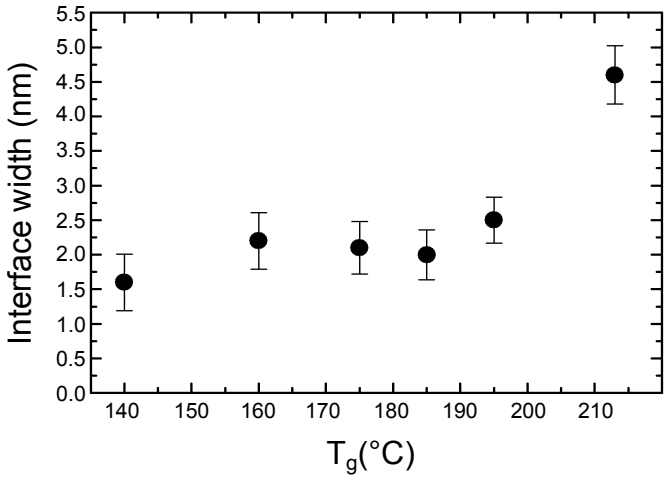

Figure 2.26 – *Interface width, determined using MEIS, as a function of the growth temperature. Error bars correspond to fit resolution.*

We have just estimated interface widths for simple structures made of HgTe/CdTe with either (211) or (100) orientation and with XRR and MEIS respectively. Despite the difference between these two techniques, they both demonstrate interface width in the same order of magnitude. From these results, we can conclude that it is preferable not to increase growth temperatures above 175 °C to preserve bottom HgTe surface state intrinsic electronic properties.

2.3.4 Determination of the diffusion coefficient

We have just estimated the evolution of the total interface width as a function of the growth temperature using both XRR and MEIS. To go one step further, we propose to study the Hg diffusion at the HgTe/CdTe interface and to determine the corresponding diffusion coefficient. In this thought, we need to extract the interdiffusion width x_{diff} from the total interface width.

One may have noticed that XRR directly takes into account the roughness and so $x_{diff} = t(HgCdTe)$. On the contrary, MEIS does not allow to distinguish interdiffusion from roughness. Therefore, to estimate interdiffusion width, the RMS roughness from HgTe top surface (determined from AFM measurements, see Fig. 2.21) is two times subtracted to take into account the effect of both top surface and bottom interface roughness. However, as previously reported from XRR measurements, top surface roughness is usually larger than that of its buried interface. Therefore, one has to keep in mind that x_{diff} values extracted from MEIS are certainly underestimated.

Using x_{diff} values obtained from both XRR and MEIS measurements, we are able to determine the associated diffusion coefficient D using the relation below:

$$x_{diff} = 2\sqrt{Dt} \tag{2.7}$$

where t is the diffusion time.

By considering that t corresponds to the growth time, we manage to estimate the diffusion coefficients for each growth temperature. The resulting D values are presented in Fig. 2.27 and are directly compared to previous studies reported in the literature [Zan86] [TS87] [THM+93], thus confirming at first order the consistency between our measurements and the state of the art about HgTe diffusion.

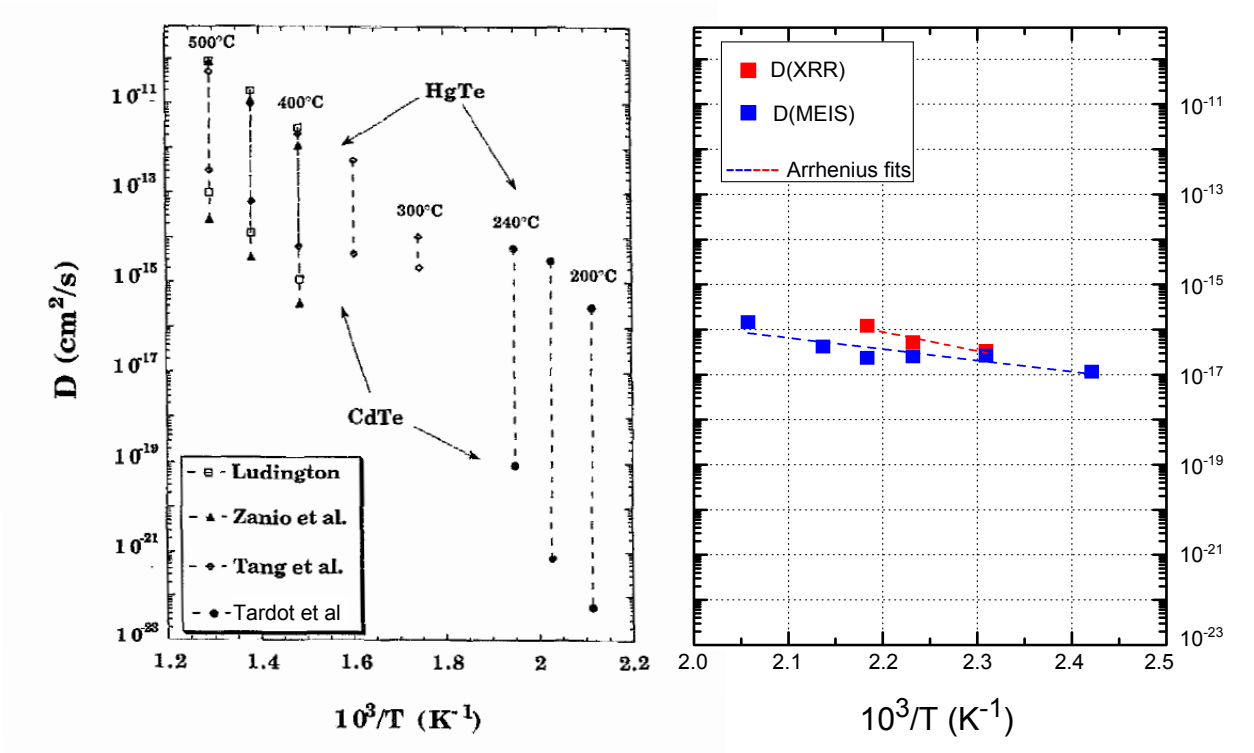

Figure 2.27 – *Comparison of the diffusion coefficients at the HgTe/CdTe interface extracted from this study (right graph) and from literature [Lud87] [Zan86] [TS87] [THM+93] (left graph) as a function of the temperature.*

The temperature dependence of D is fitted using a standard Arrhenius law:

$$D = D_0 \exp\left(\frac{-E_a}{kT}\right) \tag{2.8}$$

with D_0 the prefactor and E_a the activation energy.

This allows to determine:

- $D = D_0 \exp(-0.84[eV]/kT)$ with $D_0 = 1.97\ 10^{-7}$ cm^2/s from XRR measurements.
- $D = D_0 \exp(-0.58[eV]/kT)$ with $D_0 = 1.2\ 10^{-11}$ cm^2/s from MEIS measurements.

These two relations provide a range of diffusion coefficients in our structures. Nevertheless, the determined values of activation energy differ from what has been reported in literature [THM+93] ($E_a = 1.45$ eV).

Such a difference can however be easily explained. Indeed, all the studies concerning HgTe/CdTe interdiffusion have been carried out for infrared applications and the interdiffusion characteristics were always determined after few hours of annealing, at temperatures ranging from 110°C [ASF86] to more than 450°C [TS87] under Hg saturated vapour pressure. Our study considerably differs from that approach as we are analysing the interdiffusion between HgTe and CdTe layers grown by MBE without annealing. Therefore, the interdiffusion only occurs during the growth and the substrate cooling-down. It is important to note that the time needed to grow HgTe is very short ($\leq$ 5 min) and is thus comparable to the cooling-down time. This is suggesting that the diffusion occurring during the end-of-growth cooling-down is certainly not negligible in our study and has to be taken into account for a more accurate determination of the diffusion coefficient.

So far, we have just discussed the diffusion in the case of HgTe/CdTe structures. To translate these results to the case of capped structures, it is necessary to investigate the influence of the barrier composition and

especially of the Cd fraction on the diffusion mechanism. Literature already addresses this point and reports larger diffusion coefficient when decreasing Cd composition [APW93]. Note that this statement is suggesting that Hg plays a major role in the diffusion. This can be due to the fact that despite its important mass, this atom is very mobile or even that the process is activated by Hg vacancies [THM+93]. To gain knowledge on this diffusion process, we are using the results extracted from the HRSTEM interface study (see 2.2.3.2). Similarly to MEIS, this technique does not allow to separate interdiffusion and roughness contributions and so we obtain x_{diff} by subtracting the AFM RMS values (see Table 2.1) of HgCdTe bottom barrier for the bottom interface and of HgTe for the top interface (see Table 2.1 for the RMS values). As the top and bottom interface widths have been shown to slightly differ, we consider the range of 1.5 to 2.0 nm for which we subtract the RMS values, thus determining x_{diff} between 1.3 and 1.6 nm. Note that for this sample, the growth time is much lower than for the 100 nm-thick HgTe/CdTe samples. With these considerations, the corresponding diffusion coefficient is reported in Table 2.7 and directly compared to the diffusion at the HgTe/CdTe interface at the same growth temperature.

These results are consistent with [APW93] by suggesting a larger diffusion at the HgCdTe interface. Nevertheless, additional measurements at different growth temperatures would be needed to conclude more precisely about the diffusion with these $Hg_{0.3}Cd_{0.7}Te$ barriers.

$T_g = 160°C$	XRR	MEIS	HRSTEM
Interface	HgTe/CdTe	HgTe/CdTe	HgTe/$Hg_{0.3}Cd_{0.7}Te$
Interface width (nm)	2.2	2.2	1.5-2.0
Interdiffusion width (nm)	1.9	1.8	1.3-1.6
Diffusion coefficient (cm^2/s)	$3.0\ 10^{-17}$	$2.6\ 10^{-17}$	$3.5 - 5.3\ 10^{-17}$

Table 2.7 – *Estimation of the diffusion coefficient as a function of the characterization technique and the considered interface for $T_g = 160\ °C$.*

2.4 Conclusion

This Chapter has reported the growth process and the material characterization of the HgTe/CdTe topological insulator structures.

The adaptation of the existing micrometer-thick HgCdTe growth process has been discussed with the incorporation of a CdTe buffer layer allowing to compensate for the majority of the substrate remaining defects and to separate the topological interfaces from the substrate. The addition of HgCdTe barriers aims to protect the HgTe top surface against Hg desorption but also symmetrizes the structure. With these layers, the quality of the interfaces has been improved and the HgTe electronic properties have been significantly enhanced manifesting in a rise of carrier mobility from 15,000 to more than 600,000 cm^2/V.s.

A more specific attention has then been paid to the optimization and the characterization of the HgTe layer. A cautious control of the chemical composition has demonstrated the possibility to grow pure HgTe. The tensile strain experienced by HgTe when grown on CdTe with a larger lattice parameter has been observed and enables the opening of a $\approx$ 20 meV bulk gap between the two Γ_{8LH} and Γ_{8HH} bulk bands. With these two characteristics, HgTe is an excellent candidate to be a topological insulator. As the electronic transport is assumed to take place at the topological interfaces, several characterization techniques have been used to gain knowledge on their quality in front of the surface state wavefunction extension (4.7 nm). With interface width of about 2 nm, the structures grown at temperature $\leq$ 165 °C present all the required qualities to probe the expected topological properties of our HgTe system. Magneto-transport measurements, that will be presented in Chapter 4, demonstrate the quality of these structures and their topological nature, thus validating the agreed efforts on the optimization of the growth process.

However, despite the good results obtained with this material, further improvements are still considered and needed to further enhance the electronic properties:

- A reduction of the bulk defect density is required to determine if the bulk contribution measured in the electronic transport of thick HgTe layers is due to these defects or should be considered as intrinsic to the system. From the preliminary results obtained on the growth temperature optimization study, we envisage an increase of the growth temperature from 160 to 175/180 °C. The associated adaptation of the Hg/Te ratio should also be considered. A reduction of the II-VI ratio, i.e. reduction of the Hg flux, should indeed also help in facilitating adatom surface mobility. Therefore, similar benefits as a growth temperature increase are expected without the detrimental effect of an enhanced intermixing.

- The preliminary observation of a difference of diffusion between HgTe/CdTe and HgTe/HgCdTe interfaces raises the idea of a barrier optimization by slightly increasing Cd composition. This should allow for a reduction of the interdiffusion at the HgTe interface, authorizing a rise of the growth temperature. As increasing growth temperature decreases the bulk defect density, this solution has to be seriously considered for future work.

- An increase of the bottom HgCdTe barrier thickness can also be envisaged to move the topological interface as far as possible from the buffer layer surface which can be polluted during the cool-down to HgCdTe epitaxy temperatures.

Obviously, this is a non-exhaustive list of the potential sources of improvement of the growth process. The strategies proposed here are complementing each other and are focusing on the simultaneous reduction of the bulk defect density and the improvement of interface morphology including roughness and interdiffusion.

Chapter 3

Nanofabrication of HgTe/CdTe structures and experimental setup

In order to study the topological properties of HgTe but also to use them in circuits, the patterning of the material is a crucial point. Hg-based materials are indeed known to be hard to process and this is one of the major issues of the fabrication of InfraRed detector made of HgCdTe. The sole presence of Hg is enough to make the nanofabrication process more complex due its high desorption rate. In this Chapter, we will consider especially the fabrication of Hall bars used for the magneto-transport measurements of the HgTe layers. Even if the fabrication process of such simple devices involves conventional technology, the main difficulty lies in the adaptation of the temperature not to damage the samples and compromise the topological properties of HgTe. Therefore, all steps of the process have been developed with a temperature $\leq$ 80°C. Moreover, concerning lithography, we have decided to avoid e-beam techniques to prevent the HgTe surface from heating [YKM+94] and local charging. The laser lithography technique have been favored to design the Hall bars. The quality and the reproducibility of the final process have been checked and confirmed.

The first objective of this Chapter is to present and explain all the steps of the nanofabrication process used for the realization of samples dedicated to magneto-transport experiments. In Chapter 5, the process of fabricating the spintronic devices is the same, only a few details differ and will be specified therein. The second objective is to introduce the whole experimental setup used for the magneto-transport measurements of the Hall bars.

3.1 Process of fabrication

The nanofabrication process of HgTe-based compounds has been developed using the knowledge and the experience of the InfraRed lab of CEA-LETI concerning HgCdTe materials. The material resources and the expertise of the Nanofab group at the Néel Institute and of the Plateforme de Technologie Amont (PTA) at CEA have been used appropriately for our Hg-based structures. An existing standard nanofabrication process has indeed been adapted to our material constraints.

3.1.1 Hall bar fabrication

The Hall bars are patterned using inverse laser lithography (Heidelberg DWL66FS) characterized by a resolution of 1 μm determined by the laser wavelength. The photosensitive resist 1805 is spin-coated with the parameters: 6000 rpm, 4000 rpm^2, 30 s. The resulting 500 nm thick resist is annealed at 80°C during one minute. The resist development is then performed using a 50% Microdev solution and 50 % deionized water during one minute. It is worth noting that annealing of this resist is usually done at 115 °C, therefore decreasing the temperature down to 80 °C should lower the resolution of the patterns. This reduction of annealing temperature is the major adaptation concerning the fabrication of the Hall bars. However, no significant impact on the resolution has been noticeable regarding the size of the Hall bars. The Hall bar dimensions were indeed varied with width W between 1 and 10 μm and with length L between 8 and 40 μm keeping the aspect ratio constant. Figure 3.1 reports the technological steps for their fabrication.

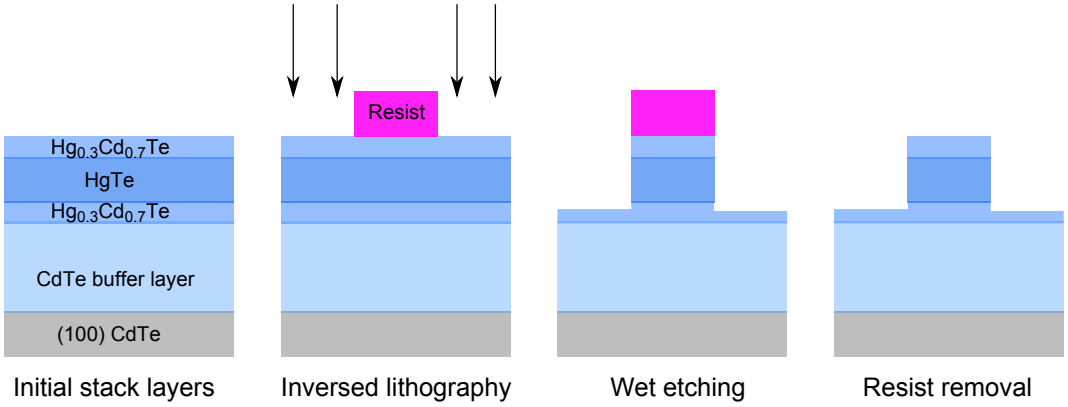

Figure 3.1 – *Steps for Hall bar fabrication.*

Once the lithography step has been performed, the Hall bars are obtained using a wet etching whose recipe has been elaborated thanks to the knowledge of the InfraRed Lab in HgCdTe nanofabrication. Wet etching was preferred instead of dry one as the use of dry etching is known to modify the electronic properties of HgCdTe layer by altering them [SMR+00] or even by converting it from p-type to n-type [BFM+96]. Being isotropic, this etch is similar in depth and width with about 100 nm of material removing in both directions. This thickness (width) of removed material is negligible in front of the micrometer-size Hall bar width, thus the resulting flanks can be considered as pretty sharp as shown in Fig. 3.2(c).

3.1.2 Metallic contacts

Electrodes are fabricated using laser lithography and Ni(10 nm)/Au (90 nm) evaporation (Plassys Evaporator) after an in-situ Ar-etch used to locally remove the capping layer above the HgTe top surface as illustrated in Fig. 3.3. Here, the use of dry etching has been unavoidable for two reasons. The first one is the need of a precise etch rate to be able to stop the process at vicinity of the HgTe top surface and such a nanometer-scale precision

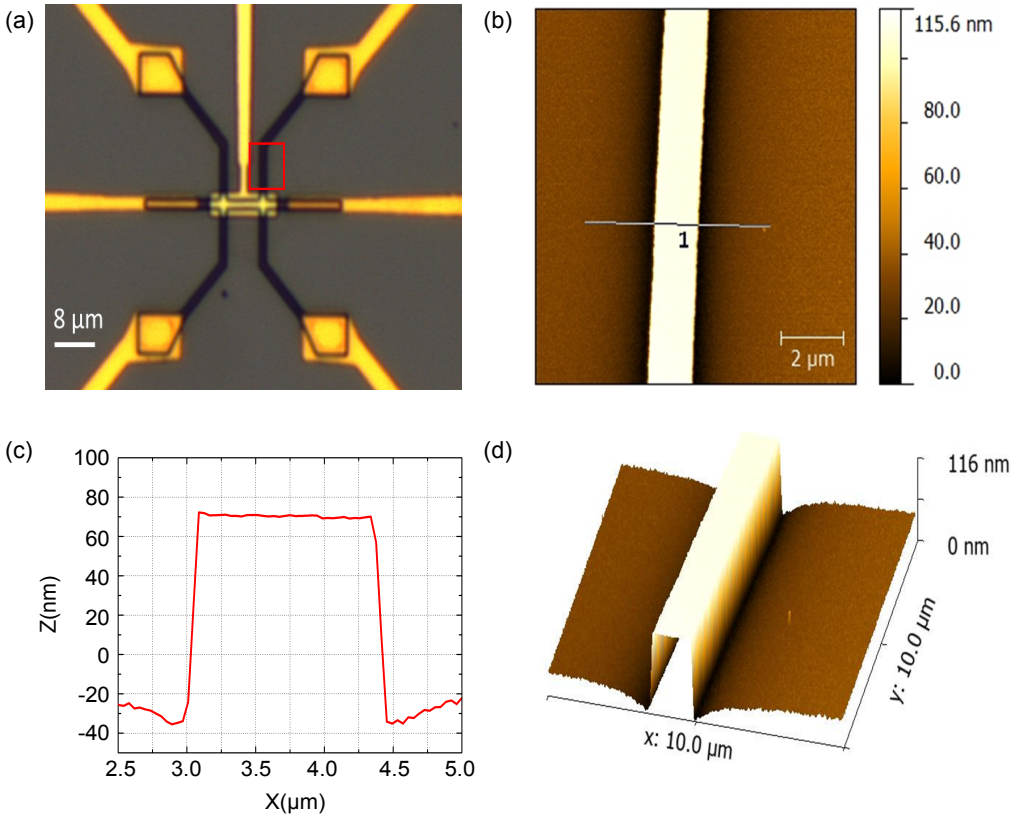

Figure 3.2 – *(a) Optical microscope image of a Hall bar. (b) Atomic Force Microscopy (AFM) images of the red zone of (a). (c) AFM extracted profile witnessing the isotropic etch on the flanks. (d) The associated three dimensional height profile.*

is not achievable using wet etching. The second reason is that we need to remove any oxide layer between the metallic deposit and the HgTe top surface, and this is only possible using an in-situ etching process (so dry etching) directly followed by the metal deposit. The HgTe layer is therefore contacted on its top interface as well as on its side surfaces as it is schematically represented in Fig. 3.3. Lift-off in acetone is used to remove the metal anywhere but in the contacts. With all the described characteristics, the contact resistance has been estimated to be about 1 kΩ.

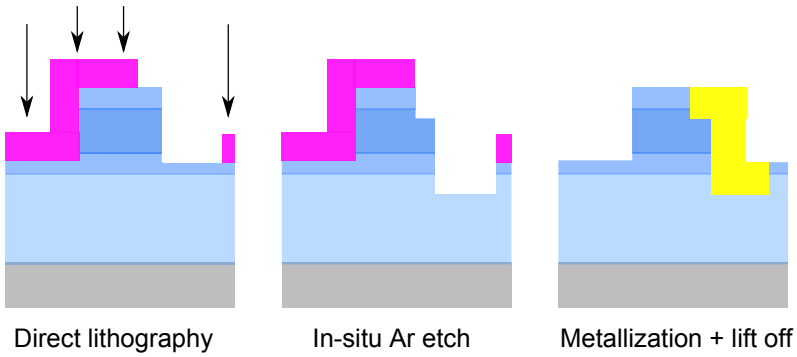

Figure 3.3 – *Steps for metallic contact fabrication.*

3.1.3 Passivation

The structures are passivated using Atomic Layer Deposition (ALD) (Fiji, Cambridge Nanotech) of Al_2O_3 high-k dielectric. Note that more than just a passivation layer, the Al_2O_3 layer also acts as the gate dielectric. The precursors are tri-methyl-aluminium (TMA) and H_2O. The deposition of about 25 nm was done at 80°C with a pulse time of 0.06 seconds and a purge time of 60 seconds for each precursors. This step of the nanofabrication process has been adapted from known recipes developed at high temperatures of about 250 °C. Here, the reduction of the temperature implies the reduction of the growth rate down to 0.81 Å/cycle and very long times of deposit.

The impact of this Al_2O_3 layer on the HgTe strain has been verified using HRXRD as it can be seen in Fig. 3.4. The HgTe peak is marked out by two black dashed lines and is clearly not moving with the addition of the Al_2O_3 layer. Only the intensity of the diffraction spectra is decreasing due to this passivation layer.

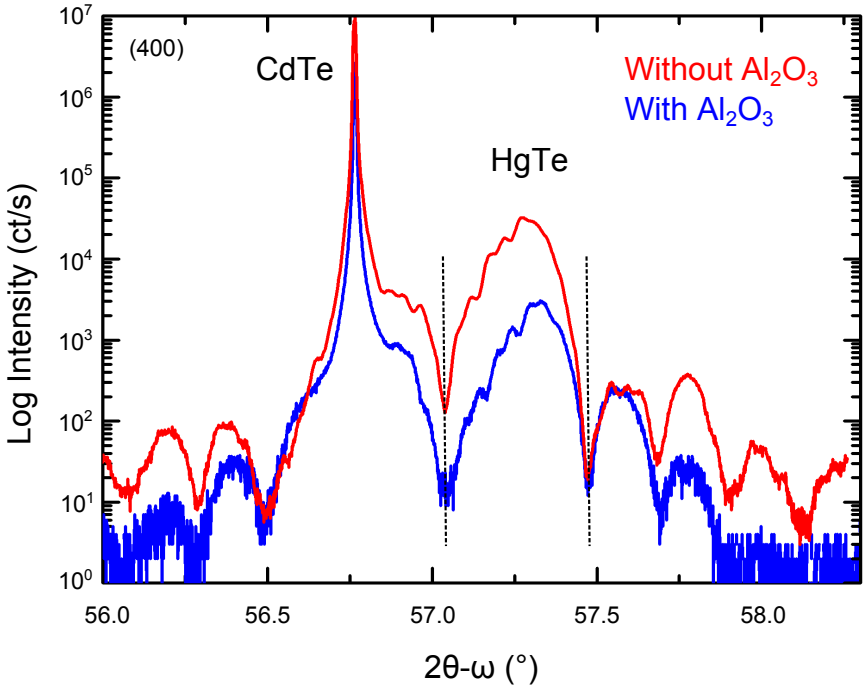

Figure 3.4 – *(400) HRXRD 2θ-ω scans of a 50 nm-thick HgTe grown on (100) CdTe (in red) and with an additional 25 nm-thick layer of Al_2O_3 (in blue). Black dashed lines mark out the HgTe peak.*

3.1.4 Top gate

The principle of the top gate fabrication is the same than for the metallic contacts and is explained step-by-step in Fig.3.5. Once all these steps have been carried out, the sample is ready to be bonded on a chip carrier.

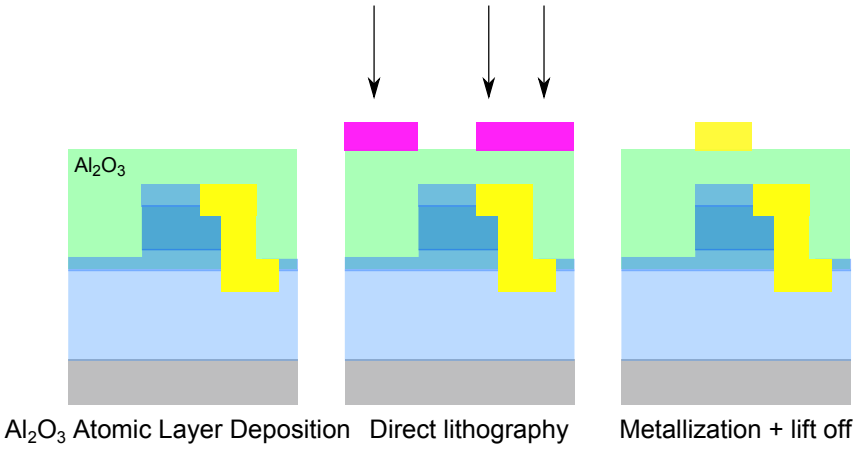

Figure 3.5 – *Steps for top gate fabrication.*

3.2 Gate depletion

The efficiency of the gate depends on the capacitance of materials deposited between the probed interface and the metallic gate contact [BBB+14]. In this nanofabrication process, the contacts are located both on the top surface and on the side of the Hall bars as illustrated by Fig. 3.5. With this configuration, they are able to probe both the top and the bottom surfaces of the topological insulator layer. If we concentrate first on the top surface, the HgTe layer is separated from the gate contact by two layers: the HgCdTe barrier and the Al_2O_3 passivation layer. These two layers will exactly behave as two capacitors in serie (see Fig. 3.6) having a total capacitance C_{top} expressed through the following relation:

$$C_{top} = \frac{C_{Al_2O_3}.C_{HgCdTe}}{(C_{Al_2O_3} + C_{HgCdTe})} \tag{3.1}$$

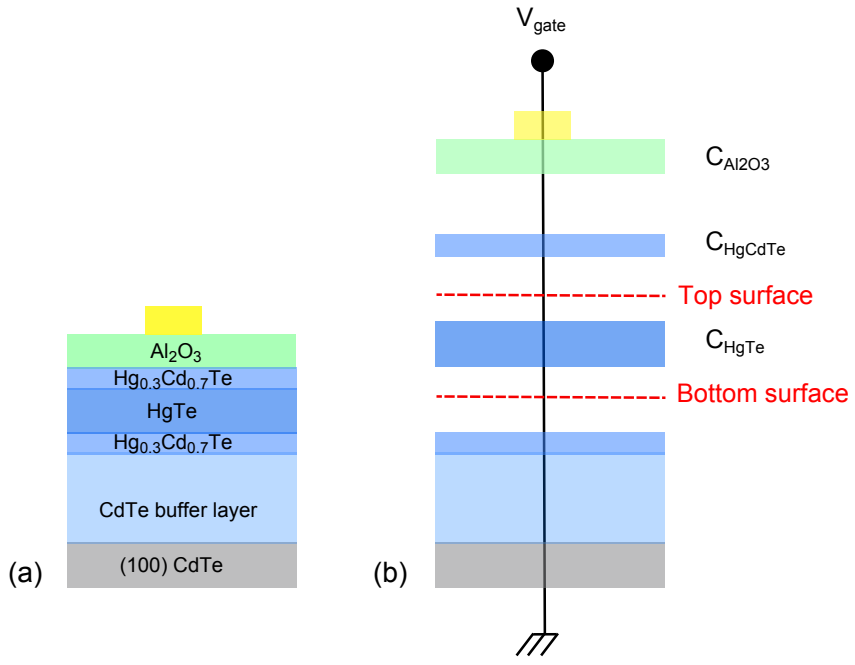

Figure 3.6 – *(a) The stack layer and (b) its capacitance equivalence.*

To calculate the depleting factor of this barrier and so the efficiency of the gate on the top surface electronic

variation, surface capacitance is used:

$$C = \frac{\epsilon_0.\epsilon_r}{d} \tag{3.2}$$

where ϵ_0 is the vaccum permittivity, ϵ_r is the material permittivity and d is the thickness of the dielectric layer.

The permittivity ϵ_r of the $Hg_{1-x}Cd_xTe$ layer is directly related to the amount of Cd x through the equation [Rol94]:

$$\epsilon_r = 20.5 - 15.6x + 5.7x^2 \tag{3.3}$$

Values of permittivity for different fraction of Cd are reported in the Table 3.1. Concerning Al_2O_3, ϵ_r value is about 8.8.

x	0.0	0.2	0.4	0.6	0.7	0.8	1.0
ϵ_r	20.8	17.8	15.3	13.2	12.4	11.5	10.5

Table 3.1 – *Permittivity values for $Hg_{1-x}Cd_xTe$.*

In order to estimate the difference of efficiency of the gate between the top and bottom interfaces, we consider e.g. a 15 nm-thick HgTe sample surrounded by 30 nm-thick HgCdTe barriers and recovered by 24 nm-thick Al_2O_3 layer. These thicknesses are representative of the samples measured in Chapter 4. Values of surface capacitance C as well as the corresponding depleting factor α are reported in Table 3.2. Note that α is obtained by the relation:

$$\alpha = \frac{C}{e} \tag{3.4}$$

where $e = 1.6\ 10^{-19}$ C. Values of α_{top} and α_{bot} are similar for such thin HgTe layer. The same exercise has been performed for several HgTe thicknesses. Figure 3.7 evidences the evolution of the ratio between α_{top} and α_{bot} as a function of the HgTe thickness emphasizing that the thicker the HgTe layer, the stronger the difference of electronic transport variation between the two interfaces.

Material	Al_2O_3	$Hg_{0.3}Cd_{0.7}Te$	HgTe
Thickness (nm)	24	30	15
Capacitance (10^{-3}F.m^{-2})	3.21	3.66	7.26
C_{top} (10^{-3}F.m^{-2})	1.72		/
α_{top}(10^{11} cm^{-2}.V^{-1})	10.8		/
C_{bot} (10^{-3}F.m^{-2})	1.50		
α_{bot}(10^{11} cm^{-2}.V^{-1})	9.3		

Table 3.2 – *Surface capacitance and gate depletion factor values for a stack made of a 15 nm-thick HgTe layer.*

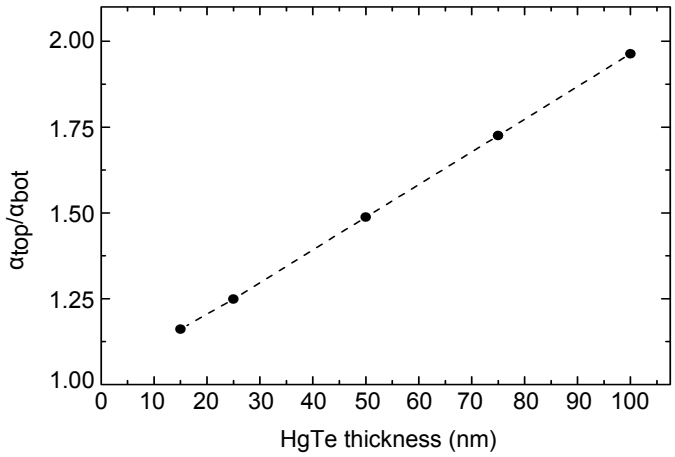

Figure 3.7 – *Evolution of the ratio between α_{top} and α_{bot} as a function of the HgTe thickness.*

Nevertheless, one has to realize that this calculation does not take into account the screening effects of the bottom surface by both the metallic top surface and the bulk. With these considerations, the ratio $\alpha_{top}/\alpha_{bot}$ is expected to be much larger.

3.3 Magneto-transport measurement experimental setup

After the nanofabrication processing of the Hall bars, the next step is to measure the fabricated samples in order to probe their electronic properties. Magneto-transport measurements are performed and are made possible thanks to cryogenics, electronics and magnetic resources available at the Néel Institute. The aim of this section is to describe the whole experimental setup.

3.3.1 Cryogenics

The magneto-transport measurements have been performed using either a ^{3}He or a ^{3}He/^{4}He dilution refrigerator. Three different cryostats have been used during this PhD. In this section, we choose to focus on the explanation of the dilution refrigerator. Figure 3.8 illustrates the Inner Vaccum Chamber (IVC) of the dilution fridge which is separated by vacuum from the surrounding ^{4}He bath. Note that the sample is mounted in vacuum inside the IVC. This figure explains the principle of a dilution cryostat which is governed by the circulation of a mixture composed of ^{4}He with 15% of ^{3}He. The dilution cryostat is made of:

- **a 1K pot**: to cool the incoming ^{3}He flow to 1.5 K by pumping on both a ^{4}He reservoir and on the reverse ^{3}He flow.
- **heat exchangers**: to transfer heat between the two counterpropagating ^{3}He flow. The presence of exchangers enables the temperature to be considerably decreased. Indeed, a temperature of about 100 mK is measured on the cold plate and of about 40 mK on the mixing chamber.
- **a mixing chamber**: to achieve the dilution process. Thanks to its low temperature, the mixing chamber separates the mixture in two phases: a concentrated phase rich in ^{3}He and a diluted phase rich in ^{4}He. The evaporation of ^{3}He from the concentrated phase to the diluted one liberates cooling power. The diluted phase is then extracted up to the still.
- **a still**: to extract the ^{3}He atoms from the ^{4}He rich phase. These atoms are pumped and then re-injected in the circulation circuit.

The samples are mounted just below the mixing chamber, thus allowing to perform magneto-transport measurements at temperatures down to around 40 mK.

Temperature-dependant analyses have also been performed using a heater localized on the mixing chamber. Temperatures up to 800 mK were available. However, in order to reach higher temperatures, the ^{3}He/^{4}He mixture has been repatriated in the tanks. The IVC was also constantly pumped in order to limit the heating exchange between ^{4}He bath and the mixing chamber. With these precautions, the heater allows to reach temperatures up to 20 K. A temperature regulator was also used to ensure a good stability.

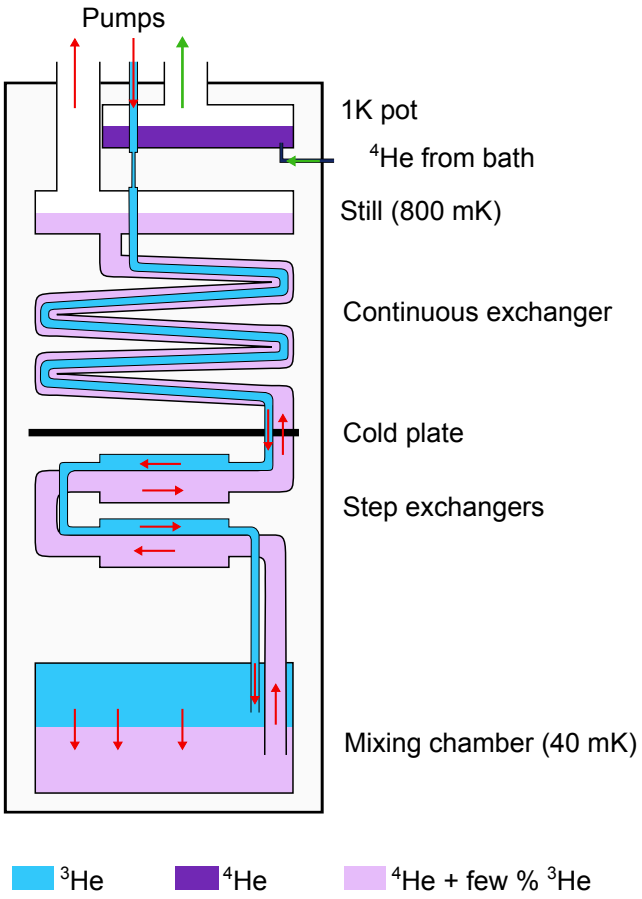

Figure 3.8 – *Schematic representation of the functioning of a dilution cryostat.*

3.3.2 Electronics

Figure 3.9 displays the experimental setup used for the Hall bar measurements. The Hall bars are measured in current bias using the association of a voltage source and a high resistance of 10 MΩ on the electrode 1. The voltage source is based on a commercial Digital-to-Analog Converter (DAC) chip which is assembled in electronic shop of Institut Néel. This high resistance value is chosen in order to be larger than the sample resistance to set the current flowing through the sample. With a voltage of 10 mV, the resulting excitation current is of 1 nA. The gate voltage is applied using the same voltage source. Both longitudinal and Hall voltages are measured using three electrodes among the 2, 3 5 and 6 ones. Figure 3.9 evidences the use of electrode 3 and 5 for Hall voltage V_{xy} measurement, 5 and 6 for longitudinal voltage V_{xx} characterization. These two voltages are measured using amplificators and a standard Lock-in acquisition (Signal Recovery 7280 and Stanford Research System SR830). It is worth noting that the filtering and thermalization of the wiring enable the stability and precision of the measurements.

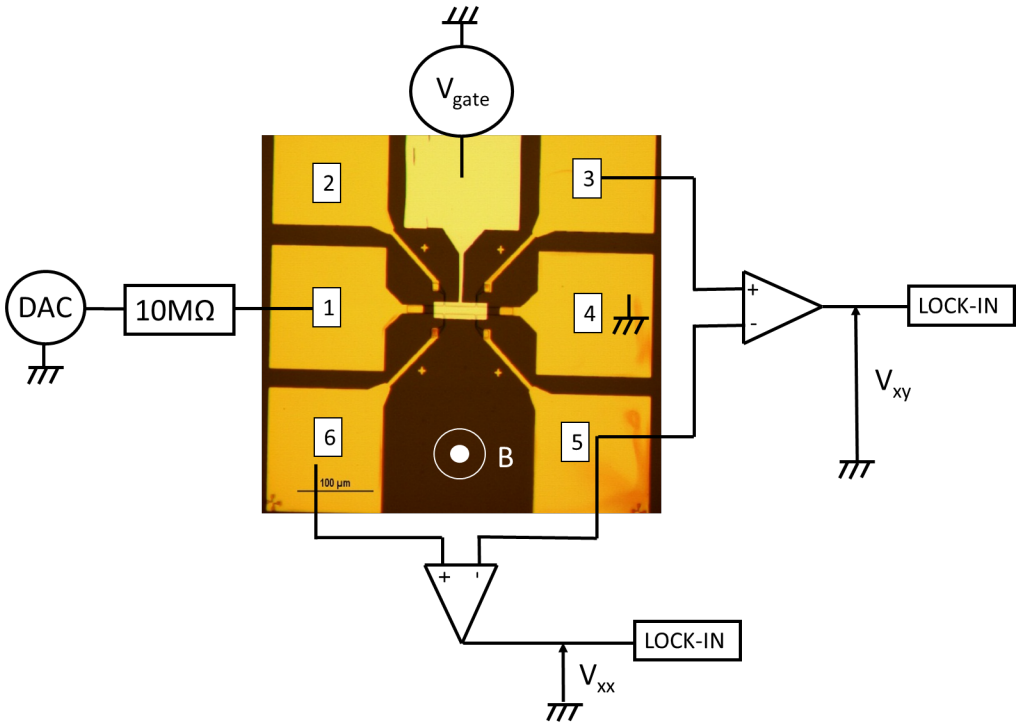

Figure 3.9 – *Experimental setup for Hall bar measurements.*

3.3.3 Gate calibration

Once the sample is electrically connected inside the dilution cryostat, the measurements may start. The first step always consist in testing the gate, meaning the available range before leaking. In practice, we have never increase the gate voltage until the leak. The typical test consists of probing the longitudinal resistance as a function of the gate voltage. The gate voltage range is increased as long as the two reverse traces of the longitudinal resistance overlap. The test stops as soon as an hysteresis effect appears as shown in the example of Fig. 3.10. Indeed, an hysteresis effect is the evidence that another 2D electron gas is charging at the HgTe/HgCdTe interfaces [HBS+06] and this gas will pollute the measurements of the topological insulator electronic properties.

This simple test allows to determine the available range of gate voltage to essentially probe the topological gas. In practice, the voltage range was sufficient to permit to explore gate voltage region of the Dirac point. The typical range was $[-1;1]$ V before hysteresis.

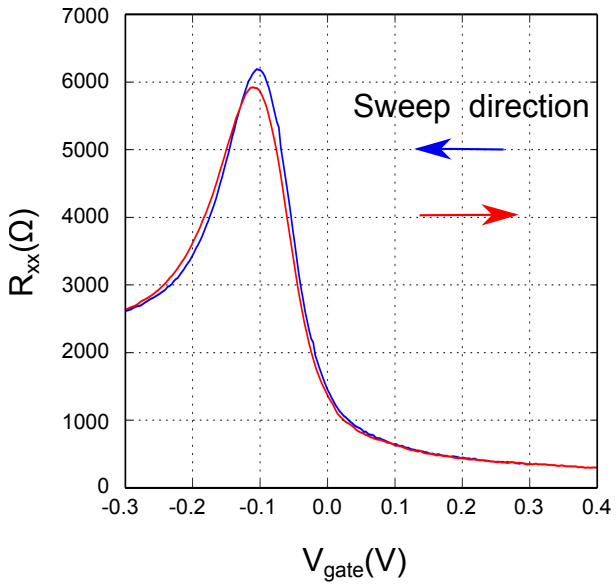

Figure 3.10 – *Longitudinal resistance R_{xx} as a function of the gate voltage at zero magnetic field. Red and blue arrows indicate the sweep direction of the corresponding curves. The shift between the red and the blue curves illustrates a beginning of hysteresis.*

3.3.4 Magnetic field control

The magnetic field is applied thanks to a superconducting magnet system composed of a 6T/3T/3T Vector Rotate Magnet (VRM) supplied in power by the Oxford Instruments Mercury IPS. The control of the magnetic field is ensured by the VRM software, developed by Oxford Instruments, and is possible in the cartesian, cylindrical and spherical coordinates. Figure 3.11 reports the three available coordinate systems for the control of magnetic field B. For the magneto-transport measurements, we have widely used the cartesian coordinate system as the magnetic field was mainly applied perpendicular ($B_\perp = B_z$) to the sample surface to probe quantum Hall effect. However, in-plane magnetic field $B_{/\!/} = (B_x, B_y)$ has also been used to do angle dependence study of the Shubnikov-de Haas oscillations. Indeed, the addition of $B_{/\!/}$ component allowed to increase the total magnetic field while keeping a constant $B_\perp$. Spherical coordinates and especially the ϕ dependence have also been used for this purpose. Details of this study are reported in Appendix B. Note that no angular correction has been added to compensate for the shift (due to the sticking step on the chip carrier) between the sample plane and the magnetic field axis plane (x, y). Tests were performed and evidenced a negligible shift.

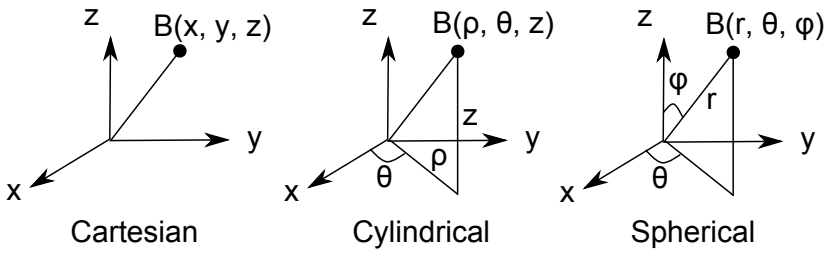

Figure 3.11 – *The three coordinate systems available for the control of magnetic field.*

3.4 Conclusion

This Chapter has reported the nanofabrication process as well as a full description of the magneto-transport experimental setup.

The Hall bar nanofabrication process has been developed and optimized to be suitable regarding Hg desorption. The main important point is that all temperatures have been set below 80°C not to damage the former stack layers and the topological properties. The study of the gate depletion efficiency has theoretically demonstrated that the contributions from top and bottom interfaces should be shifted due to a difference in the gate depletion factor. Experimental data presented in Chapter 4 will illustrate this point.

The experimental setup including cryogenics, electronics and the magnetic resources has been presented. With all these resources, gate voltage as well as magnetic field variations allow us to perform a magneto-transport study at both low and high magnetic fields for a complete electrical characterization of the structures. Results of these studies are reported in the next Chapters.

Chapter 4

Magneto-transport measurements

The aim of this Chapter is to explain and give an overview of the low temperature electronic transport measurements performed on 3D HgTe topological insulator structures. These measurements provide a way to probe the electronic properties of the metallic surface states but also highlight their topological properties.

The first electronic transport studies to be reported on 3D topological insulators were focusing on Bi-based topological insulator crystals like Bi_2Se_3 [AMR+10] or even Bi_2Te_3 [BRG15]. However due to very low mobilities in the range of 10^3 $cm^2.V^{-1}.s^{-1}$, Bi-based topological insulators require a very large magnetic field B to observe signatures of quantum Hall effect like quantized plateaus of the Hall resistance. Moreover, the large bulk conduction caused by chemical imperfections is an additional limit to the transport measurements in these systems preventing from having vanishing longitudinal resistance minima. Recently, new strategies have been proposed to grow Bi-based topological insulators with lower bulk conduction such as the use of the quaternary alloy $(Bi,Sb)_2(Te,Se)_3$ [ASS+12] [PWA+14] for which the Dirac point can be engineered to be within the bulk gap by varying the composition of the alloy. With crystals thinner than 1 μm, accessing the topological properties via transport measurements is now possible for these structures, demonstrating first evidences of weak antilocalization [PWA+14] and of quantum Hall effect with quantized plateaus and small longitudinal resistance [XML+14].

On the contrary, the HgTe topological insulator system is characterized with a high mobility in the range of 10^5 $cm^2.V^{-1}.s^{-1}$ associated to a low bulk conduction, thus allowing quantized plateaus to appear for B values as low as 1 T. Up to now, only a few studies have been reported on 3D HgTe topological insulators with thicknesses larger than 70 nm [BLN+11] [KKO+14] [BTS+14] and have demonstrated the complexity of the transport mechanism with especially the addition of several contributions besides the topological surface states [Thi14]. This highlights a remaining problem of 3D topological insulator structures which are suffering from side surface and bulk contributions preventing the observation of cancelling longitudinal resistance and thus from reaching a well-defined quantum Hall regime. Therefore, it does not allow to completely understand the quantum Hall phenomena in these structures and to point out the associated topological properties.

In this Chapter, we first present magneto-conductance measurements performed at low magnetic field for a 100 nm-thick HgTe layer. The low magnetic field measurements are used to microscopically characterize the samples by extracting electronic properties such as carrier density and mobility. These properties are a direct illustration of the quality of the samples. Additionally, high magnetic field measurements are presented to probe the band structure properties from the peculiar signatures of the Hall and the longitudinal resistances. The complexity of the transport signatures confirms the difficulty to access topological surface state properties due to the addition of bulk and side surface contributions. Our strategy to get rid of these contributions and to reach

quantum Hall regime with vanishing resistance has been to gradually reduce the HgTe thickness down to 50, 25 and finally 15 nm. With this latter HgTe thickness, bulk and side surface contributions are this time negligible, thus leading to clear quantum Hall effect signatures. Furthermore, the Dirac nature of the topological surface states is revealed using quantum Hall transport spectroscopy with temperature dependent activation process. This analysis is reported at the end of this Chapter.

The combination of all these studies for both low and high magnetic field, as a function of gate voltages, temperatures as well as HgTe thicknesses aims at characterizing the electronic transport mechanisms occurring in such 3D strained HgTe topological insulator systems.

For an easier reading of this Chapter, we have chosen to only present the detailed analysis of the 100 and 15 nm-thick HgTe samples. However the reader is invited to refer to Appendix C for the complete analysis of the 50 and 25 nm-thick HgTe samples.

4.1 Magneto-conductance measurements

In this section, we present magneto-conductance studies performed on 100 and 15 nm-thick HgTe samples. Note that for each sample, the Hall bars have the following dimensions: a length $L = 40$ μm and a width $W = 10$ μm.

Low magnetic field measurements are first presented and allow the determination of carrier density, mobility and the analysis of the longitudinal resistance R_{xx} at zero field. These quantities are providing information about the overall electronic transport of our structures.

To go one step further and access more specifically the topological surface state properties, high magnetic field measurements have been achieved. Mappings of the longitudinal and Hall resistance gate voltage and magnetic field dependences are reported. The evolution of these mapping features with the reduction of HgTe thickness reveals the reduction of the bulk and side surface contributions by decreasing the bulk to surface ratio. These contributions are even becoming completely negligible for a HgTe thickness of 15 nm, thus allowing to reach the quantum Hall effect regime with vanishing resistance. However, the price to pay is the hybridization of the two topological surface states. Already introduced in Chapter 1, this coupling mechanism is expected to lift the spin degeneracy [LSY+10] [ZLS15] and to open a gap at the Dirac point.

4.1.1 100 nm-thick HgTe layer

The magneto-transport study begins with a thick HgTe layer of 106 nm. The thickness has been accurately determined by HRXRD. Both longitudinal and Hall resistances are probed as a function of the magnetic field and the top gate voltage at 100 mK. For details about measurement methods and setup, the reader is invited to refer to Chapter 3 (see 3.3.2). Note that the range of gate voltage used for each measurement is limited to prevent from hysteresis effect, as mentioned in Chapter 3 (see 3.3.3).

4.1.1.1 Low magnetic field measurements

Low magnetic field data have been extracted for $B \leq 1$ T. In this regime, the longitudinal resistance R_{xx} does not yet manifest quantum oscillations and the Hall resistance R_{xy} is not yet quantized but is expected to linearly vary with the magnetic field B (see Fig. 4.1) with a slope R_H also called the Hall constant. Using a single carrier model and the R_{xx} and R_{xy} features, electronic properties such as the carrier density n_H and the carrier mobility μ are extracted and reported in Fig. 4.2.

Fig. 4.1 displays the R_{xy} variation with B for several values of V_{gate}. Three different behaviors are clearly noticeable:

- **I for $V_{gate} \geq$ - 0.35 V**: in this range of gate voltage, R_{xy} varies linearly with B and with a positive slope R_H. Note that R_H value is decreasing with increasing V_{gate} as it can be seen in Fig. 4.2(a). Furthermore, $\frac{1}{R_H}$ is plotted in Fig. 4.2(c) and evidences a linear variation with V_{gate}. This feature is very similar to what has been reported in graphene [WvEK+11] [WNM+08] away from the Dirac point and is thus consistent with a single carrier model where the transport is governed by electrons. Indeed, in the framework of this model (see Chapter 1 1.2.1) $\frac{1}{R_H} = ne \geq 0$ with n the electron density.
- **II for V_{gate} between -0.60 V and -0.35 V**: R_{xy} variation with B is reported for $V_{gate} = -0.50$ V. While a linear behavior with a negative slope is noticeable for $B \geq 0.3$ T, suggesting a transport carried by holes, R_{xy} transits from negative to positive for $B \leq 0.3$ T and its slope becomes even positive for $B \leq 0.1$ T. This change of slope was not observed in the regime I and is typical of the addition of another type

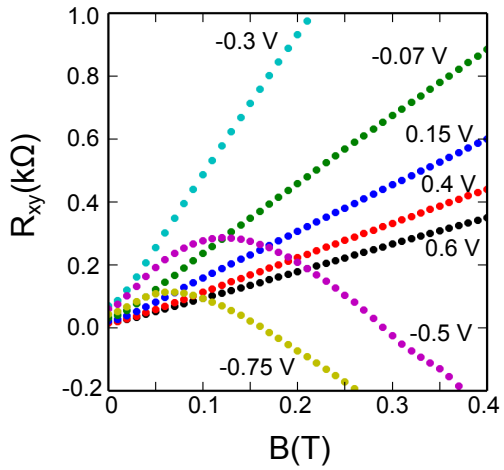

Figure 4.1 – *Hall resistance R_{xy} as a function of magnetic field B up to 0.4 T for several values of gate voltage V_{gate}. Data have been extracted at a temperature T= 60 mK with a current bias I_{bias} of 1 nA.*

of carriers, here electrons. R_H values have been extracted from the slope of R_{xy} for B limited between 0.3 and 1 T. Within these conditions, R_H is shown to linearly vary with V_{gate}, crossing especially 0, thus resulting in a divergence of $\frac{1}{R_H}$ as it can be seen in Fig. 4.2(c). Such a linear behavior of R_H suggests the transition to a two carrier model (see Chapter 1 1.2.1) which especially defines $\frac{1}{R_H} = \frac{e(n+p)^2}{n-p}$ assuming similar mobilities for electrons and holes and n, p the electron and hole density, respectively. This divergence of $\frac{1}{R_H}$ is moreover fully consistent with graphene [WvEK+11] [WNM+08] for which charge neutrality ($n = p$) is expected at the Dirac point. The corresponding position of the Charge Neutrality Point (CNP) is highlighted by an orange dashed line and will be used just after to characterize the transport.

- **III for $V_{gate} \leq$ - 0.60 V**: R_{xy} variation with B is shown in Fig. 4.1 for $V_{gate} = -0.75$ V. As in the previous case, R_{xy} is not purely linear but this time the change of slope occurs for a smaller magnetic field value at 0.07 T. The impact of additional carriers is less pronounced than in regime II. In parallel, the corresponding $\frac{1}{R_H}$ variation (still extracted for B between 0.3 and 1 T) exhibits a linear dependence with gate voltage, similarly to regime I, thus suggesting a single carrier model where the transport is this time governed by holes. Moreover, the non-linear R_{xy} behavior at very low field suggests an additional contribution of electrons.

In conclusion, the $\frac{1}{R_H}$ characteristics evidence the ambipolarity of our structures and are consistent with a Dirac cone picture. However, the R_{xy} change of slope illustrates some divergence to a single Dirac cone model with especially the addition of electrons in the hole-side. A model with two Dirac cones attributed to the top and bottom surface states appears to be more accurate and is represented by the schemes on top of Fig. 4.2(a). Top gate voltage allows to sweep Fermi level E_F from electron- to hole-side of the top surface Dirac cone. However, concerning the bottom surface, the density is expected to be less affected by the gate voltage because of the bulk and top surface state screening effects. Thus E_F always lies in the electron-side of the bottom Dirac cone, at least for the range of gate voltage used in this experiment. This scenario is consistent with our data but needs to be validated by the high magnetic field measurements.

With the validation of the $\frac{1}{R_H}$ Dirac cone picture, single carrier model can be used away from the Dirac

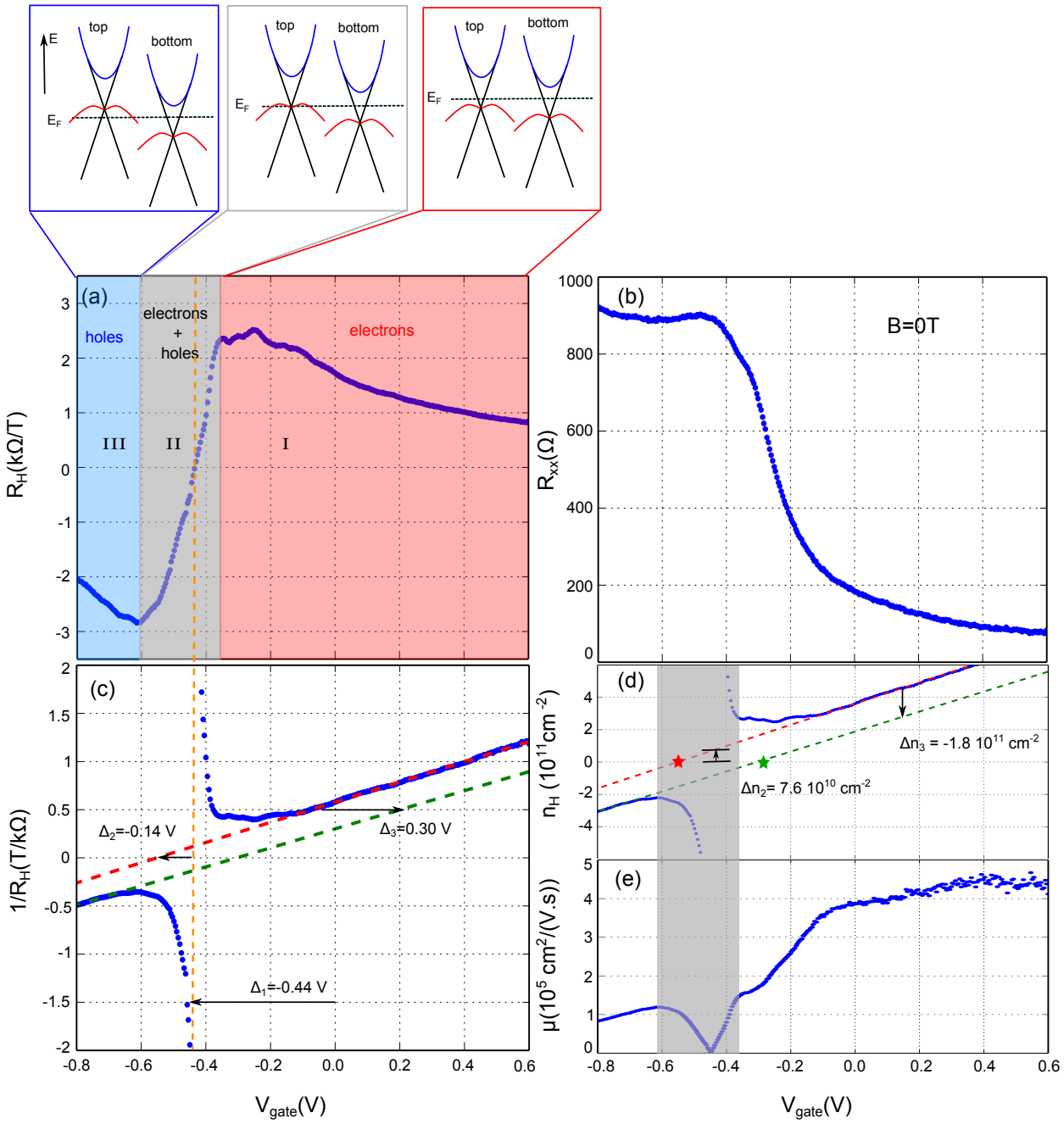

Figure 4.2 – *Low magnetic field analysis of a 100 nm-thick HgTe layer. All the presented quantities are represented as function of the gate voltage V_{gate} and have been extracted for magnetic field $B \leq 1$ T at a temperature T= 60 mK with a current bias I_{bias} of 1 nA. (a) Hall constant R_H (top schemes: top and bottom surface Dirac cones with the associated position of the Fermi level E_F). (b) Longitudinal resistance R_{xx} for B=0 T. (c) Inverse of the Hall constant $\frac{1}{R_H}$ (red and green dashed lines evidence linear variation of the branches in both electron- and hole-side). (d) Carrier density n_H. (e) Carrier mobility μ. Grey color band corresponds to the gate voltage range for which the single carrier model is not valid.*

point, i.e. outside regime II, to determine the carrier density n_H (see Fig. 4.2(d)) through the relation:

$$n_H = \frac{1}{R_H e} \tag{4.1}$$

It is worth noting that using this methodology, n_H should correspond to the top surface state carrier density.

The linear variation of the density with the gate voltage enables to characterize the gate depletion effi-

ciency with the extraction of the gate depletion factor $\alpha_H = 6.6\ 10^{11}$ cm^{-2}.V^{-1}, determined from the slope of the density linear branches fitted by red and green dashed lines. This value is reproducible for all the other samples with different thicknesses but differ from the the estimation derived from the capacitance model reported in Chapter 3 (see 3.2) which gives 10.8 10^{11} cm^{-2}.V^{-1} considering a similar structure. Such a discrepancy between the experimental and the model values is so far not understood. Note that the determination of this factor is important as it will constitute a reliable tool for the understanding of data at larger magnetic fields.

The combined analysis of $\frac{1}{R_H}$ and n_H features evidences however some discrepancies with respect to the Dirac formalism [WNM+08] with especially the identification of three voltage shifts (see Fig. 4.2(c)) and their associated densities:

- Δ_1 illustrates the gate voltage shift of the CNP (see orange dashed line in Fig.4.2(c)) from $V_{gate} = 0$ V expected for undoped sample to $V_{gate} = -0.44$ V. This negative gate voltage offset clearly evidences n-type doping of the top surface.

  By looking to both the growth and the nanofabrication (see Appendix 3) recipes, sources of doping can be identified. The growth under Te rich conditions is expected to create Hg vacancies and thus a p-type doping of the structure which does not explain the Δ_1 voltage offset. The realization of the metallic contacts and especially the dry etching with Ar ions can also impact the electronic properties of the structure and convert it from p-type to n-type [BFM+96] as already discussed in Chapter 3 (see 3.1.1). This latter point gives some insights to explain the observed n-type doping.

- the linear variation of $\frac{1}{R_H}$ in the electron-side is emphasized by the red dashed line. However, in the case of an undoped Dirac cone, one expect this line to cross zero at the CNP. Here, this is not the case and a voltage shift $\Delta_2 = -0.14$ V is estimated as reported in Fig. 4.2(c). The sign of Δ_2 suggests the presence of an additional conduction channel characterized by a density shift $\Delta n_2 = 7.6\ 10^{10}$ cm^{-2} as it can be seen in Fig. 4.2(d). The Dirac point, defined as the gate voltage for which $n_H = 0$ and highlighted by a red star, is shifted at lower gate voltage values than the CNP. This means that a non-zero electron density is needed to balance an extra hole density and reach the charge neutrality. From this, we can conclude that Δn_2 corresponds to the addition of holes to the transport.

- the linear variation of $\frac{1}{R_H}$ in the hole-side has been highlighted by the green dashed line. Red and green lines are experiencing the same linear variation with V_{gate}. However, they are separated by a voltage offset $\Delta_3 = 0.30$ V which has the peculiarity not to depend on the gate voltage. Moreover, it leads to an increased density value in the hole-side of $\Delta n_3 = -1.8\ 10^{11}$ cm^{-2} as evidenced in Fig. 4.2(d).

  This addition of holes in the transport can be potentially attributed to the surface states coupling to the Γ_{8HH} bulk band in the hole-side as previously introduced in Chapter 1 (see 1.1.6). This coupling is indeed expected to open extra conduction channels.

  Consequently, the carrier density data presented in Fig. 4.2(d) are revealing an interesting feature. The red and green dashed lines do not cross zero density at the same gate voltage position, highlighting a difference of Dirac points for electron- and hole-sides at -0.55 V (see red star) and -0.34 V (see green star), respectively. So far, this behavior is not clearly understood but is reproduced on the data at larger magnetic fields and is mostly noticed for the 25 nm-thick HgTe sample (see Appendix C Fig. C.6(a)).

To complete this low magnetic field analysis, longitudinal resistance R_{xx} is now considered. Fig. 4.2(b) displays the evolution of R_{xx} for $B = 0$ T. Similarly to R_H, three regimes are clearly visible. The first one,

corresponding to the electron-side, is characterized with a resistance value of about 100 Ω, while the third one, corresponding to the hole-side, presents resistance values of about 900 Ω. The second regime, illustrated by a resistance peak, corresponds to the transition of one major carrier type to the other. This behavior is consistent with the ambipolarity of our structures demonstrated just before. The difference of resistance between the so-called electron- and hole-sides is due to the fact that in the former regime only the surface states contribute to the transport in the range of gate voltage used, while in the latter one the coupling to the Γ_{8HH} bulk band opens extra conduction channels.

Moreover, from the combined variations of R_{xx} and R_H, mobility values μ are determined for the regime I and III, where single carrier model is valid, and are reported in Fig. 4.2(e) using the expression:

$$\mu = \frac{|R_H|}{\rho_{xx}(B = 0T)} \tag{4.2}$$

with $\rho_{xx} = R_{xx}\frac{W}{L}$.

Mobility up to about 450,000 $cm^2.V^{-1}.s^{-1}$ is measured. This high value is a good indicator of the constant efforts and improvements of the growth process presented in Chapter 2. Indeed, before improving the material and especially the roughness of the interfaces, the mobility never exceeded 17,000 $cm^2.V^{-1}.s^{-1}$ in such a thick HgTe layer [Bou13]. It is worth noting that mobility values are very high in the electron-side compared to the hole-side ($\approx 100,000$ $cm^2.V^{-1}.s^{-1}$). Such a difference of mobility is explained by the coupling to the Γ_{8HH} bulk band which perturbs the surface state transport in the hole regime as it is characterized by hole mobility lower than 1,000 $cm^2.V^{-1}.s^{-1}$ [FSW+86].

In conclusion, this whole analysis of the low magnetic field properties, such as the Hall constant, the carrier density and the carrier mobility, provides first information about electronic transport occurring in such 100 nm-thick HgTe sample. Deviations from the single carrier model are reported suggesting the contribution of the bottom surface. Moreover, deviations from the Dirac cone formalism are also observed and indicate the superposition of different contributions to the electronic transport such as bulk or even side surfaces. High magnetic field measurements are presented just after and will provide new insights to allow distinguishing these transport contributions.

4.1.1.2 High magnetic field measurements

To go one step further in the characterization of the topological surface states, the magnetic field $\vec{B} = B\vec{z}$ is increased, thus resulting in the appearance of R_{xx} quantum oscillations, attributed to contributions with a non-zero Fermi surface perpendicular to $\vec{z}$. Two-dimensional (2D) electron gas from side surfaces are thus not expected to participate. Therefore, the R_{xx} oscillatory behavior could originate from 2D top and bottom topological surface states, 2D Electron Gas (2DEG) trapped at one interface or even from the 3D bulk. Better known as Shubnikov-de Haas Oscillations (SdHO), these oscillations carry a lot of information about the electronic transport properties concerning the Landau Level (LL) energy spectrum, the effective mass of the carriers, the LL broadening or even the Berry's phase. Note that the whole next section is dedicated to the determination of these parameters. The Fast Fourier Transform (FFT) analysis of the SdHO enables to characterize and identify the origin of these oscillations. As already mentioned in Chapter 1, SdHO are illustrating the filling of individual LLs and thus their minima are separated by one unit of filling factor ν. The

relation between ν and B has already been demonstrated in Chapter 1 (see 1.58) and enables the derivation of the relation below:

$$\Delta\nu = 1 = \frac{nh}{e}\Delta(\frac{1}{B}) \tag{4.3}$$

The oscillation frequency and their density are then directly related through:

$$F = \frac{1}{\Delta(1/B)} = \frac{nh}{e} \tag{4.4}$$

Therefore, FFT allows the carrier density n of each contribution to be determined from the oscillations frequency F.

Longitudinal resistance R_{xx} quantum oscillations are observable on the mapping of Fig. 4.3(a) measured as a function of B (up to 5 T) and V_{gate} at 60 mK. Moreover, Fig. 4.3(c) proposes a closer view of R_{xx} variations in the electron-side by adjusting the scale compared to Fig. 4.3(a) for a better observation of the resistance features and especially of these quantum oscillations.

FFT analysis of R_{xx} oscillations has been performed for B values between 0.3 T and 5 T. This analysis has only been carried out in the electron-side as features of R_{xx} in the hole-side are too complicated due to the presence of several contributions and to the coupling with Γ_{8HH} bulk band in this regime. The resulting FFT amplitude is represented in Fig. 4.4(a) as a function of the frequency F for several values of V_{gate}. Two major peaks and so two major contributions are reported and highlighted by black and green arrows. The corresponding carrier density n_1 (in black) and n_2 (in green) have been extracted and plotted in Fig. 4.4(b). The low magnetic field extracted density n_H is also represented for comparison. First of all, one can notice that n_2 is constant with V_{gate} at $\approx 0.8\ 10^{11}$ cm^{-2}. On the contrary, n_1 is significantly varying with V_{gate} with an effective gate depletion factor of $\alpha_1 \approx 3.6\ 10^{11}$ cm^{-2}. V^{-1}. It is worth noting that n_1 values differ from n_H and that this shift between the two densities is even increasing with V_{gate}.

From this FFT analysis, we can conclude that one major contribution (n_1) is evidenced and is attributed to the top surface states. Being not affected by the gate voltage, the second contribution (n_2) characterizes the bottom surface states. The density shift between n_1 and n_2 can be explained by top surface state and bulk screening effects which are assumed to be important at this thickness and prevent from depleting the carriers of the bottom surface. Finally, a third contribution ($n_H - n_1 - n_2$) has been inferred and corresponds to a 2D electron gas that does not manifest into SdHO but which is unambiguously depleting by the gate voltage. Transport on the topological side surfaces meets this criterion and thus can explain this extra contribution.

In the quantum Hall state of matter, the quantum oscillations of R_{xx} are directly associated to quantized Hall resistance R_{xy} plateaus. Scaling in $\frac{h}{e^2}$, the quantum of resistance, the successive resistance plateaus are containing information about the transport mechanism meaning how the conduction channels spread and organize themselves over the sample.

R_{xx} quantum oscillations manifest themselves in the R_{xx} mapping (see Fig.4.3(a) and (c)) through the white branches identified as SdHO maxima and which are dependent on both V_{gate} and B. In parallel, R_{xy} mapping (see Fig. 4.3(b)) depicts successive resistance plateaus. These two complementary features are signatures of the Quantum Hall Effect (QHE). Nevertheless, it is worth noting that the second contribution identified from FFT analysis to be constant with gate voltage seems to be hardly distinguishable on these mappings. Moreover, the presented mappings are clearly illustrating non-regular patterns with especially a mixing of the R_{xx} maxima branches. Note that, besides, SdHO are not depicting clear vanishing minima as expected in the QH regime. All these observations suggest the addition of several contributions to the electronic transport, which is in

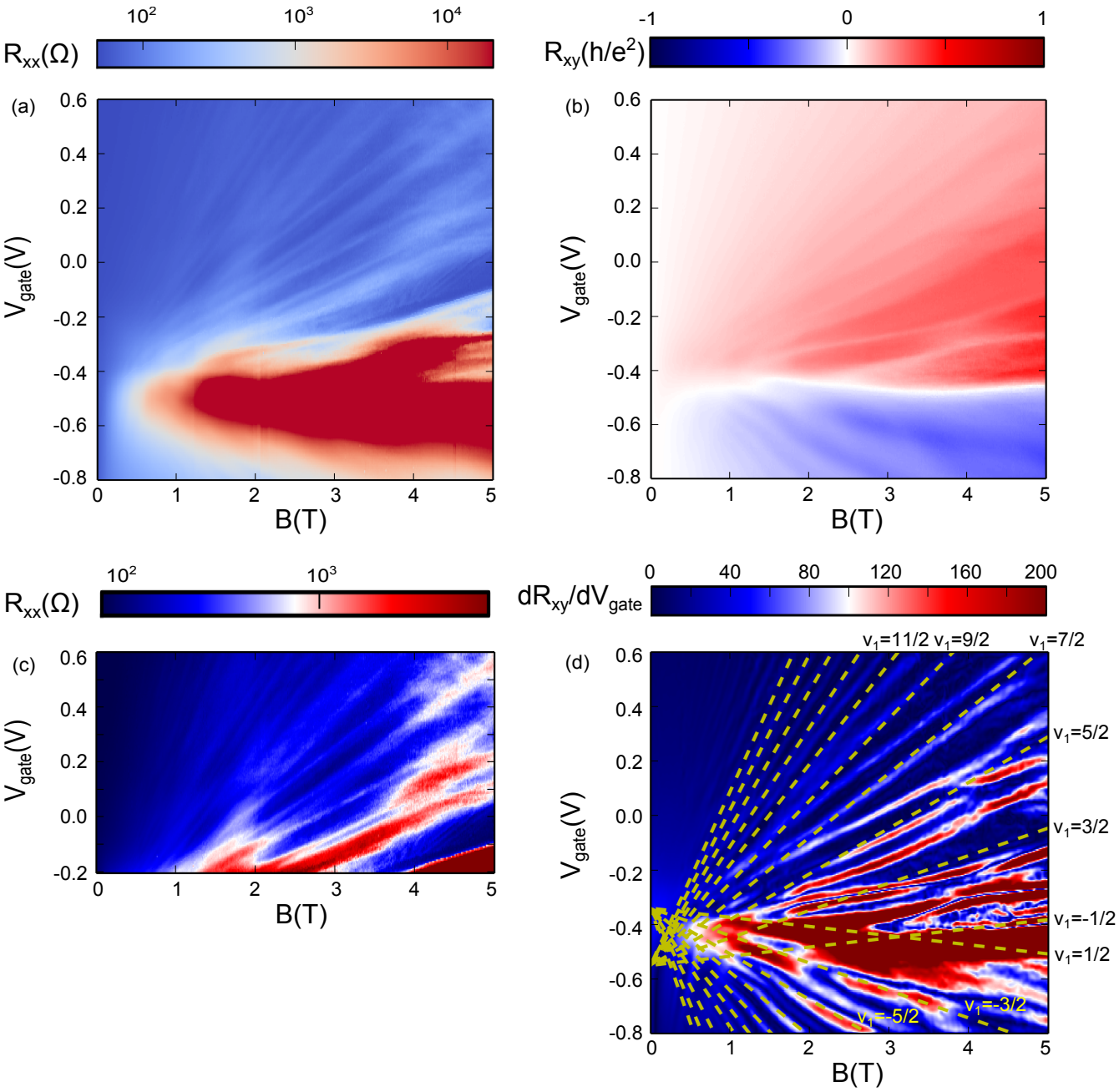

Figure 4.3 – *Magneto-transport measurements of a 100 nm-thick HgTe layer. (a) Longitudinal resistance R_{xx} (in logarithmic scale) as a function of V_{gate} and B. (b) Hall resistance R_{xy} (in units of $\frac{h}{e^2}$) as a function of V_{gate} and B. (c) Optimization of the scale for a better observation of R_{xx} features in the electron-side. (d) First derivative of R_{xy}. Zero values correspond to the energy levels. Yellow dashed lines represent the major set of Landau levels (LLs). Data have been extracted with I_{bias}=1 nA and $T = 60$ mK.*

agreement with the previous FFT measurements. Further analysis of the R_{xx} and R_{xy} features are thus needed to understand and interpret these complex quantum Hall data.

First, we concentrate on the SdHO distribution meaning their gate voltage and magnetic field dependences. The FFT analysis has enabled the gate depletion factor α_1 of the major contribution to be extracted. Moreover, as already introduced in Chapter 1 (see equation 1.58), the carrier density is directly related to the magnetic field value and to the filling factor ν. These two relations lead to the derivation of the following formula and to

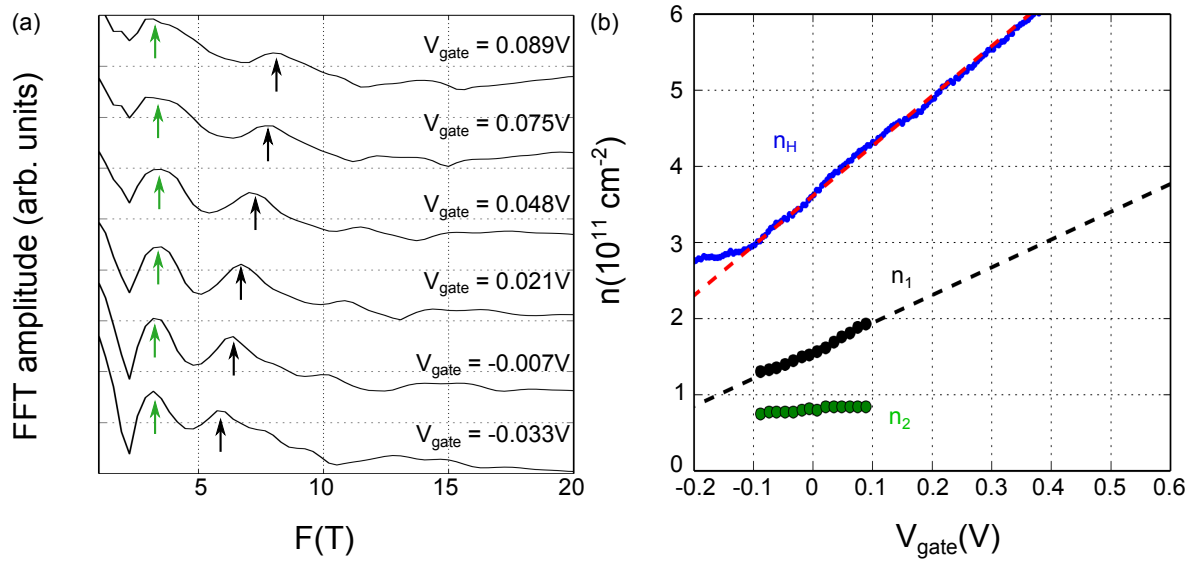

Figure 4.4 – *(a) Traces of the FFT amplitude as a function of the oscillation frequency F for several V_{gate} values witnessing the presence of two major frequencies (identified by green and black arrows) so two main transport contributions. FFT has been performed on Shubnikov-de Haas oscillations (SdHO) for B between 0.3 T and 5 T. (b) The frequencies are then translated in terms of two densities n_1 (black) and n_2 (green) and compared to the one extracted from the low magnetic field analysis n_H (blue). Red and black dashed lines are the linear fit of n_H and n_1, respectively.*

the estimation of $\frac{e}{\alpha h}$ factor:

$$V_{gate} = \nu \frac{e}{\alpha h} B \tag{4.5}$$

One value of α is therefore defining a whole set of Landau levels as represented in Fig. 4.3(d) by the yellow dashed lines. The analysis has been performed on the first derivative of R_{xy} as it enables to reproduce R_{xx} features by getting rid of the remaining resistance background which prevents R_{xx} minima to vanish. The positions of the Dirac points have been determined from the low magnetic field measurements at -0.55 V and -0.34 V for electron and hole regimes, respectively. In both the electron- and the hole-sides, the slopes of the yellow dashed lines are in partial agreement with the gate voltage and magnetic field dependences of the SdHO maxima. However, the positions of these lines do not correctly match with $\frac{dR_{xy}}{dV_{gate}}$ minima and thus do not fully reproduce the succession of LLs. Indeed, one can notice on Fig. 4.3(d) that for the higher values of V_{gate} only one half of the LLs are reproduced. These observations confirm that the electronic transport is carried out by several contributions and that the represented set of LLs is only one of them.

To gain knowledge on the filling of individual LLs, the study of R_{xx} minima positions is not sufficient and one needs to look further to the quantization values of the Hall resistance R_{xy}. At that step, it is useful to remind the expected quantization in such thick structures. With completely different signatures, the top and bottom surface states are assumed here to be independent and so the Hall conductance $\sigma_{xy} = \frac{\rho_{xy}}{\rho_{xy}^2+\rho_{xx}^2}$ (with $\rho_{xy} = R_{xy}$ and $\rho_{xx} = R_{xx}\frac{W}{L}$) is expected to follow: $\sigma_{xy} = (N_{top} + N_{bottom} + 1)\frac{e^2}{h} = (\nu_{top} + \nu_{bottom})\frac{e^2}{h}$ with N_{top} (N_{bottom}) the LL index for the top surface states (bottom surface states) and ν_{top}, ν_{bottom} the corresponding filling factors as already discussed in Chapter 1 (see 1.2.2.3.1). Therefore, integer quantization is expected in these thick structures. Note that such an integer quantization has already ben reported for 70 nm and 80 nm-thick HgTe layers [BLN+11] [KKO+14] and also for other thick 3D topological insulator systems like $BiSbTeSe_2$ compounds [XML+14].

Traces of the Hall conductance σ_{xy} and of the longitudinal conductance $\sigma_{xx} = \frac{\rho_{xx}}{\rho_{xy}^2+\rho_{xx}^2}$ are plotted on Fig. 4.5(a) for B = 3 T. Well-defined plateaus of σ_{xy} are visible on the electron-side and are scaling in $\frac{\nu e^2}{h}$ with ν corresponding to integer values. $\nu = 2, 3, 4, 5, 6, ...10$ are clearly observable, but the $\nu = 1$ is missing. In the hole-side, similar behavior is noticeable with the observation of the two plateaus $\nu = -2$ and $\nu \approx -3$. These values of quantization appear to be in a well agreement with the expectations.

In the QHE, Hall plateaus are predicted to be directly associated to longitudinal resistance minima. Therefore, the positions of these minima is expected to confirm the Hall quantization. By looking back to the R_{xx} oscillations, the positions of the yellow dashed lines are indeed also providing an information about the LLs quantization through the value of their slope. The associated filling factors values ν_1 are indicated at the edges of the mapping of Fig. 4.3(d) and correspond to half integers. These values are in agreement with the unique contribution of the top surface single Dirac cone (see Chapter 1 1.2.2.2).

Comparison between the gate voltage positions of the σ_{xy} plateaus and these yellow dashed lines for $B = 3T$ is reported in Fig. 4.5(a). Yellow dashed line positions are represented by yellow dots. One can directly notice that the $\nu = 2$, 3 and 4 plateaus are reproduced and correspond to $\nu_1 = \frac{1}{2}, \frac{3}{2}$ and $\frac{5}{2}$ respectively. A shift of $\frac{3}{2}$ is reported between ν and ν_1 and can be an evidence of the bottom surface quantization ν_2. Indeed, hosting a single Dirac cone similarly to the top surface, the bottom surface is expected to be quantized in half integer values of the quantum of conductance. Using equation 4.5 with n_2 the bottom surface density extracted from the FFT analysis, we estimate $\nu_2 = 1.1$ at 3 T. This value is quite in agreement with $\frac{3}{2}$ and so with this interpretation. However, if one focus now on the plateaus with $\nu \geq 4$, only one half of the σ_{xy} plateaus is reproduced by the positions of the dashed lines and so by the contribution of the top surface. Moreover, the shift between ν and ν_1 is no more constant. As the bottom surface is not expected to be depleted by the top gate voltage, this increase of the shift between ν and ν_1 cannot be explained by the sole addition of bottom surface quantization $\nu_2 = \frac{3}{2}$ at 3 T. Therefore, the addition of top and bottom surface quantization values does not allow to completely understand the quantization pattern obtained in such a strained 100 nm-thick HgTe sample.

To complement the analysis, the evolution of the σ_{xy} plateau quantization with magnetic field is reported in Fig. 4.5(b) with σ_{xy} traces plotted for several values of B ranging from 1 to 3.5 T. One interesting feature is the disappearance of $\nu = 2$ plateau for $B \leq 2.5$ T. Moreover, one can also notice that, for $B = 2$ T, the odd plateaus are large whereas the even ones $\nu = 4$ and $\nu = 6$ are hardly distinguishable. This reduction/suppression of the even filling factors for low magnetic field has already been reported in the literature [BLN+11][BTS+14] for similar 80 nm-thick HgTe layer and was obtained by equalizing the two surface densities by gate tuning. In our case, the suppression of the even filling factors is observed by varying V_{gate} and so cannot be attributed to a match between the surface densities. This behavior is actually looking like an effective Zeeman splitting. However, as already discussed in Chapter 1 (see 1.2.2.3.1), such splitting is not expected since each Dirac cone of a 3D topological insulator represents a unique spin specie. Such a spitting effect could indeed only occur if the two surface states with opposite chirality couple to each other. From both surface state extension of ≈ 5 nm $\ll 100$ nm and evidences of the complete screening of the bottom surface, we have concluded about the independence of the two surface states. However, this last result is raising questions especially about the existence of another coupling mechanism not yet demonstrated and which is lacking in the model derived in Chapter 1 (see 1.2.2.3.1). In this thought, the possible conduction and connexion between the top and bottom surface states by the metallic side surfaces should be further considered and investigated.

From the whole analysis including FFT and quantization studies, we can conclude that:

- two major contributions are evidenced. The first one, corresponding to the top surface, is predominant and vary significantly with V_{gate}. On the contrary, the second one is independent of V_{gate} and is attributed

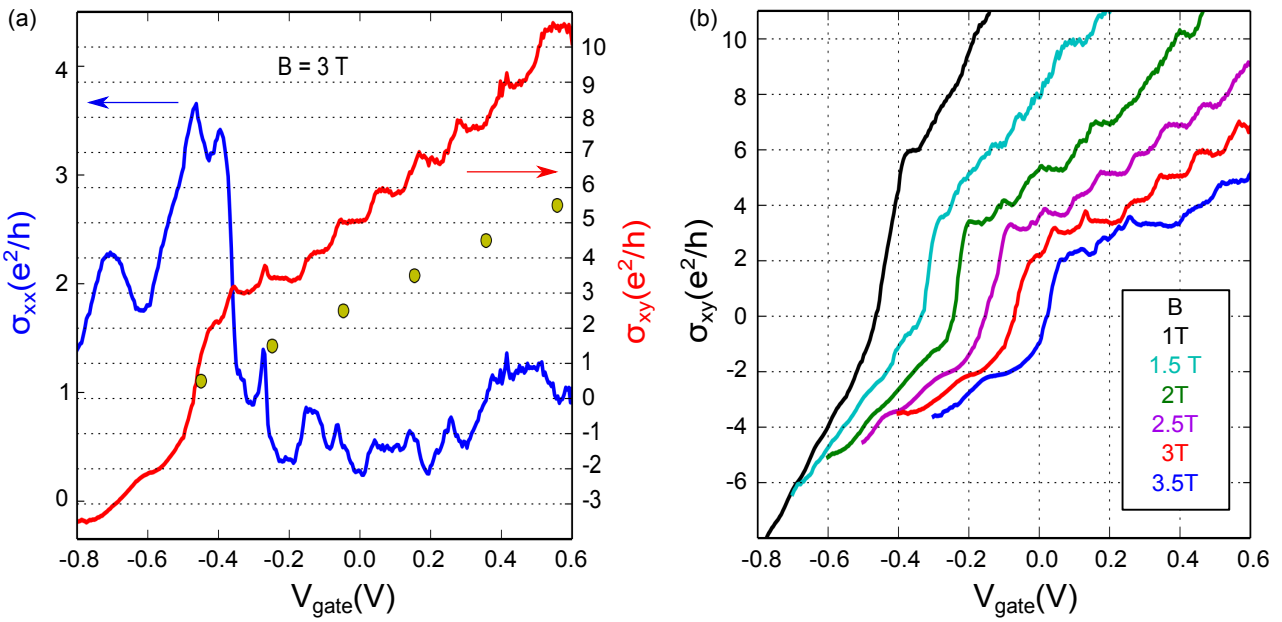

Figure 4.5 – *(a) Longitudinal σ_{xx} (blue) and Hall conductance σ_{xy} (red) traces for $B = 3$ T. (b) σ_{xy} traces as a function of V_{gate} for several values of B. Curves are shifted intentionally in V_{gate} for clarity. Data have been extracted with I_{bias}=1 nA and $T = 60$ mK.*

to bottom surface states.

- R_{xx} and σ_{xx} minima are not vanishing suggesting the addition of an extra contribution. Coupling to the bulk valence band in the hole-side and the addition of side surface transport contribution have been shown to be potential mechanism explaining the observation of these features.

- the combination of the SdHO distribution and the R_{xy} plateaus does not merge together to explain the quantization of this thick structure. Moreover, the observed quantization demonstrates some divergence with the model of independent topological surface states. Especially, the suppression of even filling factors when decreasing magnetic field is raising some questions about the interplay and the coupling mechanisms between the top and the bottom surface states.

All these observations characterize the complexity of the electronic transport in this 100 nm-thick HgTe layer. A lot of questions still need to be answered, thus preventing us from making a clear conclusion about the transport mechanisms at stake in such thick topological samples and to conclude about the topological nature of such structures.

In order to access the topological surface state properties, we decided to gradually decrease the HgTe thickness. The reduction of the bulk to surface ratio is indeed expected to lower the bulk and side surface contributions. In this thought, three samples have been fabricated and measured with the following thicknesses: 50, 25 and 15 nm. Note that the thicknesses have been accurately determined from HRXRD and XRR measurements. Detailed analysis of the 50 and the 25 nm-thick HgTe sample are provided in Appendix C and demonstrate the progressive reduction of the side surface and bulk contributions. While the 50 nm-thick sample still evidences signatures from both the top and bottom surface states and demonstrates complex transport mechanism, the 25 nm-thick sample highlights for the first time the hybridization of the two surface states,

thus giving rise to a unique topological contribution. It is worth noting that the first clear demonstration of the quantum Hall effect with vanishing resistance has been observed for this latter sample. However an additional contribution is still present for this sample preventing to unambiguously conclude about the topological nature of the structure. By continuing decreasing the HgTe thickness down to 15 nm, only the surface state contribution remains. The complete analysis of this sample is described in the following of this Chapter and enables to study a new transport regime at the vicinity of the 3D/2D limit.

4.1.2 15 nm-thick HgTe layer

Two samples are used for this analysis: sample 1 characterized with a HgTe thickness of about 13 nm and sample 2 with a HgTe thickness estimated to 15.5 nm. These two samples present very similar signatures at large magnetic field values, that is why we are treating them together. Note that, in the following, we mainly focus on sample 1. Sample 2 results are only introduced to complete the analysis.

4.1.2.1 Low magnetic field measurements

Low magnetic field extracted values of R_H, $R_{xx}(B=0T)$, $\frac{1}{R_H}$, n_H and μ are reported in Fig. 4.6 for sample 1.

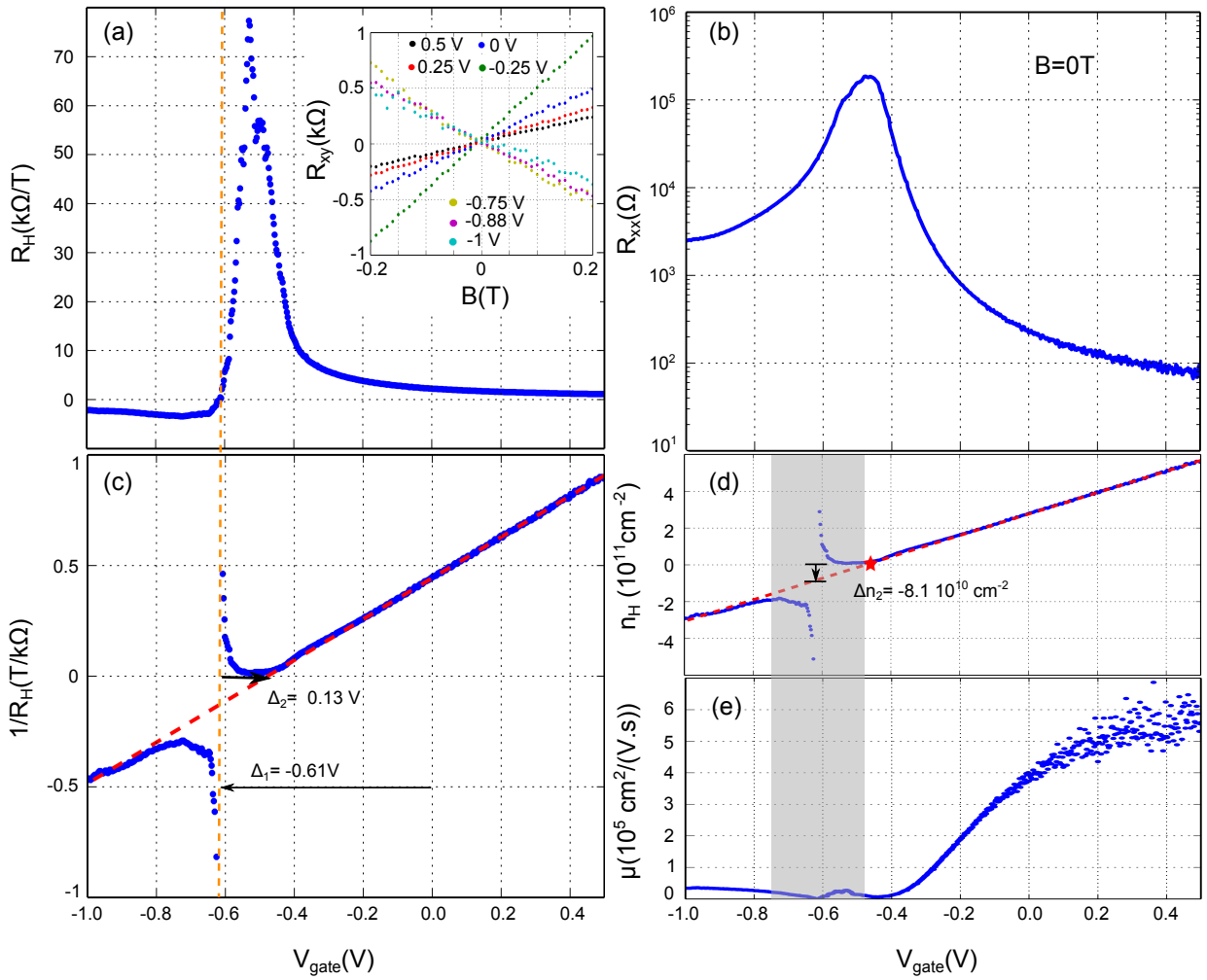

Figure 4.6 – *Low magnetic field characterization of sample 1 with $L = 40$ µm and $W = 10$ µm. All the presented quantities are represented as a function of V_{gate} and have been extracted for $B \leq 1$ T at $T = 100$ mK with I_{bias}= 1 nA. (a) R_H (inset: R_{xy} linear variation with B). (b) R_{xx} for B=0 T. (c) $\frac{1}{R_H}$.(d) n_H. (e) µ. Grey color band corresponds to the gate voltage range for which the single carrier model is not valid.*

This sample exhibits very similar features than the thicker ones concerning the ambipolar behavior, the $\frac{1}{R_H}$ variation as well as the density and the mobility values. However some differences are clearly noticeable and are listed below:

- contrary to the 100 nm-thick sample, R_{xy} linearly varies with B for the whole range of gate voltage as it can be seen in the inset of Fig. 4.6(a). No change of slope near zero field is noticeable, thus strongly demonstrating the validity of the single carrier model at this low thickness.

- the $\frac{1}{R_H}$ variation with gate voltage evidences two main differences with the 100 nm-thick sample. The first one is the vanishing Δ_3 voltage shift highlighting a significant reduction of the additional contribution to the transport, e.g. bulk, side surfaces or any other 2DEG. The second difference is the change of sign of Δ_2 from negative to positive. The associated density shift $\Delta n_2 = -8.1\ 10^{10}$ cm^{-2} illustrates this time the addition of electrons in the transport. Note that similar values of Δn_2 are reported in the Appendix C for the 50 and 25 nm-thick samples. From these two differences, the Dirac point is now unique and lies in the electron-side.

Additional measurements have been performed on sample 2 to complete this low magnetic field analysis enabling to study the R_{xx} dependence with the Hall bar length L. Fig. 4.7 displays $R_{xx}(B = 0T)$ variations as a function of $V_{gate} - V_{CNP}$ for several Hall bars with L ranging from 1 to 40 μm keeping the aspect ratio constant. Note that temperatures of measurements differ from one Hall bar to the other but are always below 100 mK. All the bars demonstrate similar variations of R_{xx} as a function of V_{gate}. Values of V_{CNP} vary from one Hall bar to the other but are always corresponding to negative values of the gate voltage which is consistent with the n-doping evidenced by Δ_1 for all the probed samples. Resistance maxima are to a first approximation increasing with L from 1 kΩ to 25 kΩ. This demonstrates a non-ballistic transport and thus suggests a metallic behavior of the surface states for which the resistance value is governed by scattering disorder potential. It is worth noting that some divergences appear in the resistance of Hall bars of same dimensions.

These observations are inconsistent with quantum spin Hall effect expected for thin HgTe topological quantum wells [KBM+08]. They demonstrate indeed that we are still probing metallic surface states and not yet quantized edge states at this thickness.

Some recent band structure calculations [LLB+16] rule out our conclusion about the metallic surface states by demonstrating the rise of a semi-metallic state when decreasing the thickness down to 15 nm for such strained structures. The Γ_{8HH} bulk band energy maxima is indeed becoming higher than the Γ_{8LH} energy minima thus closing the indirect gap. Such gap closing can thus explain itself the observed non-ballistic transport behavior. However, this is not consistent at all with the R_{xy} observed features (see inset of Fig. 4.6(a)) and especially its linear variation with B which clearly demonstrates a transport only govern by one single type of carrier in our structures, incompatible with the predicted semi-metallic state. Further studies at high magnetic field confirm our interpretation.

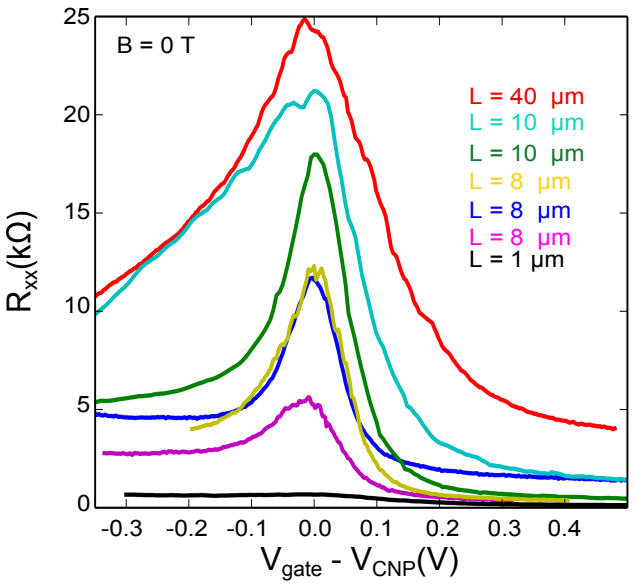

Figure 4.7 – *Longitudinal resistance R_{xx} as a function of $V_{gate} - V_{CNP}$ at zero magnetic field for sample 2. V_{CNP} is defined for each curve as the voltage V_{gate} corresponding to the R_{xx} peak maximum. The Hall bar length varies from 1 µm to 40 µm keeping the aspect ratio constant. Data are extracted for $B \leq 1T$ with a current bias of 1 nA and with $T \leq 100$ mK.*

4.1.2.2 High magnetic field measurements

By increasing the magnetic field, R_{xx} quantum oscillations are observed in the mapping of Fig. 4.8(a) obtained as a function of V_{gate} and B between -3 and 3 T at 100 mK. Contrary to the 100 nm-thick HgTe sample, R_{xx} mapping presents a single oscillation pattern confirming the absence of extra carrier contributions in this thickness range. Furthermore, zero resistance minima are visible in the electron-side, depicted in blue in the mapping of Fig. 4.8(a), thus validating the demonstration of QHE with vanishing resistance at this thickness. On the contrary, the hole-side exhibits much wider peaks with no more completely vanishing resistance. We assume this is because of the LL broadening, expected to be large in the hole-side due to the coupling to the Γ_{8HH} bulk band. Note that more details about the LL broadening and its determination in our structures are given in the next section 4.2.3.

FFT analysis of these oscillations has been performed and is reported in Fig. 4.9. It is worth noting that the 2D nature of these SdHO has been prior demonstrated using tilted magnetic-field as described in Appendix B. Contrary to the thicker samples, only one contribution is highlighted whose density n_1 is extracted and reported in Fig. 4.9(b) for comparison with n_H. The presence of this sole contribution is consistent with the expected coupling of the top and the bottom surface states at this thickness as it has already been discussed in Chapter 1 relying on the surface state extension calculations (see 1.1.4).

In the electron-side, n_1 shares the same linear behavior than n_H and so the same gate depletion factor $\alpha = 5.8\ 10^{11}$ cm^{-2}.V^{-1}. This is an indication of the suppression of side surface contributions at this thickness, compared to the features reported for the 100 nm-thick sample. On the contrary, in the hole-side, a shift of density is noticeable between n_1 and n_H, and n_1 seems to be $\approx \frac{n_H}{2}$. This density shift is probably related to the difference of behavior mentioned above between the electron- and hole-sides. To understand this asymmetry between these two regimes, quantum Hall data need to be further analysed.

We first focus on the longitudinal resistance R_{xx} mapping by studying the minima positions. Derived from

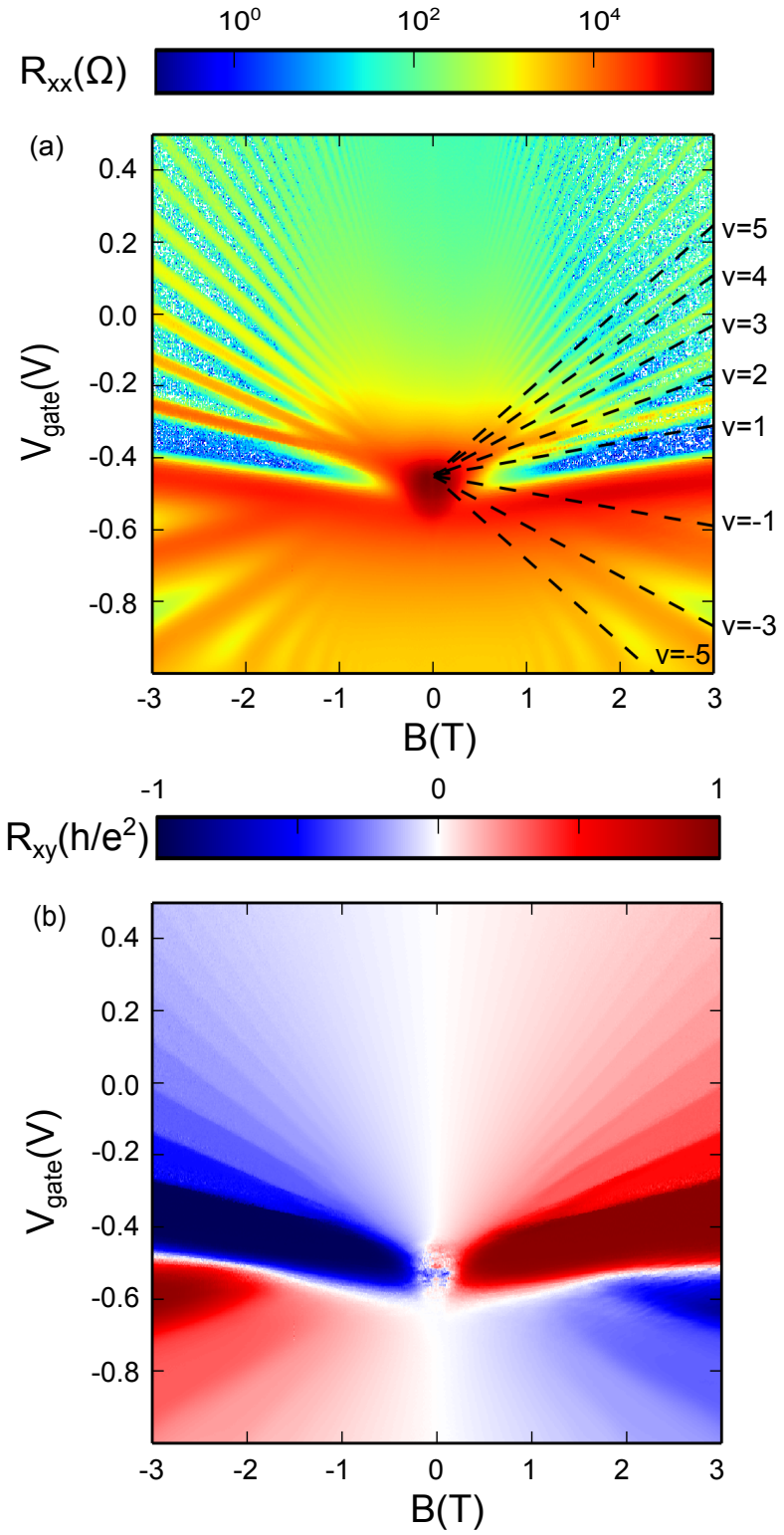

Figure 4.8 – *Magneto-conductance measurements of sample 1 with* $L = 40$ *µm and* $W = 10$ *µm. Data are extracted at* $T = 100$ *mK with a current bias of 1 nA. (a) Longitudinal resistance* R_{xx} *as a function of* V_{gate} *and* B*. The dashed lines represent the expected position of the mimima of* R_{xx} *from the density evolution with* V_{gate}*. It is worth noting that the mapping is characterized with only odd filling factors for low magnetic fields in the hole-side. (b) Hall resistance* R_{xy} *(in units of* $\frac{h}{e^2}$*) as a function of* V_{gate} *and* B*.*

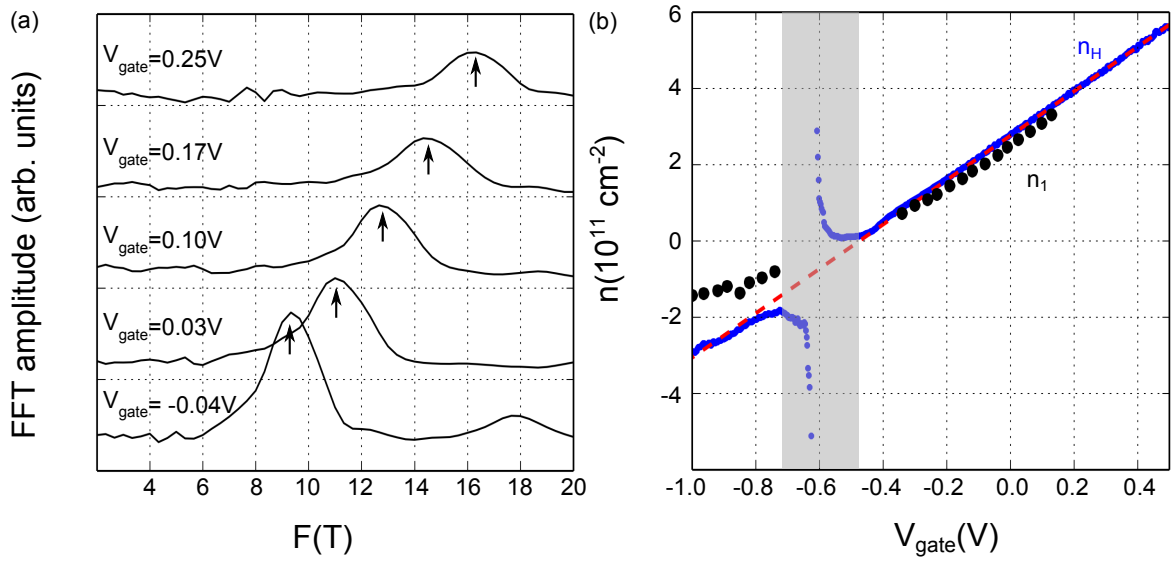

Figure 4.9 – *FFT treatment of SdHO of sample 1. (a) FFT amplitude as a function of F for several V_{gate} values. One peak is evidenced and corresponds to a unique transport contribution (identified by black arrows). (b) The associated density n_1 is compared to the one extracted from the low magnetic field analysis n_H. Red dashed line is the linear fit of n_H and the grey color band is the V_{gate} range where single carrier model is no more valid.*

the extracted electron density at low fields and the FFT analysis, the expected position of the LLs are determined from $V_{gate} = \nu \frac{e}{\alpha h} B$ and are represented by the black dashed lines in Fig. 4.8(a). The slopes of these lines are thus giving direct information about the quantization and the corresponding filling factor values are indicated on the edge of Fig. 4.8(a). The Dirac point position is in agreement with the position determined from the low magnetic field measurements (see Fig. 4.6(c)). In the electron-side, the positions of these dashed lines are consistent with R_{xx} vanishing minima and enable to reproduce the totality of the oscillation pattern, contrary to what has been reported for the 100 nm-thick sample. In the hole-side, the position of these lines are partially consistent with the resistance minima. Indeed, only the lines corresponding to odd values of filling factor are fitting the oscillation pattern. Nevertheless, despite this discrepancy between electron- and hole-side, it seems that their energy levels are attributed to the same set of LLs. This difference of quantization must be however further investigated with Hall resistance.

To validate these preliminary observations on the quantization, complementary measurements of the Hall resistance have been required. The R_{xy} mapping is presented in Fig. 4.8(b) as a function of V_{gate} and B and highlights successive resistance plateaus. Associated traces of σ_{xy} and σ_{xx} as a function of V_{gate} are plotted in Fig. 4.10 for $B = -3$ T. Well-defined plateaus are directly associated with vanishing minima in the electron-side and evidence an integer quantization. On the contrary, in the hole-side, the peaks are at least two times broader and the quantization is in -1 and -3, so only odd filling factors are reported. The agreement between the longitudinal and Hall data concerning the quantization permits to conclude that we are only probing one gas, contrary to what has been reported for the thicker samples. This gas corresponds to the two topological surface states hybridizing for such low thickness.

Furthermore, the quantization in the hole-side leads to the explanation of the density shift reported in the FFT analysis between n_1 and n_H. Indeed, if we consider $\Delta\nu = 2$, the equation 4.4 gives $F = \frac{n}{2}\frac{h}{e}$ and so we measure only half of the carrier density as it is exactly the case here.

This difference of quantization between electron- and hole-sides is raising some questions about the trans-

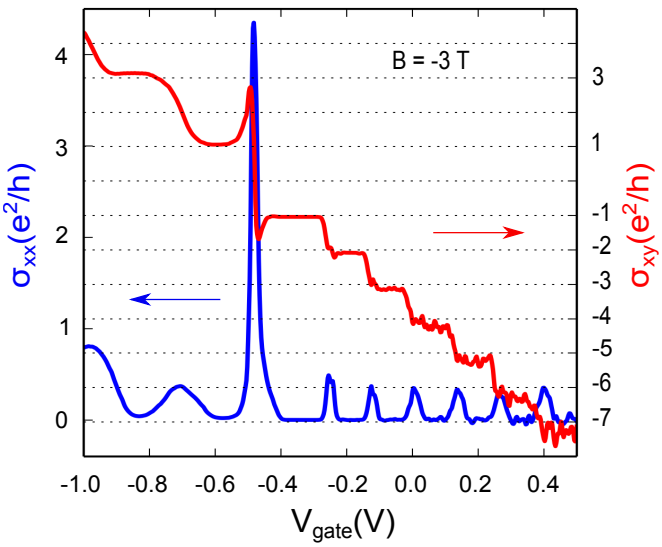

Figure 4.10 – *σ_{xx} (blue) and σ_{xy} (red) traces for $B = -3$ T for sample 1 at 100 mK. σ_{xy} is characterized with well-defined plateaus associated to a vanishing of σ_{xx} in the electron-side. These observations demonstrate that the quantum Hall regime is reached. Only odd plateaus are observed in the hole-side whereas both even and odd plateaus are observed in the electron-side.*

port mechanism at stake for such thin samples. The quantum Hall signatures expected in the particular case of two coupled surface states have already been introduced in Chapter 1 (see 1.2.2.3.2). With the coupling of the two Dirac cones, the LL index of the two surfaces are equal ($N_{top} = N_{bottom} = N$), thus resulting in the Hall conductance expression: $\sigma_{xy} = (2N+1)\frac{e^2}{h}$ highlighting a quantization with only odd filling factors. Such a quantization is observed in the hole-side but also in the electron-side for low magnetic field values. Indeed, e.g. ν= 2 is defined only for $|B|$ larger than $\approx$ 1.5 T where a clear separation of the R_{xx} maxima into two distinct branches is observed (see Fig. 4.8(a)). This is suggesting that the even filling factors are attributed to a lifting of a degeneracy with B while the odd ones are only due to Dirac fermions. The apparent asymmetry between electron- and hole-sides can be explained by the presence of the Γ_{8HH} bulk band at the energy where holes are expected to populate the Dirac cone. The coupling to the bulk band induces a large LL broadening (see next section 4.2.3 for an estimation of this quantity) which prevents from the observation of the even filling factors at such low values of magnetic field.

The induced LL broadening in the hole-side should therefore impose a larger magnetic field to resolve the splitting observed in the electron-side. To experimentally check this point, additional measurements have been performed for magnetic field values B up to 5.5 T for sample 2 and are presented in Fig. 4.11 and Fig. 4.12. The R_{xx} and R_{xy} mapping of Fig. 4.11(a) and (b) evidence the appearance of a $\nu = -2$ plateau in the hole-side for $B \geq 4.5$ T.

Complementary, σ_{xy} traces for sample 2 have been plotted in Fig. 4.12 for $B = 3$ T and $B = 5.3$ T and strongly confirm the appearance of the $\nu = -2$ filling factor in the hole-side for $B = 5.3$ T, whereas for $B = 3$ T the quantization jumps from -1 to -3.

To summarize, with negligible bulk and side surface contributions, such 15 nm-thick HgTe layers have unambiguously demonstrated quantum Hall effect with vanishing longitudinal resistance. However, the values of quantization clearly indicate that reaching this state of matter have certain consequences such as the hybridization of the top and bottom surface states and the lifting of spin degeneracy. Moreover, the coupling to the Γ_{8HH}

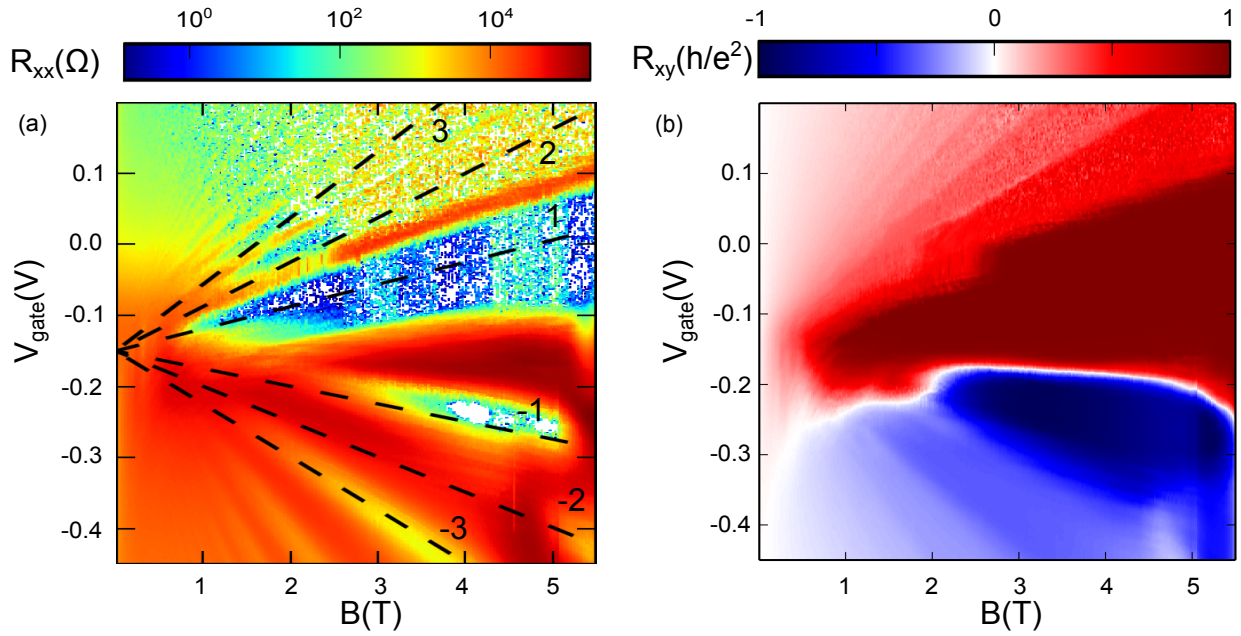

Figure 4.11 – *Magneto-conductance measurements of sample 2. (a) R_{xx} as a function of V_{gate} and B. The black dashed lines represents the expected positions of the LLs enabling to determine the filling factors. (b) R_{xy} (in unit of $\frac{h}{e^2}$) as a function of V_{gate} and B. Note that the Hall bar dimensions are $L = 8$ µm and $W = 2$ µm and data are extracted with current bias $I_{bias} = 1$ nA at $T = 93$ mK.*

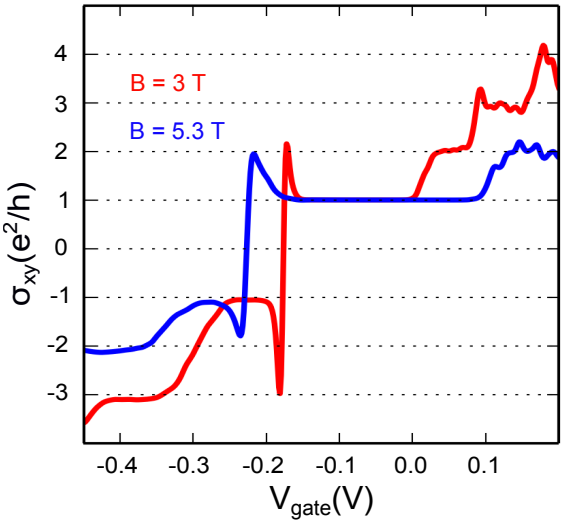

Figure 4.12 – *σ_{xy} for sample 2 as a function of V_{gate} at $B = 3$ T (red) and $B = 5.3$ T (blue) for $T = 93$ mK and $I_{bias} = 1$ nA. A clear $\nu = -2$ plateau is observed for the higher magnetic field value.*

bulk band has been identified to increase the LL broadening in the hole-side thus resulting in an apparent odd quantization at low magnetic field.

To conclude this magneto-conductance study, we propose to summarize the results presented in this section and in Appendix C in Fig. 4.13. This figure aims at illustrating the reduction of the additional contributions to the transport when decreasing the HgTe thickness. The decrease of the bulk contribution is highlighted by the Δ_3 voltage offset determined from low magnetic field measurements. The impact of side surfaces is emphasized by the evolution of the difference between the density n_H extracted from the low field measurements and the density n_1 of the major contribution. The difference of their effective gate depletion factor $\alpha_h - \alpha_1$ is extracted from the FFT measurements and is plotted here as a function of the thickness.

100 nm-thick sample has demonstrated signatures of top and bottom surface states as well as side surface and bulk contributions as reported in Fig. 4.13 with maximal values of Δ_3 and $\alpha_H - \alpha_1$. The mixing of all these transport contributions have made the analysis of the transport signatures more complex and prevent to conclude about the topological nature of these thick structures. Moreover, the suppression of the even plateaus when decreasing the magnetic field demonstrates the existence of a coupling mechanism still unknown and unexplained to date. A coupling mechanism activated by the side surfaces must be seriously envisaged and investigated. When decreasing the thickness down to 50 nm, $\alpha_H - \alpha_1$ and so the side surface contribution vanishes. Moreover, Δ_3 is significantly reduced due to the decrease of bulk to surface ratio. For the 25 nm-thick sample, an extra 2DEG has been detected and changes the sign of Δ_3. Thinner layers of about 15 nm have then be considered. Clear demonstration of the quantum Hall effect with vanishing resistance has been made possible in such thin structure thanks a significant decrease of the bulk and side surface contributions illustrated by Δ_3 and $\alpha_H - \alpha_1$ zero values in Fig. 4.13. However, the price to pay is the coupling of the two surface states lifting the spin degeneracy. These whole results are giving new insights concerning the 3D/2D topological insulator transition which is still not crossed at this thickness and are also very promising for the potential use of such thin topological insulators for applications.

In the following of this Chapter, two main points will be covered. The first one is a complete study of the SdHO of these thin structures to characterize further the topological surface state properties. The second one is the experimental demonstration using quantum Hall transport spectroscopy with temperature dependence of the Dirac nature of the carriers and of the validity of the hybridization model.

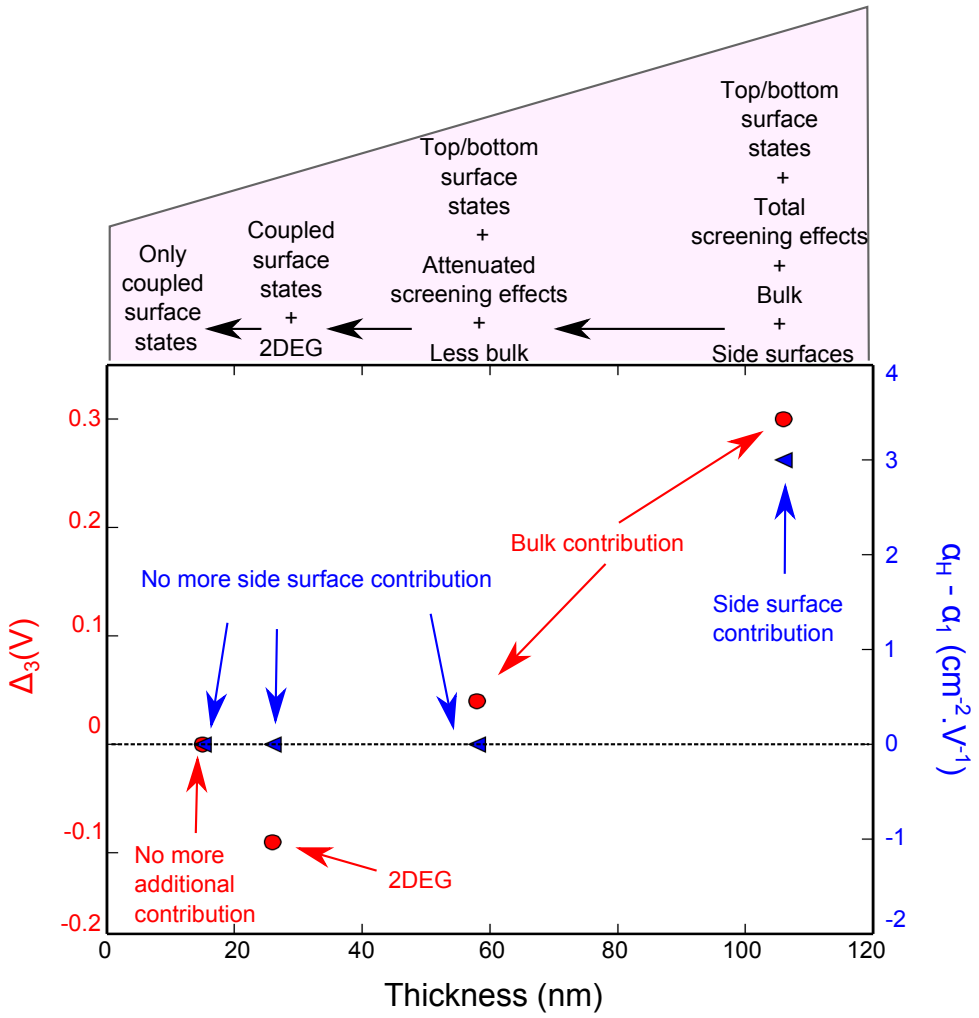

Figure 4.13 – *Evolution of the Δ_3 voltage offset and $\alpha_H - \alpha_1$, the difference of effective gate depletion factor between n_H and n_1, as a function of the HgTe thickness. The decrease of these values illustrates the reduction of the transport contributions and so of the complexity of the signatures by decreasing the HgTe thickness.*

4.2 Shubnikov-de Haas oscillations analysis

4.2.1 Definition

When varying the magnetic field or the gate voltage value, the longitudinal resistance experiences oscillations. These so-called Shubnikov-de Haas oscillations have already been observed and discussed in the previous section as indicators of Landau levels. Nevertheless, these oscillations have a larger impact as they enable to characterize further the electronic transport through their dependence in temperature, magnetic field or even through their frequency.

The resistance variation of the SdHO is expressed through:

$$R_{xx} = R(B,T)\cos\left(2\pi\left(\frac{F}{B} + \frac{1}{2} + \beta\right)\right) \tag{4.6}$$

with

$$R(B,T) = R_D.R_T = \exp\left(\frac{-\pi}{\omega_c \tau_q}\right).\frac{2\pi^2 k_B T/\hbar\omega_c}{\sinh\left(2\pi^2 k_B T/\hbar\omega_c\right)} \tag{4.7}$$

where F is the oscillations frequency, β is the Berry phase, $\omega_c = \frac{eB}{m^*}$ is the cyclotron frequency with m^* the cyclotron effective mass of carriers, and τ_q is the quantum scattering lifetime. With these dependencies, the

SdHO can be used to probe the following parameters:

- the temperature-dependence of their amplitude (R_T) leads to the determination of the carrier cyclotron mass m^*.
- the magnetic-field-dependence of their amplitude (R_D) gives access to the quantum scattering lifetime τ_q which is directly related to the LL broadening Γ.
- their frequency F directly provides an estimation of the Berry's phase β [And13]. This quantity, already introduced in Chapter 1 (see 1.2.3) is considered as a reliable indicator of the topological nature of a system. In the topological case, β is expected to be half-integer, while it will be integer for a trivial system.

The determination of the LL broadening Γ particularly motivates this SdHO analysis as it has a significant impact on the quantum Hall data of the thin samples. It seems indeed that this parameter govern the conditions of appearance of the LL splitting resulting in the integer quantization measured in both electron- and hole-sides. Characterizing this quantity should thus enable to understand further the observed transport signatures. However, the prior determination of m^* is required to extract τ_q and so Γ variations from R_D.

In this section, we will so first address the estimation of the cyclotron effective mass m^* of the carriers to be able in a second time to characterize the LL broadening Γ. Finally, the extraction of the Berry's phase will be discussed to complete the picture. It is worth noting that only the 13 nm-thick sample (sample 1 in the previous section) is considered in this section but that the 15.5 and 25 nm-thick samples present very similar results. Only the Berry's phase has been extracted for the 50 nm and 100 nm-thick samples as this characterization does not take into account oscillation amplitude and so does not require vanishing resistance minima.

4.2.2 Cyclotron effective mass of carriers

The cyclotron effective mass can be extracted from the temperature dependence of the SdHO analysis using the Lifshits-Kosevich (LK) formula [AFS82] [And74]:

$$\frac{\Delta R(B,T)}{\Delta R(B,T_{ref})} = \frac{T \sinh\left(2\pi^2 k_B T_{ref} m^*/\hbar e B\right)}{T_{ref} \sinh\left(2\pi^2 k_B T m^*/\hbar e B\right)} \tag{4.8}$$

This formula can easily be derived from SdHO expression 4.6 by considering the ratio of resistance between a temperature of reference T_{ref} and a temperature of measurement T. Note that we consider $\Delta R(B,T)$ instead of $R(B,T)$ to remove any impact of the oscillations resistance background which can depend on other factors such as additional transport contributions and their magnetic field dependence.

Figure 4.14(a) displays R_{xx} as a function of B for $V_{gate} = 0.4$ V. The temperature T is increased from 0.4 K to 20 K with 0.1 K steps below 1 K, 0.8 K steps between 1 and 5 K and finally 5 K steps between 5 and 20 K. The oscillation amplitude is decreasing with T and the oscillations become hardly distinguishable at 20 K. The determination of m^* is thus possible using the data from Fig. 4.14(a) and equation 4.8 with T_{ref} = 0.4 K. Note that amplitude variations of the oscillations have been studied for B close to 1 T to avoid spin splitting and only consider the surface state carrier intrinsic properties.

The curve of $\Delta R_{xx}(T)/\Delta R_{xx}(T = 0.4K)$ (see Fig. 4.14(b)) is fitted using the red dashed line demonstrating m_e^* value of about $0.027 \pm 0.004 m_0$. However, such fit is not so accurate. This is mainly due to the lack of data at larger temperatures but as can be seen in Fig. 4.14(a), oscillations for T larger than 10 K are difficult to resolve for small B. Due to this issue, determination of m^* is difficult in our structures.

Similar study, but in the hole-side, is presented in Fig.4.14(c) and (d). In this regime, the SdHO disappear very quickly with temperature and are no more distinguishable above 3.4 K. This behavior is attributed to the influence of the Γ_{8HH} bulk band. To properly estimate m^* in this regime, we consider only T from 0.4 to 1 K, range of T for which the oscillations are the best defined. Amplitude dependence of SdHO is reported in Fig.4.14(d) and considerably differs from what has just been reported for electrons. No saturation is visible at the lower temperatures, but on the contrary a striking increase is noticeable. Such a behavior can not be fitted by a standard metallic LK model. The coupling with bulk Γ_{8HH} states in the hole regime is expected to be at the origin of this particular feature.

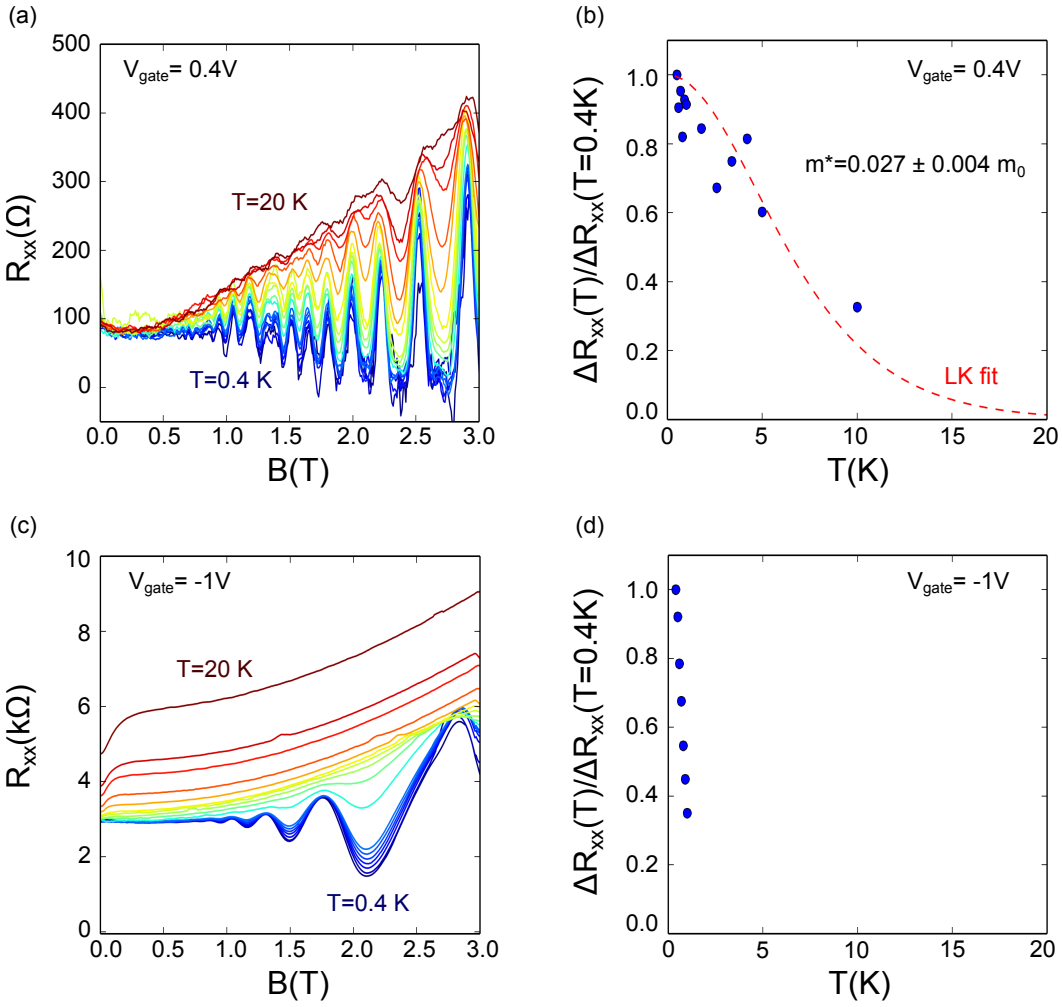

Figure 4.14 – *SdHO of the longitudinal resistance R_{xx} of sample 1 for $V_{gate} = 0.4$ V (a) and for $V_{gate} = -1$ V (c) for temperatures ranging from 0.4 K to 20 K. (b) The corresponding Lifshits-Kosevich (LK) fit for the extraction of the cyclotron effective mass m^* in the electron-side. (d) Amplitude variations of the SdHO in the hole-side (which does not enable to use LK model and thus to determine m^*).*

Nevertheless, it is possible to have an idea of the carrier cyclotron effective mass in our HgTe structures by using analogy with graphene. Due to a linear energy spectrum, one expects a zero effective mass for Dirac fermions. However, as already reported for graphene [NGM+05], Dirac fermions rest mass is zero but not the cyclotron mass. Note that SdHO amplitude dependence with temperature gives directly access to this cyclotron effective mass [Fuc13]. However, standard definition for m^* relies on energy second derivative and is only adapted for materials defined with parabolic dispersion. An alternative definition has been developed for materials with linear dispersion law [Ari12]:

$$m^* = \frac{p}{\frac{\delta E}{\delta p}} = \frac{\hbar k}{v_F} = \frac{\hbar\sqrt{\pi n}}{v_F} \tag{4.9}$$

This relation directly links the cyclotron effective mass m^* and the carrier density n.

Fig. 4.15 displays the evolution of m^*, expected from the density n_H variation (see Fig.4.6(d)) in this 13 nm-thick sample, as a function of V_{gate}. Note the red square which represents the effective mass estimated just before. These two methods appear to give consistent results. Therefore, we will use relation 4.9 to determine m^* thereafter.

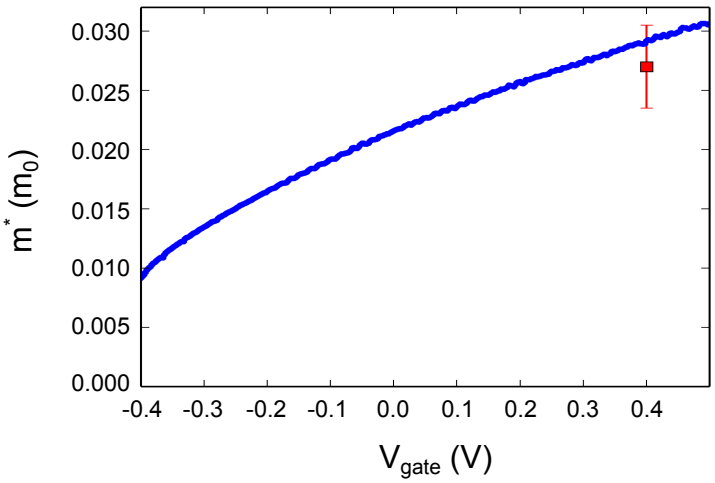

Figure 4.15 – *Evolution of m^* as a function of V_{gate} for a Dirac cone (blue dotted line). Estimation of m^* using SdHO has been performed for $V_{gate} = 0.4$ V and is represented by a red square. Error bar corresponds to the LK fit error.*

4.2.3 Landau level broadening

As explained in [HZZ09] and [YDW+12], extraction of the SdHO amplitude as a function of the magnetic field allows to obtain values of the LL broadening Γ through the determination of the quantum scattering lifetime τ_q using the relation below:

$$\frac{\Delta R_{xx}}{4R_0} = R_T.\exp\left(-\frac{\pi}{w_c\tau_q}\right) \tag{4.10}$$

with ΔR_{xx} the amplitude of the SdHO, R_0 the resistance background of the oscillations , R_T describing the temperature variations of the SdHO, and $w_c = \frac{eB}{m^*}$ the cyclotron frequency. m^* values have been determined using equation 4.9 derived just before.

Due to a non negligible bulk contribution in the hole-side, this method has been only used in the electron-side where amplitude of SdHO only depends on the surface state properties. τ_q is then directly related to Γ through $\Gamma = \frac{\hbar}{2\tau_q}$.

Figure 4.16(a) presents the evolution of R_{xx} as a function of the inverse of the magnetic field $1/B$ for $V_{gate} = 0$ V at $T = 0.4$ K. The red dots represent both the maxima and the minima which define an envelope function. ΔR_{xx} is extracted from the difference between successive maxima and minima and R_0 results from the mean value of these extrema. Figure 4.16(b) displays the evolution of $\Delta R_{xx}/R_0$ as a function of $1/B$ in a logarithmic scale. The red dashed line represents the linear fit to the data using equation 4.10. The extracted value of τ_q provides direct access to the broadening value here equal to 3.91 ± 0.04 meV.

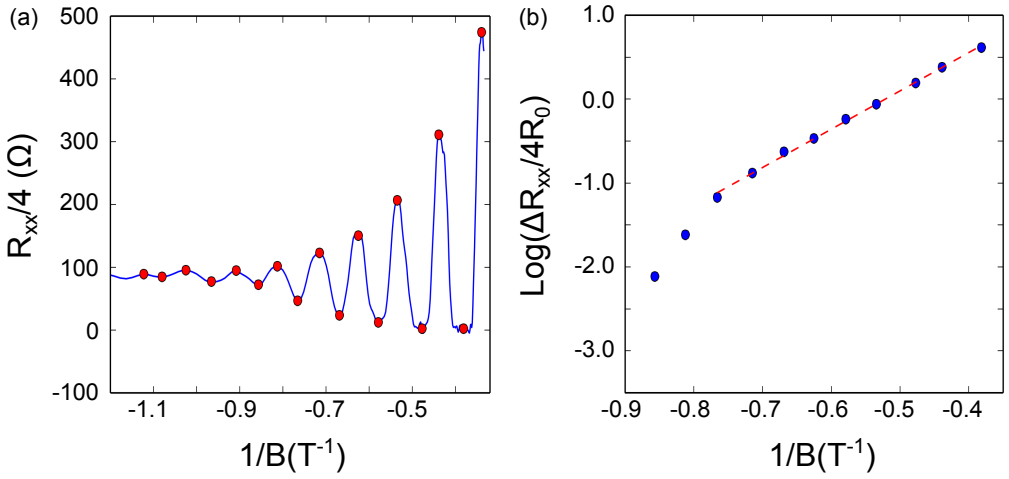

Figure 4.16 – *(a) Longitudinal resistance R_{xx} as a function of the inverse of the magnetic field for $V_{gate} = 0$ V and $T = 0.4$ K for sample 1. The red dots represent maxima and minima defining the envelope function. The difference between maxima and minima gives ΔR_{xx}. (b) ΔR_{xx} normalized by the background R_0 as a function of the inverse of the magnetic field. Blue dots represent the data and the red dashed line is a fit using relation 4.10.*

The same analysis has been performed for several values of V_{gate}. Figure 4.17(a) displays the extracted values of electron-side broadening Γ_e. Note that the broadening is decreasing with V_{gate} and thus with density n. This behavior is due to the variations of m^* with n and is consistent with R_{xx} mapping of Fig. 4.8(a). Indeed, we can see that the closer are the LLs from the Dirac point, the more important is the magnetic field value at which the splitting appears. This is especially visible with the $\nu = 2$ plateau appearing for $|B| \geq 1.5$ T while $\nu = 4$ shows up at larger gate voltage value for $|B| \geq 1.0$ T.

To have an estimation of the broadening in the hole-side, we have fitted $N = 1$ and $N = -1$ LL peaks with

a Gaussian distribution to extract the full width at half maximum (see inset of Fig. 4.17(b)). Figure 4.17(b) demonstrates the difference through the ΔV_{gate} values between hole and electron peaks. With a ratio of about 3.7, the hole broadening Γ_h has been estimated to be larger than 11 meV. More precise determination of Γ_h is complicated as it also depends on the gate voltage.

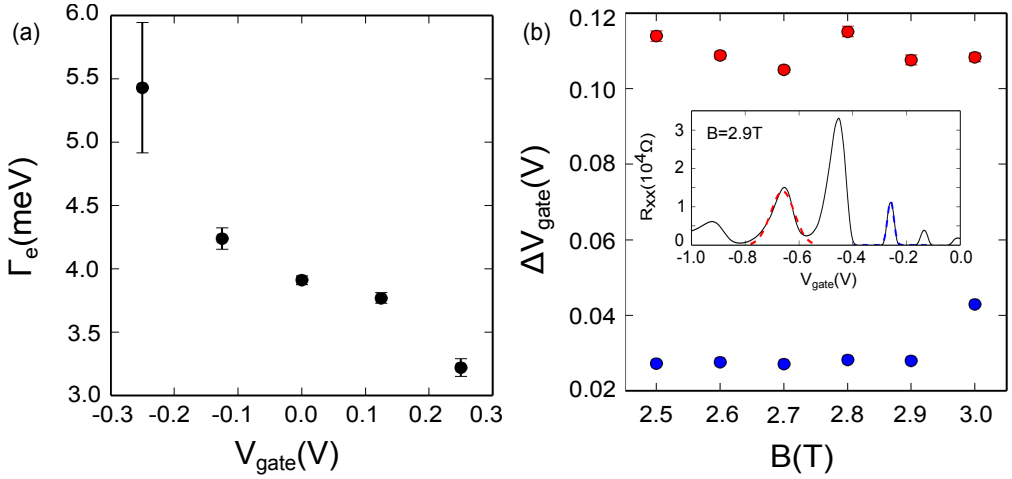

Figure 4.17 – *(a) Determination of the broadening Γ_e as a function of V_{gate} in the electron-side. Error bars correspond to fit errors. (b) Estimation of the broadening in the hole-side using comparison between FWHM ΔV_{gate} of the $N = 1$ (blue) and $N = -1$ (red) peaks (shown in the inset) as a function of B.*

4.2.4 Berry's phase

Experimentally the Berry's phase β can be determined from the analysis of the SdHO frequency F through the following relation:

$$R_{xx} \sim cos(2\pi(\frac{F}{B} + \frac{1}{2} + \beta)) \tag{4.11}$$

When taking into account minima values of R_{xx}, the following condition must be fulfilled:

$$cos(2\pi(\frac{F}{B} + \frac{1}{2} + \beta)) = -1 \tag{4.12}$$

thus leading to:

$$2\pi(\frac{F}{B} + \frac{1}{2} + \beta) = (2i+1)\pi \tag{4.13}$$

and finally:

$$\frac{F}{B} + \beta = i \tag{4.14}$$

where i is the minima index.

With this methodology, the extraction of R_{xx} minima leads to the determination of the Berry's phase whereas the extraction of the maxima gives a value shifted by $\frac{1}{2}$ [TA11].

Figure 4.18 (a) displays the resulting diagram for several values of V_{gate} for both electron- and hole-sides. Berry's phase is directly extracted from the intercept of the linear fit of i and is reported in Fig. 4.18(b) with the error bars corresponding to the fitting errors. A Berry's phase value of 0.56 ± 0.07 is determined, which is in full agreement with the expected value of $\frac{1}{2}$ for Dirac fermion transport. As one may have noticed, the ranges of considered magnetic field are not similar between electron- and hole-sides. We have chosen to focus on low magnetic field values below 1.15 T in the electron-side to prevent from splitting effects which appear for higher fields and which can be a cause of error for β as reported in [AMR+10]. Such precaution was not taken in the hole-side as this effect does not manifest between 0 and 3 T due to a larger broadening.

This linear fit of i is also providing information about the oscillation frequency F by extracting its slope. Figure 4.18(c) evidences the evolution of F with the gate voltage. Being linearly related to the Fermi surface $S_F = \frac{2\pi e}{\hbar c} F$, the observed V-shape evolution with gate voltage is an other indication of Dirac fermion transport.

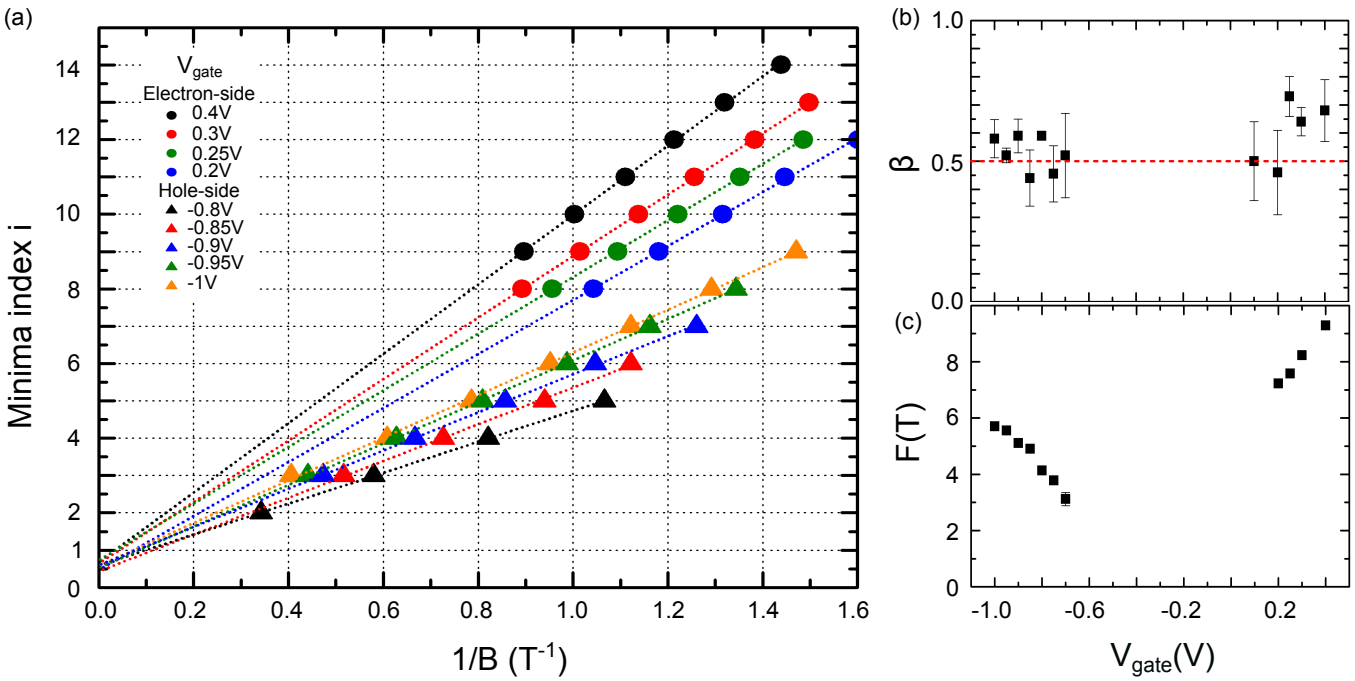

Figure 4.18 – *(a) Fan diagram of the SdHO of sample 1 for several values of V_{gate}. The minima index i is plotted as a function of the inverse of the magnetic field and linearly fitted. The slope of the fit gives access to the oscillations frequency F and the i-axis intercept evidences the Berry phase. (b) Berry phase β values and (c) SdHO frequency F for several V_{gate} values. The error bars represent the errors in the linear fit.*

SdHO analysis have provided a lot of information about the effective mass, the LL broadening and the Berry's phase of the carriers, thus allowing to complete our understanding of the quantum Hall data. The difference of LL broadening between the electron- and hole-sides explains the difference of quantization experimentally observed between these two regimes at low magnetic field values. Furthermore, with a value of 0.56 ± 0.07, the Berry's phase demonstrates the topological nature of our structures. Note that the thicker samples with 100, 50 and 25 nm-thick HgTe layers are also characterized by $\beta \approx \frac{1}{2}$.

To go one step further, SdHO temperature dependence analysis has been performed and is presented in details in the next section.

4.3 Quantum Hall transport spectroscopy: SdHO temperature-dependent analysis

This section focuses on quantum Hall transport spectroscopy and aims to experimentally determine the LL energy separation as a function of the magnetic field in order to unambiguously identify and demonstrate the Dirac nature of the carriers as previously introduced and explained in Chapter 1.

This study has been made possible thanks to the demonstration of quantum Hall effect with vanishing resistance in our structures. In this section, only results concerning sample 1 (13 nm-thick HgTe layer) are presented but sample 2 (15.5 nm-thick HgTe layer) gives very similar results.

The originality of this study essentially lies in the methods based on the temperature dependence of the QHE which were already successfully implemented in graphene [JZSK07] [GZK+07] [THM15]. As far as we know, such method has never been used for topological insulator systems as QHE measurements suffer from side surface and bulk contributions. This is principally due to the fact that the majority of topological insulators and especially the Bi-based systems are characterized by a high bulk conduction associated to low mobilities preventing the observation of the QHE with vanishing resistance. However, several studies have already been carried out concerning the LLs spectroscopy of Bi-based topological insulators and have highlighted the $\sqrt{N}$ energy difference between the levels E_N. Such studies have been performed using either scanning tunneling microscopy [HIK+10] [CSZ+10] or cyclotron resonance of the LLs [WSD+12] or even magneto-optics method [SPT+12]. A few studies using either cyclotron resonance of infra-red magnetospectroscopy have also been reported concerning HgTe 2D systems and have been mostly focused on the $N = 0$ LL [LVM+14] [ZTO+12] [OMF+11].

Here we demonstrate direct transport evidences of Dirac fermions in thin films of strained HgTe topological insulators by the analysis of the associated QHE in temperature. Moreover, we show that the coupling between the two surfaces leads to a degeneracy lifting of the Landau levels through a mechanism specific to these Dirac surface states and already explained in Chapter 1. This study provides new insights in the quantum Hall effect of 3D TI slabs, in the cross-over regime between 3D and 2D topological insulators of relevance for the design of future quantum circuit.

4.3.1 Longitudinal resistance temperature dependence

To gain knowledge on the nature of the Landau levels, we performed temperature dependence of the magneto-conductance at high fields [JZSK07] [GZK+07] [THM15].

These measurements have been performed for temperatures going from the milliKelvin range to several Kelvins. Figure 4.19 displays R_{xx} as a function of V_{gate} for the different temperature values ranging from 500 mK to 20 K . Filling factors are evidenced as R_{xx} minima. These minima are increasing with T. One can notice that minima are still visible at 20 K in the electron-side while they disappear around 4 K in the hole-side.

In such a procedure, the energy gap between LLs is estimated via thermal activation. More precisely, the temperature dependence of the longitudinal resistance R_{xx} minima is fitted using the Arrhenius law:

$$R_{xx}^{min} \sim \exp\left(\frac{-\Delta E}{2k_B T}\right) \tag{4.15}$$

with ΔE the activation energy gap, k_B the Boltzmann constant and T the temperature. This analysis has only been performed in the electron-side since the influence of the Γ_{8HH} bulk band in the hole-side changes drastically with temperature.

Figure 4.20 presents the evolution of the longitudinal resistance minima R_{xx}^{min} as a function of T for both

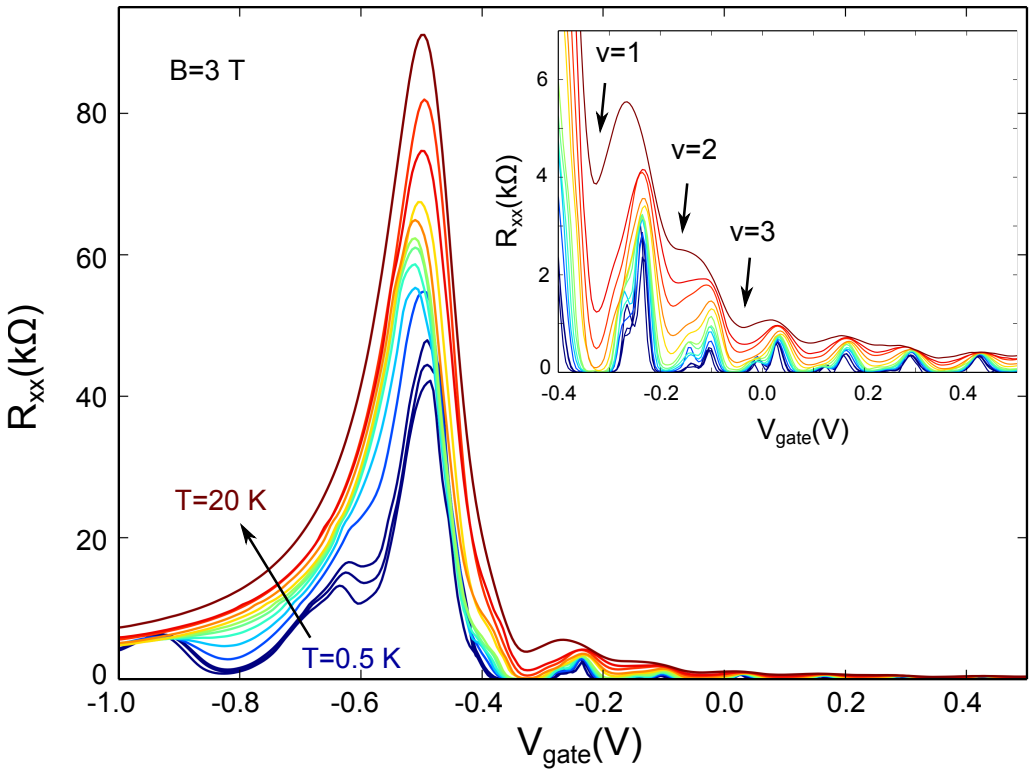

Figure 4.19 – *Longitudinal resistance of sample 1 as a function of the gate voltage for temperatures ranging from 0.5 K to 20 K. The insets is a zoom on the electron-side. The thermally activated behavior of R_{xx} minima is evidenced. Data have been extracted with $I_{bias} = 1$ nA and $B = 3$ T.*

the $\nu = 1$ and $\nu = 2$ filling factors. Similar analysis has been performed for the other filling factors from $\nu = 3$ to $\nu = 8$. The dotted lines correspond to the fits using the Arrhenius law 4.15. The slope of these fits gives direct access to the energy gap ΔE for the two filling factors and for several magnetic field values. Note that the R_{xx} temperature dependence exhibits in reality three different linear variations corresponding to three different energy gap values. We choose here to only concentrate on the more important one which is in the meV range of order, while the two others are in the μeV range of order and are therefore observed at lower temperatures.

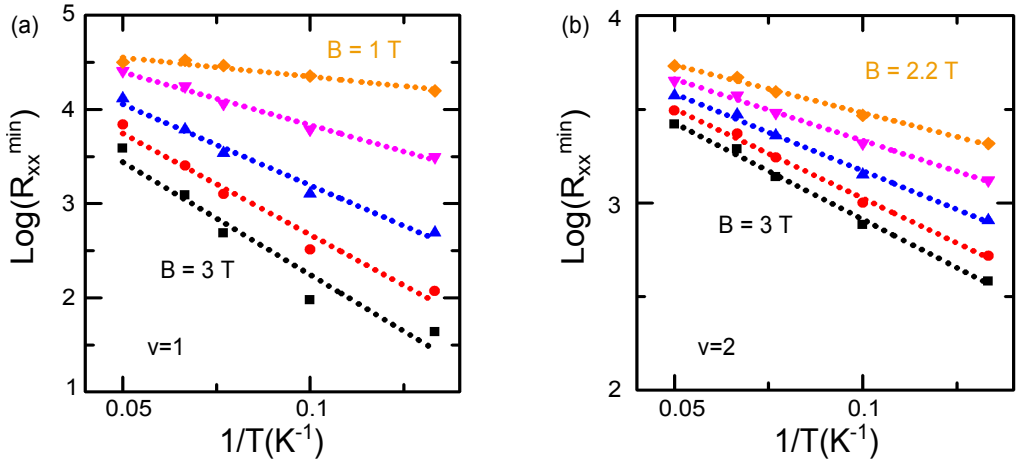

Figure 4.20 – *Temperature dependence analysis of the longitudinal resistance. Minimum of the longitudinal resistance R_{xx}^{min} as a function of temperature T for the (a) $\nu = 1$ and (b) $\nu = 2$ filling factors. These analyses allow to extract the energy gap for each filling factor for several values of B.*

To quantitatively model the energy gaps for odd and even filling factors, we consider the LL energy spectrum derived in Chapter 1 (see 1.2.2.3.2):

$$E_{N,\pm} = \pm\sqrt{2Ne\hbar v_f^2 B + (\frac{\Delta}{2} - N\beta B)^2} \pm \beta B, N \geq 1 \tag{4.16}$$

$$E_{0,\pm} = \pm|\beta B - \frac{\Delta}{2}| \tag{4.17}$$

with $\beta B = \frac{\hbar w}{2}$ (the notation used in Chapter 1). While of purely orbital nature, the term βB acts as an effective Zeeman energy and β value is fixed by the analysis of the even filling factor energy gaps performed in the next paragraph.

4.3.2 Activation energy gap for even filling factors

The resulting activation energy gaps for even filling factors where the relevant LLs are expected to be split by B are represented in Fig. 4.21. The activation energy gaps for all these LLs are similar and are linear with the magnetic field, which is consistent with a splitting origin. ΔE is fitted using the model:

$$\Delta E_{\nu=2N} = E_{N,+} - E_{N,-} + \Gamma = 2\beta B + \Gamma \tag{4.18}$$

To obtain a good agreement between the data and the model for all energy gaps, we need to take into account the width of the LL also referred as the LL broadening Γ as a constant offset in energy. Γ has been previously estimated from the SdHO in the electron-side. Here, a fixed Γ value of 3 meV is used. The slope 2β has been estimated to be about 2.07 ± 0.65 meV/T from the red dashed line fit and is similar to the Landau level splitting observed in HgTe non-topological quantum wells [GBD+15] [BLT+11].

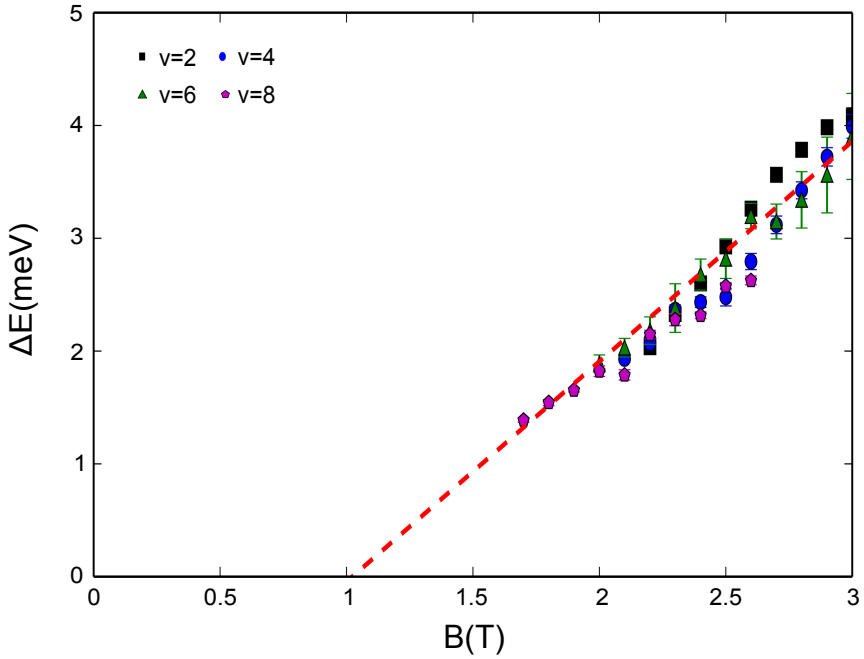

Figure 4.21 – *Activation energy gap ΔE as a function of B for even filling factors. The red dashed lines represent the result of the model $\Delta E_{\nu=2N} = E_{N,+} - E_{N,-} + \Gamma$ with a constant offset $\Gamma = 3$ meV.*

4.3.3 Activation energy gap for odd filling factors

We now focus on odd filling factors where two successive LLs have different orbitals (see Fig. 4.22). We clearly observe a non-regular energy gap separation between the successive LLs. At a fixed perpendicular magnetic field, the energy separation between LLs is decreasing with N and is increasing non-linearly with magnetic field (mostly noticed for the ν= 1 gap). Both observations are in qualitative agreement with a Dirac-like LL energy spectrum $E_N = \sqrt{2e\hbar v_f^2 NB}$. This constitutes a strong evidence of the Dirac nature of the carriers.

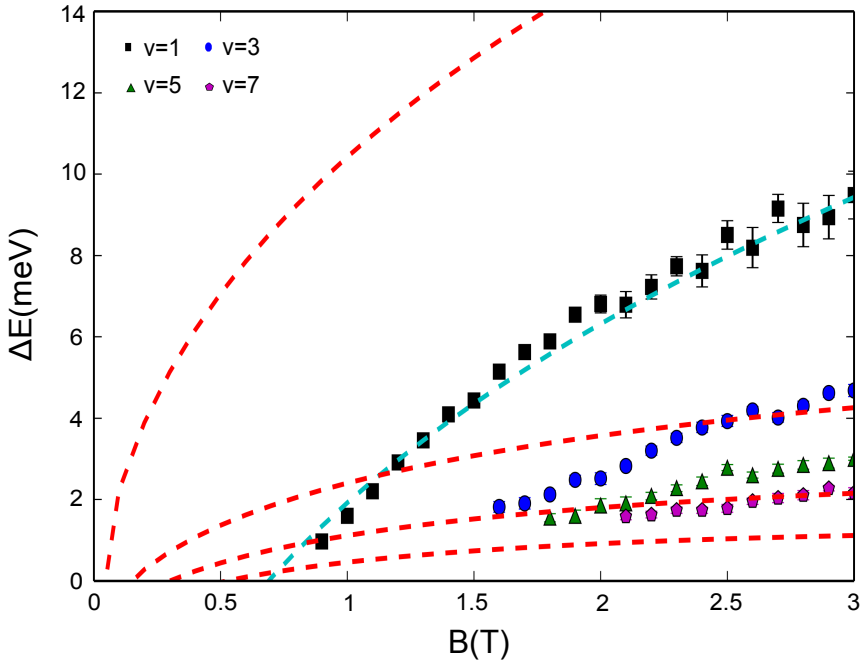

Figure 4.22 – *Activation energy gap as a function of B for odd filling factors. The red dashed lines represent the result of the model* $\Delta E_{\nu=2N+1} = E_{N+1,-} - E_{N,+} + \Gamma$ *with a constant offset* $\Gamma = 3$ *meV. Better agreement between the model and the data for* $\nu = 1$ *is obtained with a larger offset* $\Gamma = 10$ *meV (see blue dashed line). Such an increase of* Γ *is expected from the energy proximity of the* Γ_{8HH} *bulk band.*

Activation energy gap is fitted for each filling factor using the model:

$$\Delta E_{\nu=2N+1} = E_{N+1,-} - E_{N,+} + \Gamma \tag{4.19}$$

with Γ fixed to 3 meV (see red dashed lines). However, for $\nu = 1$, the fitting requires three times larger Γ due to the observed enlargement of the LL induced by the coupling to the Γ_{8HH} bulk band. This is true only for the $\nu = 1$, for which $\Delta E_1 = E_{1,-} - E_{0,+}$, due to its proximity to the Dirac point and so to the Γ_{8HH} bulk band. A larger offset $\Gamma = 10$ meV is thus considered for $\nu = 1$ and the corresponding fit is represented through the blue dashed line.

The qualitative agreement between the experimental data and the model enables Dirac fermions to be revealed in our structures. These results experimentally demonstrate the role of hybridization as a coupling mechanism leading to a lift of degeneracy.

4.3.4 Summary of the study

Fig. 4.23 summarizes on the same diagram all the relevant energy scales discussed in this study. All the energy gaps of both odd and even filling factors for different magnetic fields discussed in Fig. 4.22 and Fig. 4.21 are represented in square. The color bands correspond to the range of LLs broadening Γ_e and Γ_h extracted in the previous section. If the energy gaps ΔE of the even filling factors are smaller than LL broadening, they are supposed not to be resolved by the quantum Hall transport spectroscopy. This diagram suggests the beginning of appearance of even filling factors in the electron-side for $B_e \geq 2.4$ T and in the hole-side for $B_h \geq 6.3$ T. Such values are consistent in term of ratio with experimental data for which B_e and B_h were estimated around 1.5 T (for $\nu = 2$ for sample 1) and 4.5 T (for $\nu = -2$ for sample 2), respectively.

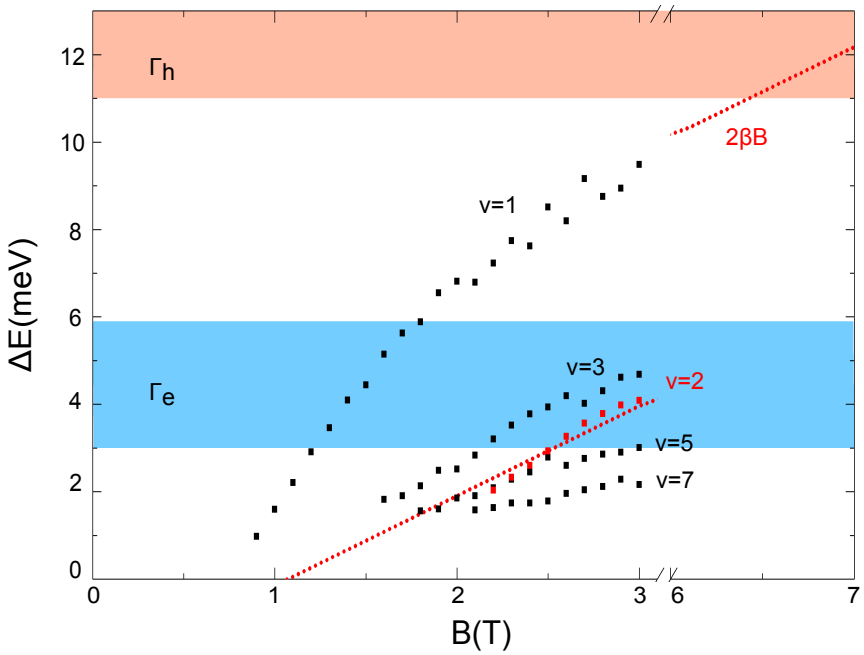

Figure 4.23 – *Final fan diagram with the odd ν=1, 3, 5, 7 (black squares), and even ν=2 (red squares) filling factors and the "effective Zeeman splitting" energy (red dotted line). Γ_h (respectively Γ_e) range is represented by a red (blue) color band. Note that the energy ranges considered for broadening values take into account variations with gate voltage.*

4.4 Conclusion

This Chapter has reported the low temperature magneto-transport measurements of HgTe topological insulator structures characterized by different HgTe thickness from 100 to 15 nm.

Low magnetic field measurements have described the electronic transport properties of each sample highlighting the ambipolarity of the structures, the linear variation of the carrier density as well as the evolution of carrier mobility when sweeping the gate voltage. All these properties demonstrate consistency with a Dirac cone-like transport behavior and also confirm the quality of the material. In the case of 100 nm-thick sample, the measurements give indications of additional contributions to the transport, especially attributed to bulk or side surfaces. Such contributions are observed to disappear for 15 nm-thick samples.

High magnetic field measurements have then been performed for each sample to access the band structure and especially the surface state properties. The association of quantum oscillations with Hall resistance plateaus has been demonstrated for each HgTe thickness, thus giving indications of quantum Hall regime in our structures.

Very complex transport signatures have been highlighted for the thicker samples of 100 nm (and 50 nm see Appendix C). While some evidences of two independent surface states have been recorded, the presence of additional contributions caused by bulk and side surfaces have also been emphasized, preventing from clear observation and characterization of the topological properties. Furthermore, signs of a splitting and so of a coupling mechanism have also been observed with the suppression of even filling factors with the reduction of magnetic field. Strong efforts should be made to gain knowledge on the origin and the effects of this coupling mechanism.

To enhance the topological properties or at least facilitate their observation, two thinner samples of 25 (see Appendix C) and 15 nm have also been investigated. Clear demonstration of the quantum Hall regime has been made possible with vanishing longitudinal resistance directly associated to the Hall plateaus. However, the establishment of this state of matter is accompanied by the hybridization of the two surface states and of their Dirac cones. The analysis of the Hall quantization especially reveals the lifting of of the spin degeneracy expected with this coupling.

With the demonstration of quantum Hall effect, quantum Hall transport spectroscopy using temperature dependence has been possible using the 15 nm-thick samples. Activation energy gap evolution with magnetic field has been experimentally determined for each filling factor value, thus leading to a clear differentiation between the nature of the odd and the even ones. Odd filling factor features are consistent with a Dirac-like energy spectrum, thus demonstrating unambiguously the Dirac nature of the carriers in our structures. The linear variation in magnetic field of the activation energy gaps of the even filling factors confirms their splitting origin. This study thus provides clear evidences of the consistency between experimental transport signatures and the hybridization model developed in Chapter 1 (see 1.2.2.3.2), thus revealing Dirac fermions and their transport mechanisms in our thin HgTe topological insulator structures.

With a clear demonstration of quantum Hall effect as well as the Dirac nature of the carriers, these results are paving the way toward applications of such thin topological insulator structures as platform for nanoelectronics, spintronics and so on.

Chapter 5

Toward spintronic applications

The topological nature of our 3D HgTe structures has been experimentally established in the previous Chapter. The aim of this perspective Chapter is now to demonstrate with some on-going studies the promising potential of HgTe for spintronic applications.

Topological insulators are currently generating a considerable and growing interest. The reason is simple and lies in the unique electronic and spin properties that arise on their surface states. Among them the spin-momentum locking property is full of promise for applications in spintronics. Indeed, with the spin locked to its momentum, an electron current flowing on topologically protected surface states turns into a dissipationless spin-polarized current, thus making topological insulator materials perfect candidates for the future of spintronic devices. The discovery of the Quantum Spin Hall Effect (QSHE) in 2007 [KWB+07] has enhanced the interest concerning these systems. Theoretical propositions emerged and essentially relied on the spin transistor idea developed by Datta and Das [DD90]. Their proposition consists in a spin field-effect transistor made of ferromagnetic source and drain to select both injected and collected spin. The spin manipulation is performed using spin precession and gate tunable spin-orbit coupling. The appearance of topological insulator systems revolutionizes this theoretical work by the replacement of ferromagnetic contacts by normal metallic ones but more specifically by the possibility of engineering the spin-polarized edge states. With this idea, Krueckl and Richter [KR11] suggested the realization of a spin transistor based on the helical edge states of a 2D topological insulator. By lateral confinement, the electronic wavefunctions of the two opposite edges overlap giving rise to a gap opening of the edge states. In these conditions, gate voltage variations are assumed to be sufficient to change the switching conditions of this transistor. Other studies have been reported suggesting for example the use of $p-n$ junctions [AGTB09]. Such junctions support, at the p and n interface, a spin-degenerate one-dimensional state where spin precession is realizable through the use of a parallel magnetic field. Up to now only one experimental demonstration of such transistor has been reported for 2D HgTe [BRN+10] [BRB+12] using QSHE as a spin current injector and inverse spin Hall effect as a spin detector and vice-versa.

Our approach is in the direct continuity to the above mentioned studies and consists in the realization of a spin-based logic element using for the first time 3D HgTe topological insulator structures. This work relies on the theoretical proposition of Ilan *et al.* [IdJM15] of a spin-based Mach-Zehnder interferometer. Such device requires the combined use of spin-momentum locking property and a $p-n$ junction.

Spin-momentum locking demonstration is here done via spin pumping measurements. With the use of a ferromagnetic layer at its resonance, a spin current is injected at the topological insulator interface. The transverse charge current is then measured to probe the efficiency of spin-electricity conversion of the topological surface state. More details about this technique and the first results obtained on our structures are given in the first part

of this Chapter. This technique is currently mostly used on Bi-based topological insulator materials [SNK+14] [JLJ+15] and also on a new topological system α-Sn [RSOF+16] but as far as we know this has never been done on HgTe. The realization of a $p-n$ junction made of 3D HgTe topological insulator is also a real challenge due to the complexity of the underlying physics, especially due to the interplay between edge states at the $p-n$ interface [AL07] [KLY+15] [MTT+15]. The first magneto-conductance measurements made on a thin 3D HgTe $p-n$ junction are presented in this Chapter.

It is important to note that this whole study is still in progress. A combination of results and perspectives is presented and aims at describing our future development strategies using HgTe topological insulators.

5.1 Spin to charge current conversion using HgTe

Spin pumping measurements are achieved to probe and evidence the spin-momentum locking property predicted for topological surface states. Magneto-transport measurements presented in Chapter 4 were only injecting and detecting charge currents giving thus no indication about the existence of such property in our structures. The spin-pumping method enables spin injection from a ferromagnetic layer to a non-magnetic layer (here the topological material) by using magnetization precession at the ferromagnetic resonance. This injected spin current is then converted into a transverse charge current by the inverse Edelstein effect [Ede90]. Characteristics of the resulting charge current provide indications about the relation between charge and spin on the HgTe topological surface states. In this section, we will briefly present the spin pumping principle and the first results on a strained 3D HgTe structure will be reported. More than just the evidence of the spin-momentum locking property, these measurements also demonstrate the potential of this topological system as spin injector or spin detector. Note that the measurements have been performed at CEA-INAC Spintec and that all the presented work results from a collaboration with P. Nöel, Y. Fu, J.P. Attané, L. Vila (CEA-INAC Spintec) and S. Gambarelli (CEA-INAC Symmes).

5.1.1 Experimental setup

Spin pumping measurements have been performed on a sample made of a 18.5 nm-thick HgTe layer grown on (100) CdTe substrate. A sketch of the sample and of the experimental setup is presented in Fig. 5.1.

In order to enhance the spin to charge conversion, an insulating barrier is introduced between the HgTe topological layer and the ferromagnetic one. For sake of convenience and to protect HgTe top surface states, a $Hg_{0.3}Cd_{0.7}Te$ top barrier is grown by MBE as for magneto-transport samples. The initial barrier thickness is 5 nm. The barrier thickness has then been decreased using an in-situ Ar etch just before the evaporation step of a 20 nm-thick NiFe ferromagnetic layer. This solution has been favored instead of directly growing samples with this barrier thickness because the growth of barrier thinner than a few nanometers does not ensure total protection of HgTe top surface against Hg desorption. Here after are only presented the results obtained on a 0.6 nm barrier thickness. At the end of the sample fabrication process, X-ray reflectivity (PANalytical Empyrean X-rays diffractometer, CEA-INAC, SGX) is used to accurately estimate the thickness of each layer.

Samples are cut in slabs of 0.4 mm x 2.4 mm and fixed on a sample holder centered inside the cavity as represented in Fig. 5.2. The cavity is irradiated by an electro-magnetic wave characterized by a frequency f ($\approx$ 9.6 GHz) and inducing a magnetic field h_{rf} at its center. An external magnetic field $\vec{H} = H\vec{y}$ is also generated by two coils surrounding the cavity and is perpendicular to $\vec{h_{rf}} = h_{rf}\vec{x}$ as shown in both figures 5.1 and 5.2. The direction of the external magnetic field H can be tuned manually from 0°to 360°in the (x,y) plane. We define the parallel direction as the y axis direction (represented in Fig. 5.1). The antiparallel direction is the opposite one at 180°.

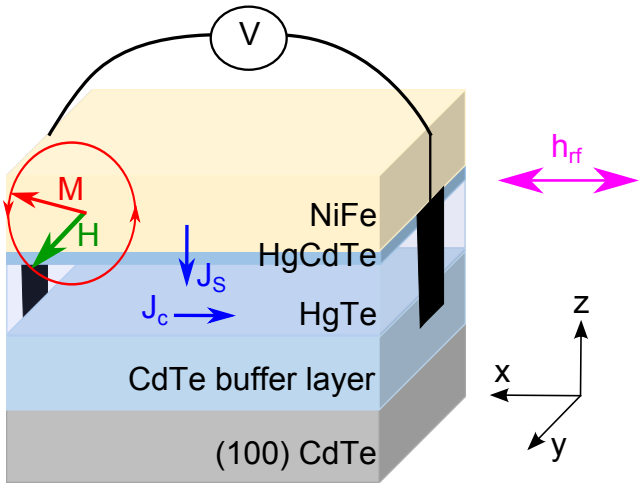

Figure 5.1 – *Scheme of the sample and of the experimental setup for spin pumping into HgTe topological insulator by FerroMagnetic Resonance (FMR) of a NiFe layer. H is the external magnetic field, h_{rf} is the microwave induced magnetic field and M is the magnetization experiencing precession. A pure spin current J_s is injected on HgTe surface states resulting in the formation of a transverse charge current J_c.*

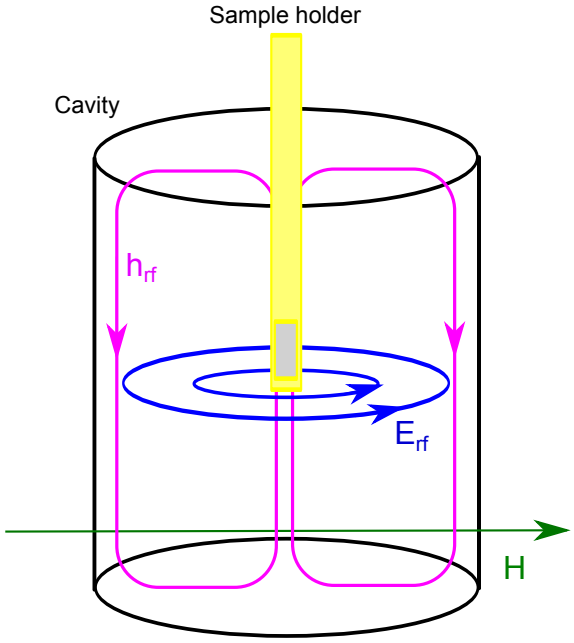

Figure 5.2 – *Schematic representation of the cylindrical cavity. The electro-magnetic wave induces a magnetic field h_{rf}. An external magnetic field H is also generated by two coils.*

The dc-voltage measurements are performed using a two-probe resistance technique. The two probes are located at the two opposite sides of the slab as shown in Fig. 5.1. It is important to notice that all the presented measurements have been performed at room temperatures.

5.1.2 Ferromagnetic resonance

The magnetization of the ferromagnetic layer is described by the Landau-Lifshitz-Gilbert (LLG) equation of motion [LL35] [Gil04]:

$$\frac{d\vec{M}}{dt} = -\gamma[\vec{M} \times \vec{H_{eff}}] + \frac{\alpha}{M}[\vec{M} \times \frac{d\vec{M}}{dt}] \tag{5.1}$$

with $\vec{M}$ the magnetization vector, $\vec{H_{eff}}$ the effective magnetic field including the external, demagnetization, and crystal anisotropy fields. $\gamma = \frac{g\mu_B}{\hbar}$ is the gyromagnetic factor with g the Landé factor and α the damping factor. One can notice that α includes both the Gilbert damping α_{FM} which is a characteristic of the ferromagnetic layer and an extra-damping $\alpha_{FM/NM}$ caused by the spin pumping mechanism between the ferromagnet and the non-magnetic material [TBB02].

This equation 5.1 is divided in two parts: the first one corresponds to an infinite magnetization precession around the $\vec{H_{ext}}$ axis and the second one introduces the damping. The microwave induced magnetic field, $\vec{h_{rf}}$ perpendicular to $\vec{H}$, drives this damped precession phenomenon.

From equation 5.1, Kittel [Kit48] established a condition to obtain the ferromagnetic resonance:

$$\omega_{res} = \mu_0\gamma\sqrt{(M_{eff} + H + H_{uni})(H + H_{uni})} \tag{5.2}$$

with $\omega_{res} = 2\pi f_{res}$, H_{uni} characterizing the magnetic anisotropy and M_{eff} the effective magnetic saturation.

In the cavity, the frequency f and so ω_{res} are fixed. It is therefore necessary to find the value of H for which the FerroMagnetic Resonance (FMR) appears. Fig. 5.3 displays the derivative of the absorption as a function of the magnetic field H. The absorption corresponds to the imaginary part of the magnetic susceptibility χ''. The resonance field H_{res} is evidenced and is equal to 102 mT. The peak-to peak magnetic field linewidth value ΔH_{pp} characterizes the quality of the layers.

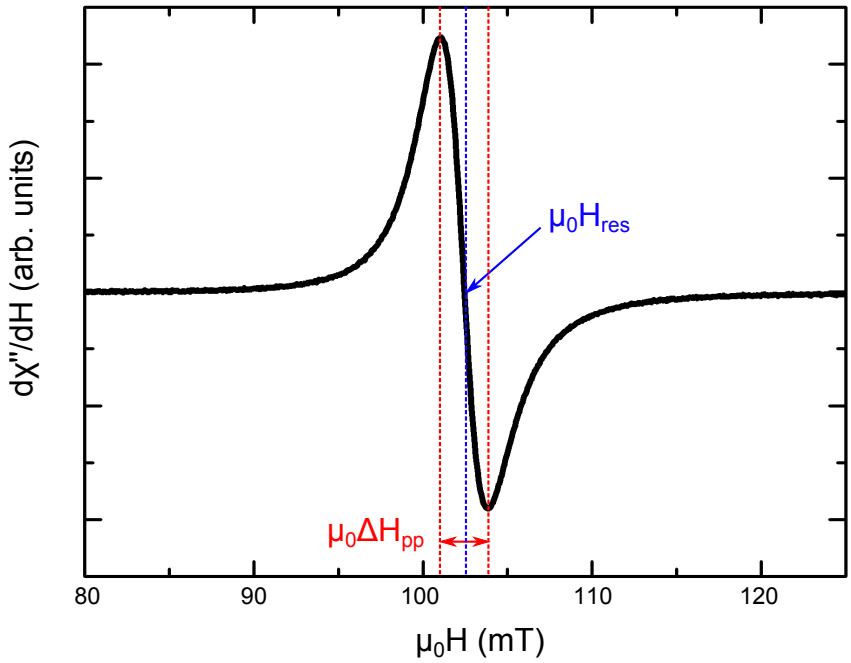

Figure 5.3 – *Ferromagnetic resonance of a stack made of NiFe (20 nm)/HgCdTe (0.6 nm)/HgTe(18.5 nm)/CdTe.*

5.1.3 Injection of spin current and inverse Edelstein effect

Once the conditions for ferromagnetic resonance fulfilled, a spin current is injected in the non-magnetic material. In the previous Chapters of this report as well as in the next section, the notion of spin-polarized current is mentioned several times, so it is of main importance to clarify the difference between a spin current and a spin-polarized current. To do so, it is useful to introduce the definition of both a charge current J_c and a spin current J_s using Fig. 5.4. A spin current is a flow of spin angular momentum, resulting from an uncompensated flow of spin up and spin down. Therefore, in this case of a pure spin current $J_c = 0$. On the contrary, a spin-polarized current is the combination of a charge current and a spin current.

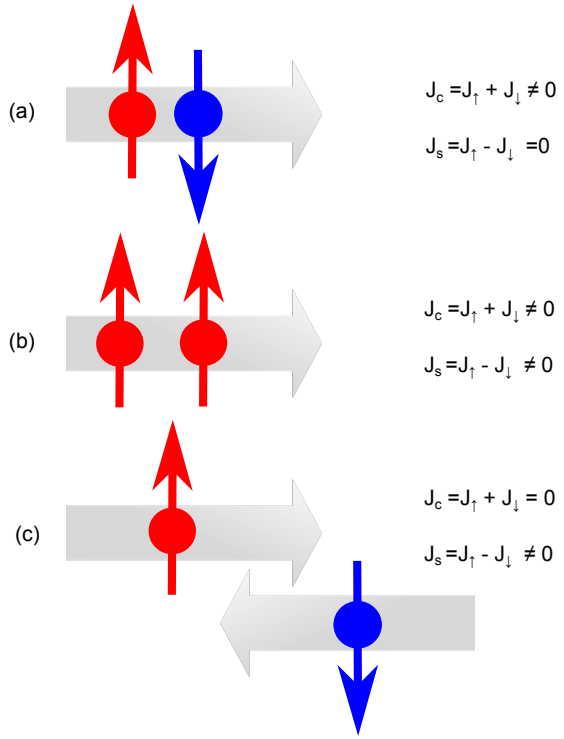

Figure 5.4 – *Definition of (a) a charge current, (b) a spin-polarized current and (c) a spin current.*

The conversion between spin current and charge current is governed by the Inverse Edelstein Effect (IEE) [Ede90]. Probably less known that the Inverse Spin Hall Effect (ISHE) [SUMT06] taking place in bulk materials, the IEE is predicted to arise in 2DEG with strong spin-orbit coupling. Rashba interfaces as well as topological insulator surface states are perfect candidates for experiencing this effect. The first experimental evidence of the IEE has been reported in 2013 by Rojas-Sanchez *et al.* [RSVD+13] at Ag/Bi interfaces. Demonstration of this effect on topological insulator surface states is nowadays of main interest as it enables to validate their applicability to spintronics [JLJ+15] [RSOF+16]. The injection of a spin current at the topological insulator interface induces a charge current along x direction in the 2DEG surface states as illustrated in Fig. 5.5 where the Fermi surface is shifted from Δk due to spin injection. The efficiency of IEE effect is measured through a current conversion ratio (see eq. 5.3). This ratio between the injected 3D spin current density (A/m^2) and the resulting 2D interfacial charge current density (A/m) has a dimension of a length and is called the spin to charge conversion length or the IEE length λ_{IEE}. Moreover, in the case of topological insulators, λ_{IEE} is related to the spin relaxation time τ through the following relation [RSOF+16]:

$$\lambda_{IEE} = \frac{J_c^{2D}}{J_s^{3D}} = \pm v_F.\tau \tag{5.3}$$

$\pm$ corresponding to the chirality of the surface states. Without gate voltage, the Fermi level has been demonstrated to be in the electron-side from low magnetic field transport measurements of Chapter 4. In this configuration λ_{IEE} is expected to be positive [RSOF+16].

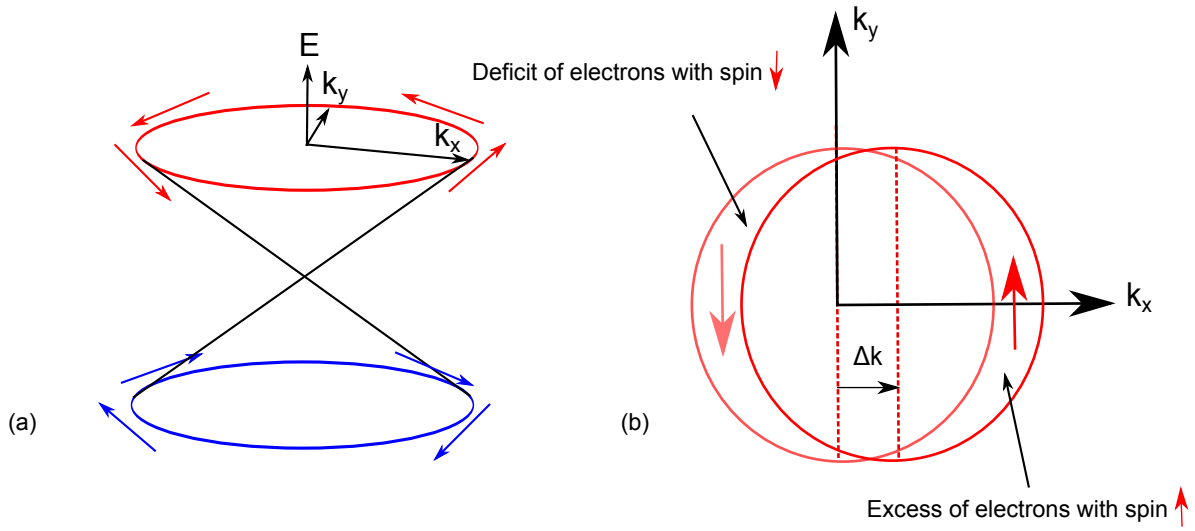

Figure 5.5 – *(a) Energy dispersion of the chiral topological surface states. (b) Fermi surface in the (k_x, k_y) plane. With the addition of a spin current J_s, the Fermi surface is shifted by Δk thus creating a charge current J_c.*

5.1.4 Ferromagnetic resonance measurements

Figure 5.6 displays several dc-voltage measurements for both parallel and antiparallel external magnetic field direction and for several values of microwave induced power. The FMR signal is reported in Fig.5.6(a) for the parallel and antiparallel direction. A slight difference of amplitude is noticeable between the two signals and can be explained by a different centering in the cavity due to thick CdTe substrate. The resonance field H_{res} has already been determined to be 102 mT with a ΔH_{pp} of 28 mT. Such a narrow peak-to peak linewidth characterizes the quality of the NiFe layer deposition and the low roughness of the stack, estimated to $\approx$ 1 nm from the XRR measurements.

The corresponding dc-voltage measurements are presented in Fig. 5.6(b). At the FMR ($H = H_{res}$), a sharp peak appears in the voltage signals. By fitting the Lorentz-shape of the voltage signals, one manage to determine their symmetric part V_{sym} which is attributed to the spin-charge conversion and their antisymmetric part $V_{antisym}$ which can be identified to the anisotropic magnetoresistance of NiFe [MPF+10]. The parallel and antiparallel measurements share the same symmetric Lorentz shape but with opposite sign. The reversibility of the voltage with the magnetic field is an indication of locking between spin and charge. From these measurements a symmetric voltage V_{sym} of about 67 μV in parallel direction and about 61 μV in antiparallel direction is extracted. The small disparity of V_{sym} values between parallel and antiparallel directions might be explained by the difference of centering in the cavity. The antisymmetric component $V_{antisym}$ is two times less important (31 μV) ensuring that such voltage signal is mainly due to spin pumping.

Figure 5.6(c) evidences dc-voltage measurements for several microwave applied power values ranging from 10 to 200 mW. The power has an effect on the amplitude of the voltage signal. V_{sym} values are extracted for each power and reported in Fig. 5.6(d). The linear dependence of V_{sym} is verified and ensures one more time that the measured voltage is mainly due to spin pumping and that we can rule out the effect of any extra contribution such as spin-Seebeck effect [RSOF+16].

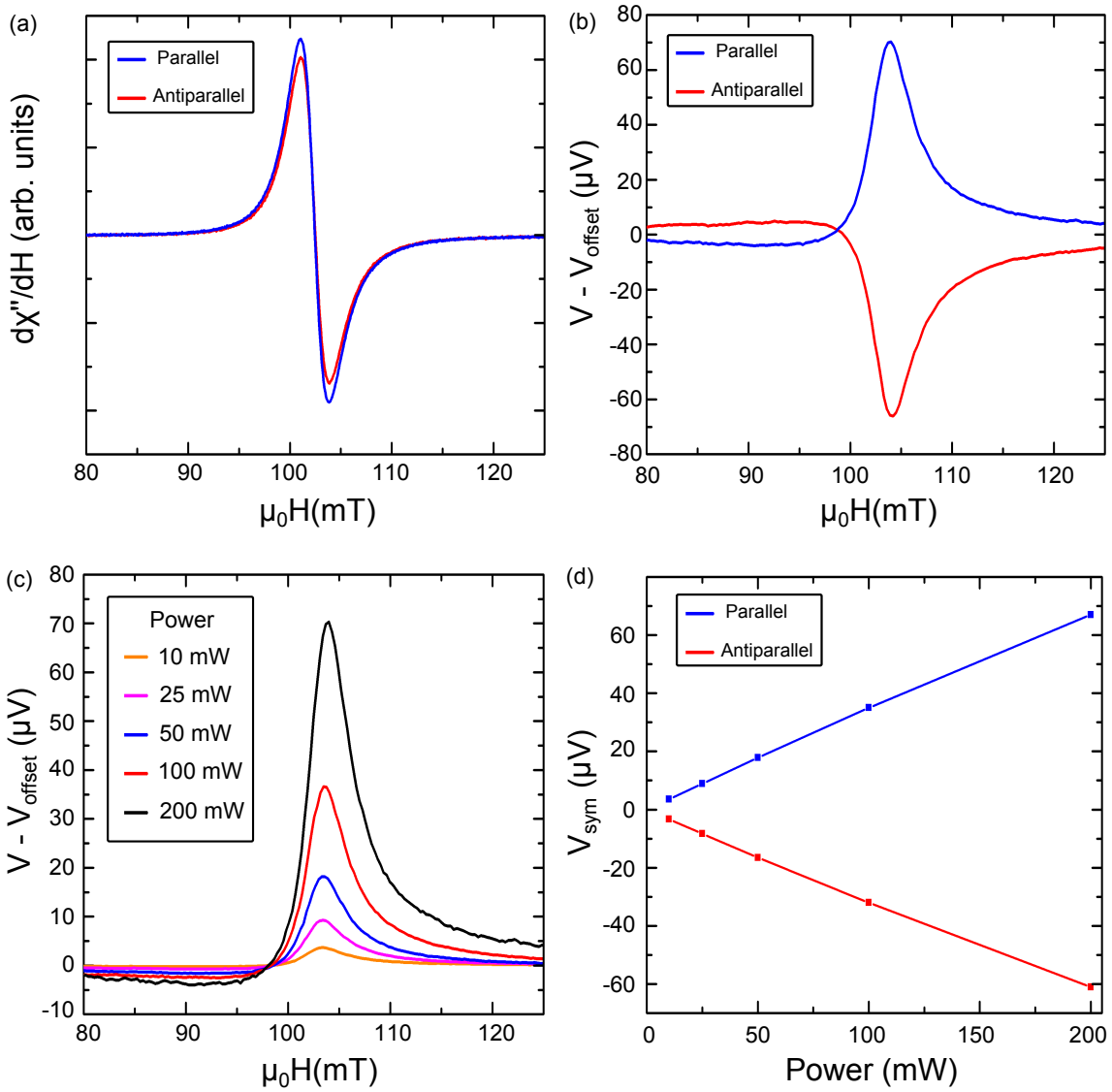

Figure 5.6 – *(a) Ferromagnetic resonance signal for both parallel and antiparallel directions of the magnetic field. (b) dc-voltage measurement at 200 mW in both directions. (c) Voltage as a function of magnetic field for several values of microwave applied power in the parallel direction. (d) Linear evolution of the symmetric voltage contribution with the power.*

5.1.5 Broadband measurements

Broadband measurements are now performed to complete the spin pumping dc-voltage measurements. The aim is to extract the value of extra-damping $\alpha_{FM/NM}$ which is needed to estimate the spin current J_s^{3D}. This extra damping comes indeed from to the additional relaxation channel opened by the HgTe layer. The resulting dissipation of angular momentum occurs through the injection of a spin current. This phenomena of spin pumping is exactly the reciprocal mechanism of the spin transfer torque, in which a spin current transfer its angular momentum to a magnet [TBB02]. Values of H_{uni} and M_{eff} are also determined.

Broadband measurement implies the realization of the ferromagnetic resonance study at different frequency values ranging from 4 to 24 GHz with a 2 GHz step. For each frequency, H_{res} and ΔH_{pp} are extracted from the FMR signal. Fig. 5.7 displays ferromagnetic resonance for each frequency. One can directly notice the increase of H_{res} and ΔH_{pp} with the frequency.

Such frequency dependence of these two parameters is reported in the two graphs of Fig. 5.8. The frequency

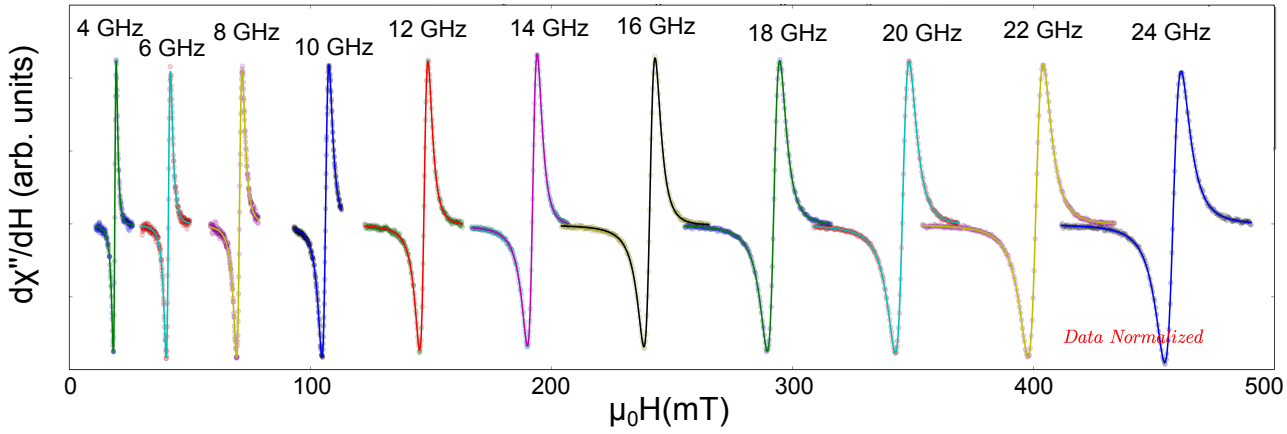

Figure 5.7 – *Ferromagnetic resonance for frequency ranging from 2 to 24 GHz. Experimental data are represented by dots and solid lines correspond to fits allowing the extraction of H_{res} and ΔH_{pp}.*

dependence of H_{res} can be fitted using the Kittel resonance condition (see eq. 5.2) thus giving access to M_{eff} and H_{uni} values estimated at 792 kA/m and -0.95 mT respectively.

Fig. 5.8(b) evidences the linear variation of ΔH_{pp} with frequency. To fit this curve, we will use the fact that for a Lorentz-shape curve, the Full Width at Half Maximum (FWHM) is related to the peak-to-peak linewidth through the relation below:

$$\Delta H_{pp} = \frac{1}{\sqrt{3}} \Delta H_{FWHM} \tag{5.4}$$

Moreover, the FWHM can be expressed as a function of the global damping α through the equation:

$$\Delta H_{FWHM} = 2\frac{\alpha\omega}{\gamma} \tag{5.5}$$

Therefore, one obtains the following relation between ΔH_{pp}, f and α:

$$\Delta H_{pp} = \Delta H_0 + \frac{4}{\sqrt{3}} \frac{\alpha\pi f}{\gamma} \tag{5.6}$$

where ΔH_0 expressed an inhomogeneous broadening caused by the presence of defects and variation of magnetic properties. Fitting the ΔH_{pp} frequency dependence via this relation (see red line in Fig. 5.8) leads to the determination of $\alpha = \alpha_{FM/NM} = 7.1\ 10^{-3}$.

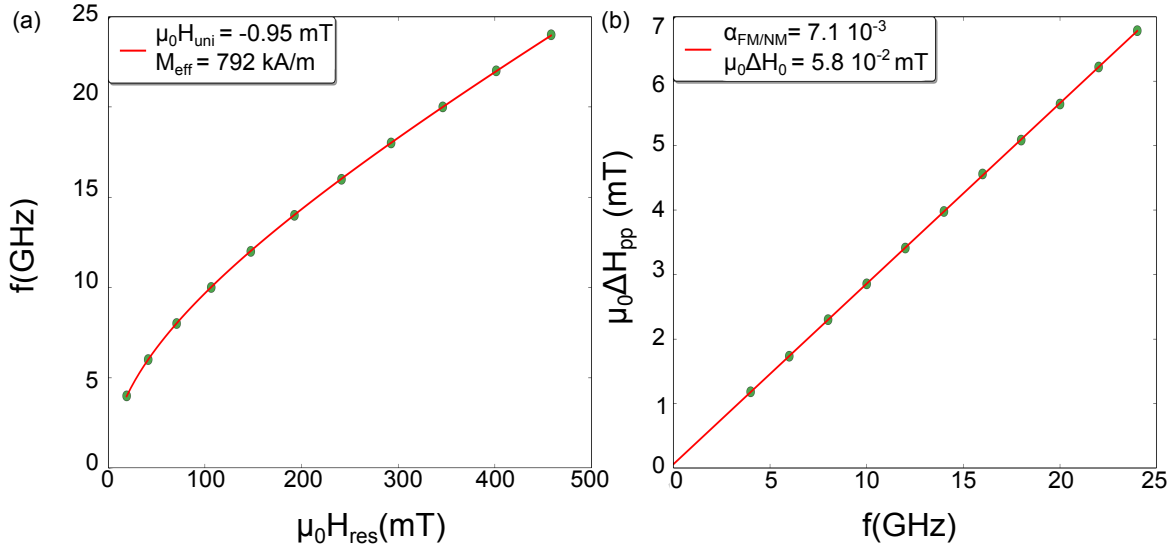

Figure 5.8 – *(a) Evolution of the frequency f with the resonance field H_{res}. (b) Evolution of the peak-to-peak linewidth ΔH_{pp} with frequency. Green points correspond to experimental data while the red solid lines are the associated fits.*

5.1.6 Extraction of the spin-to-charge conversion length

Voltage and broadband measurements lead to the determination of all relevant parameters to characterize the spin-to-charge conversion length. Tables 5.1 and 5.2 summarize these parameters, especially the two probe resistance R, V_{sym}, the resulting charge current j_c^{2D} and its normalization J_c^{2D} by the slab width W = 400 μm.

Param.	R (Ω)	V_{sym}(μV)	$V_{antisym}$ (μV)	$\mu_0 H_{res}$ (mT)	$\mu_0\Delta H_{pp}$ (mT)	h_{rf} (G)	V_{norm} (μV/G^2)	j_c^{2D} (μA/G^2)	$J_c^{2D}=j_c^{2D}/W$ (mA/(m.G^2))
Values	82.1	67.0	31.0	102	28	0.72	139	1.69	4.23

Table 5.1 – *dc-voltage extracted parameters.*

Param.	$\mu_0 H_{uni}$ (mT)	M_{eff} (kA/m)	$\alpha_{FM/NM}$
Values	-0.95	792	7.1 10^{-3}

Table 5.2 – *Broadband extracted parameters.*

The difference between the damping of the sample $\alpha_{FM/NM}$ and the intrinsic damping of the ferromagnetic material α_{FM} = 6.45 10^{-3} [LFO+16] gives access to the spin-mixing conductivity through the relation:

$$g_{eff}^{\uparrow\downarrow} = \frac{4\pi M_{eff} t_F}{g\mu_B}(\alpha_{FM/NM} - \alpha_{FM}) \tag{5.7}$$

where t_F is the thickness of the topological layer.

From the spin-mixing conductivity, one can then directly extract the spin current density [ATI+11] injected at the resonance condition:

$$J_s^{3D} = \frac{g_{eff}^{\uparrow\downarrow}\gamma^2\hbar h_{rf}^2}{8\pi\alpha_{FM/NM}^2}\left[\frac{4\pi M_{eff}\gamma + \sqrt{(4\pi M_{eff}\gamma)^2 + 4\omega^2}}{(4\pi M_{eff}\gamma)^2 + 4\omega^2}\right]\left(\frac{2e}{\hbar}\right) \tag{5.8}$$

Values of $g_{eff}^{\uparrow\downarrow}$, J_s^{3D} and finally λ_{IEE} using relations 5.7, 5.8 and 5.3 respectively, are reported in Table 5.3.

Param.	$g_{eff}^{\uparrow\downarrow}$ (nm^{-2})	J_s^{3D} (MA/m^2)	λ_{IEE} (nm)
Values	6.46	4.65	0.92

Table 5.3 – *Extracted values of the spin-mixing conductivity, the spin current and the inverse Edelstein effect length.*

With a 0.9 nm spin-to-charge conversion length, this system is comparable to another topological structure α-Sn with $\lambda_{IEE} = 2.1$ nm at room temperature [RSOF+16]. Furthermore, it also presents a more important spin-to-charge conversion length than Pt (0.2 nm), Ta (0.3 nm) and W (0.4 nm) [LFO+16], which are the best spin Hall effect materials known to date [RSRL+14] [PLL+12] [LPL+12]. This result thus strongly justifies the interest in HgTe topological insulator for spintronic applications.

ARPES measurements demonstrate $v_f = 5.10^5$ m/s [COB+13]. Therefore, the spin relaxation time can be estimated to ≈ 1.8 fs in our structures using relation 5.3. Improvement of the inverse Edelstein effect length and so of the spin relaxation time is in progress with especially a study concerning the impact of the HgCdTe barrier thickness on the efficiency of spin injection.

An other on-going study focus on the topological insulator thickness. The previous Chapter has indeed demonstrated different transport mechanisms with either independent or coupled surface states depending on the HgTe thickness. The objective here is thus to determine in which thickness regime the spin-to-charge conversion is optimal.

Moreover, the presented results have all been obtained at room temperature, whereas the bulk gap of HgTe is only $\approx 20 - 30$ meV and so is comparable to the thermal energy. Performing low temperature measurements should thus allow to decrease the impact of the bulk carriers and potentially enhance the spin-to-charge conversion efficiency.

The realization of the inverse Edelstein effect in our structures associated to the spin pumping characteristics are reliable signatures of the spin-momentum locking property. These results are promising and open the way toward the use of such 3D HgTe/CdTe topological insulator system for spintronic applications. Indeed, using this time the direct Edelstein effect, these topological structures should allow to generate spin-current without ferromagnetic materials or realize efficient systems to manipulate the magnetic state of nearby magnets by spin transfer torque.

5.2 Spin-based Mach Zehnder interferometer

With the demonstration of the spin-momentum locking property, topological insulators can be used for a wide range of applications in spintronics. Particularly, by engineering the resulting spin-polarized currents, spin-based logic elements such as spin transistor [KR11] or spin filter [IdJM15] are achievable.

With high magnetic fields, unique properties of the surface state chiral massless particles can be implemented through simple structures like $p-n$ junctions where p and n refers to hole- and electron-like regions, respectively. Such junctions are of main interest for spintronics but they could also constitute reliable building-blocks for bipolar nanoelectronics (using effects such as Klein and Zener tunneling, Veselago lenses, ...) [Mur12].

However and despite a very simple design, the underlying physics is complicated and addresses the issue of the state interplay at the junction interface [AL07] [KLY+15] [MTT+15]. A lot of magneto-transport studies have already been carried out on single layers of graphene with n and p regions obtained either by the combination of a backgate and a top gate [MMM+15] or by chemical doping [LvKS09]. With quantization dependent on both n and p region filling factors, a fully equilibrated mixing of the states has been evidenced at the $p-n$ interface [SRB+13]. As topological surface states act similarly as a graphene sheet, it is important to study the physics of $p-n$ junctions on this system [WCZZ12]. Up to now only a few experimental realizations have been reported concerning $p-n$ junction on 3D BiSbTeSe topological insulators [TTS+16] [XMC16].

This section aims at demonstrating the realization of a first $p-n$ junction using thin 3D HgTe topological insulator structures, which would constitute the building-block for the implementation of a spin-based Mach-Zehnder interferometer. First introduced in optics [GW06], Mach-Zehnder interferometer are nowadays also widely used in electronics [JCS+03] to manipulate single-channel of electrons. This project is inspired from the theoretical proposition of [IdJM15] and aims at manipulating single spin-polarized channels. Details about this development and the on-going work are presented in this section.

5.2.1 Spin-based interferometer in a $p-n$ topological insulator junction

The realization of a spin-based Mach-Zehnder interferometer acting as a spin filter and using a dual-gated 3D HgTe topological insulator is envisaged and described in the following. To understand the functioning of such a spin-based interferometer, the reader must have in mind the specificity of 3D topological insulators for which the full 2D surface is accessible for transport with no edges. The sole change of Hall conductance due to the impact of magnetic field direction and chemical potential enables a network of chiral modes to be created.

By applying a large magnetic field, the top and bottom surface states reach the quantum Hall regime. Each surface state is characterized by its Hall conductance $\sigma_{xy} = (N+\frac{1}{2})\frac{e^2}{h}$. Therefore, filling only $N=0$ Landau level (LL) results in $\nu(n) = \frac{1}{2}$ and so $\sigma_{xy}^{top} = \frac{e^2}{2h}$ and $\sigma_{xy}^{bot} = -\frac{e^2}{2h}$. The change of sign between the top and bottom surfaces is attributed to the direction of $\vec{B}$ in regards of each surface normal. In these conditions, the two surfaces are separated by one unit of σ_{xy}, therefore a single conduction channel arises at their interface that are the side surfaces. This single conduction channel is forming a chiral edge state as represented in Fig. 5.9 where the interface between the two left quadrants illustrates the propagation of this single chiral mode.

To go further, let us now consider the additional impact of the chemical potential i.e. the Fermi level energy E_F position. By sweeping E_F in the hole-side, $N=-1$ LL is filled, thus implying $\nu(p) = -\frac{1}{2}$ as it can be seen in Fig. 5.10(a). The change of sign of the filling factor is directly followed by the change of the Hall conductance one: $\sigma_{xy}^{top} = -\frac{e^2}{2h}$ and $\sigma_{xy}^{bot} = \frac{e^2}{2h}$. Therefore, new regions with different local Hall conductance complement the picture of Fig. 5.9 with the two right quadrants.

As all these regions are separated by one unit of σ_{xy}, all their interfaces are carrying single chiral modes, thus building the chiral network presented in Fig. 5.9.

The spin-based interferometer is finally obtained by wrapping this network on itself, that is sticking together the two equivalent interfaces denoted by green arrows in Fig. 5.9. The final device and the associated chiral network is represented in Fig. 5.10(b). Due to spin-momentum locking property, the chiral modes arising at the

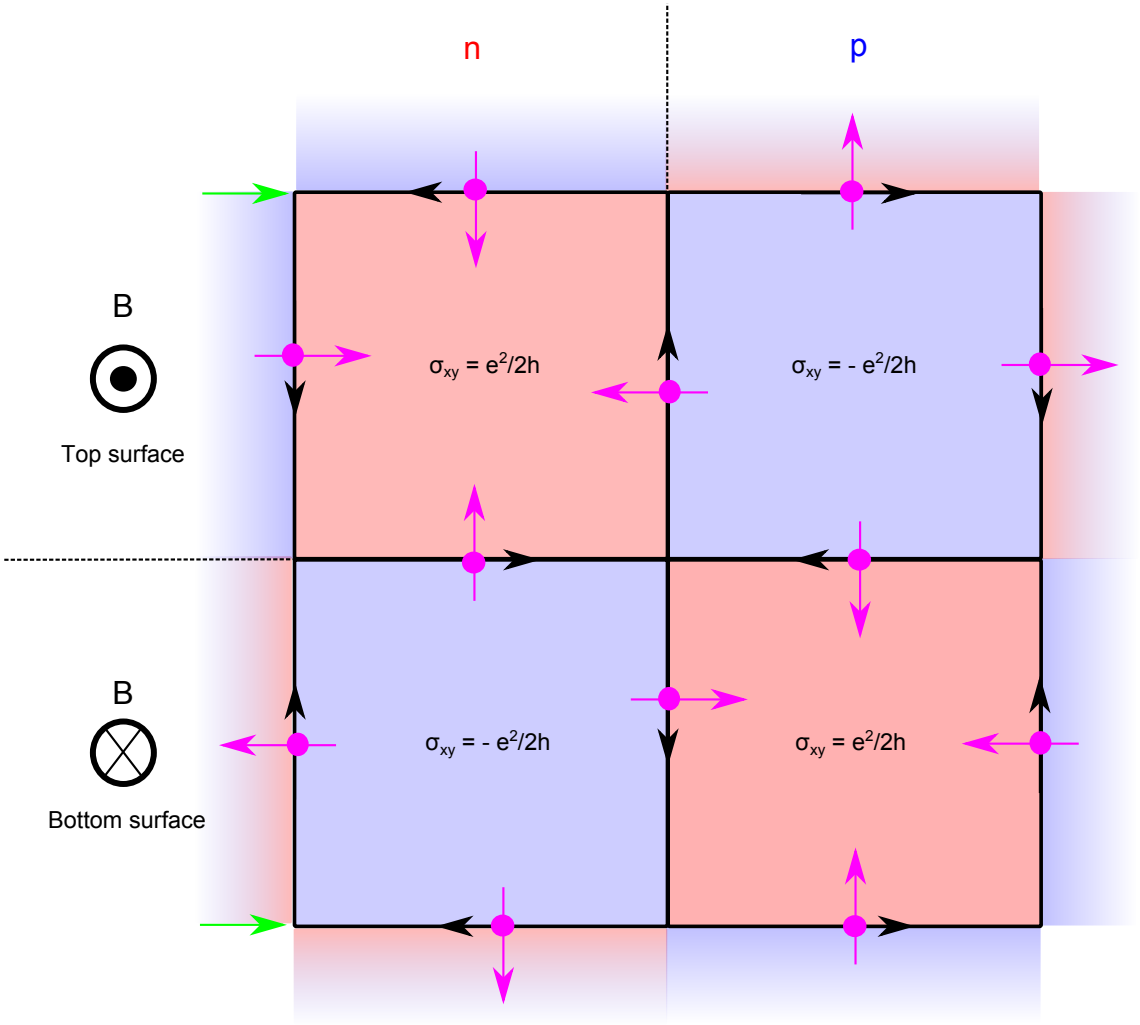

Figure 5.9 – *Single chiral modes arise at the interfaces between regions separated by one unit of Hall conductance σ_{xy}. The impact of both magnetic field direction and of the Fermi energy position enables the establishment of a complete chiral network. Black arrows indicate the direction of propagation of the Dirac fermions, the purple ones represent the associated spin-polarization and the green ones evidence two equivalent interfaces that need to be stuck together to reproduce the sample geometry.*

$n-p$ interface cannot propagate together. They are forced to split on the top and bottom surfaces, thus forming an interference loop schematically represented in Fig. 5.10(b). This interference loop is the core of the device. It is supplied by single chiral modes having a spin-polarization perpendicular to top and bottom surfaces. While in the loop, the polarization of these modes is modified and is now in the plane of these surfaces. Finally, once these chiral modes exit the interference loop, they propagate again on side surfaces either toward the source or the drain depending on their spin orientation.

The main important characteristic of this device is the existence of this interference loop on the film cross-section. Therefore, the use of an in-plane magnetic field $B_{/\!/}$ allows to generate a flux which introduces a phase shift between the two arms of the interferometer. If this phase is zero, the spin polarization of the incoming chiral mode is not modified and thus the mode is reflected. On the contrary, if the phase is π then the spin is flipped inside the loop and the mode is transmitted. Therefore, the in-plane magnetic field can be used as a switch in/off button enabling to control the reflection and transmission of this interferometer. Such a device is very similar to the spin-transistor introduced by Datta and Das [DD90] and could be used as a spin filter.

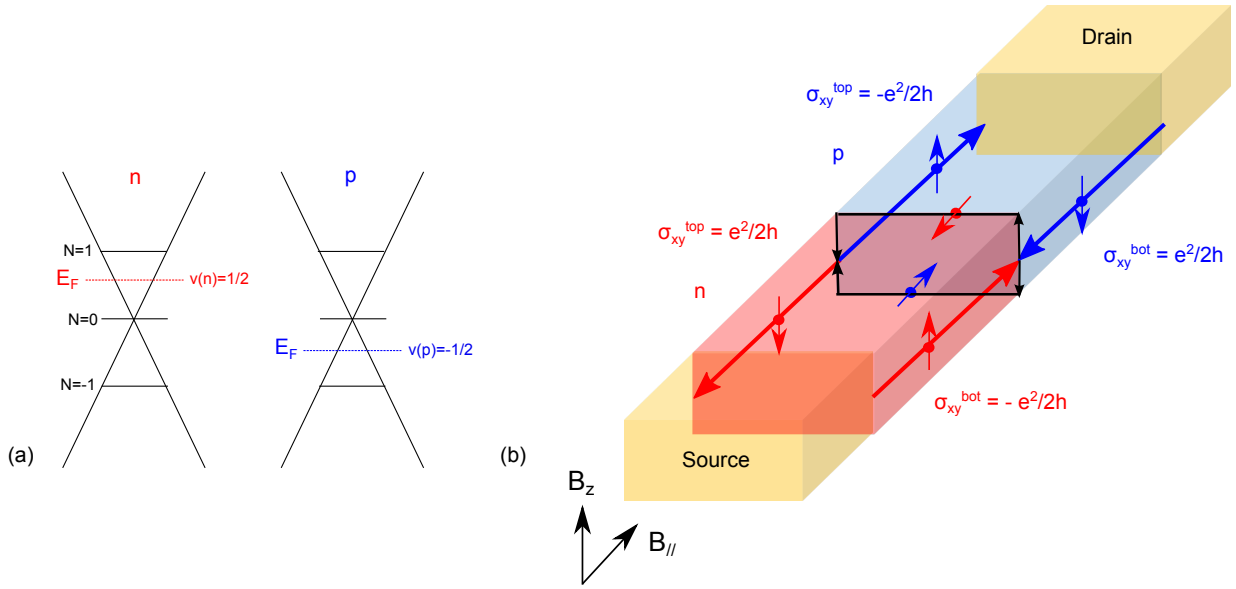

Figure 5.10 – *(a) Positions of the Fermi level E_F are indicated on the Dirac cones for both the n and p regions. (b) Schematic representation of a 3D topological insulator $p-n$ junction. A network of single chiral modes is created in the quantum Hall regime and is forming an interference loop at the $p-n$ junction interface, similar to an optical Mach-Zehnder interferometer. The in-plane magnetic field $B_{//}$ acts as a switch on/off button of this spin-filter device.*

More practically speaking, the realization of such a device requires the use of a 3D topological insulator $p-n$ junction in the quantum Hall regime with vanishing resistance. To date, only the thinnest HgTe layers are satisfying this condition. Therefore, in the following, we present the first magneto-transport measurements performed on a $p-n$ junction made of a 15.5 nm-thick HgTe layer. Our first objective is to test the functioning of such a junction with our HgTe structures.

5.2.2 Experimental setup

As the realization of a backgate is not yet managed, the $p-n$ junction is made using two top gates. The nanofabrication recipe is identical to the one described in Chapter 3 for the Hall bars used in the standard magneto-transport measurements. Only one additional step is required to obtain the second top gate. A 24 nm-thick Al_2O_3 layer is deposited by ALD on the top of the whole sample to isolate the two gates. Laser lithography and the combination of metal evaporation and lift-off are then used to design this second gate. The final structure is shown in Fig. 5.11. For simplicity, we will call region 1 and region 2 the Hall bar parts below gate 1 and 2, respectively. Being isolated, the two gates are individually controlling the carrier density of region 1 and 2 allowing unipolar $n-n$, $p-p$ as well as bipolar $p-n$ and $n-p$ junctions to be obtained.

The measurements have been performed in a four-wire configuration with standard Lock-in detection and in a dilution fridge at T= 32 mK. In the following, we will mainly discuss about the longitudinal resistance $R_{14,56}$. This resistance is measured with the current flowing between contacts 1 and 4, as represented in Fig. 5.11, and the voltage probed between contacts 5 and 6.

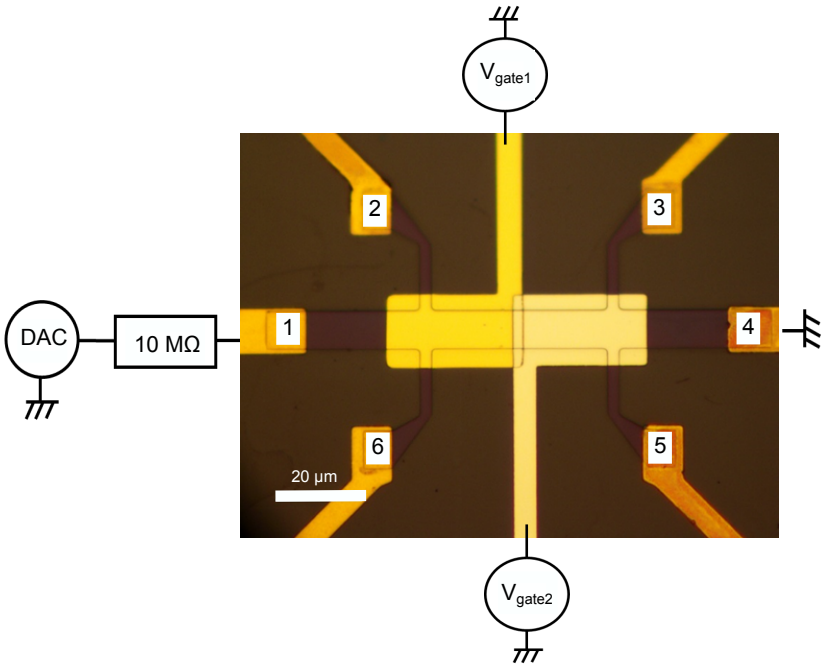

Figure 5.11 – *Experimental setup for the $p-n$ junction. Two top gates are used to obtain two regions with different Fermi energy positions. The Hall bar size is L= 40 µm and W= 10 µm.*

5.2.3 Zero magnetic field

The longitudinal resistance $R_{14,56}$ mapping is reported in Fig. 5.12 (a) as a function of V_{gate1} and V_{gate2} at $B = 0$ T. The cross-like mapping evidences four quadrants due to the independent control of the two gates.

Fig. 5.12 (b) displays two resistance traces for $V_{gate2} = -0.20$ V (red curve) and for $V_{gate1} = 0.07$ V (green curve). Electron- and hole-sides are clearly identified for each curve. Note that the voltage position of the Charge Neutrality Point (CNP) differs between these two curves due to a difference of efficiency of the two gates. The first gate is indeed separated from the HgTe layer by the HgCdTe barrier and a dielectric layer of 24 nm, while for the second the dielectric layer thickness is twice more important. Therefore, using the capacitance model derived in Chapter 3 (see 3.2), one can deduce that the second gate should be characterized by a gate depletion factor and so a gate efficiency two times less important, compared to the first one.

From these observations, four regimes are highlighted. The unipolar $n-n$ regime corresponds to the upper-right quadrant of Fig. 5.12(a), while its $p-p$ counterpart is the lower-left quadrant. The upper-left and lower-right quadrants are for their part attributed to $p-n$ and $n-p$ bipolar regimes, respectively. It is worth noting that these regimes are separated by the CNP of both regions 1 and 2. These lines are however slightly shifted from horizontal or vertical. This very weak effect is attributed to the capacitive coupling between the two top gates. The crossing of these lines characterizes the gate voltage conditions to have both regions at the Dirac point.

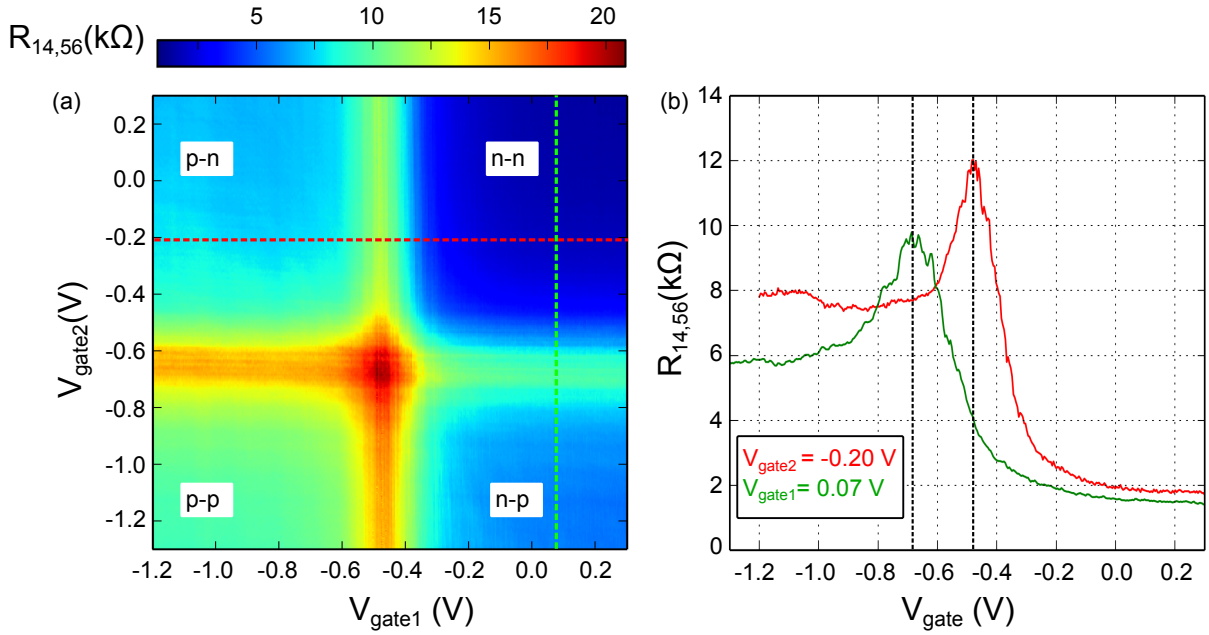

Figure 5.12 – *(a) Longitudinal resistance $R_{14,56}$ mapping as a function of both V_{gate1} and V_{gate2}. Four regimes are clearly identified. (b) $R_{14,56}$ as a function of V_{gate1} (red curve) and V_{gate2} (green curve). Data have been extracted for a 15.5 nm-thick HgTe layer with $I_{bias} = 0.5$ nA, $B = 0$ T and $T = 32$ mK.*

5.2.4 Quantum Hall effect regime

By applying a large magnetic field $\vec{B} = B\vec{z}$, regions 1 and 2 are expected to enter into the QHE regime. Fig. 5.13(a) displays $R_{14,56}$ as a function of the two gate voltages for $B = 3$ T. The cross-like pattern reported for $B = 0$ T is not fully reproduced. Only the vertical line corresponding to the CNP of region 1 is clearly observed. However, in the n regime of region 1, two different behaviors are noticeable.

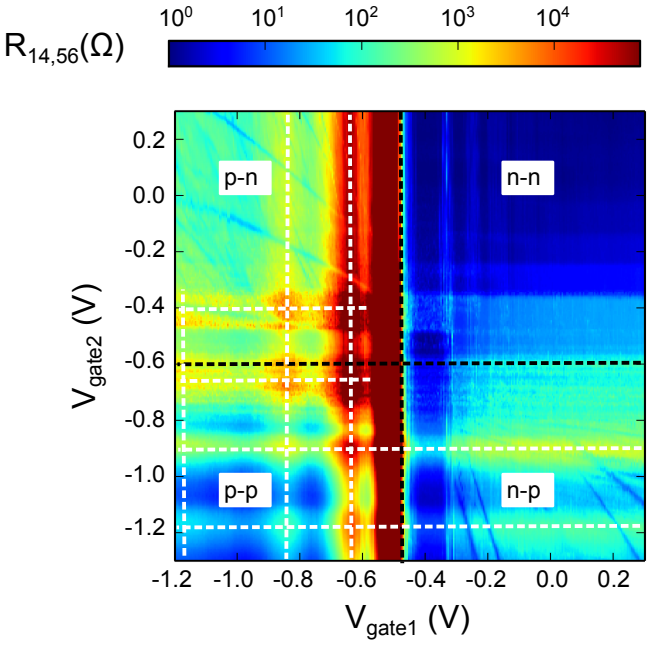

Figure 5.13 – *$R_{14,56}$ as a function of V_{gate1} and V_{gate2}. Black dashed lines separate the different unipolar and bipolar regimes. White dashed lines highlight a grid pattern of Landau levels. Data have been extracted for a 15.5 nm-thick HgTe layer at $B = 3$ T, $T = 32$ mK and $I_{bias} = 0.5$ nA.*

A succession of resistance plateaus is visible on the upper-right quadrant of Fig. 5.13, while the lower-right quadrant exhibits oscillatory patterns. These features are confirmed by the resistance trace plotted in Fig. 5.14(a) for $V_{gate1} = 0.25$ V. Moreover, this change of behavior happens exactly at the expected position of region 2 CNP, identified from the measurement at zero field. Based on these observations, the delimitation between $n-n$ unipolar and $n-p$ bipolar regimes has been made possible and is indicated in Fig. 5.13 by a black dashed line.

$R_{14,56}$ mapping is indeed revealing very interesting features with especially this quantization of the resistance in the $n-n$ regime. The resistance trace, plotted in Fig. 5.14(a) as a function of V_{gate2}, demonstrates successive plateaus with a non-integer quantization. Similarly, a resistance trace is plotted as a function of V_{gate1} in Fig. 5.14(b). The constant value of $R_{14,56}$ for $V_{gate1} \geq -0.2$ V illustrates also a well-defined resistance plateau. Note that similar quantization of the resistance has been reported in the literature for graphene $p-n$ junction [KLY+15].

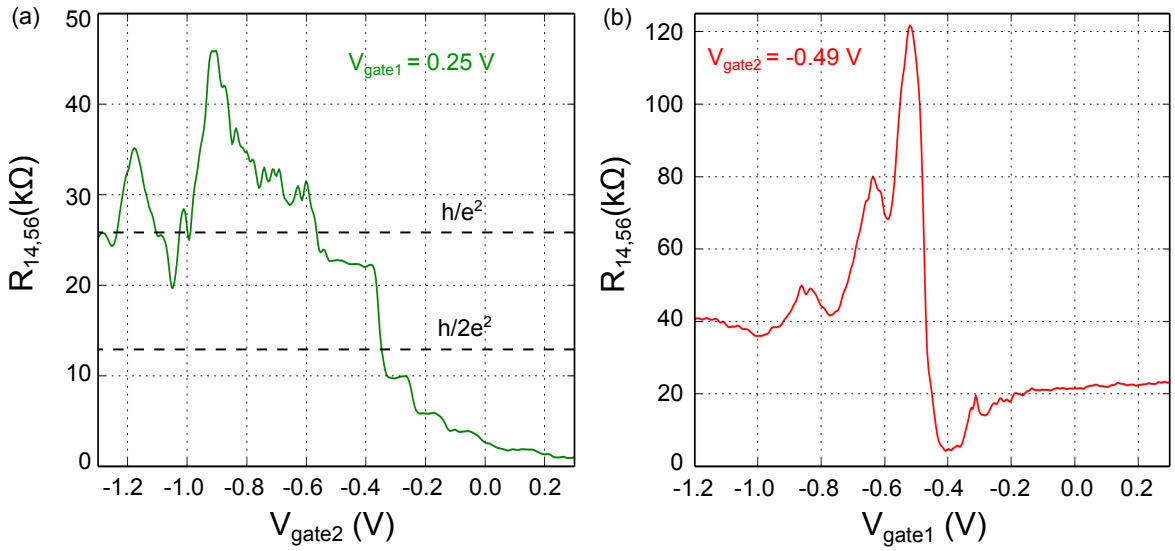

Figure 5.14 – *(a) $R_{14,56}$ trace as a function of V_{gate2} for $V_{gate1} = 0.25$ V. (b) $R_{14,56}$ trace as a function of V_{gate1} for $V_{gate2} = -0.49$ V.*

Such a resistance quantization is however not visible in the other regimes, but one can notice several resistance maxima forming a grid pattern highlighted by the white dashed lines in Fig. 5.13. This grid pattern corresponds to the crossing of the Landau levels and is mostly noticed in the unipolar $p-p$ regime. These features are similar to what has been reported for dual-gated $BiSbTeSe_2$ compound [XMC16]. In the $p-n$ and $n-p$ bipolar regimes, this pattern extends with vertical and horizontal lines respectively, thus suggesting that only one gate enables the filling of individual LLs. In both case, it appears that the p regime prevails over the n one. Such a behavior can be due to the large LL broadening of the p regime masking the contributions of the n one. Indeed, the LL broadening has been demonstrated to be much larger in the hole-side than in the electron-side in Chapter 4 (see 4.2.3).

In the following, we only focus on the $n-n$ regime as it is the only one showing clear evidences of QHE with well-defined quantized plateaus. The impact of the coupling to the Γ_{8HH} bulk band in the other regimes ($n-p$, $p-n$ and $p-p$) prevents a clear analysis of their transport properties.

To go one step further and try to understand the values of quantization observed in the $n-n$ regime, it is useful to have a look on the Landauer-Büttiker edge state formalism. Fig. 5.15 illustrates the edge state transport

expected in such unipolar junction. n_1 and n_2 refer to the polarity of region 1 and region 2, respectively. Each region is also characterized by its filling factor ν_1 and ν_2. We define $\nu = |\nu_1 - \nu_2|$ the difference of filling factor between the two regions.

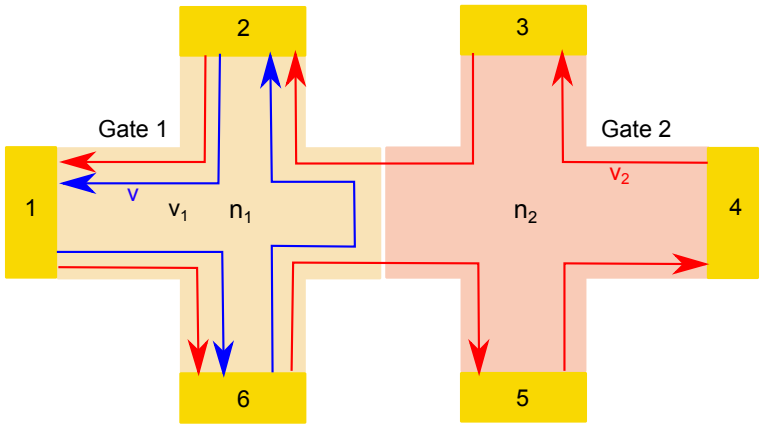

Figure 5.15 – *Scheme of the edge state transport in the case of $n-n$ unipolar junction. ν_1 and ν_2 are the filling factors of region 1 and 2, respectively. The case $\nu_1 > \nu_2$ is considered with ν the difference of filling factor between the two regions.*

The Landauer-Büttiker edge state formalism 5.9 is used to determine the expected values of quantized resistance:

$$I_i = \frac{e^2}{h} \sum_j (T_{ji} V_i - T_{ij} V_j) \tag{5.9}$$

As the current flows between contacts 1 and 4, the following conditions are considered:

$$\begin{cases} I_1 = I \\ I_4 = -I \\ V_4 = 0 \end{cases} \tag{5.10}$$

In Fig. 5.15, region 1 is depicted with a larger filling factor ν_1 than in region 2 ($\nu_1 > \nu_2$). We assume that transport through the interface (it means between contacts 3 and 2 and between 6 and 5) is carried by the edge states ν_2 common to the two regions. The remaining edge states ν only circulate inside region 1. With these considerations and from Landauer-Büttiker formalism, we obtain:

$$\begin{pmatrix} I \\ 0 \\ 0 \\ -I \\ 0 \\ 0 \end{pmatrix} = \begin{pmatrix} \nu_1 & 0 & 0 & 0 & 0 & -\nu_1 \\ -\nu_1 & \nu_1+\nu_2 & 0 & 0 & 0 & 0 \\ 0 & -\nu_2 & \nu_2 & 0 & 0 & 0 \\ 0 & 0 & -\nu_2 & \nu_2 & 0 & 0 \\ 0 & 0 & 0 & -\nu_2 & \nu_2 & 0 \\ 0 & -\nu & 0 & 0 & -\nu_2 & \nu_1 \end{pmatrix} \cdot \begin{pmatrix} V_1 \\ V_2 \\ V_3 \\ 0 \\ V_5 \\ V_6 \end{pmatrix} \tag{5.11}$$

Longitudinal resistance $R_{14,56}$ is defined as:

$$R_{14,56} = \frac{V_5 - V_6}{I} \tag{5.12}$$

so, one can determine that for a $n-n$ junction:

$$\begin{cases} R_{14,56} = \frac{|\nu_1-\nu_2|}{\nu_1\nu_2}\frac{h}{e^2}, \text{ if } |\nu_1| > |\nu_2| \\ R_{14,56} = 0, \text{ if } |\nu_1| < |\nu_2| \end{cases} \tag{5.13}$$

From these calculations, a mapping of the expected values of $R_{14,56}$ as a function of ν_1 and ν_2 has been obtained and is represented in Fig. 5.16. As the magnetic field value does not exceed 3 T in this study, one should remember that, for such thin HgTe structures, the quantization and so the filling factors ν_1 and ν_2 take integer values in the electron-side while they take only odd values in the hole-side due to the LL broadening effect.

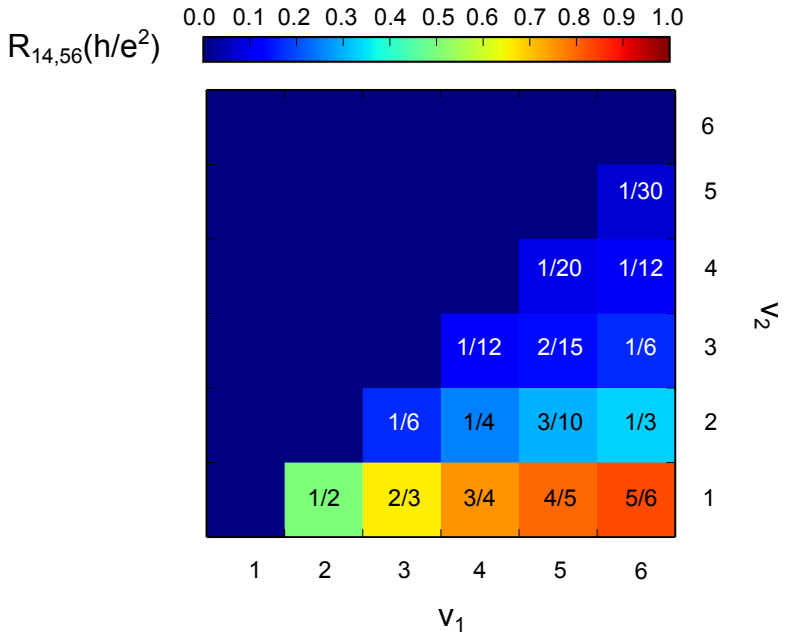

Figure 5.16 – *Expected values of $R_{14,56}$ as a function of filling factors ν_1 and ν_2 in the $n-n$ unipolar regime.*

The expected quantization values of $R_{14,56}$ have just been evidenced in the $n-n$ unipolar regime. We are now going back to experimental data and compare them to this formalism to verify the functioning of our junction.

Fig. 5.17(a) displays $R_{14,56}$ in the $n-n$ regime as a function of the two gate voltages for $B = 3$ T and $T = 32$ mK, using the same colorscale than in the mapping of Fig. 5.16. $R_{14,56}$ mapping is characterized by plateaus of resistance which are well-defined and mostly pronounced for the higher values of V_{gate1}, it means the higher values of ν_1 on the right part of the mapping. Transition from one plateau to the other is possible by sweeping V_{gate2} but also by sweeping V_{gate1}. Furthermore, the upper part of the mapping evidences vanishing resistance. All these signatures are consistent with the Landauer-Büttiker formalism results presented in Fig. 5.16.

To go further in the analysis, it is of main importance to access quantization values of the mentioned plateaus of resistance. Fig. 5.17(b) represents a trace of $R_{14,56}$ as a function of V_{gate2} for $V_{gate1} = 0.30$ V. The plateaus and their quantization are highlighted. Five plateaus are clearly defined, thus suggesting that $\nu_1 = 6$, by comparison with the mapping of Fig. 5.16. In this case, the expected values of resistance are: 0.83, 0.33, 0.16, 0.08 and 0.03. Experimental data evidence plateaus with the following quantization: 0.86, 0.38, 0.22, 0.15 and 0.06. These values are very close from the expected ones.

A similar work has been performed for several values of V_{gate1} and reported in Fig. 5.17(c). One can

directly notice a decrease of the plateaus amplitude as well as a decrease of the number of plateaus when decreasing V_{gate1} and so ν_1. This behavior is fully consistent with the expectations (see Fig. 5.16). Furthermore, quantization transits from 0.86, 0.80, 0.69, to 0.50 and then splits in two plateaus at 0.50 and 0.10 when sweeping V_{gate1} for V_{gate2} between -0.35 and -0.55 V. The first quantized values indicate that only one channel is present in region 2 and that $\nu_2 = 1$ in these voltage ranges. However, the observed splitting of quantization is not consistent with the predictions and needs to be further investigated to understand its origin.

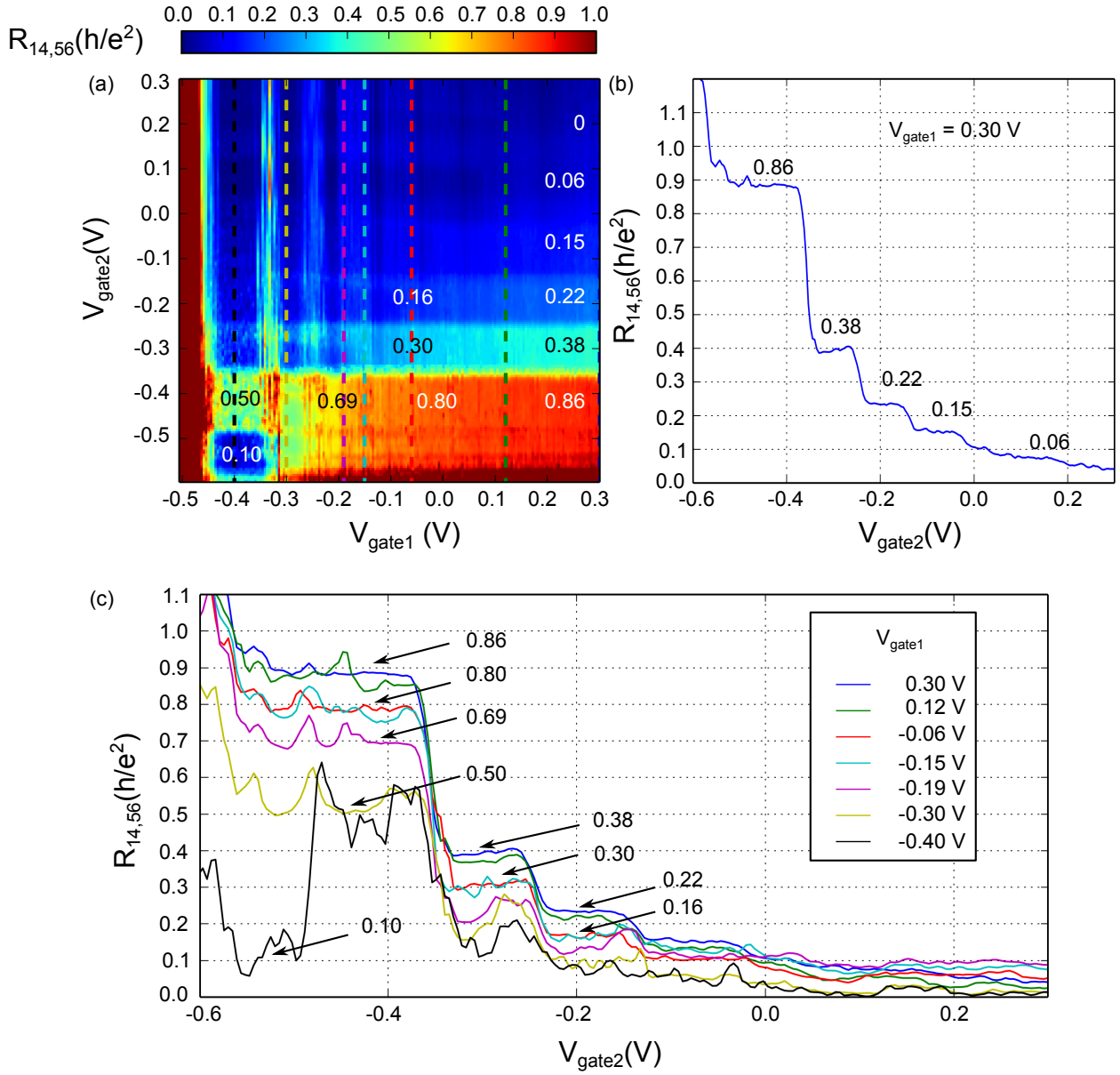

Figure 5.17 – *(a) $R_{14,56}$ mapping as a function of both V_{gate1} and V_{gate2} for B= 3 T and T=32 mK in $n-n$ regime. (b) $R_{14,56}$ trace as a function of V_{gate2} for $V_{gate1} = 0.30$ V with the corresponding quantization highlighted. (c) $R_{14,56}$ traces as a function of V_{gate2} for several values of V_{gate1}.*

To summarize, we have presented the first magneto-transport measurements on a $p-n$ junction made of 3D HgTe topological insulator. These preliminary measurements have demonstrated the ability of filling individual LLs using the two independent gate voltages. Determination of the resulting quantization has been shown to be complicated in the $p-p$, $n-p$ and $p-n$ regimes due to large LL broadening induced by the coupling to the Γ_{8HH} bulk band. The resistance quantization in the $n-n$ regime demonstrates the consistency of the transport mechanism at stake with the Landauer-Büttiker edge state formalism. Nevertheless, some divergences have been highlighted and will need to be investigated in the future.

This first study is raising a lot of questions about the feasibility of such junction with HgTe topological insulator because of the coupling to the Γ_{8HH} bulk band. To answer these questions, complementary measurements on other samples are strongly needed to verify the robustness of the observed signatures. An important work is thus required to be able to precisely conclude about the potential of HgTe topological insulators for the realization of a $p-n$ junction.

5.3 Conclusion

This Chapter has reported our first results concerning the application of HgTe topological insulator structures for spintronics.

Spin pumping measurements have been achieved and have demonstrated signatures of spin-momentum locking. Furthermore, the ability of our HgTe structures to convert a spin into a charge current has been evidenced. More specifically, the spin to charge conversion has been determined to occur on a length of 0.9 nm with a spin relaxation time in the femtosecond range. With these characteristics, HgTe topological insulator is already surpassing the best spin Hall effect materials such as Pt, Ta and W. These preliminary results acquired at room temperature are very promising and are thus justifying the use of HgTe for spintronics and especially for the generation and detection of spin currents without magnetic materials.

Then, this Chapter has focused on the implementation of a spin-based logic element using 3D HgTe topological insulators and more precisely the development of a spin-based Mach-Zehnder interferometer. Such a device can be used as a spin-filter or even as a spin transistor. However, so far, the accomplishment of this project is limited by the $p-n$ junction functioning. These first measurements enable indeed to realize that the coupling to the Γ_{8HH} bulk band can be an important limiting factor for HgTe applications. Finding solutions to decrease its impact on the transport properties is required to produce functioning devices in the future. Reduction of the dimensions from three to one dimension constitutes a promising pathway to achieve this goal.

Conclusions and Perspectives

The aim of this PhD thesis was to demonstrate the eligibility of HgTe/CdTe topological insulator for applications and especially for spintronics. Topological insulator materials are indeed very interesting in this field of research as they enable the generation of dissipation-less spin-polarized current or even pure spin current without magnetic materials.

In this work, an important part has been dedicated to the material growth optimization and improvement. Two main points have been identified as essential to guarantee the topological nature of the material: the monitoring of the chemical composition to prevent from extra Cd deposit during the growth and ensure the band structure inversion, and the control of the tensile strain for the bulk gap opening. Estimation of the critical thickness for plastic relaxation around 140 nm as well as the out-of-plane deformation around - 0.4 % enables to characterize the tensile strain and the resulting gap opening of the order of 20 meV. Furthermore, a particular attention has been paid to the improvement of surface and interface quality to limit roughness and intermixing that can alter the electronic properties by inducing potential fluctuations. An important set of material characterization techniques including MEIS, XRR and HRSTEM has been used and demonstrate interface width of about 2 nm at the usual growth temperature which is much lower than the surface state extension estimated at $\approx$ 5 nm. While further ways of improvement have already been identified such as the optimization of the growth temperature, of the Hg/Te flux ratio, ..., the present quality of the material already allows to access and to probe the topological properties of our HgTe layers.

Low temperature magneto-transport measurements have been carried out for samples with progressively decreasing HgTe thickness. With independent surface states, the thicker samples have demonstrated very complex transport signatures and mechanisms. Evidences of a new and unidentified coupling mechanism have also been reported through the suppression of the even quantized plateaus and needs to be further investigated and understood to complete and adapt the existing model. This is necessary to go further in the study of these thick 3D topological insulator structures. Furthermore, the addition of extra transport contributions, attributed to bulk and side surfaces, do not facilitate the analysis and prevent from a clear observation of the topological signatures. A strategy to get rid of these contributions in these thick structures has already been proposed and initiated through the optimization of the growth temperature to reduce the bulk defects density. While the impact of such bulk defects on transport properties is not quite clear yet, it would be important to perform similar transport measurements on a defect-free sample in the future to conclude on their action on transport properties in this system.

Furthermore, evidences of two topological surfaces have been reported. However, due to combined top surface and bulk screening effects, the electrical characterization of the bottom surface has been difficult and not very conclusive. To answer this issue and gain knowledge on the bottom surface properties, the implementation of a backgate is strongly needed. Up to now, several tests have been performed using the growth of an In-doped HgCdTe barrier or using a Te-doped InSb substrate as illustrated in Fig. 5.18. So far, In diffusion is a remaining issue and prevents from depleting carriers at the bottom interface due to high leakage currents. Strong efforts are thus needed in the material growth to enable the realization of such double gated structures essential for the

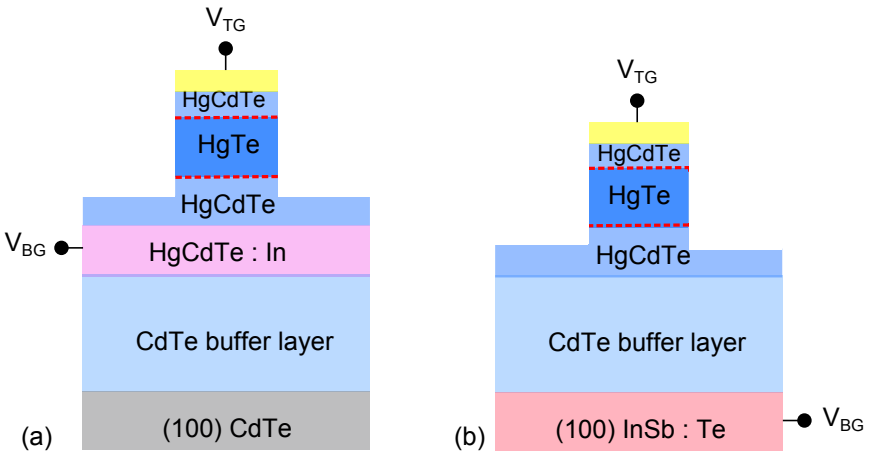

Figure 5.18 – *Adaptation of the former stack layer for the implementation of a backgate with (a) the use of a n-type In-doped HgCdTe barrier or (b) using a Te-doped InSb substrate.*

future of this project.

While the thicker HgTe samples have illustrated very complex transport mechanisms, the thinner samples considerably differ with clear and simple transport signatures associated to an unambiguous demonstration of quantum Hall effect with vanishing resistance minima. The coupling of the two surface states and their respective Dirac cones results in a unique contribution. Quantum Hall transport spectroscopy using temperature dependence has been achieved on such thin samples and enabled the demonstration of the Dirac nature of the carriers as well as a splitting mechanism governed by the hybridization of the two surface states. With these results, the topological nature and the transport mechanism of our thin HgTe structures have been confirmed.

In order to go one step further and use the topological properties for applications, confirmation of the existence of the spin-momentum locking property is required. To do so, a spin-pumping experiment has been performed enabling the injection of a pure spin-current on the HgTe top surface states. The transverse charge current measured on the HgTe top surface appears to change sign when considering opposite spin directions thus confirming the locking between the spin and the momentum. Furthermore, the conversion between spin and charge current has been prooved to occur over few nanometers with a relaxation time in the femtosecond range. These results exceed the performance of the best spin Hall effect materials known to date (W, Pt, Ta) and are thus strongly justifying the growing interest in the use of topological insulators for spintronics.

The confirmation of the spin-momentum locking property is also opening new research axis in spintronics. One of the objective of this thesis has been to use the spin-polarized current generated by the topological insulator surface states to perform a spin-based interferometer. Along these thoughts, a $p-n$ junction has first been established to gain knowledge about the spin-polarized current properties and especially the interplay between currents of opposite spin polarization. However, the first studies on these junctions are not convincing enough for the moment. The coupling with the Γ_{8HH} bulk band in the p regime is suspected to prevent the observations of the expected properties.

In the whole set of presented transport measurements, on standard Hall bars or even on the $p-n$ junctions, the bulk contribution appeared as a limit to unambiguously probe the topological properties, especially in the hole-side or p regime. To reduce the bulk contribution or at least increase the strain gap, the growth of HgSeTe can be envisioned. This ternary alloy lattice parameter being lower than that of HgTe, its growth on CdTe will generate a larger tensile strain and thus a larger strain gap opening. This perspective is promising but appears to be challenging as it requires the development of a low temperature growth process adapted to the Se constraints.

Preliminary band structure calculations and post-growth ARPES measurements are needed to characterize the position of the Dirac point in comparison with the Γ_{8HH} bulk band maxima for this topological alloy.

An other way of reducing bulk contribution is to decrease the bulk to surface ratio by reaching an unidimensional (1D) regime. As e-beam lithography techniques have to be avoided, the only available approach is the growth of bottom-up HgTe nanowires. A shell of CdTe can then be deposited to strain the HgTe core. The main difficulty of this idea lies in the growth initiation of the HgTe nanowires as the standard gold catalysis should be prohibited to prevent from amalgam formation [HSH+08]. The use of patterned substrate or even the more ambitious use of Hg droplets are considered as solutions for initiating the growth.

All these perspectives constitute challenging pathways for further improving the material quality and facilitate the access to its topological properties. In parallel, perspectives of applications are also considered. Indeed, even if only spintronic applications have been discussed in this PhD thesis, potential applications of topological material are widely spread and can even extend to quantum computing through the use of the famous Majorana fermions. These particles, predicted to arise at a topological insulator/superconductor interface, hold the peculiarity to have no spin and no charge, thus allowing information storage without dissipation. Up to now, only a few indications of their presence have been reported for HgTe structures [MBG+15] [DWB+16] [WBD+16].

All the presented perspectives constitute a non-exhaustive list of what is possible with this material and unambiguously demonstrate the promising future of HgTe topological insulators.

Appendix A

Material characterization techniques

In order to completely characterize the HgTe/CdTe structures, a set of characterization techniques has been used. Data as well as their analysis have been detailed in Chapter 2. However, as the methods and setup used are numerous and different, this Appendix provides information about the principle and the experimental setup of almost each of the characterization techniques used in this report. Note that for preventing too much going backward and forward inside this report, the main text fully describes medium energy ion scattering technique and provides also elements concerning the transmission electron microscopy techniques as these techniques are not as common and here employed in specific modes of operation.

Characterization techniques based on X-rays are introduced in the first part of this Appendix. The second part deals with techniques based on ion beams. Finally, the last part provides information on microscopy characterization techniques such as atomic force microscopy or even transmission electron microscopy.

A.1 X-rays

X-rays based characterization techniques have the advantage to non-destructively investigate the stacked layers and provide information concerning the crystalline quality, the strain, the thickness, the roughness of each layer as well as the alloy composition. In this section, High Resolution X-Rays Diffraction (HRXRD) and the particular mode of Reciprocal Space Mapping (RSM) are introduced. X-Rays Reflectivity (XRR) functioning at lower grazing angles is also considered. Specificities of each technique are highlighted.

A.1.1 High resolution X-rays diffraction

The X-ray source is composed of a copper anode on which accelerating electrons are sent. The deceleration of these electrons inside this anode as well as the de-excitation of the anode electrons are two mechanisms responsible for X-ray emission with two energy levels: Kα and Kβ. Figure A.1 presents the experimental setup of the HRXRD measurements performed on a X'pert Panalytical diffractometer. Once emitted by the source, the X-rays go through divergence slits, mirrors and soller slits allowing to focus and collimate the beam. The X-rays beam is then filtered by a four-crystals spectrometer acting as a monochromator. Note that the use of the monochromator enables the switching to the high resolution mode, only necessary for the study of very thick films for which the oscillation period is small. The resulting X-rays beam is only made of Kα_1 with a wavelength $\lambda_{K\alpha 1} = 1.5406$ Å which is then diffracted on the sample.

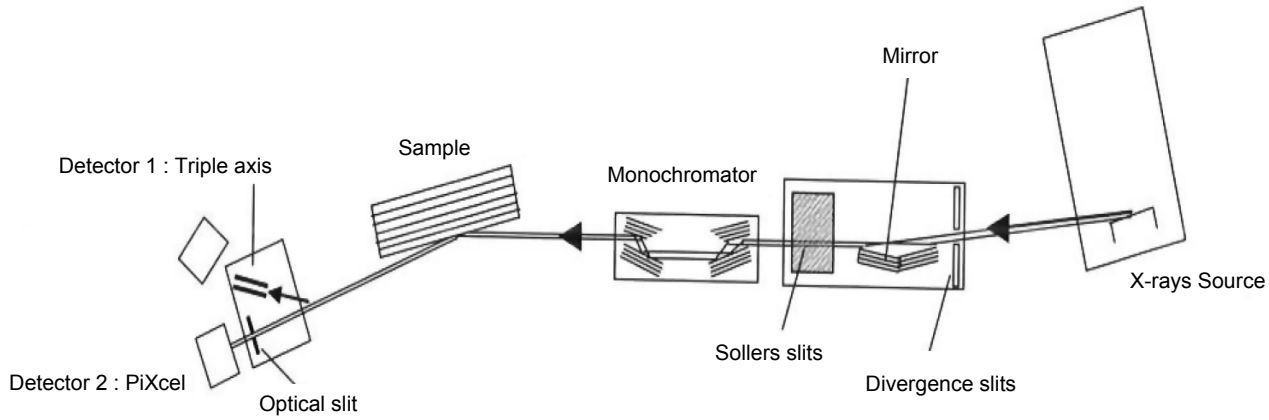

Figure A.1 – *Experimental setup based on the X'pert Panalytical diffractometer used for the HRXRD. Adapted from [Jon09].*

The diffraction condition is governed by the Bragg's law A.1 in which d_{hkl} represents the spacing between (hkl) lattice planes, hkl being the Miller indexes, θ is the Bragg angle for the (hkl) plane, λ is the X-ray wavelength, and n is the order of diffraction. The interreticular distance d_{hkl} is expressed as a function of the out-of-plane lattice parameter c using relation A.2, in the special case of face-centered cubic systems. Combining equations A.1 and A.2 leads to a direct relation between the angular position θ and the out-of-plane lattice parameter c.

$$2d_{hkl}sin\theta = n\lambda \tag{A.1}$$

$$d_{hkl} = \frac{c}{\sqrt{h^2+k^2+l^2}} \tag{A.2}$$

The diffracted X-rays are detected using a triple-axis detector in which analyser crystals lead to a cancellation of the diffracted beam divergence. In this configuration, the angular resolution is about 0.003°.

The whole experimental setup has just been introduced. However, to perform HRXRD, it is necessary to choose the good crystalline axis, thus it is useful to have a look at the extinction conditions in the case of face-centered cubic systems. Note that the diffracted intensity is directly proportional to the structure factor F_{hkl}:

$$I \sim |F_{hkl}|^2 \tag{A.3}$$

which depends on the crystal symmetry:

$$F_{hkl} = \sum_{i \in cell} f_i \exp(2i\pi(hx_i + ky_i + lz_i)) \tag{A.4}$$

where f_i is the form factor of the atom i. The unit cell of the HgTe crystal is composed of Hg atoms at (0, 0, 0) and Te atoms at $(\frac{1}{4}, \frac{1}{4}, \frac{1}{4})$ and this cell is reproduced in all the following positions : (x, y, z), (x + $\frac{1}{2}$, y+$\frac{1}{2}$, z) ; (x

+ $\frac{1}{2}$, y , z +$\frac{1}{2}$) and (x , y+$\frac{1}{2}$, z + $\frac{1}{2}$). With these symmetry conditions, the form factor is now expressed through:

$$F_{hkl} = (1+\exp(i\pi(h+k))+\exp(i\pi(h+l))+\exp(i\pi(k+l)))(f_{Hg}+f_{Te}\exp\left(2i\pi(\frac{h}{4}+\frac{k}{4}+\frac{l}{4})\right)) \tag{A.5}$$

and one can directly deduce the extinction conditions from the h, k, l values. Table A.1 reports the resulting intensity values depending on the h,k and l parity. Maximum intensity values are expected for h,k,l being all even integers whereas diffracted intensity cancels out if the parity is not conserved. Our structures having either (100) or (211) crystalline orientation, the HRXRD measurements in symmetric configuration will therefore be carried out using either $(h,k,l) = (2n,0,0)$ or $(4n,2n,2n)$, with n an integer.

hkl	h,k,l odd	h,k,l even	h,k,l not the same parity
F_{hkl}	$4(f_{Hg}-f_{Te})$	$4(f_{Hg}+f_{Te})$	0

Table A.1 – *Extinction condition for face-centered cubic crystals.*

A.1.2 Reciprocal space mapping

Using HRXRD, Reciprocal Space Mapping (RSM) [LBG+97] consists in recording a series of 2θ - ω spectra for different values of ω, thus mapping the reciprocal space around a given diffraction spot. When the RSM is performed in a non-symmetrical crystallographic direction, it contains in-plane and out-of-plane information leading to an estimation of the strain state of the layer with respect to the substrate. In the case of a fully strained layer (see Fig. A.2 (a)), the RSM evidences two majors peaks corresponding to the substrate and the film. These peaks are perfectly vertically aligned due to the fact that the in-plane lattice parameter of the substrate a_s and that of the film a_{fs} are the same in this case. However, when the film begins to relax (see Fig. A.2(b)), its lattice parameter comes back to its strain-free value a_f. This is directly evidenced in the RSM spectra by a shift of the film peak from the vertical alignment toward the relaxation line (see red lines in Fig. A.2(b)).

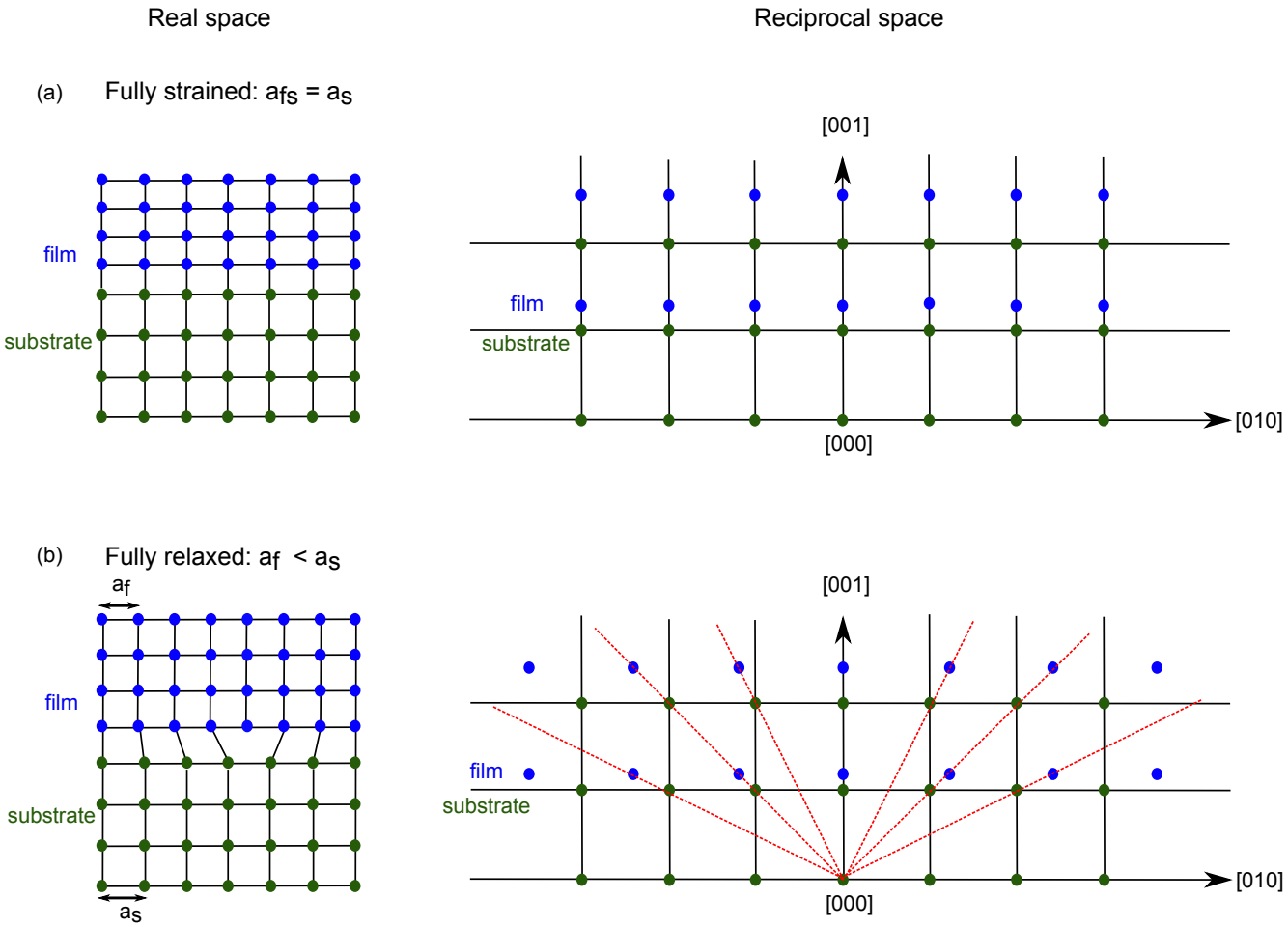

Figure A.2 – *Schematic representation illustrating the principle of reciprocal space mapping. (a) The film is fully strained: the substrate (in green) and the film (in blue) peaks are vertically aligned.(b) The film is completely relaxed: the film peaks are no more vertically aligned with those of the substrate. Red dashed lines represent the unstrained material lines.*

A.1.3 X-rays reflectivity

Implementation of XRR is very close to that of XRD but with low grazing angles. This technique aims to probe the thicknesses, roughnesses and densities of each layer of the stack and is governed by the Snell-Descartes law at low angles:

$$\theta_i = n\theta_t \tag{A.6}$$

where θ_i is the incident angle, θ_t is the transmitted angle and n is the refractive index of the material (by definition the refractive index of air is assumed to be 1). n is expressed as:

$$n = 1 - \delta + i\beta \tag{A.7}$$

where δ and β are the dispersion and the absorption corrections, respectively. δ and β are dependent on the material density as well as on its atomic structure as emphasized by equations A.8 and A.9:

$$\delta = \frac{\lambda^2}{2\pi} r_0 \rho (f^0(0) + f'(\lambda)) \tag{A.8}$$

with r_0 the classical radius of an electron, ρ the material density (g/cm^3), λ the X-ray wavelength, $f^0(0)$ the form factor and $f'(\lambda)$ the real part of the dispersion correction of the atomic form factor.

$$\beta = \frac{\lambda^2}{2\pi} r_0 \rho f''(\lambda) \tag{A.9}$$

with $f''(\lambda)$ the imaginary part of the dispersion correction.

The order of magnitude of δ is about 10^{-5}, and β is even smaller. Therefore, n is slightly lower than unity, thus implying the existence of a critical angle acting as a threshold for total reflection. Figure A.3 illustrates the two behaviors as a function of this critical angle θ_c. For $\theta_i < \theta_c$, the X-rays experiences a total reflection. For $\theta_i > \theta_c$, the X-rays enter the material and are reflected and transmitted at surface and interfaces resulting in constructive interferences related to material thickness. The extraction of such critical angle gives direct information about the material density as θ_c is related to δ with the relation:

$$\theta_c = \sqrt{2\delta} \tag{A.10}$$

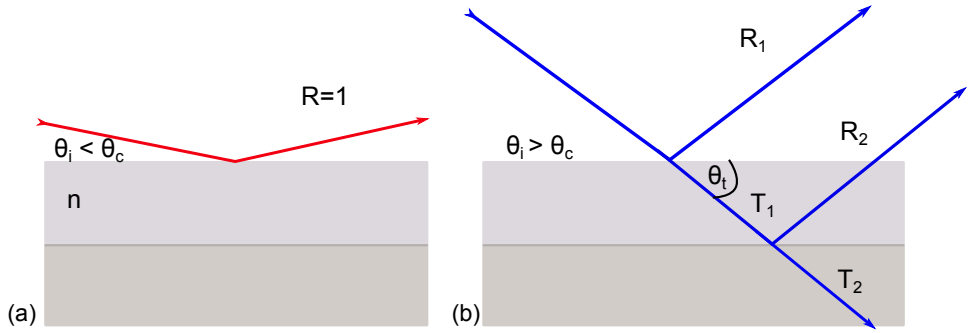

Figure A.3 – *Schematic representation of the XRR principle. (a) $\theta_i < \theta_c$: total reflection of the incident X-rays. (b) $\theta_i > \theta_c$: X-rays are both reflected and transmitted resulting in the measurement of constructive interferences due to material thickness.*

Figure A.4 summarizes all the information that can be extracted from a XRR spectra. The critical angle gives

access to the density as well as the oscillation amplitude which illustrates a density contrast. The thickness is extracted from the oscillation periodicity and the roughness has an impact on the oscillation intensity especially at high angles. Further details about the extracted parameters and their influence on the XRR spectra can be found in [Yas10].

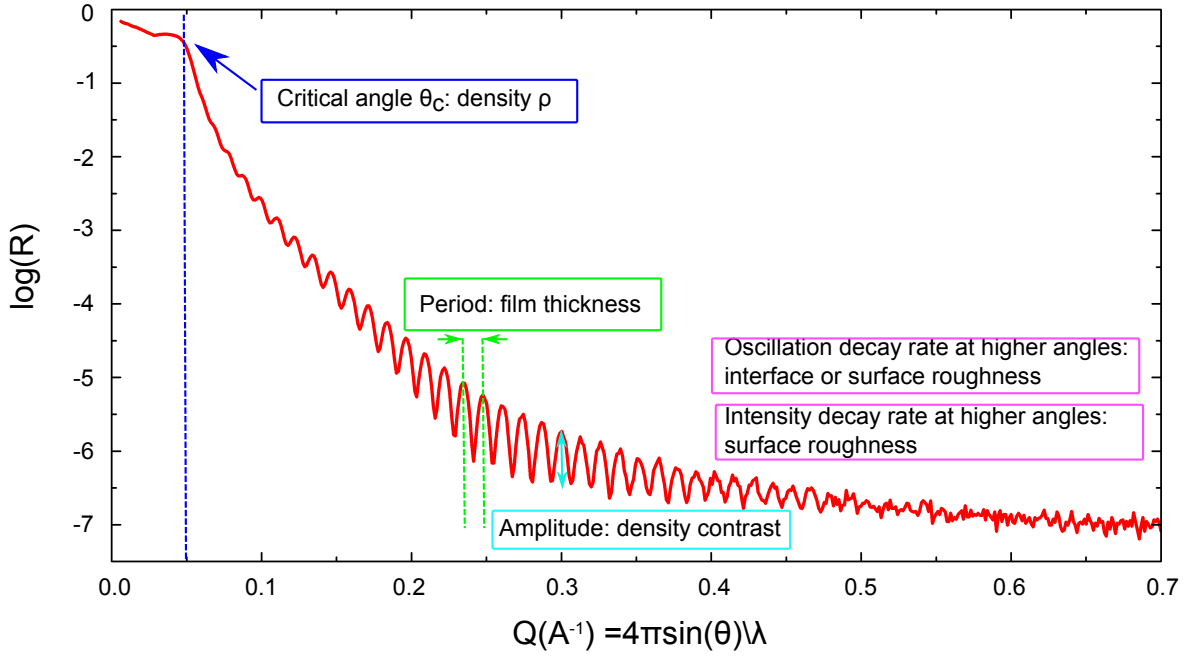

Figure A.4 – *Typical XRR spectra (here a 50 nm-thick HgTe layer grown on a (100) CdTe substrate). The critical angle gives access to the density of the HgTe layer. The oscillation period characterizes the layer thickness. The amplitude reveals the density contrast between the layer and the substrate and finally the damping of the oscillations at higher angles evidences the roughness of both the buried interface and top surface.*

A.2 Ion beams

Two characterization techniques have been used based on ion beams. While Medium Energy Ion Scattering (MEIS) has been fully described in the main text, Time-Of-Flight Secondary Ion Mass Spectrometry (TOF-SIMS) has just been mentioned and not detailed due to a lack of resolution.

In this section, we explain briefly TOF-SIMS principle and we present some measurement aiming to determine the interface width of a HgTe/CdTe structure. Resolution issues are highlighted and justify the use of other characterization techniques such as XRR, MEIS and TEM for the characterization of the interfaces.

TOF-SIMS is a characterization technique used to analyse the chemical composition. An ion beam is projected on the sample resulting in the ejection of secondary ions which are collected in a mass spectrometer. The mass of these secondary ions is related to the atomic mass of the sample elements and therefore gives access to its composition. For further description of this technique, the reader might refer to [Zal94].

TOF-SIMS measurements have been performed on the Nanocharacterization Platform CEA Grenoble using Cs^+ ions at the energy of 500 eV. The aim was to to obtain a chemical profile of the HgTe/CdTe structures. This study focuses on a 83 nm-thick HgTe layer grown on (211)B CdTe substrate at 185°C. Fig. A.5 displays the chemical profiles with Hg and Cd concentrations obtained after normalization to the Te signal which is considered to be unity in the whole structure. Chemical profiles are compared with second Fick's law of

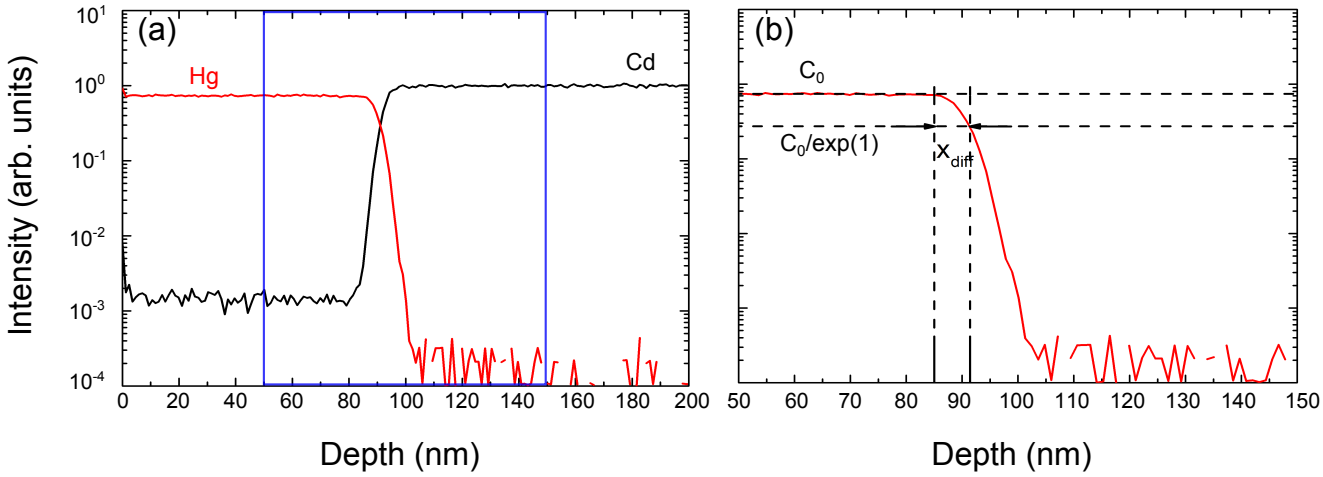

Figure A.5 – *Time of flight-secondary ion mass spectrometry measurement of a 83 nm-thick HgTe layer grown on (211)B CdTe substrate. (a) Hg (red) and Cd (black) concentration ratio evolution through the whole structure. (b): Zoom on the blue square of (a) for the determination of Hg diffusion length. Black dashed horizontal lines represent* C_0 *and* $C_0/\exp(1)$.

diffusion [Cra75] applied for thin films where the diffusion coefficient D and the surface concentration of Hg C_0 are assumed to be constant. The concentration C of Hg through the structure evolves as:

$$C(x,t) = C_0 \exp\left(\frac{-x^2}{4Dt}\right) \tag{A.11}$$

With respect to equation A.11, the interface width ($x_{diff} = 2\sqrt{Dt}$) can be estimated as the length after which C_0 is divided by $\exp(1)$. On Fig. A.5, a diffusion length of 6.1 nm is estimated. However, this result should be analyzed taking into account the TOF-SIMS depth resolution which is not known precisely for these materials but can be estimated in the range of at least 2 nm/decade for these experimental conditions. Therefore, the interface width can be considered between 2 and 4 nm for this structure.

With such a resolution, it is difficult to conclude on the quality of the interfaces. Therefore, other characterization techniques have been favored to determine the chemical composition near the interfaces.

A.3 Microscopy

Two different types of microscopy techniques have been used in this PhD. Atomic Force Microscopy (AFM) has been performed to characterize surface morphology and especially the roughness. Transmission Electron Microscopy (TEM) has been carried out to access the buried characteristics of the material such as its chemical composition, the presence of defects, the sharpness of its interfaces and so on. Details about these characterization techniques are the contents of this section.

A.3.1 Atomic Force Microscopy

AFM (VEECO D3100, Institut Néel Grenoble) is a characterization technique used for topographic studies of the surfaces. Tapping mode is used as represented in Fig. A.6. In this functioning mode, the cantilever is forced to vibrate with a certain amplitude at its resonance frequency. As soon as the cantilever contacts the sample surface, the resonance frequency changes and a feedback is done on the vibration amplitude of the cantilever. Scanning this difference of vibration amplitude directly gives access to the morphology of the sample surface

and especially determines its 2D height profile. Roughness (Root Mean Square RMS) values can be extracted with an accuracy of the order of one Angstrom. For our samples, AFM tapping mode has been used with Olympus AC160TS tips having a resonant frequency of 300 Hz.

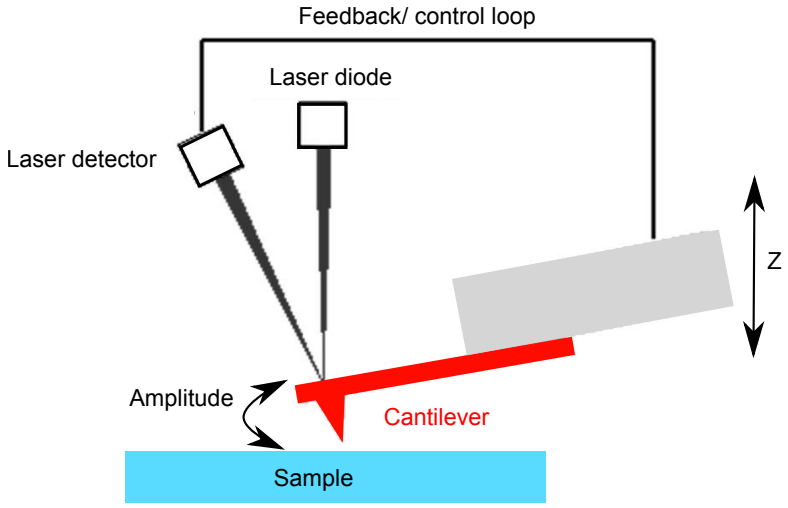

Figure A.6 – *Atomic force microscopy in tapping mode.*

A.3.2 Transmission electron microscopy

TEM has been widely used for our HgTe structures to characterize the chemical composition, the bulk defect density, the strain profile of a whole stack as well as the width of the interfaces. Each of these characterizations has been performed using a particular TEM mode. Scanning TEM (STEM) and Energy Dispersive X-rays spectroscopy (EDX), high resolution STEM as well as Nanobeam Precession Electron Diffraction (NPED) are all the TEM techniques that have been used in this PhD. The aim of this section is to give some keys for understanding the specificities of each of these modes and techniques. One can note that all the TEM characterizations have been performed on the Nanocharacterization Platform of CEA Grenoble in a collaboration with P.H. Jouneau, B. Haas and J.P. Rouvière.

A sketch of a TEM column is presented in Fig. A.7(a). Note that the electron beam is generated from an emission source located at the top of the microscope column. The association of lens and apertures allows for the electron beam convergence on the sample. The convergence angle of the beam is a variable parameter defining especially the resolution of the measurement. With sample thinner than 100 nm, the electrons are mostly transmitted. Depending on their scattering angles, these electrons will provide either chemical or structural information. Several detectors are available in the microscope column to collect all of these electrons as represented in Fig. A.7(a). Each detector and their associated specificities are discussed thereafter.

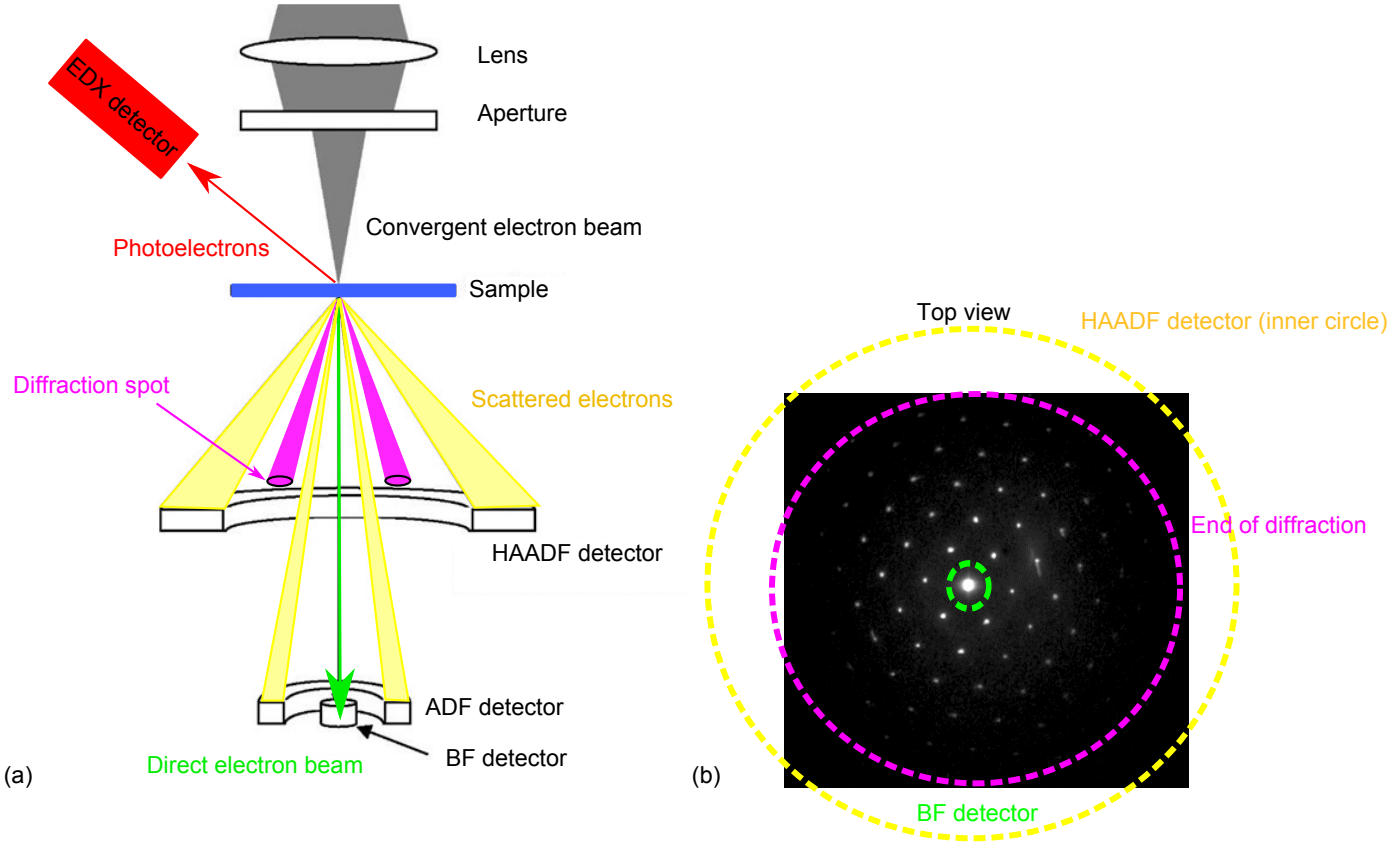

Figure A.7 – *(a) Transmission Electron Microscope (TEM) column with the convergent electron beam focusing on the sample. Bright Field (BF) detector measures the directly transmitted electron beam. High Angle Annular Dark Field (HAADF) detector collects the scattered electrons. Diffraction patterns can also be obtained in the focal plane using the small scattered electrons. The Energy Dispersive X-rays spectrometer (EDX) collects the photoelectrons. (b) A typical TEM diffraction pattern. The brightest spot in the center corresponds to the direct beam. The others evidence crystallographic axis.*

A.3.2.1 TEM: diffraction mode

With an electron beam accelerated at an energy of hundreds of kV, TEM enables electron diffraction to be performed. With such energy, the diffraction is very sensitive to variations of the crystalline network that cannot be evidenced by HRXRD. Moreover, with this range of energy, only the small angle scattered electrons contribute to the diffraction and are focused on a focal plane where a diffraction pattern is formed. This diffraction pattern corresponds to a section of the reciprocal lattice and each spot characterizes a crystallographic plane. The positions of these spots are used to determine the crystallographic axis and their lattice spacing. A typical diffraction pattern is presented in Fig. A.7(b). The brightest spot in the center corresponds to the direct electron beam.

Note that this diffraction mode is especially used to orientate the sample along a particular crystallographic direction in order to perform structural study such as observation of defects or even strain analysis.

A.3.2.2 Scanning TEM

STEM is probably the most known and used TEM mode. By scanning a sample with a focused electron beam, STEM generates a transmitted signal which is directly correlated to the beam position, thus allowing to obtain an image of the sample with a high spatial resolution. Several detectors are available in the microscope column (see Fig. A.7(a)) and enable to collect complementary information. Among these detectors, three have been used in this PhD:

- High Angle Annular Dark Field (HAADF): this detector is made of a large diameter ring which collects the large angle scattering signal as represented in Fig. A.7. Therefore, it is mostly sensitive to the sample chemical composition. The STEM HAADF image intensity is indeed directly related to the atomic mass with a contrast scaling in $Z^{1.7}$ [Pen89]. Heavy atoms are thus appearing bright while light atoms are dark.
- Bright Field (BF): this detector is located in the continuity of the optical axis in the center of the microscope column to collect the direct transmitted electron beam. Therefore, this detector is highly sensitive to the quality of the crystalline network. Any defects within the sample will indeed prevent the perfect transmission of this beam and thus will be observable on the BF image with a darker intensity.
- EDX detector: EDX is a chemical analysis technique detecting the X-rays emitted from the sample during bombardment by an electron beam. As soon as the electron beam reaches the sample, the electrons from the sample's atoms are ejected. They are immediately replaced by electrons of higher energy level thus giving rise to the emission of X-ray photons. The chemical nature of the sample's atoms is then determined through the X-ray energy of the photoelectrons.

Note that STEM measurements have been performed on a Osiris microscope at a beam voltage of 80 kV. High resolution STEM measurements have for their part been carried out on a FEI Titan Ultimate microscope at 200 kV and with a beam resolution of about 1 Å.

A.3.2.3 Nanobeam precession electron diffraction

The NPED technique is used with TEM in diffraction mode. The precession of the electron beam is obtained by scanning it with a constant angle around the optical axis as illustrated in Fig. A.8(a). With this precession motion, the electron beam illuminates part of the crystal that is larger than the unit cell. The resulting diffraction patterns are forming disks which are then compensated and turned into spots by alignment tuning (descan coils). The reader is invited to refer to [RBM+13] to see TEM images of this transition from diffraction disks to diffraction spots. This technique allows to obtain an homogeneous contrast in the spots but also to observe more numerous diffraction spots. These improvements are directly observable by comparing the diffraction patterns of Fig. A.8(b) and (c), corresponding to a case without and with precession, respectively. With these characteristics, NPED technique enables an improvement of the diffraction spot resolution, meaning a more accurate determination of the lattice parameters and so of the strain values.

However, one may have noticed that the diffraction spots are wide in comparison with standard TEM diffraction (see Fig. A.7(b)), meaning that the beam and so the spatial resolution is poorer. This lack of spatial resolution is a direct consequence of the precession motion. In these conditions, our experiments have been performed using a FEI Titan Ultimate microscope at 200 kV and with a beam resolution of about 2 nm.

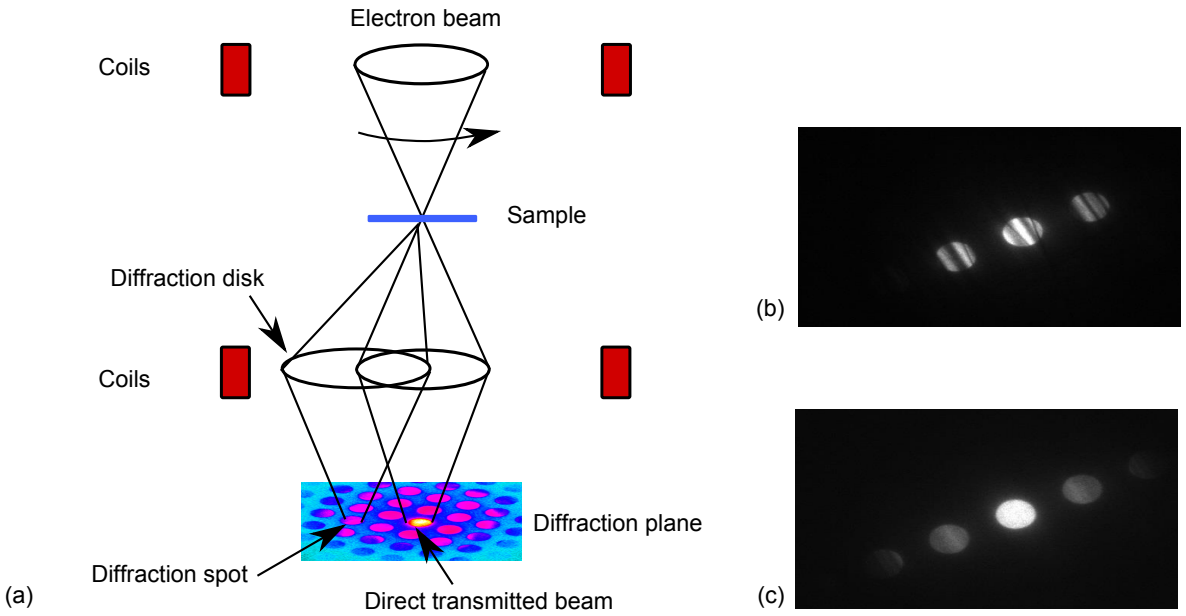

Figure A.8 – *(a) Schematic representation illustrating the beam precession used for nanobeam precession electron diffraction TEM technique. Typical diffraction spots obtained (b) without and (c) with precession in the case of a tilted sample.*

Appendix B

Two-dimensional nature of the Shubnikov-de Haas oscillations

In order to demonstrate the two-dimensional (2D) nature of the Shubnikov-de Haas Oscillations (SdHO), tilted magnetic field has been used.

For topological insulator systems, SdHO angular dependence particularly enables to highlight 2D transport arising on the surface states [RTS+10]. This technique is especially achieved for Bi-based topological insulators, for which the bulk part is non negligible, leading to the separation between the surface and the bulk contributions [TA10].

To perform SdHO angular dependence analysis, the magnetic field has been applied with an angle ϕ ranging from 0 to 90°. Definition of ϕ is found in the inset of Fig. B.1(b) with the magnetic field applied perpendicular to the sample surface for $\phi = 0\,°$. For supplementary description of magnetic field control, the reader can refer to Chapter 3 (see 3.3.4).

Figure B.1(a) displays the longitudinal resistance R_{xx} as a function of the gate voltage V_{gate} and the magnetic field B for a 13 nm-thick HgTe sample. Three mappings are reported corresponding to three different angles: ϕ=0°, 45°and 90°. SdHO are clearly visible for the first two angles. They are shifted toward higher B values for $\phi = 45°$to reproduce the former values of $B_\perp$ and finally completely disappear for in-plane magnetic field ($\phi = 90°$), thus witnessing the 2D origin of the quantum oscillations. Indeed, in the case of 3D transport, the oscillations would have persisted for the latter magnetic field orientation as reported by Eto *et al.* in [ERT+10]. Moreover, Fig. B.1(b) emphasizes that the oscillations are only $B_\perp$ dependent as their positions are identical regardless the angle value.

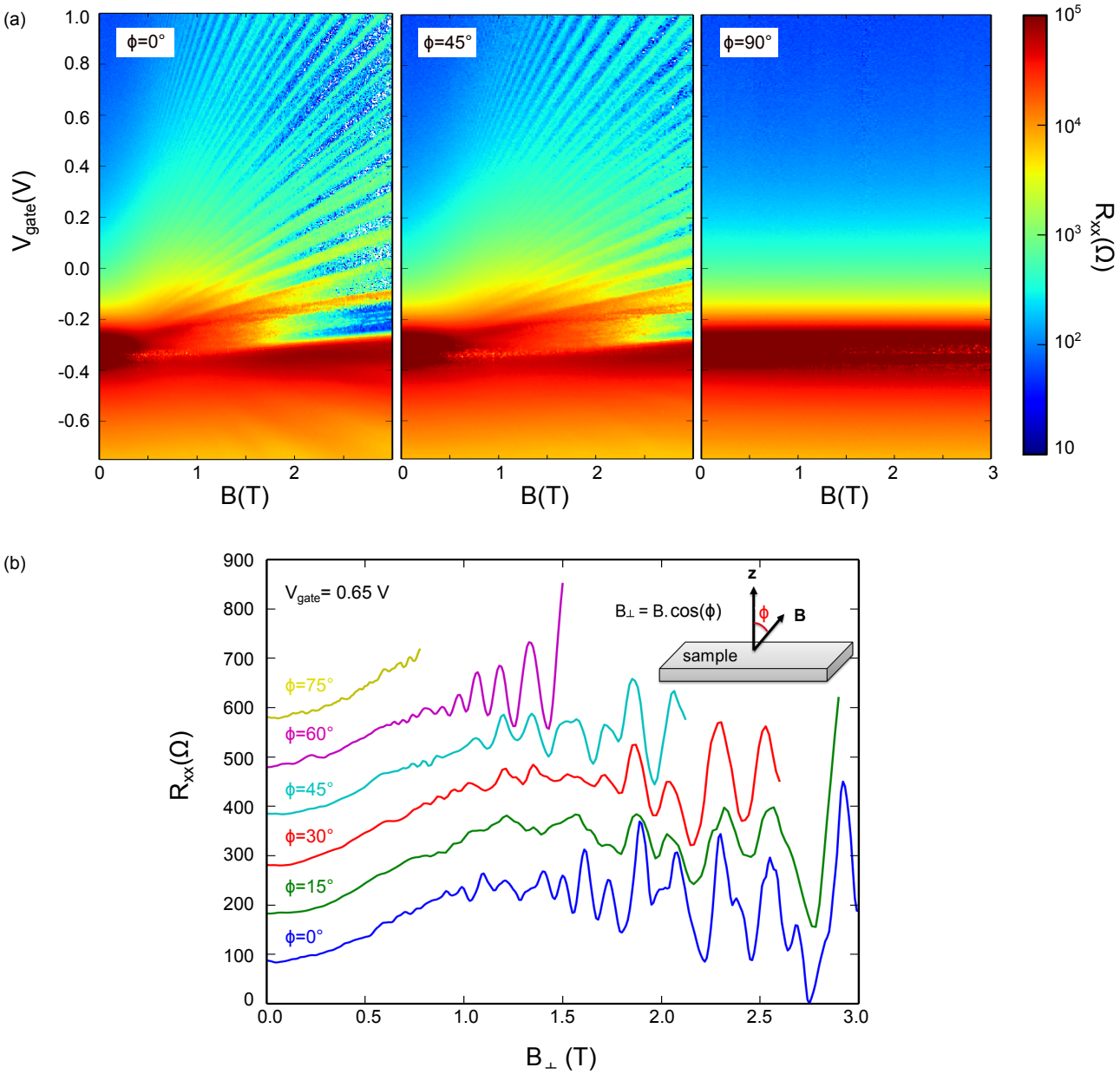

Figure B.1 – *Angle-dependence magneto-transport experiment performed on a 13 nm-thick HgTe layer. (a) Longitudinal resistance R_{xx} as a function of the magnetic field B and the gate voltage V_{gate} for $\phi = 0$, 45 and 90°. Quantum oscillations are no more visible at 90°highlighting the 2D character of these Shubnikov-de Haas Oscillations (SdHO). (b) R_{xx} as a function of $B_\perp$ for different angles ranging from 0 to 75°. All curves have been shifted vertically for clarity. The position of the oscillations remains the same for each angle meaning that only the perpendicular component of the magnetic field impacts the SdHO. Data have been extracted with $I_{bias} = 1$ nA at $T = 75$ mK.*

Appendix C

Magneto-transport measurements for 50 and 25 nm-thick HgTe layers

In order to complement the magneto-transport study reported in Chapter 4 on 100 and 15 nm-thick HgTe layers, we present here the results obtained at intermediate thicknesses of 50 and 25 nm. The objective is to follow the evolution of the different transport contributions, such as the bulk, the side surfaces but also the interplay between the surface states when reducing HgTe thickness. Note that the Hall bars studied in this Appendix are all characterized by a length $L = 40$ μm and a width $W = 10$ μm.

C.1 50 nm-thick HgTe layer

A 50 nm-thick HgTe layer is first considered and is analysed similarly as the 100 nm-thick sample (see Chapter 4 4.1.1). The difference and the evolution of the electronic properties caused by the thickness reduction will be highlighted. Note that the thickness of the layer has been determined at 58 nm from HRXRD measurements.

C.1.1 Low magnetic field measurements

Low magnetic field B variations of the Hall R_{xy} and longitudinal R_{xx} resistances are used to successively determine the Hall constant R_H, the carrier density n_H and the carrier mobility μ. Note that here we consider only magnetic field values lower than 1 T. All these quantities and their gate voltage variations are presented in Fig. C.1.

A lot of similarities with the 100 nm-thick sample are noticeable such as the ambipolar behavior, the gate offset doping Δ_1, the density and the mobility orders of magnitude. Furthermore, a gate depletion factor α_H of about 7.0 10^{11} cm^{-2}.V^{-1} has been determined from the density linear variation with gate voltage and is similar to that extracted for the 100 nm-thick sample (6.6 10^{11} cm^{-2}.V^{-1}). This similarity is expected as the top gates are realized using the same recipe for each sample. The slight difference can be easily explained by small variation in the HgCdTe barrier thickness from one growth run to the other.

However, the thickness reduction from 100 to 50 nm is accompanied by a change of some of the transport signatures:

- the Δ_2 voltage shift, visible on the $\frac{1}{R_H}$ variations (see Fig. C.1(c)), is no more negative but positive, thus

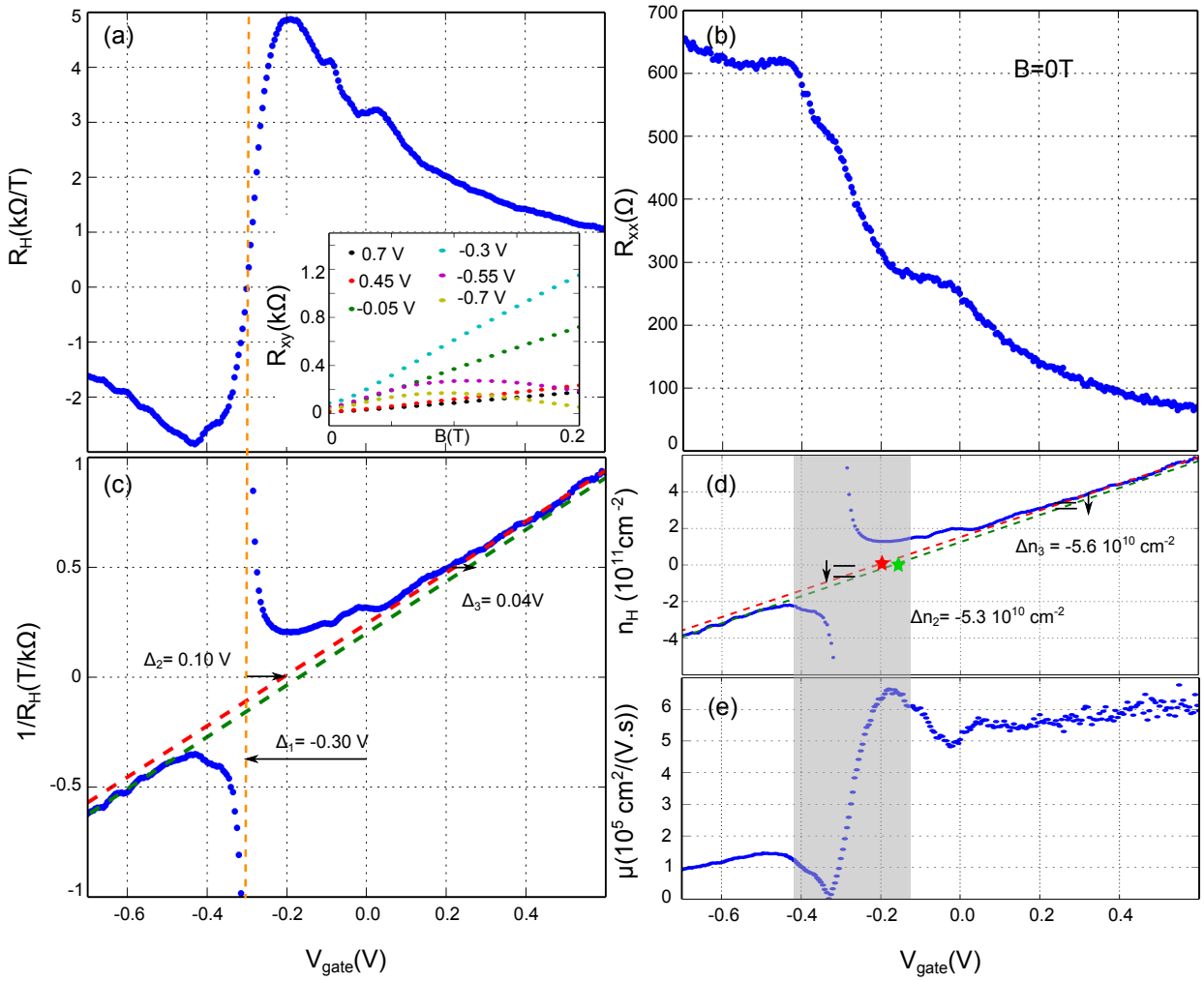

Figure C.1 – *Low magnetic field analysis of a 50 nm-thick HgTe layer. All the presented quantities are represented as a function of the gate voltage V_{gate} and have been extracted for magnetic field $B \leq 1$ T at a temperature $T = 55$ mK with a current bias $I_{bias} = 1$ nA. (a) Hall constant R_H (inset: Hall resistance R_{xy} variation with magnetic field B for several gate voltage V_{gate} values). (b) Longitudinal resistance R_{xx} for B=0 T. (c) $\frac{1}{R_H}$. (d) Carrier density n_H. (e) Carrier mobility μ. Grey color band corresponds to the gate voltage range for which the single carrier model is not valid.*

suggesting this time the addition of electrons to the transport with the density $\Delta n_2 = -5.3\ 10^{11}$ cm^{-2} (see Fig. C.1(d)). This change of sign is also accompanied by a shift of the Dirac point (defined as the gate voltage position for which $n_H = 0$ and highlighted by a red star in Fig. C.1(d)) in the electron-side. Note that electron- and hole-sides are delimited by the Charge Neutrality Point (CNP), defined as the gate voltage position for which $R_H = 0$, which is highlighted by an orange dashed line in Fig. C.1(c).

- Δ_3 is considerably reduced to $-5.6\ 10^{10}$ cm^{-2}, meaning at least three times less important than for the 100 nm-thick sample ($-1.8\ 10^{11}$ cm^{-2}). This behavior agrees with a decrease of the bulk contribution with the rise of the surface to bulk ratio. With this reduction of Δ_3, the two Dirac points, corresponding to electron- and hole-sides (see red and green stars in Fig. C.1(d)), are now very close.

- the longitudinal resistance $R_{xx}(B = 0T)$ is represented in Fig. C.1(b). One can directly notice the presence of two resistance shoulders, one for $V_{gate} \approx -0.1$ V and the second one for $V_{gate} \approx -0.4$ V. This point differs from what has been previously reported for the 100 nm-thick sample, where only one resistance shoulder was noticeable and attributed to a change of major carriers. These features suggest

the superposition of contributions originated from two different Dirac cones at both top and bottom surfaces. Screening effects are indeed expected to be less important at this thickness. High magnetic field measurements will provide more insights to confirm this assumption.

C.1.2 High magnetic field measurements

By increasing the magnetic field, R_{xx} quantum oscillations, also referred as Shubnikov-de Haas Oscillations (SdHO), appear and are observable in Fig. C.2(a) through the white branches corresponding to oscillation maxima. Figure C.2(c) proposes a closer view on these oscillations in the electron-side.

Fast Fourier Transform (FFT) analysis has been achieved on the R_{xx} mapping for B between 0.3 and 3 T and is reported in Fig. C.3. This analysis has been performed on a limited range of gate voltage due to the complexity of R_{xx} patterns which does not allow to extract clear frequency peaks on the whole mapping. Two major contributions are determined as it can be seen in Fig. C.3(a) and are highlighted by green and black arrows. One can notice that these peaks are not so well-defined, compared to the 100 nm-thick sample, thus resulting in imprecision in the frequency extraction. The associated carrier density n_1 and n_2 are plotted in Fig. C.3(b) and directly compared to the low magnetic field extracted density n_H. Two major differences with the 100 nm-thick sample are immediately observable. First, n_2 is no more a constant but is varying with V_{gate}. Second, n_1 is sharing the same linear behavior than n_H.

From these observations, we can conclude that n_1 is the major contribution and corresponds to the top surface states, while n_2 is attributed to the bottom surface. Indeed, with the thickness reduction, the screening effects of bulk are expected to be less important and to allow the carriers from the bottom surface to be depleted. Finally, the match between n_1 and n_H confirms the absence of side surface contribution for this thickness, in comparison with the features reported for the 100 nm-thick sample (see Chapter 4 4.4).

Additional FFT analysis has also been performed on the hole-side and evidences a density shift between n_H and n_1, contrary to what has been reported in the electron-side. The origin of this density shift is not clear to date. One must recall that similar density shift has been noticed for the 15 nm-thick HgTe layer in Chapter 4 (see Fig. 4.9). However, in this case, the two surfaces were hybridized and the LL broadening prevented from the observation of the even filling factors originated from a splitting mechanism, thus the observed density was two times less important than expected. With a thickness of 50 nm, hybridization is not expected. However, the study of the 100 nm-thick sample evidences an other coupling mechanism which is not hybridization and which still needs to be identified. From this discussion, we can conclude that the explanation of this density shift might be this unknown coupling mechanism. Further studies and investigations are obviously needed to conclude on this point.

To go one step further and understand the quantum Hall data, let us first consider the study of the R_{xx} oscillations. Similarly to the 100 nm-thick sample, R_{xx} mapping exhibits very complex patterns.

The gate depletion factor of the major contribution $\alpha_1 = \alpha_H$ ($7.0\ 10^{11}$ cm^{-2}.V^{-1}) enables the expected position of the Landau Levels (LLs) to be determined. These LLs are represented through the yellow dashed lines in Fig. C.2(d). The position of the Dirac points has been fixed relying on the low magnetic field measurements (see Fig. C.1(d)). Similarly to the 100 nm-thick sample, these lines are not correctly fitting the fan diagram but their slopes are consistent with the SdHO evolution maxima with B and V_{gate}, but principally for $B \geq 2$ T. A change of slope is clearly noticed for $B \approx 2$ T, thus strongly confirming the existence of another contribution. The reader might remember the previous discussion on $R_{xx}(B = 0T)$ which was evidencing the potential existence of a second Dirac point at $V_{gate} \approx -0.42$ V. Based on this observation and on the slope of R_{xx} and

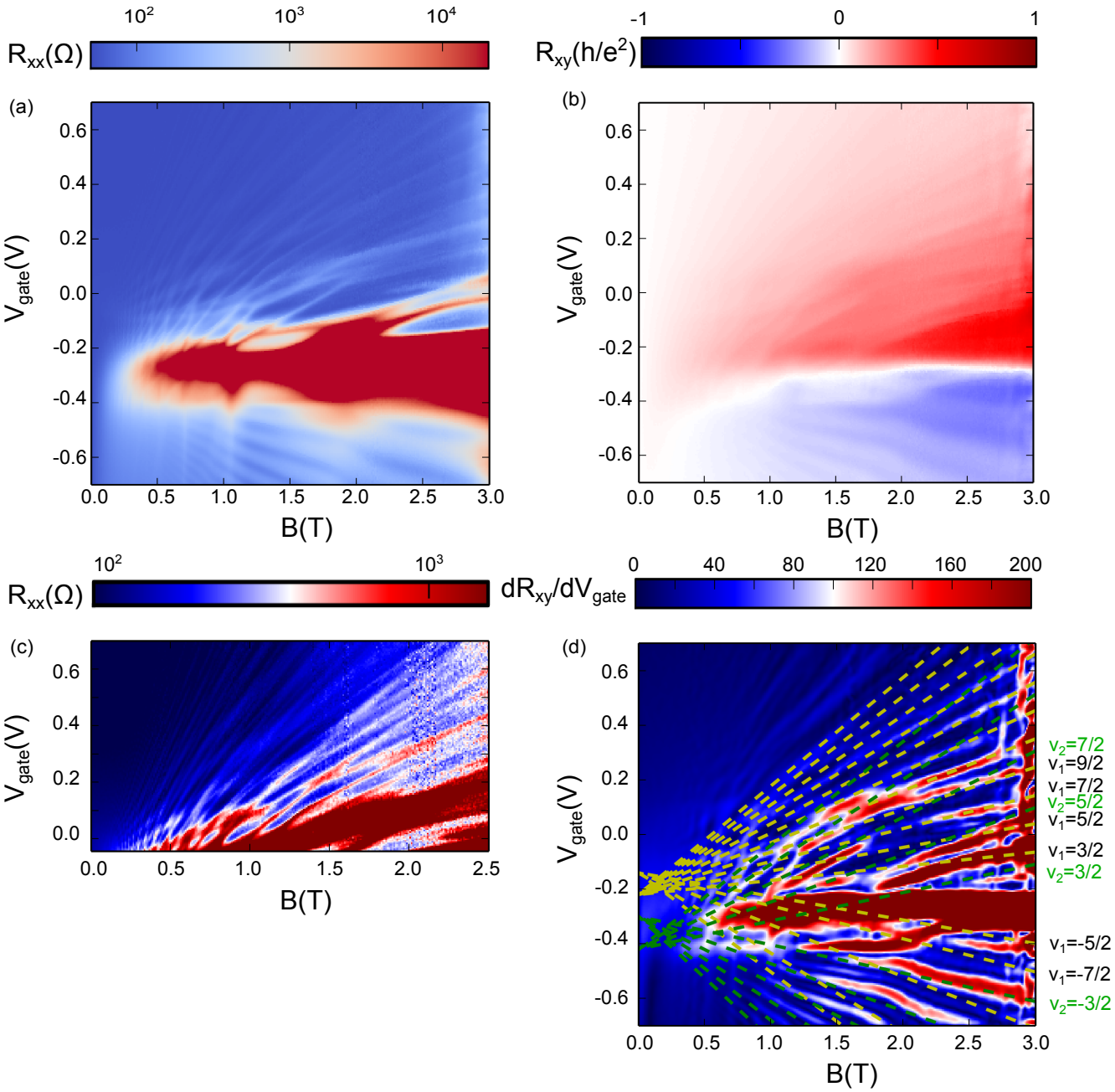

Figure C.2 – *Magneto-transport measurements of a 50 nm-thick HgTe layer. (a) Longitudinal resistance R_{xx} (in logarithmic scale) as a function of V_{gate} and B. The complexity of the mapping is clearly visible. (b) Hall resistance R_{xy} (in units of $\frac{h}{e^2}$) as a function of V_{gate} and B. (c) Optimization of the scale for a better observation of R_{xx} features in the electron-side. (d) First derivative of R_{xy} with the two identified major sets of LLs represented by yellow and green dashed lines. Data have been extracted with $I_{bias} = 1$ nA and $T = 55$ mK.*

$\frac{dR_{xy}}{dV_{gate}}$ maxima branches for $B \leq 2$ T, we manage to determine another set of LLs represented by green dashed lines in Fig. C.2(d). With a gate depletion factor of about 3.5 10^{11} cm^{-2}.V^{-1}, this second set of LLs appears to match with $\frac{dR_{xy}}{dV_{gate}}$ and so R_{xx} minima positions for $B \leq 2$ T especially in the hole-side.

Note that these two sets of LLs only consider half-integer values of filling factors, which is consistent with top and bottom surface single Dirac cones. While the addition of these two sets of LLs is somehow a confirmation of the participation of top and bottom surface states to the transport, it is not sufficient to conclude on the quantization and on the transport mechanism occurring at this thickness. Complementary measurements of the Hall resistance are needed.

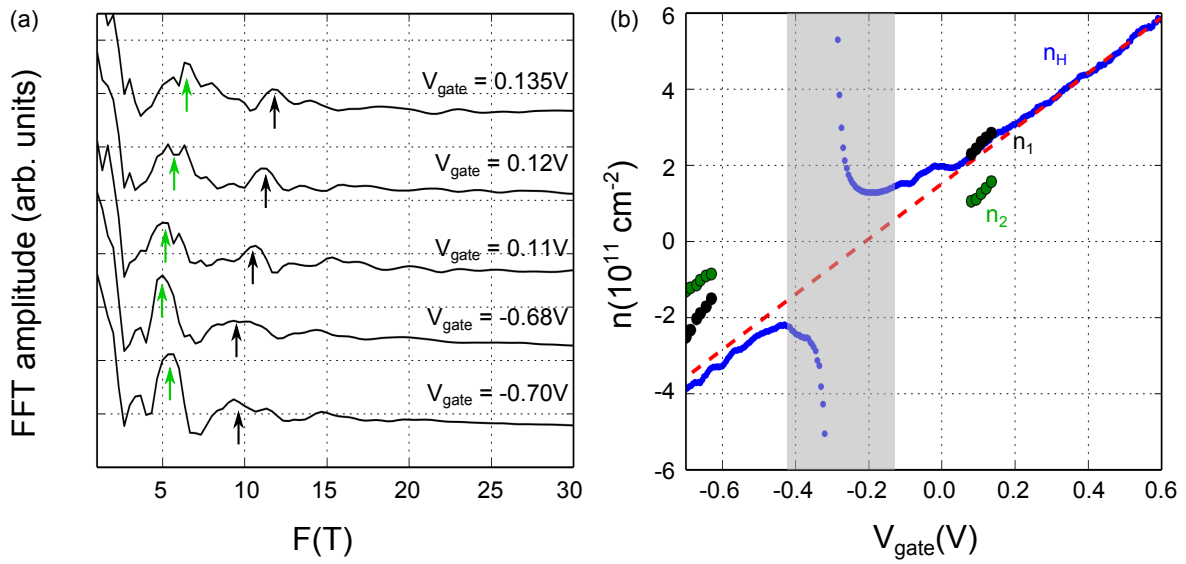

Figure C.3 – *FFT analysis of R_{xx} Shubnikov-de Haas Oscillations (SdHO) for a 50 nm-thick HgTe layer. (a) FFT amplitude as a function of the frequency F for several values of V_{gate}. Two major frequencies and so contributions are emphasized by green and black arrows. (b) FFT extracted densities n_1 (black) and n_2 (green) are compared to the one obtained from Hall resistance variation at low magnetic field n_H (blue). Red dashed line is the linear fit of n_H in the electron-side and the grey color band corresponds to the gate voltage range for which the single carrier model is not valid.*

R_{xy} mapping is reported in Fig. C.2(b) as a function of B and V_{gate}. With a thickness of about 50 nm, the top and bottom surface states are expected not to hybridize as already discussed in Chapter 1 (see 1.1.4) relying on the surface state extension. Therefore, the quantization is expected to be similar to the 100 nm-thick HgTe layer.

Traces of σ_{xy} and σ_{xx} are plotted on Fig. C.4 (a) for B = 2.7 T to complement this analysis. σ_{xx} and σ_{xy} features are similar to the 100 nm-thick sample with Hall conductance plateaus directly associated to non-vanishing longitudinal conductance minima. In the hole-side, $\nu = -2$ is unambiguously evidenced. For the other plateaus it is less accurate and one can wonder if the quantization is going in: -3, -5 or in -4, -6. Moreover, in the electron-side, even if the quantization seems to be in integer values, with the non-accuracy in the plateau definition it is difficult to conclude. Additional σ_{xy} traces are plotted in Fig. C.4(b) for several values of B. The trace at 3 T evidences only even filling factors in the hole-side, thus suggesting that the previous quantization at 2.7 T was also with even integers. Such quantization is raising a lot of questions about the transport mechanisms at stake in such 50 nm-thick structure. The interplay between the two Dirac cone LLs which are varying simultaneously with V_{gate} and B makes this analysis even more complex preventing to clearly conclude about the topological nature of this system.

In conclusion, the cross-analysis of low and high magnetic field measurements enables to get an overview of the transport mechanisms of a 50 nm-thick HgTe layer and to conclude that:

- two major contributions have been demonstrated and both exhibit signatures consistent with Dirac cones. They have thus been attributed to the top and bottom surface states. The gate voltage variation reported for the second contribution illustrates the reduction of the screening effects for this thickness.
- contrary to the case of 100 nm-thick sample, FFT analysis does not show evidence of extra contribution,

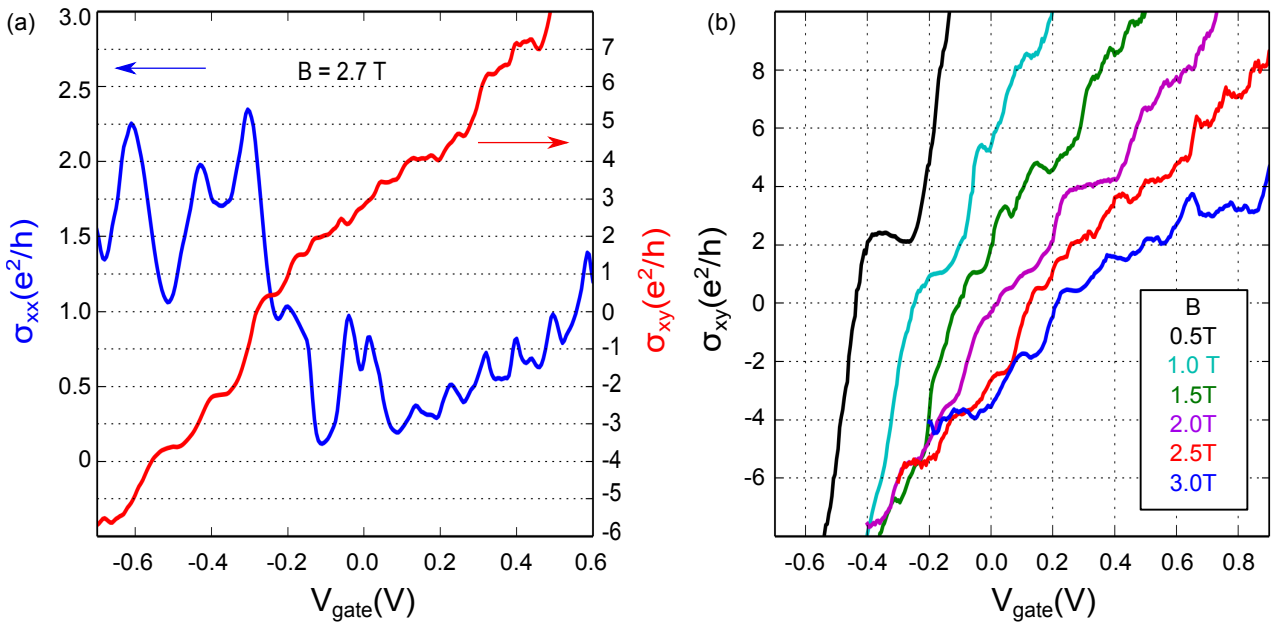

Figure C.4 – *(a) Longitudinal σ_{xx} and Hall σ_{xy} conductances for a 50 nm-thick HgTe layer at $B = 2.7$ T. (b) σ_{xy} traces for several values of B. The curves have been shifted horizontally for clarity. Data are extracted with $I_{bias} = 1$ nA and $T = 55$ mK.*

especially from side surfaces in the electron-side. Indeed, density of the top surface state is similar to the one extracted at low magnetic field. Therefore, features of longitudinal resistance in the electron-side such as non-vanishing minima are mostly due to the interplay between the two Dirac cones.

- the question of the interplay between these two Dirac cone LLs has also been evoked due to the quantization values which are not accurate and which tend to evidence an even integer quantization. This effect can be due to the same coupling mechanism already mentioned for the 100 nm-thick sample but this point needs confirmation.

With the absence of side surface contributions and the evidence of two Dirac cones, backgating this sample could be very interesting. Indeed, by playing on the two surface state densities, one can manage to align the top and bottom surface Dirac points. This should potentially allow to obtain clearer QHE signatures that can be very useful for a better understanding of the transport mechanisms at stake. In a second time, this should potentially permit to use such thick structures for applications. Up to now, some tests have been done by adding an In-doped HgCdTe barrier to the stack layer or even by doing the growth on Te-doped InSb doped substrates but without success. High leakage currents, due to In diffusion, are preventing from depleting the bottom surface carriers. Strong efforts are thus needed to obtain dual-gated structures and go further in the electrical characterization of such thick samples.

C.2 25 nm-thick HgTe layer

The thickness of the HgTe layer is decreased again and we are now considering a 25 nm-thick sample. A thickness of 26 nm has been estimated from HRXRD measurements.

C.2.1 Low magnetic field measurements

The low magnetic field extracted values of R_H, $R_{xx}(B=0T)$, $\frac{1}{R_H}$, n_H as well as μ are presented in Fig. C.5.

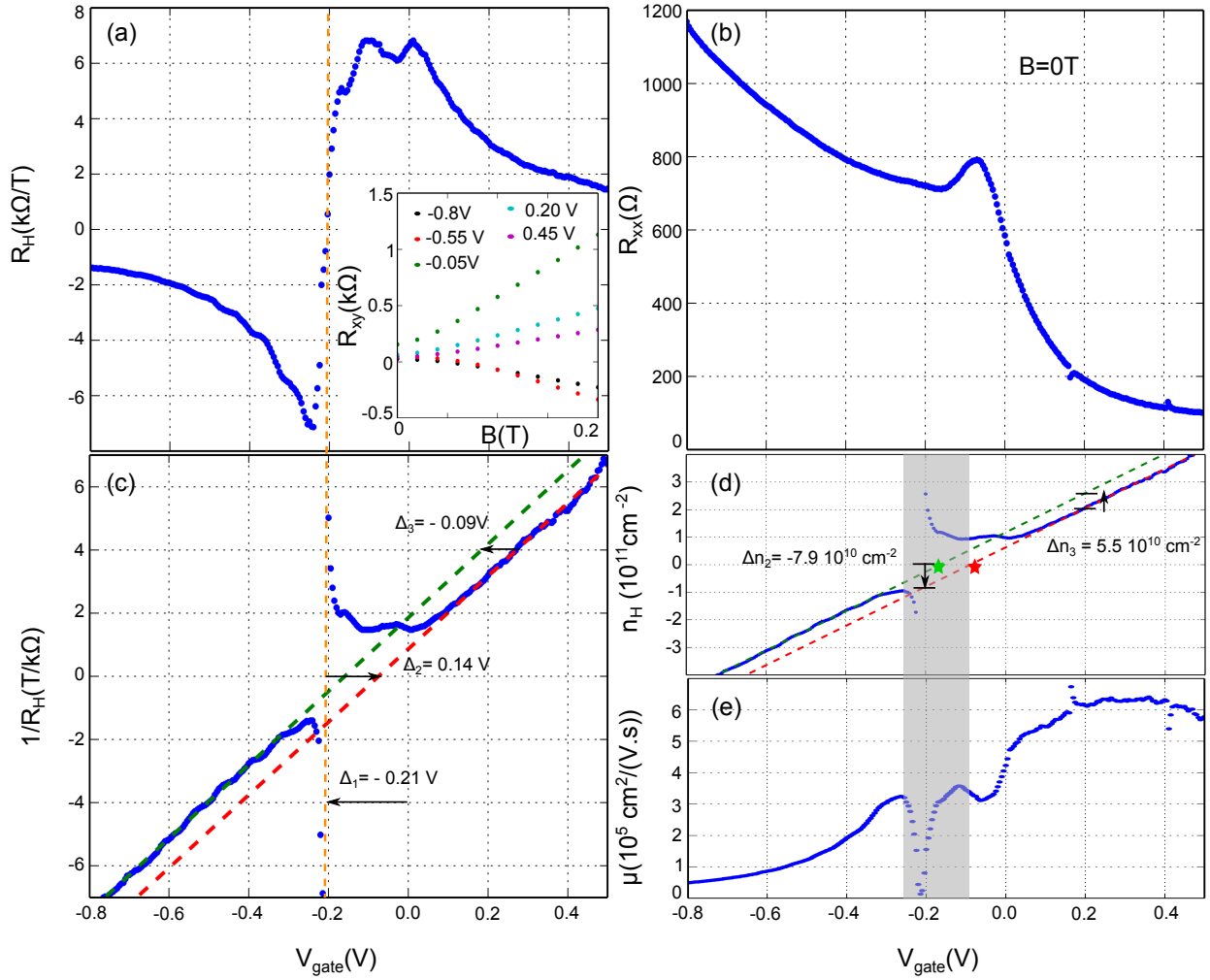

Figure C.5 – *Low magnetic field analysis of a 25 nm-thick HgTe layer. All the presented quantities are represented as a function of V_{gate} and have been extracted for $B \leq 1$ T, with $I_{bias} = 1$ nA at a temperature of about 70 mK. (a) R_H (inset: R_{xy} variation with B for several V_{gate} values). (b) R_{xx} for B=0 T. (c) $\frac{1}{R_H}$. (d) n_H. (e) μ. Grey color band corresponds to the gate voltage range for which the single carrier model is not valid.*

The gate voltage dependence of all these parameters is similar to the two thicker samples (100 and 50 nm) reported previously. In particular, the positive sign of Δ_2 and its associated density $\Delta n_2 = -7.9\ 10^{10}$ cm^{-2} are comparable to the 50 nm-thick sample ($-5.3\ 10^{10}$ cm^{-2}).

However, two features differ from the characteristics of the 50 nm-thick sample and are:

- Δ_3 voltage offset becomes negative as it can be seen in Fig. C.5(c). This voltage shift is characterized by a density $\Delta n_3 = 5.5\ 10^{10}$ cm^{-2} as represented in Fig. C.5(d), suggesting the addition of electrons to the transport. The picture of extra hole density from the Γ_{8HH} bulk band is thus no more sufficient to explain this voltage offset.

- $R_{xx}(B = 0T)$ is reported in Fig. C.5(b) as a function of V_{gate}. Contrary to what has been reported for the 50 nm-thick sample and similarly to the 100 nm-thick one, only one resistance peak is noticeable. In the electron-side, resistance values of about 100 Ω are reported. However, in the hole-side, the resistance value is not fixed but continues to significantly increase with gate voltage. Such behavior is similar to the resistance variation observed for the 50 nm-thick sample in between the two resistance shoulders characterizing Dirac points, thus suggesting the addition of another contribution.

By confronting the characteristics of $\frac{1}{R_H}$ and $R_{xx}(B = 0T)$ to the previous analysis on thicker samples, we can conclude on the presence of another contribution to the electronic transport. However, these signatures differ from what have been reported previously and thus do not correspond to side surfaces or to a simple impact of the bulk. Another type of contribution is investigated. High magnetic field measurements will be necessary to gain knowledge and conclude about the nature of this additional contribution.

C.2.2 High magnetic field measurements

Quantum oscillations of R_{xx} appear with the rise of B as it can be seen in Fig. C.6(a), corresponding to the R_{xx} mapping as a function of B up to 3 T and V_{gate} at 70 mK.

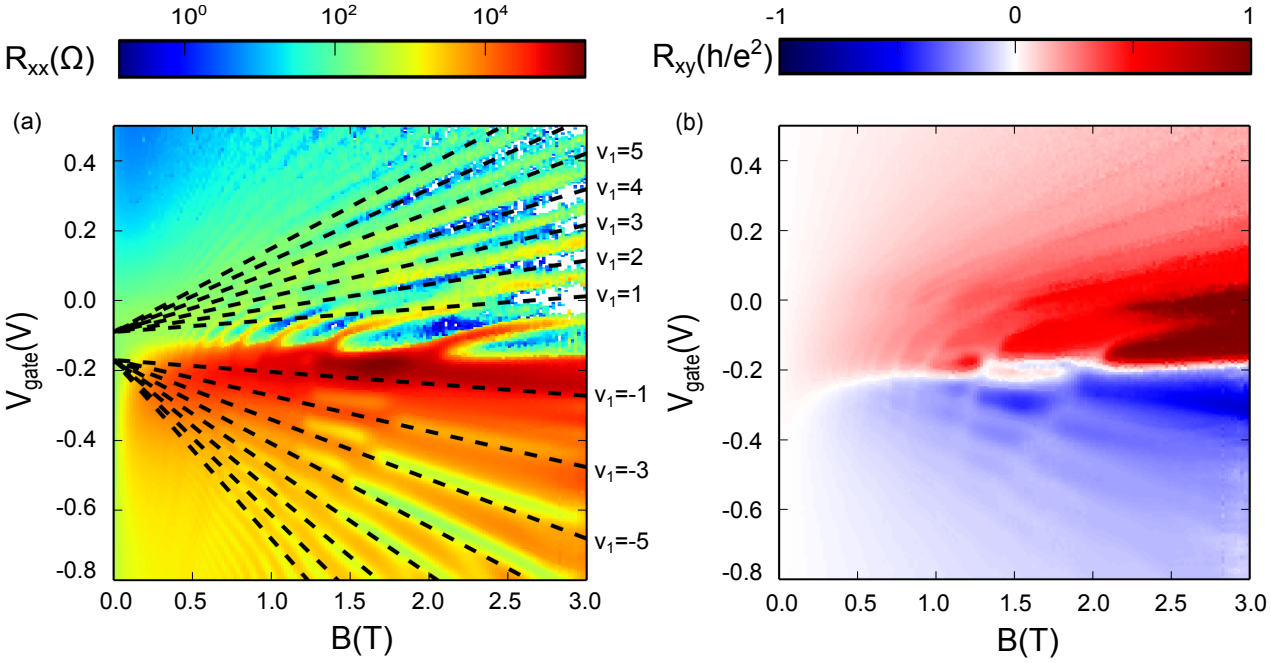

Figure C.6 – *Magneto-transport measurements of a 25 nm-thick HgTe layer with $L = 40$ µm and $W = 10$ µm. (a) Longitudinal resistance R_{xx} (in logarithmic scale) as a function of V_{gate} and B. The black dashed lines represent a set of LLs. (b) Hall resistance R_{xy} (in units of $\frac{h}{e^2}$) as a function of V_{gate} and B. Data are extracted with $I_{bias} = 1$ nA and $T = 70$ mK.*

The FFT analysis performed on the R_{xx} mapping is reported in Fig. C.7. Based on the analysis of the thicker samples and on the low magnetic field evidences of an additional contribution, one expect to extract three contributions corresponding to the top surface states, the bottom surface states and this still unknown additional contribution. However, as one can directly notice, only two contributions are identified in both electron- and hole-sides. This first observation is raising the question about the coupling of the two surface states for this 25

nm-thick HgTe layer and recalls the discussion concerning the surface state extension presented in Chapter 1 (see 1.1.4).

Similarly to the 50 nm-thick sample, n_1 and n_H are sharing the same linear variation, at least in the electron-side. This is confirming the absence of side surface contribution, compared to the 100 nm-thick sample. Concerning the second contribution, n_2 is linear with V_{gate} and exhibits a much lower effective gate depletion factor $\alpha_2 = 3.4\ 10^{11}\ \text{cm}^{-2}.\text{V}^{-1}$. This value is two times less important than the depletion factor of the first contribution ($7.1\ 10^{11}\ \text{cm}^{-2}.\text{V}^{-1}$).

Moreover, additional FFT treatment has been achieved in the hole-side. In this regime, n_1 is no more matching n_H but it seems that $n_1 \approx \frac{n_H}{2}$. Such a shift is similar to what has been observed in Chapter 4 for the 15 nm-thick sample and has been attributed to the the coupling to the Γ_{8HH} bulk band. However, here, while the hybridization of the two surface states has been predicted by the calculations of Chapter 1 (see 1.1.4), the presence of two contributions highlighted by the FFT raises some doubts about this hybridization. Quantization analysis is required to verify this point. The FFT analysis in the hole-side presents an other interesting feature with a change of behavior of the second contribution n_2 which becomes almost constant with V_{gate} with a gate depletion factor $\alpha_2' = 0.8\ 10^{11}\ \text{cm}^{-2}.\text{V}^{-1}$. Such important change of behavior between electron- and hole-sides has never been reported for the contributions of thicker samples.

From the FFT analysis, we can conclude that there is a major contribution characterized by n_1 and which presents similar signatures than the topological surface states reported for the thicker samples. A second contribution is also present (n_2) and has peculiar features. The study of both the R_{xx} SdHO and of the Hall quantization are thus needed to go further and clearly identify these contributions.

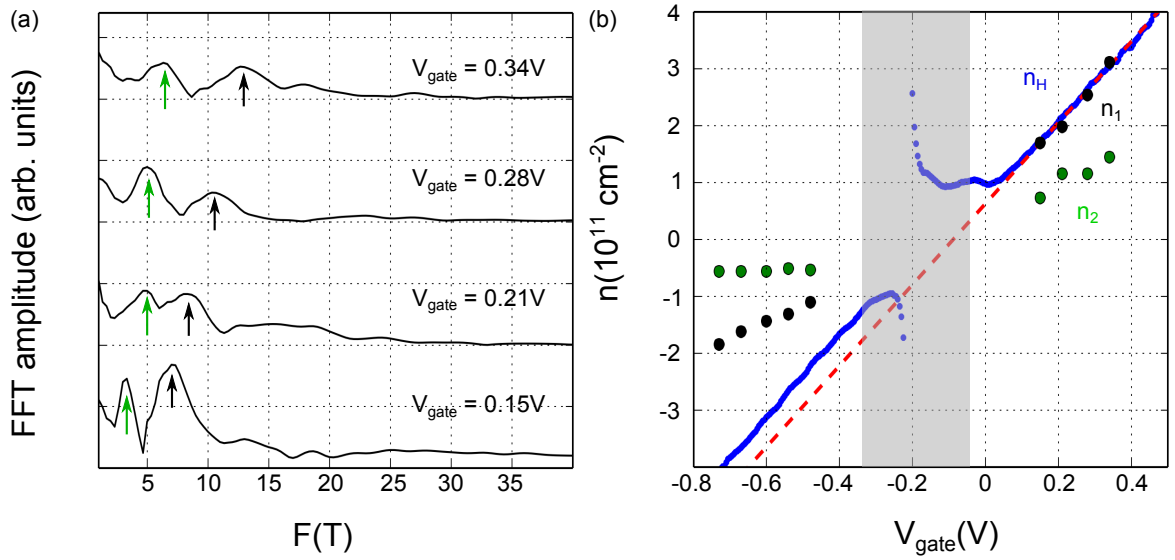

Figure C.7 – *FFT treatment of SdH oscillations of a 25 nm-thick HgTe layer. (a) FFT amplitude as a function of F for several V_{gate} values. Two peaks are evidenced and evidence two transport contributions (identified by green and black arrows). (b) The associated densities n_1 (black) and n_2 (green) compared to the one extracted from the low magnetic field analysis n_H (blue). Red dashed line is the linear fit of n_H in the electron-side and the grey color band is the V_{gate} range where single carrier model is not valid.*

First, we consider the R_{xx} oscillations. Contrary to the complex fan diagrams presented for the thicker samples (and similarly to the 15 nm-thick sample in Chapter 4, see 4.1.2.2), here the SdHO distribution is much more simple. Moreover, one can distinguish zero resistance minima in the electron-side, thus evidencing for the first time clear signatures of QHE. Nevertheless, this behavior differs in the hole-side with much broader

SdHO peaks and no more vanishing minima. We assume this is due to the LL broadening which is much more important in the hole-side due to the coupling to the Γ_{8HH} bulk band as demonstrated in Chapter 4 (see 4.2.3).

Furthermore, the addition of another contribution is noticeable in the hole-side with the apparition of large R_{xx} branches crossing the first set of LLs. These branches correspond to SdHO maxima which are significantly varying with V_{gate} and even change their curvature in the vicinity of the Dirac point resulting in the curved pattern visible for V_{gate} between 0.0 V and -0.2V.

From the low magnetic field measurements, the gate depletion factor of the major contribution has been extracted and enables the position of the expected LLs to be determined. The black dashed lines plotted in Fig. C.6(a) correspond to these positions. Note that the Dirac points have been positioned based on the low magnetic field determined positions for both the electron and hole regimes. It immediately appears that these black dashed lines perfectly reproduce the R_{xx} minima and so the LLs. Such a consistency between the data and these lines was not observed for the thicker samples. Moreover, what is really interesting to emphasize is that despite if the electron- and hole-sides differs in behavior, it seems that their energy levels can be attributed to the same set of LLs, thus strongly confirming the Dirac nature of this contribution.

However, this set of LLs does not allow to reproduce the energy levels from the second contribution. Using the gate depletion depletion factor α_2 and α_2', we manage to fit the R_{xx} minima positions of this contribution in both the electron- (see green dashed lines in Fig. C.8) and hole-sides (see blue dashed lines). With a Dirac point at -0.38 V, the green lines appear to be fully consistent with positions of vanishing R_{xx} minima, especially for V_{gate} between -0.2 V and 0.0 V where curved branches are reported. Note that for $V_{gate} \geq 0$ V, this contribution is completely coupled with the first one and only the black dashed lines fit the R_{xx} pattern. Blue lines are for their part representing evolution of this same contribution but in the hole-side. With a Dirac point at -1.7 V, these lines accurately reproduce the positions of the R_{xx} minima.

From these observations, we can conclude on the consistency between the R_{xx} mapping signatures and the FFT extracted contribution characteristics. However, even if all the R_{xx} mapping features are now explained, we do not have enough information to conclude about the nature of each contribution. Quantization analysis is thus needed to clarify the situation.

As previously reported for the thicker samples, the slopes of these dashed lines represented in Fig. C.6(a) and C.8(a) allow for the determination of the LLs quantization. Here and contrary to what has been reported for the 100 nm- and the 50 nm-thick samples, the slopes of these lines indicate integer values of filling factor, thus agreeing with a scenario of coupling of the top and bottom surface Dirac cones. Furthermore, one can already note a difference of quantization between electron- and hole-sides with integer and only odd filling factors respectively.

As evidences of a coupling of the surface states have been demonstrated, it is useful to remind the expected quantization in this case. As already introduced and discussed in Chapter 1 1.2.2.3.2, the coupling of the two Dirac cones equalizes the top and bottom surface LLs index: $N_{top} = N_{bottom} = N$, thus resulting in $\sigma_{xy} = (2N+1)\frac{e^2}{h}$. Therefore, only odd values of filling factors are expected. However, the hybridization enables the spin degeneracy to be lifted resulting in the appearance of even plateaus becoming more robust when increasing magnetic field.

To go one step further and confirm the first observations on the quantization, traces of σ_{xy} and σ_{xx} are plotted on Fig. C.9 for B = 2.8 T (a) and B = 1.5 T (b). One can immediately notice that, for B = 2.8 T, Hall plateaus are directly associated to vanishing conductance minima. Moreover, the quantization demonstrates integer plateaus in the electron-side and only odd ones in the hole-side. This quantization is in full agreement

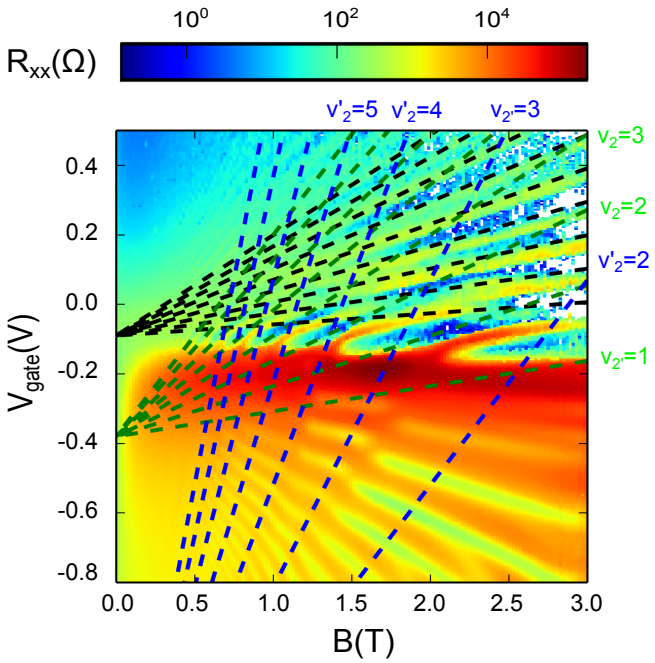

Figure C.8 – *R_{xx} mapping as a function of V_{gate} and B for a 25 nm-thick HgTe layer. Dashed lines indicate the different contributions. The black dashed lines correspond to the first and major contribution. The green and blue dashed lines represent a second contribution but with different gate depletion factor.*

with our previous observations on the R_{xx} mapping but also with the quantization model for two coupled surface states. The absence of even filling factors associated to large resistance peaks in the hole-side is attributed to an important LL broadening in this regime caused by the coupling to Γ_{8HH} bulk band (see Fig. 1.13 in Chapter 1). The LL resolution thus does not allow to observe these even values in the considered range of magnetic field.

However, by decreasing the magnetic field down to $B = 1.5$ T, the quantization differs with especially the appearance of a $\nu = 0$ plateau. Moreover, in the hole-side the former odd quantization transforms in an even one and especially presents $\nu = -2$ and $\nu = -4$ plateaus. Such a change in the quantization strongly confirms the presence of another gas.

To identify this gas, σ_{xy} mapping and associated traces following the variation of the second contribution are reported in Fig. C.10. The quantization is reported directly on the σ_{xy} mapping. A $\Delta\nu = 1$ difference of quantization is noticeable when sweeping B between the orange and the black traces. This directly evidences the impact of this gas on the transport. As it does not increase ν by a half-integer value but by an integer one, this contribution can not be of topological origin, otherwise this would mean that two sets of top and bottom topological surfaces are present and this is impossible.

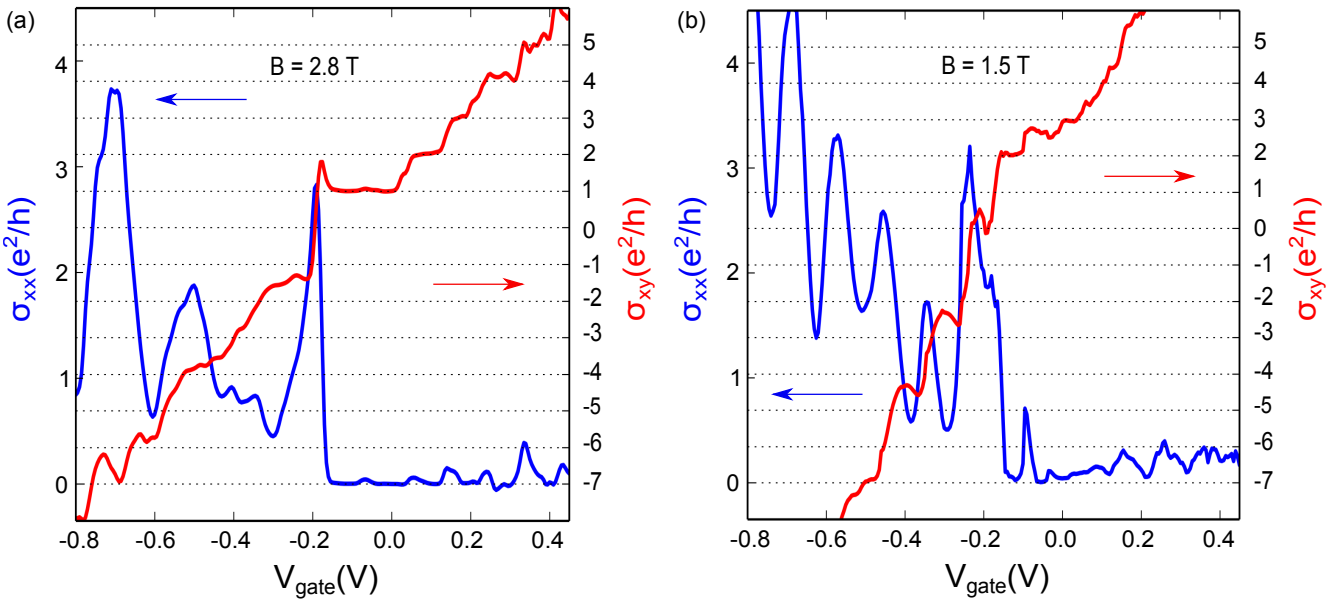

Figure C.9 – *Longitudinal and Hall conductances of a 25 nm-thick HgTe layer with* $L = 40\mu m$ *and* $W = 10\mu m$. *Data are extracted with* $I_{bias} = 1$ *nA and* $T = 70$ *mK. (a)* σ_{xx} *and* σ_{xy} *traces for* $B = 2.8$ *T.* σ_{xy} *is characterized with well-defined plateaus associated to a vanishing of* σ_{xx} *in the electron-side. Not accurate quantization is observed in the hole side manifesting the presence of an additional contribution due to the bottom interface. (b)* σ_{xx} *and* σ_{xy} *traces for* $B = 1.5$ *T. The interplay between the two contributions results in a zero-like plateau.*

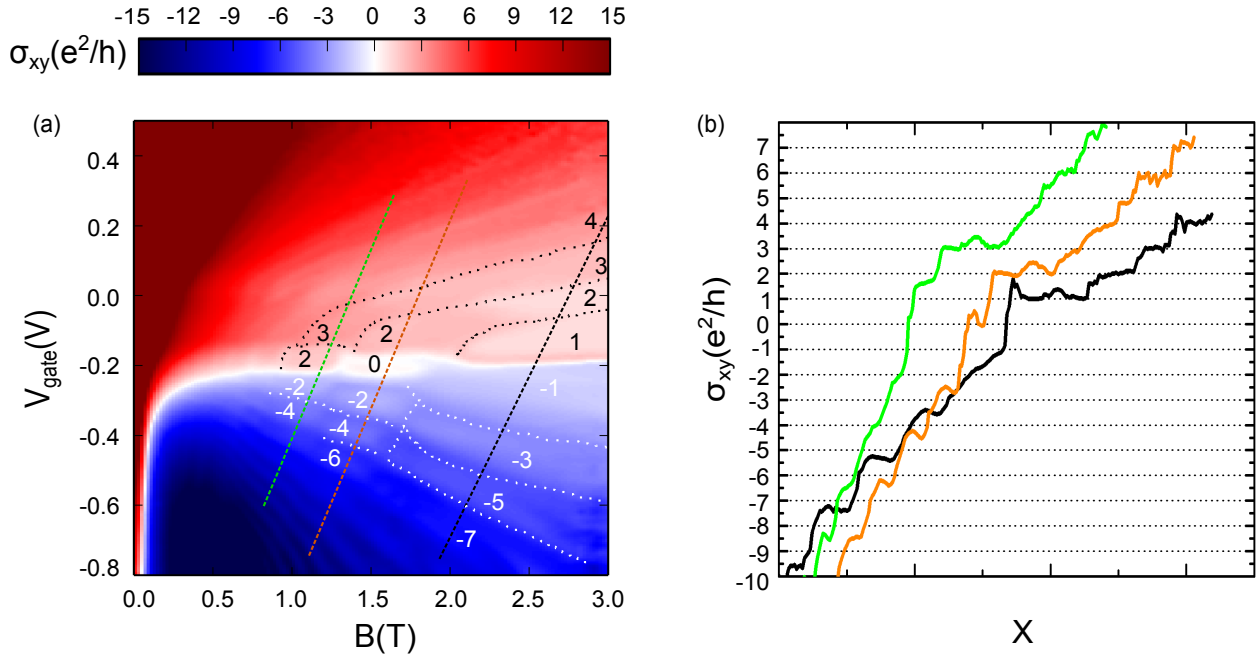

Figure C.10 – *(a) Hall conductance* σ_{xy} *mapping as a function of* V_{gate} *and* B. *(b)* σ_{xy} *traces following the dashed lines in (a). Data are extracted with* $I_{bias} = 1$ *nA and* $T = 70$ *mK.*

This whole analysis based on low and high magnetic field measurements gives information about transport mechanisms occurring in the case of a 25 nm-thick HgTe layer. A lot of important aspects have been mentioned throughout the analysis and are summed up here with appropriate conclusions:

- two major contributions have been clearly identified. Using FFT, R_{xx} LLs position as well as the Hall resistance values, the coupling of the two topological surface states has been demonstrated for this

thickness. The second contribution can be attributed to a 2DEG trapped at one interface.

- the coupling between the two surface states enables a new regime corresponding to the 3D/2D limit to be probed. Moreover, it simplifies a lot the transport signatures and for the first time enables a clear demonstration of quantum Hall effect. The experimental data and more specifically the quantization values validate the model developed in Chapter 1 for the thin structures (see 1.2.2.3.2).

- the presence of an extra 2DEG can explain the change of sign of Δ_3 by adding electrons and thus decreasing the $|n_H|$ values in the hole-side.

The results on these thin structures are very promising thanks to the definition of QHE. The idea is now to continue decreasing the HgTe thickness to get rid of the remaining extra contribution but also to try to reach the 3D/2D topological insulator transition. In this thought, 15 nm-thick samples have been considered and are described in details in Chapter 4 (see 4.1.2).

Bibliography

[AFS82] T. Ando, A.B. Fowler, and F. Stern. Electronic properties of two-dimensional systems. *Reviews of Modern Physics*, 54 (2):437–672, 1982.

[AGTB09] A.R. Akhmerov, C.W. Groth, J. Tworzydlo, and C.W.J. Beenakker. Switching of electrical current by spin precession in the first Landau level of an inverted-gap semiconductor. *Phys. Rev. B*, 80:195320, 2009.

[AL07] D.A. Abanin and L.S. Levitov. Quantized transport in graphene p-n junctions in a magnetic field. *Science*, 317:641–643, 2007.

[AMR+10] J.G. Analytis, R.D. McDonald, S.C. Riggs, J.H. Chu, G.S. Boebinger, and I.R. Fisher. Two-dimensional surface state in the quantum limit of a topological insulator. *Nature Phys.*, 6:960–964, 2010.

[And74] T. Ando. Theory of Quantum Transport in a Two-Dimensional Electron System under Magnetic Fields. iv. Oscillatory Conductivity. *Journal of the Physical Society of Japan*, 37 (5):1233–1237, 1974.

[And13] Y. Ando. Topological Insulator Materials. *Journal of the Physical Society of Japan*, 2013.

[APW93] N.A. Archer, H.D. Palfrey, and A.F.W. Willoughby. Growth Method, Composition, and Defect Structure Dependence of Mercury Diffusion in $Cd_xHg_{l-x}Te$. *Journ. of Elec. Mat.*, 22:967–971, 1993.

[Ari12] V. Ariel. Effective Mass and Energy-Mass Relationship. *arXiv*, 1205.3995, 2012.

[ASF86] D.K. Arch, J.L. Staudenmann, and J.P. Faurie. Layer intermixing in HgTe-CdTe superlattices. *Appl. Phys. Lett.*, 48:1588, 1986.

[ASS+12] T. Arakane, T. Sato, S. Souma, K. Kosaka, K. Nakayama, M. Komatsu, T. Takahashi, Z. Ren, K. Segawa, and Y. Ando. Tunable Dirac cone in the topological insulator $Bi_{2-x}Sb_xTe_{3-y}Se_y$. *Nature Communications*, 3:636, 2012.

[ATI+11] K. Ando, S. Takahashi, J. Ieda, Y. Kajiwara, H. Nakayama, T. Yoshino, K. Harii, Y. Fujikawa, M. Matsuo, S. Maekawa, and E. Saitoh. Inverse spin-Hall effect induced by spin pumping in metallic systems. *Journ. of Appl. Phys.*, 109:103913, 2011.

[BA07] M. Björck and G. Andersson. GenX: an extensible X-ray reflectivity refinement program utilizing differential evolution. *J. Appl. Cryst.*, 40:1174–1178, 2007.

[BB83] J.H. Basson and H. Booyens. The Introduction of Misfit Dislocations in HgCdTe Epitaxial Layers. *Phys. Stat. Sol. (a)*, 80:663, 1983.

[BBB+14] Y. Baum, J. Böttcher, C. Brüne, C. Thienel, L.W. Molenkamp, A. Stern, and E.M. Hankiewicz. Self-consistent k- p calculations for gated thin layers of 3D Topological Insulators. *Phys. Rev. B*, 89(245136), 2014.

[BBP+13] P. Ballet, X. Baudry, B. Polge, D. Brellier, J. Merlin, and P. Gergaud. Strain Determination in Quasi-Lattice-Matched LWIR HgCdTe/ CdZnTe Layers. *Journal of Electronic Materials*, 42(11):3133–3137, 2013.

[BFM+96] E. Belas, J. Franc, P. Moravec, R. Grill, H. Sitter, and P. Hoschl. Type conversion of p-(HgCd)Te using H2/CH4 and Ar reactive ion etching. *Semicond. Sci. Technol.*, 11:1116–1120, 1996.

[BGR93] D. Bagot, R. Granger, and S. Rolland. Thermal Expansion Coefficient and Bond Strength in $Hg_{1-x}Cd_xTe$ and $Hg_{1-x}Zn_xTe$. *Phys. Stat. Sol. (b)*, 177:295, 1993.

[BHZ06] B.A. Bernevig, T.L. Hughes, and S.-C. Zhang. Quantum Spin Hall Effect and Topological Phase Transition in HgTe Quantum Wells. *Science*, 314:1757, 2006.

[BLN+11] C. Brüne, C. X. Liu, E. G. Novik, E. M. Hankiewicz, H. Buhmann, Y. L. Chen, X. L. Qi, Z. X. Shen, S. C. Zhang, and L. W. Molenkamp. Quantum Hall Effect from the Topological Surface States of Strained Bulk HgTe. *Phys. Rev. Lett.*, 106:126803, 2011.

[BLT+11] B. Büttner, C. X. Liu, G. Tkachov, E. G. Novik, C. Brüne, H. Buhmann, E. M. Hankiewicz, P. Recher, B. Trauzettel, S. C. Zhang, and L. W. Molenkamp. Single valley Dirac fermions in zero-gap HgTe quantum wells. *Nature Phys.*, 7:418–422, 2011.

[Bou13] C. Bouvier. *Preuves expérimentales d'un transport de surface sur un isolant topologique 3D HgTe/CdTe sous contrainte*. PhD thesis, Ecole Doctorale de Physique de Grenoble, 2013.

[BP74] G.L. Bir and G.E. Pikus. *Symmetry and Strain-induced Effects in Semiconductors*. 1974.

[BR96] G. Bauer and W. Richter. *Optical Characterization of Epitaxial Semiconductor Layers*. Springer, 1996.

[BRB+12] C. Brüne, A. Roth, H. Buhmann, E.M. Hankiewicz, L.W. Molenkamp, J. Maciejko, X.-L. Qi, and S.-C. Zhang. Spin polarization of the quantum spin Hall edge states. *Nature Physics*, 8:485–490, 2012.

[BRG15] S. Barua, K.P. Rajeev, and A.K. Gupta. Evidence for topological surface states in metallic single crystals of Bi_2Te_3. *J. Phys.: Condens. Matter*, 27:015601, 2015.

[BRN+10] C. Brüne, A. Roth, E.G. Novik, M. König, H. Buhmann, E.M. Hankiewicz, W. Hanke, J. Sinova, and L.W. Molenkamp. Evidence for the ballistic intrinsic spin Hall effect in HgTe nanostructures. *Nature Physics*, 6:448–454, 2010.

[BTB+14] P. Ballet, C. Thomas, X. Baudry, C. Bouvier, O. Crauste, T. Meunier, G. Badano, M. Veillerot, J. P. Barnes, P. H. Jouneau, and L. P. Lévy. MBE Growth of Strained HgTe/CdTe Topological Insulator Structures. *J. Electron. Mater.*, 43:2955–2962, 2014.

[BTS+14] C. Brüne, C. Thienel, M. Stuiber, J. Bottcher, H. Buhmann, E. G. Novik, C.-X. Liu, E. M. Hankiewicz, and L. W. Molenkamp. Dirac-Screening Stabilized Surface-State Transport in a Topological Insulator. *Phys. Rev. X*, 4:041045, 2014.

[BWTS86] J.D. Benson, B.K. Wagner, A. Torabi, and C.J. Summers. Surface stoichiometry and reaction kinetics of molecular beam epitaxially grown (001) CdTe surfaces. *Appl. Phys. Lett.*, 49:1034–1036, 1986.

[CAD+10] E. Chen, D. Apalkov, Z. Diao, A. Driskill-Smith, D. Druist, D. Lottis, V. Nikitin, X. Tang, S. Watts, S. Wang, S.A. Wolf, A.W. Ghosh, J.W. Lu, S.J. Poon, M. Stan, W.H. Butler, S. Gupta, C.K.A. Mewes, T. Mewes, and P.B. Visscher. Advances and Future Prospects of Spin-Transfer Torque Random Access Memory. *IEEE Transactions on Magnetics*, 46:1873–1878, 2010.

[CDB+16] D. Cooper, T. Denneulin, N. Bernier, A. Béché, and J.L. Rouvière. Strain mapping of semiconductor specimens with nm-scale resolution in a transmission electron microscope. *Micron*, 80:145–165, 2016.

[CL75] G. Cliff and G.W. Lorimer. The quantitative analysis of thin specimens. *Journal of Microscopy*, 103:203–207, 1975.

[COB+13] O. Crauste, Y. Ohtsubo, P. Ballet, P. Delplace, D. Carpentier, C. Bouvier, T. Meunier, A. Taleb-Ibrahimi, and L. P. Lévy. Topological surface states of strained Mercury-Telluride probed by ARPES. *arXiv:1307.2008*, 2013.

[Cra75] J. Crank. *The Mathematics of Diffusion*. Clarendon Press Oxford, 1975.

[CS75] R.I. Cottam and G.A. Saunders. The elastic behavior of mercury telluride. *J. Phys. Chem. Solids,*, 36:187–192, 1975.

[CS07] J. Chu and A. Sher. *Physics and Properties of Narrow Gap Semiconductors*. Springer Science and Business Media, 2007.

[CS10] J. Chu and A. Sher. *Device Physics of Narrow Gap Semiconductors*. Springer New York Dordrecht Heidelberg London, 2010.

[CSZ+10] P. Cheng, C. Song, T. Zhang, Y. Zhang, Y. Wang, J.F. Jia, J. Wang, Y. Wang, B.F. Zhu, X. Chen, X. Ma, K. He, L. Wang, X. Dai, Z. Fang, X. Xie, X.L. Qi, C.X. Liu, S.C. Zhang, and Q.K. Xue. Landau Quantization of Massless Dirac Fermions in Topological Insulator. *Phys. Rev. Lett.*, 105:076801, 2010.

[CTDL77] C. Cohen-Tannoudji, B. Diu, and F. Laloë. *Quantum mechanics, volume II*. Hermann, 1977.

[CVL+12] H. Cao, R. Venkatasubramanian, C. Liu, J. Pierce, H. Yang, M.Z. Hasan, Y. Wu, and Y.P. Chen. Topological insulator Bi_2Te_3 films synthesized by metal organic chemical vapor deposition. *Appl. Phys. Lett.*, 101:162104, 2012.

[CWBS80] J.G. Collins, G.K. White, J.A. Birch, and T.F. Smith. Thermal expansion of ZnTe and HgTe and heat capacity of HgTe at low temperatures. *J. Phys. C: Solid St. Phys.*, 13:1649–1656, 1980.

[DD90] S. Datta and B. Das. Electronic analog of the electro-optic modulator. *Appl. Phys. Lett.*, 56:665, 1990.

[DJ87] B.W. Dodson and Tsao J.Y. Relaxation of strained layer semiconductor structures via plastic flow. *App. Phys, Lett.*, 51(17):1325–1327, 1987.

[DRDdJ12] H. Demers, R. Ramachandra, D. Drouin, and N. de Jonge. The Probe Profile and Lateral Resolution of Scanning Transmission Electron Microscopy of Thick Specimens. *Microsc. Microanal.*, 18(3):582–590, 2012.

[DWB+16] R.S. Deacon, J. Wiedenmann, E. Bocquillon, F. Dominguez, T.M. Klapwijk, P. Leubner, C. Brüne, E. M. Hankiewicz, S. Tarucha, K. Ishibashi, H. Buhmann, and L.W. Molenkamp. Josephson radiation from gapless Andreev bound states in HgTe-based topological junctions. *arXiv*, 1603.09611, 2016.

[Ede90] V.M. Edelstein. Spin polarization of conduction electrons induced by electric current in two-dimensional asymmetric electron systems. *Solid State Communications*, 73(3):233–235, 1990.

[ERT+10] K. Eto, Z. Ren, A.A. Taskin, K. Segawa, and Y. Ando. Angular-dependent oscillations of the magnetoresistance in Bi_2Se_3 due to the three-dimensional bulk Fermi surface. *Phys. Rev. B*, 81:195309, 2010.

[FAB+88] R.D. Feldman, R.F. Austin, P.M. Bridenbaugh, A.M. Johnson, W.M. Simpson, B.A. Wilson, and C.E. Bonner. Effects of Zn to Te ratio on the molecular beam epitaxial growth of ZnTe on GaAs. *Journ. of Appl. Phys.*, 64:1191, 1988.

[FKM07] L. Fu, C.L. Kane, and E.J. Mele. Topological Insulators in Three Dimensions. *Phys. Rev. Lett.*, 98:106803, 2007.

[FM13] M. Franz and L. Molenkamp. *Topological Insulators*. Elsevier, 2013.

[FMP82] J.P. Faurie, A. Million, and J. Piaguet. CdTe/HgTe multilayers grown by molecular beam epitaxy. *Appl. Phys. Lett.*, 41 (8):713–715, 1982.

[FSW+86] J.P. Faurie, I.K. Sou, P.S. Wijewarnasuriya, S. Rafol, and K.C. Woo. Hole Hall-mobility enhancement in HgTe-$Hg_{1-x}Cd_xTe$ heterojnnctions. *Phys. Rev. B*, 34:6000–6002, 1986.

[Fuc13] J-N. Fuchs. *Dirac fermions in graphene and analogues: magnetic field and topological properties*. Habilitation à diriger des recherches, 2013.

[FVMK16] M.H. Fischer, A. Vaezi, A. Manchon, and E.A. Kim. Spin-torque generation in topological insulator based heterostructures. *Phys. Rev. B*, 93:125303, 2016.

[FZH+00] P. Ferret, J.P. Zanatta, R. Hamelin, S. Cremer, A. Million, M. Wolny, and G. Destefanis. Status of the MBE technology at Leti LIR for the manufacturing of HgCdTe focal plane arrays. *Journal of Electronic Materials*, 29 (6):641–647, 2000.

[GBD+15] Y. S. Gui, C. R. Becker, N. Dai, J. Liu, Z. J. Qiu, E. G. Novik, M. Schäfer, X. Z. Shu, J. H. Chu, H. Buhmann, and L. W. Molenkamp. Giant spin-orbit splitting in a HgTe quantum well. *Phys. Rev. B*, 70:115328, 2015.

[Gil04] T.L. Gilbert. A Phenomenological Theory of Damping in Ferromagnetic Materials. *IEEE TRANSACTIONS ON MAGNETICS*, 40 (6):3443–3449, 2004.

[GW06] E.P. Goddwin and J.C. Wyant. *Field Guide to Interferometric Optical Testing*. Bellingham, WA, 2006.

[GZK+07] A.J.M. Giesbers, U. Zeitler, M.I. Katsnelson, L.A. Ponomarenko, T.M. Mohiuddin, and J.C. Maan. Quantum-Hall Activation Gaps in Graphene. *Phys. Rev. Lett.*, 99:206803, 2007.

[Has10] M.Z. Hasan. Berry's phase and quantization in topological insulators. *Physics*, 3:62, 2010.

[HBS+06] J. Hinz, H. Buhmann, M. Schäffer, V. Hock, C.R. Becker, and L.W. Molenkamp. Gate control of the giant Rashba effect in HgTe quantum wells. *Semicond. Sci. Technol.*, 21:501–506, 2006.

[HIK+10] T. Hanaguri, K. Igarashi, M. Kawamura, H. Takagi, and T. Sasagawa. Momentum-resolved Landau-level spectroscopy of Dirac surface state in Bi_2Se_3. *Phys. Rev. B*, 82:081305(R), 2010.

[HKW13] L. He, X. Kou, and K.L. Wang. Review of 3D topological insulator thin-film growth by molecular beam epitaxy and potential applications. *Phys. Status Solidi RRL*, 7:50–63, 2013.

[HMY+89] K.A. Harris, T.H. Myers, R.W. Yanka, L.M. Mohnkern, R.W. Green, and N. Otsuka. Microstructural defect reduction in HgCdTe grown by photoassisted molecular-beam epitaxy. *J. Vac. Sci. Techno. A*, 8 (2):1013–1019, 1989.

[HSC82] G.L. Hansen, J.L. Schmit, and T.N. Casselman. Energy gap versus alloy composition and temperature in $Hg_{1-x}Cd_x$Te. *J. Appl. Phys.*, 53:7099, 1982.

[HSH+08] R. Haakenaasen, E. Selvig, S. Hadzialic, T. Skauli, V. Hansen, J.E. Tibballs, L. Trosdahl-Iversen, H. Steen, S. Foss, J. Tafto, M. Halsall, and J. Orr. Nanowires in the CdHgTe Material System. *Journal of Electronic Materials*, 37(9):1311–1317, 2008.

[HXQ+09] D. Hsieh, Y. Xia, D. Qian, L. Wray, H. Dil, F. Meier, J. Osterwalder, L. Patthey, J.G. Checkelsky, N.P. Ong, A.V. Fedorov, H. Lin, A. Bansil, D. Grauer, Y.S. Hor, R.J. Cava, and M.Z. Hasan. A tunable topological insulator in the spin helical Dirac transport regime. *Nature*, 460:1101–1105, 2009.

[HZZ09] X. Hong, K. Zou, and J. Zhu. Quantum scattering time and its implications on scattering sources in graphene. *Phys. Rev. B.*, 80:241415(R), 2009.

[IdJM15] R. Ilan, F. de Juan, and J.E. Moore. Spin-Based Mach-Zehnder Interferometry in Topological Insulator p-n Junctions. *Phys. Rev. Lett.*, 115:096802, 2015.

[IL09] H. Ibach and H. Lüth. *Solid-State Physics. An Introduction to Principles of Materials Science*. Springer, 2009.

[Jal12] D. Jalabert. Real space structural analysis using 3D MEIS spectra from a toroidal electrostatic analyzer with 2D detector. *Nuclear Instruments and Methods in Physics Research B*, 270:19–22, 2012.

[JCS+03] Y. Ji, Y. Chung, D. Sprinzak, M. Heiblum, D. Mahalu, and H. Shtrikman. An electronic Mach-Zehnder interferometer. *Nature*, 422:415–418, 2003.

[JLJ+15] M. Jamali, J.S. Lee, J.S. Jeong, F. Mahfouzi, Y. Lv, Z. Zhao, B.K. Nikolic, K.A. Mkhoyan, N. Samarth, and J.-P. Wang. Giant Spin Pumping and Inverse Spin Hall Effect in the Presence of Surface and Bulk Spin-Orbit Coupling of Topological Insulator Bi_2Se_3. *Nano Letters*, 15:7126–7132, 2015.

[Jon09] A. Jonchère. Etude par diffraction X des contraintes et des phénomènes de relaxation dans les hétérostructures CdHgTe/CdZnTe orientées (211)B. Technical report, CEA LETI, 2009.

[JPGB+12] D. Jalabert, D. Pelloux-Gervais, A. Béché, J.M. Hartmann, P. Gergaud, J.L. Rouvière, and B. Canut. Depth strain profile with sub-nm resolution in a thin silicon film using medium energy ion scattering. *Phys. Status Solidi A*, 209:262–265, 2012.

[JZSK07] Z. Jiang, Y. Zhang, H.L. Stormer, and P. Kim. Quantum Hall States near the Charge-Neutral Dirac Point in Graphene. *Phys. Rev. Lett.*, 99:106802, 2007.

[Kan57] E.O. Kane. Band structure of Indium Antimonide. *Journal of Physics and Chemistry of Solids*, 1(4):249–261, 1957.

[KBM+08] M. Konig, H. Buhmann, L.W. Molenkamp, T. Hughes, C.-X. Liu, X.-L. Qi, and S.-C. Zhang. The Quantum Spin Hall Effect: Theory and Experiment. *Journal of the Physical Society of Japan*, 77:031007, 2008.

[KBZ+16] D. A. Kozlov, D. Bauer, J. Ziegler, R. Fischer, M. L. Savchenko, Z. D. Kvon, N. N. Mikhailov, S. A. Dvoretsky, and D. Weiss. Probing quantum capacitance in a 3D topological insulator. *Phys. Rev. Lett.*, 116:166802, 2016.

[KDP80] K.V. Klitzing, G. Dorda, and M. Pepper. New Method for High-Accuracy Determination of the Fine-Structure Constant Based on Quantized Hall Resistance. *Phys. Rev. Lett.*, 45:494, 1980.

[Kit48] C. Kittel. On the Theory of Ferromagnetic Resonance Absorption. *Phys. Rev.*, 73 (2):155–161, 1948.

[KKO+14] D. A. Kozlov, Z. D. Kvon, E. B Olshanetsky, N. N. Mikhailov, S. A. Dvoretsky, and D. Weiss. Transport Properties of a 3D Topological Insulator based on a Strained High-Mobility HgTe Film. *Phys. Rev. Lett.*, 112:196801, 2014.

[KLY+15] N. N. Klimov, S. T. Le, J. Yan, P. Agnihotri, E. Comfort, J. U. Lee, D. B. Newell, and C. A. Richter. Edge-state transport in graphene p-n junctions in the quantum Hall regime. *Phys. Rev. B*, 92:241301(R), 2015.

[KM05] C. L. Kane and E. J. Mele. Quantum Spin Hall Effect in Graphene. *Phys. Rev. Lett.*, 95:226801, 2005.

[KMN+07] P. Kok, W.J. Munro, K. Nemoto, T.C. Ralph, J.P. Dowling, and G.J. Milburn. Linear optical quantum computing with photonic qubits. *Rev. Mod. Phys.*, 79:135, 2007.

[KR11] V. Krueckl and K. Richter. Switching Spin and Charge between Edge States in Topological Insulator Constrictions. *Phys. Rev. Lett.*, 107:086803, 2011.

[KS88] R.J. Koestner and H.F. Schaake. Kinetics of molecular-beam epitaxial HgCdTe growth. *J. Vac. Sci. Technol. A*, 6 (4):2834–2839, 1988.

[KWB+07] M. König, S. Wiedmann, C. Brüne, A. Roth, H. Buhmann, L.W. Molenkamp, X.-L. Qi, and S.-C. Zhang. Quantum Spin Hall Insulator State in HgTe Quantum Wells. *Science*, 318:766–770, 2007.

[LBG+97] M. Li, C.R. Becker, R. Gall, W. Faschinger, and G. Landwehr. X-ray reciprocal space mapping of a (112) oriented HgTe/$Hg_{0.1}Cd_{0.9}$Te superlattice. *Appl. Phys. Lett.*, 71(13):1822–1824, 1997.

[Lee09] D.H. Lee. Surface States of Topological Insulators: The Dirac Fermion in Curved Two-Dimensional Spaces. *Phys. Rev. Lett.*, 103:196804, 2009.

[LFO+16] E. Lesne, Y. Fu, S. Oyarzun, J.C. Rojas-Sanchez, D.C. Vaz, H. Naganuma, G. Sicoli, J.P. Attané, M. Jamet, E. Jacquet, J.M. George, A. Barthélémy, H. Jaffrès, A. Fert, M. Bibes, and L. Vila. Highly efficient and tunable spin-to-charge conversion through Rashba coupling at oxide interfaces. *Nature Materials*, 2016.

[LL35] L. Landau and E. Lifshits. On the theory of the dispersion of magnetic permeability in ferromagnetic bodies. *Phys. Zeitsch. der Sow*, 8:153–169, 1935.

[LLB+16] P. Leubner, L. Lunczer, C. Brüne, H. Buhmann, and L.W. Molenkamp. Strain Engineering of the Band Gap of HgTe Quantum Wells using Superlattice Virtual Substrates. *arXiv*, 1608.01581, 2016.

[LPL+12] L. Liu, C.F. Pai, Y. Li, H.W. Tseng, D.C. Ralph, and R.A. Buhrman. Spin-Torque Switching with the Giant Spin Hall Effect of Tantalum. *Science*, 336:555–558, 2012.

[LPMM89] G. Lentz, A. Ponchet, N. Magnea, and H. Mariette. Growth control of CdTe/CdZnTe (001) strained layer superlattices by reflection high energy electron diffraction oscillations. *Appl. Phys. Lett.*, 55:2733, 1989.

[LSY+10] H.Z. Lu, W.Y. Shan, W. Yao, Q. Niu, and S.Q. Shen. Massive Dirac fermions and spin physics in an ultrathin film of topological insulator. *Phys. Rev. B*, 81:115407, 2010.

[Lud87] B.W. Ludington. *Mater. Res. Soc. Symp. Proc.*, 90:437, 1987.

[LvKS09] T. Lohmann, K. von Klitzing, and J.H. Smet. Four-terminal Magneto-Transport in Graphene p-n Junctions Created by Spatially Selective Doping. *Nano Letters*, 9 (5):1973–1979, 2009.

[LVM+14] J. Ludwig, Yu. B. Vasilyev, N. N. Mikhailov, J. M. Poumirol, Z. Jiang, O. Vafek, and D. Smirnov. Cyclotron resonance of single-valley Dirac fermions in nearly gapless HgTe quantum wells. *Phys. Rev. B*, 89:241406(R), 2014.

[LYS09] J. Linder, T. Yokoyama, and A. Sudbo. Anomalous finite size effects on surface states in the topological insulator Bi_2Se_3. *Phys. Rev. B*, 80:205401, 2009.

[LZY+10] C.X. Liu, H. Zhang, B. Yan, X.L. Qi, T. Frauenheim, X. Dai, Z. Fang, and S.C. Zhang. Oscillatory crossover from two-dimensional to three-dimensional topological insulators. *Phys. Rev. B*, 81:041307(R), 2010.

[MAHB91] J.R. Meyer, D.J. Arnold, C.A. Hoffman, and F.J. Bartoli. Interface roughness limited electron mobility in HgTe-CdTe superlattices. *Appl. Phys. Lett.*, 58:2523, 1991.

[MB74] J.W. Matthews and A.E. Blakeslee. Defects in epitaxial multilayers. i Misfit dislocations. *Journal of Crystal Growth*, 27:118–125, 1974.

[MB07] J.E. Moore and L. Balents. Topological invariants of time-reversal-invariant band structures. *Phys. Rev. B*, 75:121306(R), 2007.

[MBG+15] L. Maier, E. Bocquillon, M. Grimm, J.B. Oostinga, C. Ames, C. Gould, C. Brüne, H. Buhmann, and L.W. Molenkamp. Phase-sensitive SQUIDs based on the 3D topological insulator HgTe. *arXiv*, 1510.04426, 2015.

[MBVdV+87] P.M.J. Maree, J.C. Barbour, J.F. Van der Veen, K.L. Kavanagh, C.W.T. Bulle-Lieuwma, and M.P.A. Viegers. Generation of misfit disiocations in semiconductors. *J. Appl Phys.*, 62(11):4413–4420, 1987.

[Mel66] A.C. Melissinos. *Experiments in Modern Physics*. Academic Press, 1966.

[MGG+11] I.M. Miron, K. Garello, G. Gaudin, P.J. Zermatten, M.V. Costache, S. Auffret, S. Bandiera, B. Rodmacq, A. Schuhl, and P. Gambardella. Perpendicular switching of a single ferromagnetic layer induced by in-plane current injection. *Nature*, 476:189–193, 2011.

[Mil82] A. Million. *Etude de l'épitaxie par jets moléculaires des composées II-VI : CdTe et $Cd_xHg_{1-x}Te$*. PhD thesis, INP Grenoble, 1982.

[MLR+14] A.R. Mellnik, J.S. Lee, A. Richardella, J.L. Grab, P.J. Mintun, M.H. Fischer, A. Vaezi, A. Manchon, E.A. Kim, N. Samarth, and D.C. Ralph. Spin-transfer torque generated by a topological insulator. *Nature*, 511:449–451, 2014.

[MMM+15] S. Morikawa, S. Masubuchi, R. Moriya, K. Watanabe, T. Taniguchi, and T. Machida. Edge-channel interferometer at the graphene quantum Hall pn junction. *Appl. Phys. Lett.*, 106:183101, 2015.

[MOCGP88] A. Million, L. Oi Ciaccio, J.P. Gailliard, and J. Piaguet. Molecular-beam epitaxy of $Cd_xHg_{1-x}Te$ at D-LETI-LlR. *J. Vac. Sci. Technol. A*, 6 (4):2813–2820, 1988.

[MPF+10] O. Mosendz, J. E. Pearson, F. Y. Fradin, G. E. W. Bauer, S. D. Bader, and A. Hoffmann. Quantifying Spin Hall Angles from Spin Pumping: Experiments and Theory. *Phys. Rev. Lett.*, 104:046601, 2010.

[MTT+15] S. Matsuo, S. Takeshita, T. Tanaka, S. Nakaharai, K. Tsukagoshi, T. Moriyama, T. Ono, and K. Kobayashi. Edge mixing dynamics in graphene p-n junctions in the quantum Hall regime. *Nature Communications*, 6:8066, 2015.

[Mur12] R. Murali. *Graphene Nanoelectronics: From Materials to Circuits*. Springer Science Business Media, 2012.

[NGM+05] K.S. Novoselov, A.K. Geim, S.V. Morozov, D. Jiang, M.I. Katsnelson, I.V. Grigorieva, S.V. Dubonos, and A.A. Firsov. Two-dimensional gas of massless Dirac fermions in graphene. *Nature*, 438:197–200, 2005.

[NPJJ+05] E.G. Novik, A. Pfeuffer-Jeschke, T. Jungwirth, V. Latussek, C.R. Becker, G. Landwehr, H. Buhmann, and L.W. Molenkamp. Band structure of semimagnetic $Hg_{1-y}Mn_yTe$ quantum wells. *Phys. Rev. B*, 72:035321, 2005.

[OMF+11] M. Orlita, K. Masztalerz, C. Faugeras, M. Potemski, E. G. Novik, C. Brüne, H. Buhmann, and L. W. Molenkamp. Fine structure of zero-mode Landau levels in $HgTe/Hg_xCd_{1-x}Te$ quantum wells. *Phys. Rev. B*, 83:115307, 2011.

[PB85] R. People and J.C. Bean. Calculation of critical layer thickness versus lattice mismatch for Ge_x $Si_{(1-x)}$/Si strained-layer heterostructures. *Appl. Phys. Lett.*, 47(3):322–324, 1985.

[Pen89] S.J. Pennycook. Z-contrast STEM for materials science. *Ultramicroscopy*, 30:58–69, 1989.

[PLL+12] C.F. Pai, L. Liu, Y. Li, H.W. Tseng, D.C. Ralph, and R.A. Buhrman. Spin transfer torque devices utilizing the giant spin Hall effect of tungsten. *Appl. Phys. Lett.*, 101:122404, 2012.

[PSB+11] H. Paik, D.I. Schuster, L.S. Bishop, G. Kirchmair, G. Catelani, A.P. Sears, B.R. Johnson, M.J. Reagor, L. Frunzio, L.I. Glazman, S.M. Girvin, M.H. Devoret, and R.J. Schoelkopf. Observation of High Coherence in Josephson Junction Qubits Measured in a Three-Dimensional Circuit QED Architecture. *Phys. Rev. Lett.*, 107:240501, 2011.

[PWA+14] Y. Pan, D. Wu, J.R. Angevaare, H. Luigjes, E. Frantzeskakis, N. de Jong, E. Van Heumen, T.V. Bay, B. Zwartsenberg, Y.K. Huang, M. Snelder, A. Brinkman, M.S. Golden, and A. de Visser. Low carrier concentration crystals of the topological insulator $Bi_{2-x}Sb_xTe_{3-y}Se_y$: a magneto-transport study. *New Journal of Physics*, 16:123035, 2014.

[QHX+10] D.-X. Qu, Y.S. Hor, J. Xiong, R.J. Cava, and N.P. Ong. Quantum Oscillations and Hall Anomaly of Surface States in the Topological Insulator Bi_2Te_3. *Science*, 329:821–824, 2010.

[RBM+13] J.L. Rouvière, A. Béché, Y. Martin, T. Denneulin, and D. Cooper. Improved strain precision with high spatial resolution using nanobeam precession electron diffraction. *Appl. Phys. Lett.*, 103:241913, 2013.

[RE72] B.J. Roman and A.W. Ewald. Stress-Induced Band Gap and Related Phenomena in Gray Tin. *Phys. Rev. B*, 5(10):3914–3932, 1972.

[Rol94] S. Rolland. *Dielectric constant and refractive index of HgCdTe in Properties of Narrow Gap Cadmium-based compounds*. Inspec, 1994.

[Roy09] R. Roy. Topological phases and the quantum spin Hall effect in three dimensions. *Phys. Rev. B*, 79:195322, 2009.

[RSOF+16] J.C. Rojas-Sanchez, S. Oyarzun, Y. Fu, A. Marty, C. Vergnaud, S. Gambarelli, L. Vila, M. Jamet, Y. Ohtsubo, A. Taleb-Ibrahimi, P. Le Févre, F. Bertran, N. Reyren, J.M. George, and A. Fert. Spin to Charge Conversion at Room Temperature by Spin Pumping into a New Type of Topological Insulator: α-sn Films. *Phys. Rev. Lett.*, 116:096602, 2016.

[RSRL+14] J.C. Rojas-Sanchez, N. Reyren, P. Laczkowski, W. Savero, J.P. Attané, C. Deranlot, M. Jamet, J.M. George, L. Vila, and H. Jaffrès. Spin Pumping and Inverse Spin Hall Effect in Platinum: The Essential Role of Spin-Memory Loss at Metallic Interfaces. *Phys. Rev. Lett.*, 112:106602, 2014.

[RSVD+13] J.C. Rojas-Sanchez, L. Vila, G. Desfonds, S. Gambarelli, J.P. Attané, J.M. De Teresa, C. Magen, and A. Fert. Spin-to-charge conversion using Rashba coupling at the interface between non-magnetic materials. *Nature Communications*, 4:2944, 2013.

[RTS+10] Z. Ren, A.A. Taskin, S. Sasaki, K. Segawa, and Y. Ando. Large bulk resistivity and surface quantum oscillations in the topological insulator Bi_2Te_2Se. *Phys. Rev. B*, 82:241306(R), 2010.

[SC01] T. Skauli and T. Colin. Accurate determination of the lattice constant of molecular beam epitaxial CdHgTe. *Journal of Crystal Growth*, 222:719–725, 2001.

[SLS10] W.-Y. Shan, H.-Z. Lu, and S.-Q. Shen. Effective continuous model for surface states and thin films of three-dimensional topological insulators. *New Journal of Physics*, 12:043048, 2010.

[SMR+00] E.P.G. Smith, C.A. Musca, D.A. Redfern, J.M. Dell, and L. Faraone. H2-Based Dry Plasma Etching for Mesa Structuring of HgCdTe. *Journal of Electronic Materials*, 29 (6):853–8589, 2000.

[SNK+14] Y. Shiomi, K. Nomura, Y. Kajiwara, K. Eto, M. Novak, K. Segawa, Y. Ando, and E. Saitoh. Spin-Electricity Conversion Induced by Spin Injection into Topological Insulators. *Phys. Rev. Lett.*, 113:196601, 2014.

[SOL+11] B. Sacépé, J.B. Oostinga, J. Li, A. Ubaldini, N.J. Couto, E. Giannini, and A.F. Morpurgo. Gate-tuned normal and superconducting transport at the surface of a topological insulator. *Nature Communications*, 2:575, 2011.

[SPT+12] A.A. Schafgans, K.W. Post, A.A. Taskin, Y. Ando, X.L. Qi, B.C. Chapler, and D.N. Basov. Landau level spectroscopy of surface states in the topological insulator $Bi_{0.91}Sb_{0.09}$ via magneto-optics. *Phys. Rev. B*, 85:195440, 2012.

[SRB+13] H. Schmidt, J. C. Rode, C. Belke, D. Smirnov, and R. J. Haug. Mixing of edge states at a bipolar graphene junction. *Phys. Rev. B*, 88:075418, 2013.

[Ste98] A. Steane. Quantum computing. *Rep. Prog. Phys.*, 61:117, 1998.

[SUMT06] E. Saitoh, M. Ueda, H. Miyajima, and G. Tatara. Conversion of spin current into charge current at room temperature: Inverse spin-hall effect. *Appl. Phys. Lett.*, 88:182509, 2006.

[SW75] T.F. Smith and G.K. White. The low-temperature thermal expansion and Gruneisen parameters of some tetrahedrally bonded solids. *J. Phys. C: Solid State Phys.*, 8:2031–2042, 1975.

[TA10] K. Taskin, A.A. Segawa and Y. Ando. Oscillatory angular dependence of the magnetoresistance in a topological insulator $Bi_{1-x}Sb_x$. *Phys. Rev. B*, 82:121302(R), 2010.

[TA11] A.A. Taskin and Y. Ando. Berry phase of nonideal Dirac fermions in topological insulators. *Phys. Rev. B*, 84:035301, 2011.

[TBB02] Y. Tserkovnyak, A. Brataas, and G. E. W. Bauer. Enhanced Gilbert Damping in Thin Ferromagnetic Films. *Phys. Rev. Lett.*, 88:117601, 2002.

[Thi14] C. Thienel. *Exploring the transport properties of the three-dimensional topological insulator material HgTe*. PhD thesis, Julius-Maximilians-Universität Würzburg, 2014.

[THM+93] A. Tardot, A. Hamoudi, N. Magnea, P. Gentile, and J.L. Pautrat. Nonlinear interdiffusion in semiconductor superlattices: Case of CdTe-HgTe. *Appl. Phys. Lett.*, 62:2548, 1993.

[THM15] K. Takase, H. Hibino, and K. Muraki. Probing the extended-state width of disorder-broadened Landau levels in epitaxial graphene. *Phys. Rev. B*, 92:125407, 2015.

[TS87] M.F.S. Tang and D.A. Stevenson. Interdiffusion and related defect mechanisms in the HgTe-CdTe system. *J. Vac. Sci. Technol. A*, 5:3124, 1987.

[TSC+99] S. Tehrani, J.M. Slaughter, E. Chen, M. Durlam, J. Shi, and M. DeHerren. Progress and outlook for MRAM technology. *IEEE Transactions on Magnetics*, 35:2814–2819, 1999.

[TTS+16] N.H. Tu, Y. Tanabe, Y. Satake, K. Huynh, and K. Tanigaki. n-plane Topological p-n Junction in the Three-Dimensional Topological Insulator $Bi_{2-x}Sb_xTe_{3-y}Se_y$. *arXiv*, 1603.07535, 2016.

[WBD+16] J. Wiedenmann, E. Bocquillon, R.S. Deacon, S. Hartinger, O. Herrman, T.M. Klapwijk, L. Maier, C. Ames, C. Brüne, C. Gould, A. Oiwa, K. Ishibashi, S. Tarucha, H. Buhmann, and L.W. Molenkamp. 4π-periodic Josephson supercurrent in HgTe-based topological Josephson junctions. *Nature Communications*, 7:10303, 2016.

[WBW+91] Y.S. Wu, C.R. Becker, A. Waag, M.M. Kraus, R.N. Bicknell-Tassius, and G. Landwehr. Correlation of the Cd-to-Te ratio on CdTe surfaces with the surface structure. *Physical Review B*, 44(16):8904–8911, 1991.

[WCZZ12] J. Wang, X. Chen, B.-F. Zhu, and S.-C. Zhang. Topological p-n junction. *Phys. Rev. B*, 85:235131, 2012.

[WGC97] W.S. Warren, N. Gershenfeld, and I. Chuang. The Usefulness of NMR Quantum Computing. *Science*, 277:1688–1690, 1997.

[WNM+08] T.O. Wehling, K.S. Novoselov, S.V. Morozov, E.E. Vdovin, M.I. Katsnelson, A.K. Geim, and A.I. Lichtenstein. Molecular Doping of Graphene. *Nano Letters*, 8:173–177, 2008.

[WSD+12] A. Wolos, S. Szyszko, A. Drabinska, M. Kaminska, S. G. Strzelecka, A. Hruban, A. Materna, and M. Piersa. Landau-Level Spectroscopy of Relativistic Fermions with Low Fermi Velocity in the Bi_2Te_3 Three-Dimensional Topological Insulator. *Phys. Rev. Lett.*, 109:247604, 2012.

[WvEK+11] S. Wiedmann, H. J. van Elferen, E. V. Kurganova, M. I. Katsnelson, A. J. M. Giesbers, A. Veligura, B. J. van Wees, R. V. Gorbachev, K. S. Novoselov, J. C. Maan, and U. Zeitler. Coexistence of electron and hole transport in graphene. *Phys. Rev. B*, 84:115314, 2011.

[WYF14] S.-C. Wu, B. Yan, and C. Felser. Ab initio study of topological surface states of strained HgTe. *EPL*, 107:57006, 2014.

[XMC16] Y. Xu, I. Miotkowski, and Y.P. Chen. Quantum transport of two-species Dirac fermions in dual-gated three-dimensional topological insulators. *Nature Communications*, 7:11434, 2016.

[XML+14] Y. Xu, I. Miotkowski, C. Liu, J. Tian, H. Nam, N. Alidoust, J. Hu, C.K. Shih, M.Z. Hasan, and Y.P. Chen. Observation of topological surface state quantum Hall effect in an intrinsic three-dimensional topological insulator. *Nature Physics*, 10:956–963, 2014.

[XQH+09] Y. Xia, D. Qian, D. Hsieh, L. Wray, A. Pal, H. Lin, A. Bansil, D. Grauer, Y.S. Hor, R.J. Cava, and M.Z. Hasan. Observation of a large-gap topological-insulator class with a single Dirac cone on the surface. *Nature Physics*, 5:398–402, 2009.

[Yas10] M. Yasaka. X-ray Reflectivity measurement. *The Rigaku Journal*, 26(2), 2010.

[YDW+12] A.F. Young, C.R. Dean, L. Wang, P. Cadden-Zimansky, K. Watanabe, T. Taniguchi, J. Hone, K.L. Shepard, and P. Kim. Spin and valley quantum Hall ferromagnetism in graphene. *Nature Phys.*, 8:550, 2012.

[YKM+94] M. Yasuda, H. Kawata, K. Murata, K. Hashimoto, Y. Hirai, and N. Nomura. Resist heating effect in electron beam lithography. *J. Vac. Sci. Technol. B*, 12:1362, 1994.

[YLZ+13] Y. Yan, Z.-M. Liao, Y.-B. Zhou, H.-C. Wu, Y.-Q. Bie, J.-J. Chen, J. Meng, X.-S. Wu, and D.-P. Yu. Synthesis and Quantum Transport Properties of Bi_2Se_3 Topological Insulator Nanostructures. *Scientific Reports*, 3:1264, 2013.

[YTK+15] R. Yoshimi, A. Tsukazaki, Y. Kozuka, J. Falson, K.S. Takahashi, J.G. Checkelsky, N. Nagaosa, M. Kawasaki, and Y. Tokura. Quantum Hall effect on top and bottom surface states of topological insulator $(Bi_{1-x}Sb_x)_2Te_3$ films. *Nature Communications*, 6:6627, 2015.

[Zal94] P.C. Zalm. Secondary ion mass spectrometry. *Vacuum*, 45:753–772, 1994.

[Zan86] K.R. Zanio. The effect of interdiffusion on the shape of HgTe-CdTe superlattices. *J. Vac. Sci. Technol. A*, 4:2106, 1986.

[ZCS12] Z. Zhu, Y. Cheng, and U. Schwingenschlögl. Band inversion mechanism in topological insulators: A guideline for materials design. *Phys. Rev. B*, 85:235401, 2012.

[ZHC+10] Y. Zhang, K. He, C.-Z. Chang, C.-L. Song, L.-L. Wang, X. Chen, J.-F. Jia, Z. Fang, X. Dai, W.-Y. Shan, S.-Q. Shen, Q. Niu, X.-L. Qi, S.-C. Zhang, X.-C. Ma, and Q.-K. Xue. Crossover of the three-dimensional topological insulator Bi_2Se_3 to the two-dimensional limit. *Nature Physics*, 6:584–588, 2010.

[Zie77] J.F. Ziegler. Helium Stopping Powers and Ranges in All Elements. *Pergamon Press, Oxford*, 1977.

[ZLS15] S.B. Zhang, H.Z. Lu, and S.Q. Shen. Edge states and integer quantum Hall effect in topological insulator thin films. *Scientific Reports*, 5:13277, 2015.

[ZTO+12] M. Zholudev, F. Teppe, M. Orlita, C. Consejo, J. Torres, N. Dyakonova, M. Czapkiewicz, J. Wrobel, G. Grabecki, N. Mikhailov, S. Dvoretskii, A. Ikonnikov, K. Spirin, V. Aleshkin, V. Gavrilenko, and W. Knap. Magnetospectroscopy of two-dimensional HgTe-based topological insulators around the critical thickness. *Phys. Rev. B.*, 86:205420, 2012.